Habilitation à diriger des recherches en sciences

Université Paris Diderot

Matthias González

Simulations d'hydrodynamique radiative : applications à l'astrophysique de laboratoire et perspectives en formation des étoiles massives

soutenue publiquement le 27 octobre 2017 devant le jury composé de :

M.	Dominique	Aubert	MCU HDR	Université de Strasbourg	Rapporteur externe
M.	Andrea	Ciardi	MCU HDR	Université Pierre et Marie Curie	Rapporteur externe
M.	Jacques	Le Bourlot	PU	Université Paris Diderot	Rapporteur interne
Mme	Frédérique	Motte	DR	CNRS	Examinatrice
M.	Rodolphe	Turpault	PU	Bordeaux-INP	Examinateur

Remerciements

Je tiens tout d'abord à remercier les membres de mon jury d'avoir bien voulu prendre un peu de leur temps pour participer à l'évaluation de cette HDR.

J'ai une pensée particulière pour ceux, ils se reconnaîtront, qui m'ont encouragé, poussé, avec insistance pour certains, à passer mon HDR, et ce depuis déjà quelques années. Je souhaite bon courage à ceux qui se lancent dans l'aventure, de gré ou de force. Merci à Diego pour m'avoir aidé sur le chemin tortueux des formalités administratives de l'université.

Je pense également à mes collègues enseignants-chercheurs de l'UFR avec qui j'ai eu l'occasion d'enseigner et avec qui je peux partager mes questionnements en termes de pédagogie et de formation. Merci en particulier à Véronique et Cyril, qui m'ont fait l'amitié de venir à ma soutenance.

Cela fait maintenant un peu plus de 17 ans que j'ai franchi la porte du SAp pour la première fois pour y effectuer mes différents stages ingénieur. Je pense à ceux qui m'ont accueilli alors que je n'étais encore qu'élève-ingénieur et qui m'ont donné l'opportunité de découvrir le monde de la recherche en astrophysique : Romain, Edouard et Jean-Pierre.

Je remercie également le laboratoire AIM dans son ensemble. Je mesure la chance que j'ai de travailler dans un environnement aussi stimulant et enrichissant.

Un grand merci aux membres actuels et passés du laboratoire LMPA : Thierry, Sébastien, Patrick, Edouard, Romain, Frédéric, Jean-Pierre... Je profite de l'opportunité qui m'est donnée pour les remercier de l'ambiance, des discussions et de l'émulation scientifique qui ont rythmé mon quotidien durant ces nombreuses années. C'est grâce à eux que j'ai le courage d'affronter le RER B aussi souvent que ma charge d'enseignement me le permet. Un merci particulier à Thierry et Sébastien pour leur bienveillance et leurs encouragements.

Enfin, un grand merci à Amélie pour son soutien infaillible et à Miguel et Pablo pour animer mon quotidien.

Table des matières

Deuxième Partie : Travaux de recherche

Première Partie :

Curriculum Vitae

Matthias González
Né le 7 mai 1980
à Fontenay-aux-Roses (92)
Nationalité franco-espagnole
Marié, 2 enfants

Laboratoire AIM (UMR 7158)
CEA Saclay, DRF/IRFU/SAp
L'Orme des Merisiers, bât. 709
91191 Gif-sur-Yvette Cedex
01 69 08 17 79
matthias.gonzalez@cea.fr

Carrière

2009- : maître de conférences à l'Université Paris 7-Denis Diderot, affecté au laboratoire AIM (UMR 7158)

2006-2009 : post-doctorat à l'Instituto de Fusión Nuclear (IFN/DENIM) Universidad Politécnica de Madrid (Espagne) avec Pedro Velarde Mayol

2003-2006 : thèse à AIM (UMR 7158) sous la direction de Jean-Pierre Chièze et Edouard Audit

Diplômes

2003-2006 : Thèse de doctorat en astrophysique, Université Paris XI mention très honorable

2002-2003 : DEA Astrophysique et instrumentations associées de l'Université Paris VI, mention Bien

1999-2002 : École Centrale de Nantes option Mécanique des Fluides Numérique, mention Bien

2001-2002 : DEA Dynamique des fluides et transferts option modélisation numérique, mention Bien

2000-2001 : Maîtrise de Physique de l'Université des Sciences et Techniques de Nantes, mention Assez Bien

Distinctions

2009 : lauréat d'une bourse Juan de la Cierva du ministère espagnol des Sciences et de l'Innovation

2007 : lauréat d'une bourse Lavoisier du ministère français des Affaires Étrangères et Européennes

Production scientifique

Conférences

- EWASS 2017, Prague (République Tchèque), 26-30 juin 2017, **poster**
- SFDE 2016, Quy Nhon (Vietnam), 25-29 juillet 2016, **poster**
- EPOS 2016, Ringberg (Allemagne), 27 juin-1er juillet 2016, **poster**
- Journées de la SF2A 2015, Toulouse (France), 2-5 juin 2015, **présentation**
- HEDLA 2014, Bordeaux (France), 12-16 mai 2014, **présentation invitée**
- Astronum-2013, Biarritz (France), 1-5 juillet 2013, **présentation invitée**
- Forum ILP 2011, Praz-sur-Arly (France), 6-11 février 2011, **présentation invitée**
- Frontiers in Computational Astrophysics, Lyon (France), 11-15 octobre 2010, **présentation**
- Astronum-2009, Chamonix (France), 29 juin - 3 juillet 2009, **présentation invitée**
- HEDLA 2008, Saint-Louis (Missouri, États-Unis), 11-15 avril 2008, **présentation**
- Astronum-2007, Paris (France), 11-16 juin 2007, **présentation invitée**
- Journées de la SF2A 2006, Paris (France), 26-30 juin 2006, **présentation**
- 29th ECLIM, Madrid (Espagne), 12-16 juin 2006, **présentation**
- Journées de la SF2A 2005, Strasbourg (France), 27 juin-1er juillet 2005, **présentation**
- HEDLA 2004, Tucson (Arizona, États-Unis), 10-13 mars 2004, **poster**

Workshops

- `CoCoNuT` meeting 2015, Málaga (Espagne), 18-20 novembre 2015
- Enseigner la physique à l'Université, Paris, 6-7 juillet 2015
- `Ramses` User Meeting, Saclay, 25-27 juin 2014
- Journées Plasmas à l'UPMC, Paris, 27 mars 2014, **présentation invitée**
- Forum de prospective du PNPS, Besançon, 24-26 février 2014, **présentation invitée**
- Workshop ANR SN2NS, Paris, 3-5 février 2014, **présentation invitée**
- Workshop radiative transfer, Saclay, 30 septembre-2 octobre 2013, **présentation invitée**
- ANR Starshock Kick-off meeting, Paris, 23-24 avril 2009, **présentation**

- Perspectives in Radiative Transfer and Interferometry, Lyon, 14-16 mai 2007, **présentation invitée**
- Forum ILP, Arcachon, 25-30 mars 2007, **présentation**
- TUIXS project simulation workshop, Madrid (Espagne), 22-23 février 2007, **présentation invitée**
- Atelier formation étoiles massives, Bordeaux, 18-19 février 2007, **présentation invitée**
- IPAM Long Program : Grand Challenge Problems in Computational Astrophysics. Workshop IV : Transfer Phenomena, Los Angeles (États-Unis), 16-20 mai 2005
- ANR Horizon Kick-off meeting, Paris, 13 septembre 2004, **présentation**

Séminaires

- Univ. Tübingen (Allemagne) 9 mai 2017, séminaire invité
- GRAAL (Montpellier) 9 décembre 2009, séminaire invité
- LERMA (Meudon) 25 janvier 2008
- CELIA (Bordeaux) 18 janvier 2007

Diffusion des travaux

Vulgarisation

- Article dans La Recherche décembre 2015 sur la fontaine aux supernovæ
- Article dans HPC Magazine sur le méso-challenge sélectionné en 2013 : N. Vaytet, J. Masson, B. Commerçon, M. González et G. Chabrier "Simulations de formations d'étoiles à petites et grandes échelles" lien

Diffusion

- Mise en ligne du code astrophysique `HERACLES` : lien
- 2015- : co-responsable du site web et de la communication du groupe simulations numériques d'AIM
- 2011 : co-organisateur de séminaires et journal-club du groupe simulations numériques d'AIM

Conférences et workshops invités

Conférences invitées

- HEDLA 2014, Bordeaux (France), 12-16 mai 2014, **présentation invitée**

- Astronum-2013, Biarritz (France), 1-5 juillet 2013, **présentation invitée**
- Forum ILP 2011, Praz-sur-Arly (France), 6-11 février 2011, **présentation invitée**
- Astronum-2009, Chamonix (France), 29 juin - 3 juillet 2009, **présentation invitée**

Workshops invités

- Journées Plasmas à l'UPMC, Paris, 27 mars 2014, **présentation invitée**
- Forum de prospective du PNPS, Besançon, 24-26 février 2014, **présentation invitée**
- Workshop ANR SN2NS, Paris, 3-5 février 2014, **présentation invitée**
- Workshop radiative transfer, Saclay, 30 septembre-2 octobre 2013, **présentation invitée**
- Perspectives in Radiative Transfer and Interferometry, Lyon, 14-16 mai 2007, **présentation invitée**

Participation à des jurys de thèse

- Raj Laxmi Singh, UPMC, 2 mars 2017, examinateur

Comité de suivi de thèse

- 2016-2019 : membre expert du comité de suivi de thèse de Salvatore Colombo, doctorant au LERMA
- 2016-2019 : membre local ("parrain") du comité de suivi de thèse de 8 doctorants à AIM (Quentin André, Mansour Benbakoura, Roxane Barnabé, Antonello Calabrò, Francis Fortin, Maximilien Franco, Barbara Perri, Morgan Schmitz)
- 2015-2018 : membre du comité de suivi de thèse de Mathilde Gaudel, doctorante à AIM
- 2014-2017 : membre du comité de suivi de thèse de Yueh-Ning Lee, doctorante à AIM
- 2013-2016 : membre du comité de suivi de thèse de Alan Loh, doctorant à AIM

Responsabilités scientifiques

Service

2006-2014 : maintien du code astrophysique `HERACLES` : lien

Projets scientifiques

- Membre chaque année de demande de temps de calcul sur les moyens nationaux GENCI (campagne DARI environ 1 million d'heures CPU chaque année)
- Membre d'une demande méso-challenge (porteur Neil Vaytet) sélectionnée en 2013 : "Global and Local Star Formation with State-of-the-Art Physics"
- Porteur d'une demande PRACE Preparatory Access sélectionnée en 2011 : "HERACLES hybride" sur le portage du code `HERACLES` en OPEN-MP+MPI
- Membre du projet lauréat du Grand Prix scientifique de la Fondation Simone et Cino del Duca (porteur Romain Teyssier) sélectionné en 2011
- Membre de l'ANR COSMIS (2011-2015, porteur Patrick Hennebelle)

Conférences

- Membre du LOC des Journées de la SF2A 2014, Paris, 3-6 juin 2014
- Membre du SOC du Forum ILP 2014, Orcières, 2-7 février 2014

Responsabilités

- 2010-2014 : membre nommé du conseil scientifique du Campus Spatial de l'Université Paris Diderot

Responsabilités administratives

- 2016- : point de contact de l'ED 560 STEP'UP pour le laboratoire AIM
- 2016- : correspondant des doctorants 2016-2019 du laboratoire AIM
- 2016- : Membre nommé du Conseil des BIATSS de l'UFR de Physique de l'Université Paris Diderot
- 2015- : Membre élu du Conseil d'UFR de Physique de l'Université Paris Diderot
- 2015- : Membre élu du Conseil National des Universités, section 34
- 2011, 2012 : Membre nommé de jurys de sélection de Maître de Conférences à l'UFR de Physique de l'Université Paris Diderot (APC en 2011 et AIM en 2012).

Responsabilités pédagogiques

- 2012-2015 : Membre nommé du conseil des enseignements de l'UFR de Physique de l'Université Paris Diderot

- 2012-2016 : Responsable du cours de méthodes numériques (1ère année d'école d'ingénieur EIDD, université Paris Diderot)

Encadrement doctoral et scientifique

Encadrement de stagiaires

- Raphaël Mignon-Risse (M2 Astronomie et Astrophysique - Île de France) du 20 mars au 30 juin 2017. "Etude de la formation des étoiles massives : effet du transfert radiatif". 100% d'encadrement
- Aloÿs Dufour (M2 Dynamique des fluides et énergétiques - Orsay) du 15 février au 24 juin 2016. "Approche analogique de l'explosion des supernovæ par la fontaine SWASI". 80% d'encadrement (le reste par Thierry Foglizzo)
- Thomas Padioleau (M1 modélisation et simulation - Orsay) du 15 avril au 31 août 2016. "Étude du feedback stellaire sur la fragmentation des cœurs denses". 50% d'encadrement (le reste par Patrick Hennebelle)
- Martin Gérard (M2 modélisation et simulation - INSTN) du 1er avril au 30 juin 2015. "Étude théorique des explosions asymétriques des supernovæ". 15% d'encadrement (le reste par Thierry Foglizzo)
- Adrien Kuntz et David Martin (L3 ENS Ulm) du 1er au 31 juillet 2014. "Étude des instabilités hydrodynamiques du dispositif SWASI et conséquences astrophysiques". 15% d'encadrement (le reste par Thierry Foglizzo)
- Hana Benhizia (1ère année de l'EIDD) en juin 2013. Stage d'un mois sur l'étude du transfert radiatif. 100% d'encadrement

Encadrement de thésitifs

- Raphaël Mignon-Risse (01/10/2017-30/09/2020)
  Obtention d'une bourse à l'école doctorale 560 STEP'UP pour commencer une thèse sous ma direction à l'automne 2017
- Pascal Tremblin (01/10/2009-30/09/2012)
  Thèse sous la direction de Edouard Audit et Vincent Minier sur l'effet de l'ionisation dans les nuages moléculaires et la formation stellaire. J'ai collaboré avec Pascal Tremblin sur l'utilisation et l'implémentation des modules de photo-ionisation et de gravité dans le code `HERACLES` (encadrement approximatif de 5%)

Encadrement de post-doctorants

- Mario Flock (02/01/2012-31/08/2015). Étude des disques protoplanétaires. Implémentation de l'algorithme de transfert radiatif dans le code `PLUTO` pour les premières simulations globales de disques magnétohydrodynamiques radiatifs (encadrement approximatif de 10%, le reste par Sébastien Fromang). cf. Flock *et al.* 2013b

- Titos Matsakos (01/09/2011-01/12/2013). Étude MHD des colonnes d'accrétion stellaires (encadrement approximatif de 5%, le reste par Jean-Pierre Chièze et Chantal Stehlé). cf. Matsakos *et al.* 2013
- Neil Vaytet (06/01/2009-05/01/2011). Développement du module M1 multigroupe dans le code `HERACLES` et applications aux chocs radiatifs en laboratoire (encadrement approximatif de 25%, le reste par Edouard Audit). Je collabore toujours étroitement avec Neil Vaytet qui est actuellement post-doctorant au Center for Star and Planet Formation (Université de Copenhague). cf. Vaytet *et al.* 2012; 2013

Enseignement universitaire

Vacations pendant la thèse

2004

Université Versailles Saint Quentin en Yvelines
TP d'électronique en DEUG MIAS 1ère année : 32hETD

2005

Université Paris Sud XI
TP numérique en M2 (Optique, Matière, Plasmas) : 8hETD

Vacations en post-doctorat

2008-2009

Universidad Complutense de Madrid
cours de dynamique des fluides en M1 Erasmus-Mundus (Fusion Science and Engineering Physics) : 1h30

Universidad Politécnica de Madrid
TD méthodes numériques en hydrodynamique à haute densité d'énergie en M2 (Sciences et Technologies Nucléaires) : 6hETD

cours en L3 (ATHENS Course Introduction to Nuclear Energy) : 1.5hETD

Service d'enseignement en tant que maître de conférences à l'Université Paris Diderot

2009-2010 (122hETD)
décharge d'1/3 de service en tant que néo-recruté

- TP de méthodes numériques en M1 (Sciences Physiques pour l'Ingénieur) : 36hETD
- colles en hydrodynamique en L1 : 44hETD
- TD d'hydrodynamique en L1 : 42hETD

2010-2011 (185,5hETD)

- TP de méthodes numériques en M1 (Sciences Physiques pour l'Ingénieur) : 36hETD
- TP de programmation en python en L2 (physiciens) : 45,5hETD
- TD de mécanique en L1 (groupe de chimistes et de physiciens) : 104hETD

2011-2012 (186hETD)

- cours d'initiation à l'astrophysique à des étudiants non scientifiques en L2 : 25hETD
- TD de mécanique en L1 (groupe de chimistes et physiciens) : 104hETD
- TP de programmation en python en L2 (physiciens) : 21hETD
- TP de méthodes numériques en 1ère année d'école d'ingénieur EIDD : 36hETD

2012-2013 (197hETD)

- TD de mécanique en L1 (groupe de chimistes et STEP) : 104hETD
- TP de programmation en python en L2 (physiciens) : 21hETD
- Cours de méthodes numériques en 1ère année d'école d'ingénieur EIDD : 36hETD
- TP de méthodes numériques en 1ère année d'école d'ingénieur EIDD : 36hETD
- Responsable du cours de méthodes numériques

2013-2014 (173hETD)

- TD de 1ère année de médecine (PACES) : 28hETD
- TD de mécanique en L1 (groupe de maths) : 52hETD
- TP de programmation en python en L2 (physiciens) : 21hETD
- Cours de méthodes numériques en 1ère année d'école d'ingénieur EIDD : 36hETD
- TP de méthodes numériques en 1ère année d'école d'ingénieur EIDD : 36hETD
- Responsable du cours de méthodes numériques

2014-2015 (180hETD)

- TD de 1ère année de médecine (PACES) : 84hETD
- TD de mécanique en L1 (groupe de CPEI) : 60hETD
- Cours de méthodes numériques en 1ère année d'école d'ingénieur EIDD : 36hETD
- Responsable du cours de méthodes numériques

2015-2016 (193,5hETD)

- TD de 1ère année de médecine (PACES) : 84hETD
- TD de mécanique en L1 (groupe de maths et CPEI) : 60hETD
- TD de thermodynamique en L1 (groupe de CPEI) : 13,5hETD
- Cours de méthodes numériques en 1ère année d'école d'ingénieur EIDD : 36hETD
- Responsable du cours de méthodes numériques

2016-2017 (173,5hETD)

- TD de 1ère année de médecine (PACES) : 112hETD
- TD d'hydrodynamique en M1 : 10,5hETD
- TP de flux et lois de conservation en L2 : 18hETD
- TP d'électromagnétisme en L2 : 15hETD
- report de 2015-2016 : 18hETD

Exposé synthétique des recherches

Domaines de recherche - description sommaire

Mon activité porte sur la modélisation, via des simulations numériques haute performance, de l'hydrodynamique radiative appliquée à l'astrophysique de laboratoire et à la physique de la formation stellaire. Je développe activement les codes numériques que j'utilise ensuite sur les grands moyens de calcul nationaux.

Mots-clés : transfert de rayonnement - hydrodynamique radiative - physique stellaire - astrophysique de laboratoire - simulation numérique - calcul haute performance

Astrophysique de laboratoire

Modélisation d'expériences de chocs radiatifs

collaboration : Neil Vaytet (Université de Copenhague), Chantal Stehlé, Laurent Ibgui (Observatoire de Paris), Frédéric Thais (CEA IRAMIS), Jean-Pierre Chièze (AIM)

Publications associées : Ibgui *et al.* 2012a;b; 2013b, Vaytet *et al.* 2012; 2013, González *et al.* 2014, Ibgui *et al.* 2015

Les installations de lasers de puissance permettent depuis une vingtaine d'années d'atteindre en laboratoire des énergies et des températures proches des conditions astrophysiques, en particulier des chocs d'accrétion stellaires. Des expériences permettent de produire des chocs radiatifs dans des cellules de gaz (xénon ou argon) à quelques dizaines voire centaines de km/s. Les résultats de ces expériences permettent une meilleure compréhension de la physique de ces chocs et participent aussi à la validation croisée entre simulation et expérimentation.

Mes simulations ont permis d'analyser les résultats expérimentaux obtenus lors de campagne d'expériences auprès du laser PALS (Prague). En particulier, mes résultats de simulations d'hydrodynamique radiative ont ensuite été utilisées pour un post-traitement par un code de transfert radiatif plus fin (`IRIS` développé par L. Ibgui) dans le but d'en extraire des spectres d'émission et d'intercomparer avec les résultats expérimentaux.

Nous avons aussi mené une étude plus théorique des chocs radiatifs. En particulier, nous avons étudié l'influence du nombre de groupes de fréquences considérés sur la structure de ces chocs. Nous avons montré que la prise en compte de plusieurs groupes induit de grandes différences par rapport à des simulations grises (c'est-à-dire ne considérant aucune dépendance spectrale),

et ce même pour un faible nombre de groupes. Dans nos conditions expérimentales, il faut par exemple un minimum de 50 groupes pour atteindre une convergence numérique sur la taille du précurseur radiatif.

Modélisation de la fontaine aux supernovæ

collaboration : Thierry Foglizzo (AIM)
Publications associées : Foglizzo *et al.* 2015

En 2012, Thierry Foglizzo a construit un analogue hydrodynamique de l'accrétion de gaz sur la proto-étoile à neutron dans les supernovæ à effondrement de cœur. Il s'agit d'une expérience à eau peu profonde, dans laquelle les ondes de gravité de surface jouent le rôle des ondes acoustiques du gaz stellaire. Cette expérience permet de mieux appréhender le mécanisme de l'instabilité advective-acoustique SASI, possiblement à l'origine des asymétries d'explosion de supernova. Son analogue dans l'expérience, SWASI, est une instabilité lié à un cycle entre ondes gravitaires et perturbations de vorticité.

Dans la première version du prototype expérimental, la fontaine était fixe et autorisait donc l'injection de l'eau sans moment cinétique initial (analogue d'un effondrement du gaz purement radial dans le cas astrophysique). Grâce à des simulations numériques shallow-water, nous avons pu comparer les fréquences expériementales et numériques des modes d'instabilité de SWASI.

Puis une nouvelle version de l'expérience a été construite, autorisant la rotation de la structure sur elle-même. Elle permet de prendre en compte l'injection d'un gaz avec un moment cinétique initial non nul et de voir son influence sur la rotation finale de l'étoile à neutrons ainsi que sur le sens de rotation des modes spiraux de l'instabilité. Nous avons montré un excellent accord entre simulation et expérience sur les taux de croissance de l'instabilité SWASI. Ce dispositif a de plus permis de mettre en évidence des conditions favorables à l'émergence de l'instabilité low-T/|W|.

Chocs d'accrétion stellaires

collaboration : Titos Matsakos, Jean-Pierre Chièze (AIM), Chantal Stehlé, Laurent Ibgui (Observatoire de Paris), Salvatore Orlando et Sara Bonito (Palermo, Italie)
Publications associées : Matsakos *et al.* 2013, Ibgui *et al.* 2014a;b, Matsakos *et al.* 2014a;b

Les étoiles jeunes accrètent de la matière depuis leur disque d'accrétion jusqu'à leur chromosphère par le biais de colonnes d'accrétion. A la base de ces colonnes se produisent des chocs d'accrétion. Des arguments théoriques et numériques prédisent des oscillations quasi-périodiques de l'émission de ces chocs qui ne sont pourtant pas observées.

Par le biais de simulations magnéto-hydrodynamiques 2D avec pertes radiatives et conduction, nous avons étudié si des perturbations de densité dans la colonne d'accrétion ou des fluctuations de la chromosphère pouvaient supprimer les oscillations. En analysant une large gamme de perturbations et de valeurs de champ magnétique, nous avons mis en évidence un régime pour lequel des fibrilles pouvaient osciller de manière indépendante, faisant disparaître les oscillations quasi-périodiques globales et permettant un meilleur accord avec les observations.

Disques d'accrétion protoplanétaires

collaboration : Mario Flock et Sébastien Fromang (AIM).
Publications associées : Flock *et al.* 2013a;b

La physique des disques protoplanétaires est un enjeu essentiel pour comprendre la formation des planètes. Les observations récentes ont permis de contraindre certains paramètres physiques comme la masse et la taille du disque ou le rapport de masse entre gaz et poussière. Toutefois, l'interprétation de ces observations est principalement fondée sur des modèles 2D de disques radiatifs visqueux. Cette viscosité est induite par la turbulence magnéto-hydrodynamique issue de l'instabilité magnéto-rotationnelle (MRI).

Nous avons réalisé les premières simulations 3D magnéto-hydrodynamiques radiatives d'un disque protoplanétaire stratifié, incluant de manière auto-consistante la MRI et l'irradiation due à l'étoile centrale. Nous avons trouvé que les propriétés de la turbulence sont similaires à des simulations globales localement isothermes. Toutefois, nous avons mis en évidence que le profil vertical en température est différent (avec un profil plat dans le plan médian) des modèles classiques simplifiés de disques visqueux.

Développements de codes numériques

Transfert radiatif

Une partie de mes recherches porte sur un travail théorique de la modélisation du transfert radiatif. La puissance des super-calculateurs ne permet pas encore de coupler dynamiquement la résolution des équations de l'"hydrodynamique avec celle du transfert radiatif dans toute sa complexité (dépendance spectrale, spatiale et temporelle). Il est nécessaire de faire des approximations pour la résolution du transfert radiatif. De nombreuses méthodes existent reposant sur différents types d'approximation. J'utilise pour ma part la méthode M1 dans le code `HERACLES` et la méthode de diffusion à flux limité (FLD) dans le code `RAMSES`. Lorsque la dépendance spectrale du transfert est négligée (on ne considère que des moyennes sur tout le spectre), on parle de méthode grise. A l'inverse, lorsque l'on tient compte de cette

dépendance, on considère les quantités radiatives constantes par morceaux sur des domaines spectraux appelés groupes de fréquence, et la méthode est qualifiée de multigroupe.

Code `HERACLES`

Une partie de mes recherches se fondent sur des simulations numériques réalisées grâce au code `HERACLES` dont je suis l'un des principaux auteurs. Une partie importante de mon temps de recherche est donc dédié au maintien et au développement continu de ce code. Ce travail purement numérique est un investissement lourd mais nécessaire pour que le code reste compétitif.

- développement d'un module pouvant traiter une gravité constante externe, en lien avec le travail du doctorant Pascal Tremblin (AIM) sur la formation des piliers dans les régions HII
- développement d'un module de transfert radiatif de diffusion à flux limité couplé à l'hydrodynamique et extension au cas multigroupe du module M1 déjà développé lors de ma thèse.
- ouverture du code au domaine public avec mise en ligne d'une version téléchargeable et mise en place de tests automatiques permettant à la fois de contrôler régulièrement les développements faits en interne et d'aider à la prise en main du code par des équipes externes
- développement d'une version hybride (MPI+OpenMP) de l'algorithme hydrodynamique et de turbulence forcée, avec Pierre Kestener (CEA, Maison de la Simulation). Test de scalabilité sur la machine CURIE.

Code `RAMSES`

collaboration : Benoît Commerçon (CRAL, ENS Lyon) et Neil Vaytet (Université de Copenhague).

Publications associées : González *et al.* 2015

Dans un certain nombre d'applications astrophysiques, le nombre très important d'échelles de distance à résoudre impose d'avoir recours à un code avec raffinement adaptatif de maillage et non à grille fixe. C'est le cas par exemple dans l'étude de la formation stellaire, où il faut résoudre les échelles depuis le nuage moléculaire jusqu'aux étoiles. C'est dans l'optique d'utiliser `RAMSES` pour la formation d'étoiles massives que je me suis investi dans le développement du transfert radiatif de ce code.

- extension du module de diffusion à flux limité grise développé par Benoît Commerçon au cas multigroupe pour tenir compte de la dépendance spectrale des opacités et des énergies radiatives
- mise en place de tests automatiques permettant de valider chaque nuit les développements du code, en comparant les résultats à des solutions analytiques ou de référence

— mise en place d'une version commune de `RAMSES` à partir des différentes versions disponibles à AIM (Patrick Hennebelle) et au CRAL (Benoît Commerçon). Cette version commune est pour l'instant privée (ici) mais a pour vocation d'être ouverte à la communauté dans un futur proche

Liste complète des publications scientifiques

Les données ci-dessous sont tirées du site ADS (lien vers mes publications sur ADS) et sont actualisées en date du 18 mai 2017

- 15 publications de rang A (revues internationales à comité de lecture) : 4 en 1er auteur, 3 en 2^{e} auteur, 4 en 3^{e} auteur, 2 en 4^{e} auteur
- 20 publications de rang B (mémoires de colloques internationaux)
- 275 citations de mes articles, h-index = 7

Publications en cours

1. Commerçon, B, M. **González**, N. Vaytet. "Massive star formation : fragmentation, disk and outflow". *To be submitted to A&A*.
2. Vaytet, N., B. Commerçon, J. Masson, M. **González** et G. Chabrier. "Simulating the second Larson core formation with non-ideal MHD". *To be submitted to A&A*.
3. Foglizzo, T., M. **González**, R. Kazeroni. "Asymmetric instabilities during the collapse of a rotating stellar core : shallow water experiment and modeling". *in prep.*

Publications de rang A

1. Ibgui, L., C. Stehlé, M. **González**, J.-P. Chièze, L. de Sá, T. Lanz et I. Hubeny (2015). "Assessment of the gray M_1 model in the case of a laboratory radiative shock simulation". In : *High Energy Density Physics* 17, p. 98–105. doi : 10.1016/j.hedp.2014.10.006.
2. Didelon, P., F. Motte, P. Tremblin, T. Hill, S. Hony, M. Hennemann, P. Hennebelle, L. D. Anderson, F. Galliano, N. Schneider, T. Rayner, K. Rygl, F. Louvet, A. Zavagno, V. Könyves, M. Sauvage, P. André, S. Bontemps, N. Peretto, M. Griffin, M. **González**, V. Lebouteiller, D. Arzoumanian, J.-P. Bernard, M. Benedettini, J. Di Francesco, A. Men'shchikov, V. Minier, Q. Nguyên Luong, P. Palmeirim, S. Pezzuto, A. Rivera-Ingraham, D. Russeil, D. Ward-Thompson et G. J. White (2015). "From forced collapse to H ii region expansion in Mon R2 : Envelope density structure and age determination with Herschel". In : *A&A* 584, A4, A4. doi : 10.1051/0004-6361/201526239.
3. **González**, M., N. Vaytet, B. Commerçon et J. Masson (2015). "Multigroup radiation hydrodynamics with flux-limited diffusion and adaptive mesh refinement". In : *A&A* 578, A12, A12. doi : 10.1051/0004-6361/201525971.
4. Foglizzo, T., R. Kazeroni, J. Guilet, F. Masset, M. **González**, B. K. Krueger, J. Novak, M. Oertel, J. Margueron, J. Faure, N. Martin, P. Blottiau, B. Peres et G. Durand (2015). "The Explosion Mechanism of Core-Collapse Supernovae : Progress in Supernova Theory and Experiments". In : *PASA* 32, e009, p. 9. doi : 10.1017/pasa.2015.9.
5. Flock, M., S. Fromang, M. **González** et B. Commerçon (2013b). "Radiation magnetohydrodynamics in global simulations of protoplanetary discs". In : *A&A* 560, A43, A43. doi : 10.1051/0004-6361/201322451.
6. Matsakos, T., J.-P. Chièze, C. Stehlé, M. **González**, L. Ibgui, L. de Sá, T. Lanz, S. Orlando, R. Bonito, C. Argiroffi, F. Reale et G. Peres (2013). "YSO accretion shocks : magnetic, chromospheric

or stochastic flow effects can suppress fluctuations of X-ray emission". In : *A&A* 557, A69, A69. DOI : 10.1051/0004-6361/201321820.

7. VAYTET, N., M. **González**, E. AUDIT et G. CHABRIER (2013). "The influence of frequency-dependent radiative transfer on the structures of radiative shocks". In : *J. Quant. Spec. Radiat. Transf.* 125, p. 105–122. DOI : 10.1016/j.jqsrt.2013.03.003.
8. STEHLÉ, C., M. **González**, M. KOZLOVA, B. RUS, T. MOCEK, O. ACEF, J. P. COLOMBIER, T. LANZ, N. CHAMPION, K. JAKUBCZAK, J. POLAN, P. BARROSO, D. BAUDUIN, E. AUDIT, J. DOSTAL et M. STUPKA (2010). "Experimental study of radiative shocks at PALS facility". In : *Laser and Particle Beams* 28, p. 253–261. DOI : 10.1017/S0263034610000121.
9. BUSQUET, M., F. THAIS, M. **González** et E. AUDIT (2010). "Measure of precursor electron density profiles of laser launched radiative shocks". In : *Journal of Applied Physics* 107.8, p. 083302. DOI : 10.1063/1.3330636.
10. STEHLÉ, C., A. CIARDI, J.-P. COLOMBIER, M. **González**, T. LANZ, A. MAROCCHINO, M. KOZLOVA et B. RUS (2009b). "Scaling stellar jets to the laboratory : The power of simulations". In : *Laser and Particle Beams* 27, p. 709. DOI : 10.1017/S0263034609990449.
11. **González**, M., E. AUDIT et C. STEHLÉ (2009). "2D numerical study of the radiation influence on shock structure relevant to laboratory astrophysics". In : *A&A* 497, p. 27–34. DOI : 10.1051/0004-6361/20079136.
12. VELARDE, P., M. **González**, C. GARCÍA-FERNÁNDEZ, E. OLIVA, A. KASPERCZUK, T. PISARCZYK, J. ULLSCHMIED, C. STEHLÉ, B. RUS, D. GARCÍA-SENZ, E. BRAVO et A. RELAÑO (2008). "Simulations of radiative shocks and jet formation in laboratory plasmas". In : *Journal of Physics Conference Series* 112.4, 042010, p. 042010. DOI : 10.1088/1742-6596/112/4/042010.
13. BUSQUET, M., E. AUDIT, M. **González**, C. STEHLÉ, F. THAIS, O. ACEF, D. BAUDUIN, P. BARROSO, B. RUS, M. KOZLOVA, J. POLAN et T. MOCEK (2007). "Effect of lateral radiative losses on radiative shock propagation". In : *High Energy Density Physics* 3, p. 8–11. DOI : 10.1016/j.hedp.2007.01.002.
14. **González**, M., E. AUDIT et P. HUYNH (2007). "HERACLES : a three-dimensional radiation hydrodynamics code". In : *A&A* 464, p. 429–435. DOI : 10.1051/0004-6361:20065486.
15. **González**, M. et E. AUDIT (2005b). "Numerical Treatment of Radiative Transfer". In : *Ap&SS* 298, p. 357–362. DOI : 10.1007/s10509-005-3969-2.

Publications de rang B

1. Vaytet, N., G. Chabrier, E. Audit, B. Commerçon, J. Masson, M. **González**, J. Ferguson et F. Delahaye (2015). "Protostellar Collapse Using Multigroup Radiation Hydrodynamics". In : *Astronomical Society of the Pacific Conference Series*. Sous la dir. de N. V. Pogorelov, E. Audit et G. P. Zank. T. 498. Astronomical Society of the Pacific Conference Series, p. 133.
2. Ibgui, L., L. de Sá, C. Stehlé, J.-P. Chièze, S. Orlando, I. Hubeny, T. Lanz, T. Matsakos, M. **González** et R. Bonito (2014a). "3D Gray Radiative Properties of a Radiation Hydrodynamic Model of a YSO Accretion Shock". In : *8th International Conference of Numerical Modeling of Space Plasma Flows (ASTRONUM 2013)*. Sous la dir. de N. V. Pogorelov, E. Audit et G. P. Zank. T. 488. Astronomical Society of the Pacific Conference Series, p. 83.
3. **González**, M., N. Vaytet, E. Audit et G. Chabrier (2014). "The Influence of Frequency-dependent Radiative Transfer on Radiative Shock Precursors". In : *8th International Conference of Numerical Modeling of Space Plasma Flows (ASTRONUM 2013)*. Sous la dir. de N. V. Pogorelov, E. Audit et G. P. Zank. T. 488. Astronomical Society of the Pacific Conference Series, p. 71.
4. Matsakos, T., J.-P. Chièze, C. Stehlé, M. **González**, L. Ibgui, L. de Sá, T. Lanz, S. Orlando, R. Bonito, C. Argiroffi, F. Reale et G. Peres (2014b). "3D YSO accretion shock simulations : a study of the magnetic, chromospheric and stochastic flow effects". In : *IAU Symposium*. Sous la dir. de P. Petit, M. Jardine et H. C. Spruit. T. 302. IAU Symposium, p. 66–69. doi : 10.1017/S1743921314001744.
5. Ibgui, L., S. Orlando, C. Stehlé, J.-P. Chièze, I. Hubeny, T. Lanz, L. de Sá, T. Matsakos, M. **González** et R. Bonito (2014b). "3D Gray Radiative Properties of Accretion Shocks in Young Stellar Objects". In : *European Physical Journal Web of Conferences*. T. 64. European Physical Journal Web of Conferences, p. 4005. doi : 10.1051/epjconf/20136404005.

6. Matsakos, T., J.-P. Chièze, C. Stehlé, M. **González**, L. Ibgui, L. de Sá, T. Lanz, S. Orlando, R. Bonito, C. Argiroffi, F. Reale et G. Peres (2014a). "3D numerical modeling of YSO accretion shocks". In : *European Physical Journal Web of Conferences*. T. 64. European Physical Journal Web of Conferences, p. 4003. doi : 10.1051/epjconf/20136404003.
7. Flock, M., S. Fromang, M. **González** et B. Commerçon (2013a). "First Radiation Magnetohydrodynamic Global Simulations Of Protoplanetary Disks". In : *Protostars and Planets VI Posters*, p. 52.
8. Ibgui, L., I. Hubeny, T. Lanz, C. Stehlé, M. **González** et J. P. Chièze (2013). "3D Spectral Radiative Transfer with IRIS : Application to the Simulation of Laboratory Models of Accretion Shocks in Young Stellar Objects". In : *Numerical Modeling of Space Plasma Flows (ASTRONUM2012)*. Sous la dir. de N. V. Pogorelov, E. Audit et G. P. Zank. T. 474. Astronomical Society of the Pacific Conference Series, p. 66.
9. — (2012b). "3D numerical simulations of laboratory models of accretion shocks in young stellar objects". In : *SF2A-2012 : Proceedings of the Annual meeting of the French Society of Astronomy and Astrophysics*. Sous la dir. de S. Boissier, P. de Laverny, N. Nardetto, R. Samadi, D. Valls-Gabaud et H. Wozniak, p. 347–350.
10. Vaytet, N., E. Audit, B. Dubroca et M. **González** (2012). "A Numerical Model for Multigroup Radiation Hydrodynamics". In : *Numerical Modeling of Space Plasma Slows (ASTRONUM 2011)*. Sous la dir. de N. V. Pogorelov, J. A. Font, E. Audit et G. P. Zank. T. 459. Astronomical Society of the Pacific Conference Series, p. 180.
11. Ibgui, L., M. **González**, C. Stehlé, I. Hubeny et T. Lanz (2012a). "3D modeling of accretion shocks in young stellar objects : Simulation of laboratory experiments". In : *EAS Publications Series*. Sous la dir. de C. Stehlé, C. Joblin et L. d'Hendecourt. T. 58. EAS Publications Series, p. 149–154. doi : 10.1051/eas/1258024.
12. Stehlé, C., M. **González**, E. Audit et T. Lanz (2009a). "Radiative Shocks in the Context of Young Stellar Objects : A Combined Analysis from Experiments and Simulations". In : *Protostellar Jets in Context*. Sous la dir. de K. Tsinganos, T. Ray et M. Stute, p. 359–365. doi : 10.1007/978-3-642-00576-3_43.
13. **González**, M., P. Velarde et C. García-Fernández (2008). "First Comparison of Two Radiative Transfer Methods : M_1 and S_n Techniques". In : *Numerical Modeling of Space Plasma Flows*. Sous la dir. de N. V. Pogorelov, E. Audit et G. P. Zank. T. 385. Astronomical Society of the Pacific Conference Series, p. 91.

14. **González**, M., E. Audit, C. Stehle et M. Busquet (2008). “The influence of radiation on shocks structure in laboratory astrophysics”. In : *APS Meeting Abstracts*, p. 15002.
15. Busquet, M., E. Audit, C. Stehle, M. **González**, F. Thais, B. Rus, O. Acef, P. Barroso, A. Bar-Shalom, D. Bauduin, M. Kozlova, T. Lery, A. Madouri, T. Mocek et J. Polan (2006). “Laboratory Astrophysics : effects on radiative shock of lateral radiative losses.” In : *APS Meeting Abstracts*, 1072P.
16. **González**, M., C. Stehlé, E. Audit, M. Busquet, B. Rus et F. Thais (2006). “Modelling and laboratory experiments of astrophysical radiative shocks”. In : *SF2A-2006 : Semaine de l’Astrophysique Francaise*. Sous la dir. de D. Barret, F. Casoli, G. Lagache, A. Lecavelier et L. Pagani, p. 467.
17. **González**, M., E. Audit et T. Lery (2006). “Radiation hydrodynamics simulations of jets - ISM interactions”. In : *SF2A-2006 : Semaine de l’Astrophysique Francaise*. Sous la dir. de D. Barret, F. Casoli, G. Lagache, A. Lecavelier et L. Pagani, p. 235.
18. Audit, E. et M. **González** (2006). “HERACLES : a three dimensional radiation hydrodynamics code”. In : *EAS Publications Series*. Sous la dir. de P. Stee. T. 18. EAS Publications Series, p. 115–128. doi : 10.1051/eas:2006008.
19. **González**, M. et E. Audit (2005a). “HERACLES : a new, parallelized, multi-geometry, three dimensional radiation hydrodynamics code”. In : *SF2A-2005 : Semaine de l’Astrophysique Francaise*. Sous la dir. de F. Casoli, T. Contini, J. M. Hameury et L. Pagani, p. 751.
20. — (2005c). “Numerical Treatment of Radiative Transfer”. In : *High Energy Density Laboratory Astrophysics*. Sous la dir. de G. A. Kyrala, p. 357. doi : 10.1007/1-4020-4162-4_53.

Articles de vulgarisation

- Article dans La Recherche décembre 2015 sur la fontaine aux supernovæ
- Article dans HPC Magazine sur le méso-challenge sélectionné en 2013 : N. Vaytet, J. Masson, B. Commerçon, M. González et G. Chabrier "Simulations de formations d’étoiles à petites et grandes échelles" lien

Deuxième Partie :

Travaux de recherche

Introduction

Le fil conducteur de mes recherches est la simulation numérique lourde de phénomènes (astro-)physiques, et tout particulièrement du transfert radiatif. J'ai utilisé la modélisation numérique comme outil pour aborder les différentes thématiques scientifiques que j'ai pu étudier. Je me suis intéressé au couplage du transfert radiatif avec l'hydrodynamique d'un point de vue dynamique. En effet, le transfert peut être appréhendé selon deux optiques différentes : le considérer comme un outil de diagnostic et d'interprétation, ou comme un élément dynamique de la situation. Dans le premier cas, aucune rétroaction n'existe entre la structure hydrodynamique et le rayonnement, qui peut alors être traité dans toute sa complexité spectrale et directionnelle. C'est l'approche choisie par exemple dans les atmosphères d'étoiles pour déterminer le spectre émergent. Toutefois, il est des situations où le rayonnement joue un rôle prépondérant et structure la dynamique du flot : énergie et impulsion sont échangées entre les photons et le gaz. L'hydrodynamique radiative, cadre de mon travail de recherches, relève de ce second choix.

Les champs d'application de l'hydrodynamique radiative sont très vastes. En astrophysique, elle concerne des objets couvrant une large gamme d'échelles temporelles et spatiales. Elle intervient dans toutes les phases de l'évolution stellaire : chocs radiatifs d'accrétion lors de la formation des proto-étoiles, jets moléculaires radiatifs des étoiles jeunes, concurrence dans les atmosphères entre transports convectif et radiatif pendant la phase de séquence principale, et enfin chocs radiatifs lors de l'explosion des supernovæ.

Mes recherches s'inscrivent dans le cadre de l'astrophysique de laboratoire au sens de la prospective INSU 2015-2020 : les expériences de laboratoire et les simulations numériques. Jusqu'en 2013-2014, j'utilisais mes simulations presque exclusivement dans le cadre des expériences de chocs radiatifs. J'ai activement participé au développement du code `HERACLES`, en étant le principal développeur du module de transfert radiatif de ce code. J'ai ensuite utilisé cet outil dans la modélisation des chocs radiatifs étudiés en laboratoire.

Depuis 2014, tout en gardant cette forte composante de développement numérique, j'ai changé de domaine d'application et me suis tourné vers l'étude de la formation d'étoiles et celui des supernovæ. Pour cela, j'ai aussi changé d'outil numérique. J'ai développé un module de transfert radiatif

multigroupe dans le code `RAMSES` pour la formation d'étoiles. Quant aux supernovæ, j'ai utilisé le code `Jupiter` pour modéliser une expérience analogue en eau peu profonde : la fontaine aux supernovæ.

Ce manuscrit s'articule autour de trois chapitres. Dans le premier, je décris mon outil de travail que sont les simulations numériques d'hydrodynamique radiative, en détaillant en particulier les modèles de transfert radiatif que j'utilise. Dans le second, je décris mes activités en lien avec les expériences d'astrophysique en laboratoire : les chocs radiatifs puis la fontaine aux supernovæ. Enfin, dans le troisième, je détaille mes recherches sur la formation d'étoiles massives.

Chapitre 1

Simulations numériques d'hydrodynamique radiative

La puissance croissante des moyens de calcul permet d'atteindre des résolutions inégalées ou d'aborder des problèmes jusqu'ici inaccessibles. La simulation numérique est à l'heure actuelle un des piliers fondamentaux de la recherche en astrophysique, au même titre que la théorie, l'observation ou l'instrumentation.

Cette approche numérique est complémentaire des autres approches. En effet, les simulations numériques reposent sur des modèles physiques simplifiés. Elles doivent pour cela être validées par des calculs analytiques et des résultats expérimentaux avant d'être utilisées pour analyser les observations. Ces différents outils de recherche sont donc intimement liés et, par des validations croisées, aident à approfondir nos connaissances de l'hydrodynamique radiative.

Lors de mes recherches, je participe très activement au développement de codes numériques lié au calcul intensif de haute performance (High Performance Computing ou HPC).

Ce chapitre décrit le cadre dans lequel s'inscrivent mes développements numériques. Je décris dans un premier temps les équations de l'hydrodynamique radiative, puis les différents codes que j'ai développés avant de détailler les perspectives envisagées sur ce volet purement numérique.

1.1 Hydrodynamique d'un fluide parfait

Dans tout mon travail sur les écoulements astrophysiques, l'hydrodynamique est modélisée par un fluide parfait, obéissant donc aux équations d'Euler :

$$\left\{\begin{array}{lll} \partial_t\rho & +\nabla\cdot[\rho\mathbf{u}] & = 0 \\ \partial_t(\rho\mathbf{u}) & +\nabla\cdot[\rho\mathbf{u}\otimes\mathbf{u}+P\mathbb{I}] & = \mathbf{F} \\ \partial_t E & +\nabla\cdot[\mathbf{u}(E+P)] & = \mathbf{F}\cdot\mathbf{u} \end{array}\right. \tag{1.1}$$

avec ρ la densité, $\mathbf{u}$ la vitesse, P la pression, E l'énergie volumique totale $\frac{P}{\gamma-1}+\frac{1}{2}\rho u^2$ (dans le cas d'une équation d'état de type gaz parfait) et $\mathbf{F}$ la force volumique extérieure (comme la gravité par exemple).

1.2 Hydrodynamique radiative

1.2.1 Transfert radiatif

Lorsque le rayonnement est suffisamment couplé à l'hydrodynamique, il convient de résoudre dynamiquement et simultanément les équations d'Euler et l'équation du transfert :

$$(\frac{1}{c}\frac{\partial}{\partial t}+\mathbf{n}\cdot\nabla)I(\mathbf{x},t;\mathbf{n},\nu)=\eta(\mathbf{x},t;\mathbf{n},\nu)-\chi(\mathbf{x},t;\mathbf{n},\nu)I(\mathbf{x},t;\mathbf{n},\nu) \tag{1.2}$$

avec I l'intensité spécifique à une position $\mathbf{x}$, au temps t, dans une direction $\mathbf{n}$ et une fréquence ν ; c la vitesse de la lumière dans le vide, η le coefficient d'émission et χ celui d'extinction.

À l'équilibre thermodynamique local, l'équation du transfert s'écrit :

$$\begin{aligned}(\frac{1}{c}\frac{\partial}{\partial t}+\mathbf{n}\cdot\nabla)I(\mathbf{x},t;\mathbf{n},\nu) &= \sigma_a^\nu(B(\mathbf{x},t,\nu)-I(\mathbf{x},t;\mathbf{n},\nu))-\sigma_s^\nu I(\mathbf{x},t;\mathbf{n},\nu) \\ &\quad +\sigma_s^\nu\int_{4\pi}p^\nu(\mathbf{n}.\mathbf{n}')I(\mathbf{x},t;\mathbf{n}',\nu)d\mathbf{n}'\end{aligned} \tag{1.3}$$

en introduisant le coefficient d'absorption σ_a et celui de diffusion σ_s, $p^\nu(\mathbf{n}.\mathbf{n}')$ la fonction de redistribution angulaire de la diffusion (supposée ici ne dépendre que de l'angle entre la direction principale de propagation et la direction considérée), ainsi que la fonction de Planck définie par :

$$B(\mathbf{n},\nu,T)=\frac{2h\nu^3}{c^2}[\exp(\frac{h\nu}{kT})-1]^{-1} \tag{1.4}$$

où T désigne la température de la matière, h la constante de Planck, et k la constante de Boltzmann.

1.2.2 Modèle aux moments

L'équation du transfert dépendant de sept variables, il est trop coûteux numériquement de la résoudre directement avec les équations de l'hydrodynamique tridimensionnelle sur des milliers de pas de temps. Il convient alors

de faire des simplifications. L'une des possibilités est de prendre les moments de cette équation et faire ainsi disparaître la dépendance angulaire. C'est d'ailleurs la même approche qui est prise en hydrodynamique lorsqu'on considère les équations d'Euler plutôt que l'équation de Boltzmann. Si l'on considère les deux premières équations d'évolution des moments, on obtient le système :

$$\left\{ \begin{array}{rcl} \frac{\partial E_r^\nu}{\partial t} + \nabla \cdot \mathbf{F}_r^\nu &=& \sigma_a^\nu (4\pi B(\nu) - cE_r^\nu) \\ \frac{1}{c}\frac{\partial \mathbf{F}_r^\nu}{\partial t} + c\nabla \cdot \mathbb{P}_r^\nu &=& -(\sigma_a^\nu + (1-g^\nu)\sigma_s^\nu)\mathbf{F}_r^\nu \end{array} \right. \tag{1.5}$$

avec g^ν le moment d'ordre un de la fonction de redistribution angulaire de la diffusion p^ν, $E_r^\nu = \frac{1}{c}\oint I d\Omega$ l'énergie radiative, $F_r^\nu = \oint I \mathbf{n} d\Omega$ le flux radiatif et $P_r^\nu = \frac{1}{c}\oint I \mathbf{n} \otimes \mathbf{n} d\Omega$ la pression radiative, les moments d'ordre zéro, un et deux de l'intensité spécifique I.

1.2.3 Relations de fermeture

Pour pouvoir résoudre le système d'équations 1.5 ci-dessus, il convient de spécifier une relation de fermeture reliant la pression radiative à l'énergie et au flux radiatifs.

La diffusion à flux limité

Le modèle d'hydrodynamique radiative le plus utilisé consiste en fait à ne s'intéresser qu'à l'équation d'évolution de l'énergie radiative. La relation de fermeture lie alors le flux radiatif à l'énergie. C'est ce qu'on appelle le modèle de diffusion à flux limité (FLD) qui s'écrit

$$\frac{\partial E_r^\nu}{\partial t} + \nabla \cdot \frac{-c\lambda \nabla E_r^\nu}{(\sigma_a^\nu + (1-g^\nu)\sigma_s^\nu)} = \sigma_a^\nu (4\pi B(\nu) - cE_r^\nu) \tag{1.6}$$

avec λ un limiteur de flux ad-hoc permettant de conserver des valeurs de flux physiquement admissibles (Levermore et Pomraning 1981).

Initialement, cette méthode a été privilégiée dans une grande majorité de codes numériques d'hydrodynamique radiative car elle est très peu chère en temps de calcul : ZEUS-FLD (Turner et Stone 2001), COSMOS (Anninos *et al.* 2003), Whitehouse *et al.* (2005), PLUTO (Kolb *et al.* 2013, Flock *et al.* 2013b). Toutefois, cette théorie ne peut pas traiter de manière correcte les régions de transport, et ne permet pas de traiter un rayonnement à forte anisotropie angulaire. En particulier, on voit que le flux radiatif est toujours colinéaire et proportionnel au gradient de l'énergie, ce qui n'est pas vrai dans les régions optiquement minces. Cette caractéristique ne permet donc pas de conserver les ombres (González *et al.* 2007). Afin de s'affranchir de cette prescription du flux, d'autres modèles considérant aussi l'équation d'évolution du flux radiatif sont apparus.

Le modèle M1

Lorsqu'on considère les deux équations aux moments, il faut une relation de fermeture reliant le tenseur de pression radiative à l'énergie et au flux radiatif. Si l'on considère que la fonction de distribution des photons est axisymétrique autour d'une direction $\mathbf{n}$, on peut alors écrire le tenseur de pression sous la forme :

$$\mathbb{P}_r = (\frac{1-\chi}{2}\mathbb{I} + \frac{3\chi-1}{2}\mathbf{n}\otimes\mathbf{n})E_r \tag{1.7}$$

avec $\mathbf{n} = \frac{\mathbf{F_r}}{F_r}$ le vecteur unitaire aligné avec le flux radiatif, et χ un coefficient appelé le facteur d'Eddington dépendant de E_r et F_r.

Les différents modèles diffèrent par la forme du facteur d'Eddington utilisée. En ce qui nous concerne, nous nous sommes intéressés au modèle pour lequel $\chi = \frac{3+4f^2}{5+2\sqrt{4-3f^2}}$, avec $f = \frac{F_r}{cE_r}$ le flux réduit. Ce modèle M1 peut être obtenu de deux manières distinctes. Soit en appliquant une transformation de Lorentz à une distribution isotrope de photons (Levermore 1984), soit en maximisant l'entropie radiative (Dubroca et Feugeas 1999) de la distribution de photons sous-jacente.

Contrairement aux modèles OTVET (Gnedin et Abel 2001) ou de Davis *et al.* (2012) qui sont des relations de fermeture non locales, l'avantage du modèle M1 est d'avoir une relation de fermeture analytique et locale. Elle admet les bonnes limites diffusive et de transport (milieux optiquement épais et optiquement minces respectivement), et est fondée sur un principe physique de maximisation d'entropie. La localité fait que ce modèle est avantageux en termes de temps de calcul mais est aussi à l'origine de ses limitations. En effet, le modèle M1 est particulièrement bien adapté pour les champs de rayonnement simples, que ce soit en limite diffusive ou de transport. Toutefois, il atteint ses limites lorsque plusieurs sources diffusives dans un milieu optiquement mince coexistent (instabilité double faisceau Frank *et al.* 2012).

Il est intéressant de noter que le facteur d'Eddington χ peut être relié au limiteur de flux λ apparaissant dans les modèles FLD par la relation $\chi = \lambda+\lambda^2R^2$ avec $R = \|\nabla E_r\|/((\sigma_a+(1-g)\sigma_s)E_r)$. Ainsi, pour chaque choix de χ correspond un choix de λ. Plusieurs formulations ont été proposées dans la littérature pour λ (Kershaw 1976, Minerbo 1978, Levermore 1984). Notons que récemment Murchikova *et al.* 2017 ont étudié l'influence de ce choix de fermeture dans le cas du transfert appliqué aux neutrinos émis par une proto-étoile à neutrons dans le cadre des supernovæ à effondrement gravitationnel. Ils concluent qu'aucune fermeture n'est meilleure qu'une autre dans toutes les situations et que pour chaque choix une configuration peut être trouvée dans laquelle le résultat est moins bon.

Le modèle M1 a été développé pour la première fois en 3D dans le code `HERACLES` (cf. section 1.3.1, González *et al.* 2007). Depuis, il a été implémenté dans d'autres codes d'hydrodynamique radiative : `ATON` (Aubert et

Teyssier 2008), `RAMSES-RT` (Rosdahl *et al.* 2013), `Athena-Hyperion` (Skinner et Ostriker 2013), `EMMA` (Aubert *et al.* 2015).

1.2.4 Approximation multigroupe

Quel que soit le modèle aux moments choisi (FLD ou M1 par exemple), il convient ensuite de spécifier pour combien de fréquences on compte résoudre le système. Les moyens numériques actuels ont permis de s'affranchir de l'approximation grise qui consistait à ne considérer qu'une moyenne générale sur tout le spectre de fréquence. Sont apparues les méthodes dites multigroupes, où l'on considère N_g groupes de fréquences dans lesquelles les grandeurs radiatives sont constantes. L'approximation grise correspond simplement à prendre $N_g = 1$. Si l'on considère N_g groupes, il faut donc spécifier N_g relations de fermeture. Une façon naturelle d'étendre la relation de fermeture 1.7 du modèle M1 gris serait de maximiser l'entropie radiative totale. Toutefois, c'est une procédure complexe et qui donne des résultats en très bon accord avec une approche beaucoup plus simple. Turpault (2005) a montré qu'on pouvait écrire la relation 1.7 pour chaque groupe de fréquences indépendamment : $\mathbb{P}_g = (\frac{1-\chi_g}{2}\mathbb{I} + \frac{3\chi_g-1}{2}\mathbf{n_g}\otimes\mathbf{n_g})E_g$. C'est cette approche que nous avons donc adoptée. Les équations complètes du modèle d'hydrodynamique M1 multigroupe, écrites dans le repère comobile et sans diffusion, sont alors (Vaytet *et al.* 2011) :

$$\left\{\begin{array}{lcl}
\partial_t\rho + \nabla\cdot(\rho\mathbf{u}) & = & 0 \\
\partial_t(\rho\mathbf{u}) + \nabla\cdot(\rho\mathbf{u}\otimes\mathbf{u} + P\mathbb{I}) & = & \displaystyle\sum_{g=1}^{Ng}(\sigma_{Fg}/c)\mathbf{F}_g - \rho\nabla\Phi \\
\partial_t E + \nabla\cdot(\mathbf{u}(E+P)) & = & \displaystyle -\sum_{g=1}^{Ng}\Big(c(\sigma_{Pg}\Theta_g(T) - \sigma_{Eg}E_g) \\
 & & -(\sigma_{Fg}/c)\mathbf{u}\cdot\mathbf{F}_g\Big) \\
\partial_t E_g + \nabla\cdot\mathbf{F}_g + \nabla\cdot(\mathbf{u}E_g) & + & \mathbb{P}_g : \nabla\mathbf{u} \\
-\nabla\mathbf{u} : \displaystyle\int_{\nu_{g-1/2}}^{\nu_{g+1/2}}\partial_\nu(\nu\mathbb{P}_\nu)d\nu & = & c\big(\sigma_{Pg}\Theta_g(T) - \sigma_{Eg}E_g\big) \\
\partial_t\mathbf{F}_g + c^2\nabla\cdot\mathbb{P}_g + \nabla\cdot(\mathbf{u}\otimes\mathbf{F}_g) & + & \mathbf{F}_g\cdot\nabla\mathbf{u} \\
-\nabla\mathbf{u} : \displaystyle\int_{\nu_{g-1/2}}^{\nu_{g+1/2}}\partial_\nu(\nu\mathbb{Q}_\nu)d\nu & = & -\sigma_{Fg}c\mathbf{F}_g
\end{array}\right. \tag{1.8}$$

où nous avons défini

$$X_g = \int_{\nu_{g-1/2}}^{\nu_{g+1/2}} X_\nu d\nu \tag{1.9}$$

avec $X = E$, $\mathbf{F}$, $\mathbb{P}$, $\mathbb{Q}$ qui représentent l'énergie, le flux, la pression et le flux de chaleur radiatif dans chaque groupe g compris entre les fréquences $\nu_{g-1/2}$ et $\nu_{g+1/2}$ ($\mathbb{Q}$ est le moment d'ordre 3 de l'intensité spécifique), et $\Theta_g(T)$ est

l'énergie des photons ayant une distribution de Planck à la température T dans un groupe donné. Les coefficients σ_{Pg}, σ_{Eg} et σ_{Fg} sont les moyennes des σ_ν dans un groupe donné pondérées respectivement par la fonction de Planck, l'énergie radiative et le flux radiatif.

Ce sont ces équations multigroupes (modèle M1 ou FLD) que j'ai résolues dans les différents codes numériques que j'ai développés.

1.3 Les codes numériques développés

Je décris succinctement ici les deux codes numériques dont j'ai co-développé le module de tansfert radiatif, plus de détails sur l'implémentation numérique se trouvant dans les articles joints à la section 1.5.

Ces deux codes sont de type volumes finis et reposent sur des méthodes de Godunov avec résolution de problèmes de Riemann aux interfaces. La résolution de la partie hydrodynamique des équations 1.8 est traitée de façon explicite par un algorithme de MUSCL-Hancock. Quant à la partie transfert radiatif que j'ai développée, les conditions de stabilité explicites liées à la vitesse de la lumière sont trop restrictives. Cette partie est donc résolue de manière implicite avec des algorithmes d'inversion matricielle itérative.

1.3.1 `HERACLES`

`HERACLES` est un code à maillage fixe cartésien, cylindrique ou sphérique. Il résout les équations de l'hydrodynamique radiative dans le cadre du modèle M1. Je suis l'un des principaux développeurs de ce module de transfert radiatif. Ce module repose sur une méthode implicite de résolution avec un algorithme de Gauss-Seidel pour l'inversion du système linéaire associé. González *et al.* 2007 (article joint à la section 1.5) détaille l'implémentation numérique du modèle gris ainsi que les tests de validation. J'en résume ici les points essentiels. J'ai calculé analytiquement les valeurs propres du système d'équations obtenues afin de diminuer la diffusion numérique du schéma. De nombreux tests d'`HERACLES` ont permis de montrer sa meilleure précision par rapport aux modèles FLD, préservant par exemple les ombres. Cette préservation est particulièrement importante pour de nombreuses topologies, par exemple dans le cadre de la formation d'étoiles (milieu interstellaire inhomogène, disque protoplanétaire optiquement épais...). De plus, `HERACLES` montre un bon accord avec les codes Monte-Carlo qui résolvent exactement l'équation du transfert, notamment dans des situations avec scattering, difficiles à résoudre par d'autres méthodes. Cela prouve la pertinence du modèle M1 à la fois physiquement et numériquement.

J'ai par la suite implémenté une version multigroupe du modèle M1, cf. article Vaytet *et al.* (2013) joint à la fin du chapitre 2.1.4. Pour mes recherches, j'ai utilisé `HERACLES` pour la modélisation des chocs radiatifs (cf.

section 2.1), mais ce code a aussi été utilisé dans le cadre d'autres applications : la formation des régions HII (Tremblin *et al.* 2012), la dynamique du milieu interstellaire (Audit et Hennebelle 2005), l'interaction des ejecta de supernova avec le milieu circumstellaire (Dessart *et al.* 2017)...

Lors de mon post-docorat à l'Instituto de Fusión Nuclear (DENIM, Madrid), j'ai mené une comparaison entre le modèle M1 et le modèle aux ordonnées discrètes ou S_n (utilisé dans le code `ARWEN`, Ogando et Velarde 2001). Cette méthode est utilisée par exemple dans les codes FLASH (Rijkhorst *et al.* 2006), principalement dédié aux phénomènes de transport dans les supernovæ, et PENCIL (Heinemann *et al.* 2006), dédié à la turbulence interstellaire et aux jets dans les disques d'accrétion. Dans un premier temps, des simulations purement radiatives ont montré que le modèle M1 donnait de très bons résultats dans le cas d'une source unique (ponctuelle ou étendue) tandis que pour des sources multiples la solution était sous-estimée près de la source et sur-estimée loin de celle-ci. Pour ce qui est de la méthode S_n, la solution est toujours sous-estimée en raison du nombre limité de rayons lumineux pour discrétiser la sphère unité, phénomène appelé effet de rayon. Les différences entre les méthodes sont de l'ordre de quelques pourcents. Dans le cas d'une onde de Marshak, c'est-à-dire lors d'un couplage entre matière et rayonnement par le biais de la température uniquement (le fluide est au repos), les différences obtenues sur la température de la matière peuvent atteindre 18%. Notons au passage que le bruit inhérent à la méthode S_n dû à l'effet de rayon peut engendrer des instabilités numériques.

Nous avons ensuite étendu ces comparaisons en utilisant des cas-tests publiés pour lesquels une solution de référence analytique ou numérique était connue (González *et al.* 2009). Ces résultats ont montré que le modèle M1 approximait très bien les méthodes de transport dans la plupart des cas, y compris lors de la prise en compte des phénomènes de scattering. Dans des géométries complexes où des phénomènes d'ombre apparaissent, le modèle M1 atteint ses limites, tout en étant toutefois meilleur que le modèle classique de diffusion. Nous avons ensuite utilisé ces deux méthodes pour simuler un cas-test idéalisé de l'éclairement d'une cible de fusion inertielle montrant encore une fois des résultats similaires tant du point de vue du chauffage de la cible que de la chronométrie associée.

Dans la problèmatique des chocs radiatifs expérimentaux (cf. chapitre 2.1), le code de transfert radiatif `IRIS` (Ibgui *et al.* 2013a) a été utilisé pour post-traiter les résultats d'`HERACLES`. Les résultats des deux codes ont été comparés et ont montré un bon accord loin des parois (Ibgui *et al.* 2015), prouvant encore une fois la pertinence du modèle M1.

1.3.2 `RAMSES`

Dans un certain nombre d'applications astrophysiques, le nombre très important d'échelles de distance à résoudre impose d'avoir recours à un code

avec raffinement adaptatif de maillage et non à grille fixe. C'est le cas par exemple dans l'étude de la formation stellaire, où il faut résoudre les échelles depuis le nuage moléculaire ($\simeq 1$ pc $= 10^{13}$ km) jusqu'aux étoiles ($\simeq 10^3$ km), couvrant ainsi une gamme de 10 ordres de grandeur.

Dans le cadre de mes recherches en lien avec la formation d'étoiles massives (cf. chapitre 3), je me suis naturellement tourné vers l'utilisation du code `RAMSES` (Teyssier 2002).

`RAMSES` avait un module de diffusion à flux limité (FLD) dans l'approximation grise (Commerçon 2009). Nous avons étendu ce module au cas multigroupe pour tenir compte de la dépendance spectrale des opacités et des énergies radiatives. González *et al.* 2015 (article joint à la section 1.5) détaille cette implémentation. Elle a en particulier nécessité de changer l'algorithme d'inversion itérative. Alors que dans le cas gris, la matrice était symétrique et pouvait donc être inversée par une méthode de gradient conjugué, dans le cas multigroupe, les termes d'échanges d'énergie entre les groupes rendent la matrice non symétrique. Nous avons donc utilisé la méthode de bi-gradient conjugué pour inverser ce nouveau système. Nous avons fait plusieurs tests académiques pour montrer le bon scaling de la méthode et de son implémentation. Enfin, nous avons montré par le biais d'une simulation test que cette nouvelle méthode était adaptée au cadre de la formation stellaire.

1.4 Perspectives : préparer l'exascale

Les simulations numériques de calcul haute performance sont au cœur de ma recherche. Il est donc crucial de garder des outils numériques performants qui évoluent en fonction des avancées des super-calculateurs.

En plus de l'augmentation régulière de la puissance de calcul (barrière téraflopique franchie en 2000, barrière pétaflopique franchie en 2008), de nouvelles architectures ont vu le jour ces dernières années avec des machines hétérogènes et des accélérateurs de type GPU ou Xeon-Phi. L'architecture des grands calculateurs est ainsi en passe de subir des modifications profondes avec le passage à l'exaflopique. Il faut donc réfléchir dès à présent aux évolutions des codes numériques actuels pour qu'ils puissent tirer profit des machines qui seront construites dans un avenir proche (tolérance aux pannes, gestion des I/O sur des centaines de milliers de cœurs, architecture hétérogène...).

Dans ce contexte et au sein du projet COAST, une collaboration a été initée entre AIM (Patrick Hennebelle et moi-même) et la Maison de la Simulation (Edouard Audit, Pierre Kestener et Pascal Tremblin) dans le but de développer un nouvel outil numérique permettant l'exploitation des super-calculateurs de nouvelle génération qui arriveront dans les prochaines années.

Des efforts importants ont déjà été effectués avec la réalisation d'un code à maillage cartésien fixe entièrement sur GPU. Toutefois, comme souligné

précédemment, le maillage adaptatif reste indispensable dans bon nombre d'applications astrophysiques, dont la formation d'étoiles en particulier. Le passage de ce type de code sur GPU ou sur des machines hétérogènes reste très délicat. Le but de cette collaboration est de développer un code AMR démonstrateur efficace.

Pour ce faire, l'idée est de découpler au maximum les algorithmes physiques (hydrodynamique, MHD, gravité, transfert radiatif) de la "couche" bas niveau liée à la gestion de la grille AMR et de la mémoire. Cela permettra ensuite de s'adapter aux nouvelles architectures de machine en ne modifiant que la couche bas niveau, en minimisant l'impact sur les algorithmes liés à la physique. Nous nous appuierons pour cela sur l'utilisation de la bibliothèque p4est (Burstedde *et al.* 2011) qui permet de gérer des forêts d'octree AMR de manière efficace jusqu'à 100 000 cœurs CPU. Le but est donc de construire un démonstrateur utilisant `p4est` pour la gestion de l'AMR et de développer les algorithmes physiques dont nous avons besoin.

Un premier travail a déjà été réalisé au sein de la maison de la simulation avec le développement d'un algorithme d'hydrodynamique de type volumes finis/Godunov : c'est le code canoP. Il s'agira de poursuivre ces efforts en y intégrant dans un premier temps un solveur de MHD et un solveur de gravité. Des tests (scaling, temps de calcul) seront menés sur des cas simples pour comparer les performances de `canoP` à celles de `RAMSES`.

Dans un second temps, un solveur de transfert radiatif sera aussi implémenté. Pour les méthodes implicites itératives, nous pourrons utiliser la bibliothèque d'algèbre linéaire PETSc. Il existe déjà des fonctionnalités dans p4est permettant de coupler ces deux bibliothèques (Isaac et Knepley 2015). L'avantage sera ensuite de pouvoir utiliser au choix toutes les méthodes classiques d'inversion de matrices déjà implémentées de manière optimisée dans `PETSc`.

1.5 Publications choisies

González *et al.* 2007 : modèle M1 gris développé dans le code `HERACLES`

González *et al.* 2015 : modèle FLD multigroupe développé dans le code `RAMSES`

A&A 464, 429–435 (2007)
DOI: 10.1051/0004-6361:20065486

Astronomy & Astrophysics

HERACLES: a three-dimensional radiation hydrodynamics code⋆

M. González[1,2], E. Audit[1,2], and P. Huynh[3]

[1] CEA-Saclay, DSM/DAPNIA/Service d'Astrophysique, 91191 Gif-sur-Yvette Cedex, France
e-mail: mgonzale@cea.fr
[2] AIM – Unité Mixte de Recherche CEA, CNRS, Université Paris VII, UMR No. 7158, France
[3] CEA-Saclay, DSI/DIR, 91191 Gif-sur-Yvette Cedex, France

Received 24 April 2006 / Accepted 8 November 2006

ABSTRACT

Aims. We present a new three-dimensional radiation hydrodynamics code called HERACLES that uses an original moment method to solve the radiative transfer.
Methods. The radiation transfer is modelled using a two-moment model and a closure relation that allows large angular anisotropies in the radiation field to be preserved and reproduced. The radiative equations thus obtained are solved by a second-order Godunov-type method and integrated implicitly by using iterative solvers. HERACLES has been parallelized with the MPI library and implemented in Cartesian, cylindrical, and spherical coordinates. To characterize the accuracy of HERACLES and to compare it with other codes, we performed a series of tests including purely radiative tests and radiation-hydrodynamics ones.
Results. The results show that the physical model used in HERACLES for the transfer is fairly accurate in both the diffusion and transport limit, but also for semi-transparent regions.
Conclusions. This makes HERACLES very well-suited to studying many astrophysical problems such as radiative shocks, molecular jets of young stars, fragmentation and formation of dense cores in the interstellar medium, and protoplanetary discs.

Key words. radiative transfer – scattering – hydrodynamics – methods: numerical

1. Introduction

Since we receive almost all the information from astrophysical objects in the form of photons, there has been a long tradition of radiative transfer in the astrophysical community. However, most of the time, radiation is used as a probe of the physical system under study. For that purpose radiative transfer is treated in great detail, using complex spectral opacities and without assuming local thermodynamical equilibrium (Hauschildt et al. 1997; Kurucz 1996). However, in many cases, radiation cannot be considered as a passive probe of the physical system, but it has to be considered as an important dynamical constituent.

For this reason, and thanks to the ever-increasing computing power available, there has been a rise in the interest in radiation-hydrodynamics, that is, in the dynamical coupling of gas and radiation. However, using the radiative transfer models developed in the context of spectral analysis for radiation-hydrodynamics is far out of the reach of present computers. Therefore, in order to study the dynamics of multi-dimensional systems including radiative transfer, one has to greatly simplify the full transfer equation, which depends upon six variables in a three-dimensional problem.

Our objective is to propose a radiative transfer model that can preserve and reproduce large angular anisotropies in the radiation field, which properly treats the time dependence of the radiation field and which couples naturally to the modern high-resolution numerical schemes used for hydrodynamics. All this, of course, has to be obtained at a reasonable numerical cost.

Different physical approximations have been developed to model radiative transfer in particular cases. Within the limit of large optical thickness, the diffusion approximation can be used (Mihalas & Mihalas 1984; Dai & Woodward 1998; Turner & Stone 2001). On the other hand, the transport limit is reached for transparent media. Particular methods have been implemented to describe this regime (Dai & Woodward 2000).

In many problems of physical interest, regions of large opacities are found next to transparent regions. One possibility for treating these problems is to couple two approximate models, i.e. one for each region. However, this introduces large drawbacks due to the domain partition, some loss in accuracy in the transition zone; and most of the time the semi-transparent regions would not be described correctly. Monte-Carlo codes that directly solve the transfer equation (Mihalas & Mihalas 1984; Pascucci et al. 2004, and references therein) can describe both regimes; however, they are difficult to couple to hydrodynamical codes and are very costly, especially in the diffusion regime.

Other techniques have therefore been developed based on discretization both in angles and space. One of them consists in choosing a set of discrete directions and in computing the integral over solid angle by a weighted sum over these directions. This technique, called the discrete ordinates method, can solve radiative transfer problems with relatively good accuracy and moderate computing cost. Although it has been greatly extended since Chandrasekhar first introduction, it still has two major drawbacks: ray effects and false scattering (Coelho 2002). False scattering (equivalent to the false diffusion in hydrodynamics) is due to the spatial discretization and may be reduced by refining the grid. The ray effect appears in free-streaming

⋆ Appendices are only available in electronic form at http://www.aanda.org

regions and consists in anomalous distortions of radiation intensity. Moreover, this method cannot properly treat the specularly reflected beams because of the choice of discrete directions.

To overcome this problem, both the short or the long characteristic methods choose the photons trajectories as privileged directions (Rukolaine et al. 2002). In these methods, the radiative transfer equation is integrated over ray propagation. In the long characteristic algorithm, the ray is projected from each grid point to the domain boundaries where specific intensity is known via boundary conditions. This method is unfortunately very time-consuming and not well-suited to three-dimensional problems. That is why, in the short characteristic method, the rays are projected only to the neighboring cells (van Noort et al. 2002). This is much less time-consuming, but the interpolations needed along grid lines make it more diffusive than the long characteristic one.

Instead of trying to solve the full transfer equation as in the Monte-Carlo, the discrete ordinates, or the characteristic methods, it is also possible to use another class of methods that consists in solving an approximate simplified model. This class is dedicated to model situations where radiative transfer is strongly coupled with other phenomena (fluid motion, chemical reactions, etc.) as is the case in our domain of interest. These methods consider the moments of the radiative transfer equation and consist in choosing a closure relation to solve them. The most common of these methods is the flux-limited diffusion, which solves the evolution of the first moment (radiative energy) and uses a closure relation valid in the diffusion limit, which is an isotropic radiative pressure tensor. In this scheme, the flux is always colinear and proportional to the gradient of radiative energy. In addition, the equation is modified with an ad-hoc function (the flux limiter) in order to ensure that the radiative flux remains in physically acceptable limits. This method is very useful in diffusive regions because it gives good results at a reasonable computational cost. Nevertheless, it should be used with care when dealing with free-streaming regions. Another method of closing the system is the variable tensor Eddington formalism (VTEF). It solves, in a first step, the moment equations with a fixed Eddington tensor and then computes the new tensor by solving the transfer equation locally with a fixed source function (Gehmeyr & Mihalas 1993; Stone et al. 1992) or with an approximate time dependence (Hayes & Norman 2003). If this procedure is iterated until the value of the source converges, one has a means of solving the transfer equation exactly. The VTEF methods give better results than the flux-limited diffusion but are much more complex because they require the local resolution of the transfer equation at each time step.

We have chosen in this work to use a moment model to describe radiative transfer but with a more general closure relation than the flux-limited diffusion, but one that is nevertheless analytical. This model allows treatment of radiative transfer from the diffusion to the free-streaming regime at, as we will show, a relatively low cost and with good accuracy. Furthermore, since we use a moment model, elastic scattering can be taken into account at almost no extra cost and with a reasonable accuracy, which is not the case for the other methods described before. In the next section, we present the moment model and our chosen closure. Section 3 describe the numerical scheme and its actual parallel implementation. The next section presents some multidimensional tests to verify our code both on purely radiative problems and on radiation hydrodynamics, as well as some performance analysis. Finally, the last section presents a summary and concluding remarks.

2. The physical model

For most problems and for the foreseeable future, solving the full transfer equation in three dimensions is much too costly both in time and memory. This problem is even greater if one wants to couple the radiative transfer with hydrodynamics to study multidimensional time-dependent problems. For this reason, we decided to use a moment model that is much less expensive than the full transfer equation and couples naturally to hydrodynamics.

The radiative transfer equation for the specific intensity is

$$\left(\tfrac{1}{c}\tfrac{\partial}{\partial t} + \boldsymbol{n}\cdot\boldsymbol{\nabla}\right) I(\boldsymbol{x},t;\boldsymbol{n},\nu) = \sigma_{\rm a}^{\nu} B(\boldsymbol{x},t,\nu) - \sigma^{\nu} I(\boldsymbol{x},t;\boldsymbol{n},\nu) + \sigma_{\rm s}^{\nu}\int_{4\pi} g(\boldsymbol{n},\boldsymbol{n'}) I(\boldsymbol{x},t;\boldsymbol{n'},\nu)\mathrm{d}\boldsymbol{n'} \quad (1)$$

where c is the speed of light, $\sigma_{\rm a}^{\nu}$ the absorption coefficient, $\sigma_{\rm s}^{\nu}$ the scattering coefficient, $\sigma^{\nu} = \sigma_{\rm s}^{\nu} + \sigma_{\rm a}^{\nu}$ the total cross section, B the black body specific intensity, and g the scattering angular redistribution function. $\boldsymbol{n}$, $\boldsymbol{r}$, and t are the angular, spatial, and temporal variables.

Integrating Eq. (1) and Eq. (1) $\times\boldsymbol{n}$ over solid angle yields

$$\begin{cases} \partial_t E_{\rm r}^{\nu} + \nabla\cdot\boldsymbol{F}_{\rm r}^{\nu} = \sigma_{\rm a}^{\nu}(4\pi B - cE_{\rm r}^{\nu}) \\ \partial_t \boldsymbol{F}_{\rm r}^{\nu} + c^2\nabla\cdot\mathbb{P}_{\rm r}^{\nu} = -(\sigma^{\nu} - g_1\sigma_{\rm s}^{\nu})c\boldsymbol{F}_{\rm r}^{\nu} \end{cases} \quad (2)$$

where g_1 is the first moment of the angular redistribution function. Here, $E_{\rm r}$, $\boldsymbol{F}_{\rm r}$, and $\mathbb{P}_{\rm r}$ are respectively the radiative energy density, the radiative energy flux, and the radiative pressure, which are defined in terms of the zeroth, first, and second moments of the specific intensity as:

$$\begin{aligned} E_{\rm r}^{\nu} &= \tfrac{1}{c}\oint_{4\pi} I(\boldsymbol{x},t;\boldsymbol{n},\nu)\mathrm{d}\boldsymbol{n} \\ \boldsymbol{F}_{\rm r}^{\nu} &= \oint_{4\pi} \boldsymbol{n}\, I(\boldsymbol{x},t;\boldsymbol{n},\nu)\mathrm{d}\boldsymbol{n} \\ \mathbb{P}_{\rm r}^{\nu} &= \tfrac{1}{c}\oint_{4\pi} \boldsymbol{nn}\, I(\boldsymbol{x},t;\boldsymbol{n},\nu)\mathrm{d}\boldsymbol{n}. \end{aligned} \quad (3)$$

In this paper we concentrate on gray moment model, but the work we present can easily be generalized to multigroup radiative transfer (Turpault 2005). Assuming an isotropic scattering ($g_1 = 0$) and averaging the system (2) over frequency gives

$$\begin{cases} \partial_t E_{\rm r} + \nabla\cdot\boldsymbol{F}_{\rm r} = c(\sigma_{\rm P} a_{\rm r} T^4 - \sigma_{\rm E} E_{\rm r}) \\ \partial_t \boldsymbol{F}_{\rm r} + c^2\nabla\cdot\mathbb{P}_{\rm r} = -c(\sigma_{\rm F} + \sigma_{\rm s})\boldsymbol{F}_{\rm r} \end{cases} \quad (4)$$

where $\sigma_{\rm P}$ (respectively $\sigma_{\rm E}$ and $\sigma_{\rm F}$) are the means of $\sigma_{\rm a}^{\nu}$ weighted by the Planck function (respectively the radiative energy and flux) and $\sigma_{\rm s}$ the mean of the $\sigma_{\rm s}^{\nu}$ weigthed by the radiative flux. Therefore, if the frequency-dependent opacity coefficients ($\sigma_{\rm a}^{\nu}$ and $\sigma_{\rm s}^{\nu}$) are known, as well as the underlying specific intensity (which is the case in our model, see below), these means can be computed precisely.

Unfortunately, the previous system is not closed since the radiative pressure is not known. The pressure is then often expressed as $\mathbb{P}_{\rm r} = \mathbb{D}E_{\rm r}$ where $\mathbb{D}$ is the Eddington tensor. There are many physical approximations that can be used to determine the Eddington tensor. The simplest one is to use the Eddington tensor given by the diffusion limit: $\mathbb{D} = \mathbb{I}/3$, where $\mathbb{I}$ is the identity matrix. This corresponds to an isotropic radiation field. We also chose an analytical Eddington tensor in order to keep the method simple and cost competitive. But, as we will see, the underlying photon distribution function (or equivalently the specific intensity) is not isotropic, which makes the method applicable to a wide range of conditions.

In order to close system (4), we want to express the Eddington tensor, and therefore the underlying specific intensity, only in terms of $E_{\rm r}$ and $\boldsymbol{F}_{\rm r}$. It is then natural to suppose that the direction of the radiative flux is an axis of symmetry of the local

specific intensity. With this assumption, the Eddington tensor is given by (Levermore 1984)

$$\mathbb{D} = \frac{1-\chi}{2}\mathbb{I} + \frac{3\chi-1}{2}\boldsymbol{n}\otimes\boldsymbol{n} \tag{5}$$

where $\mathbb{I}$ is the identity matrix, χ is called the Eddington factor, and $\boldsymbol{n}$ a unit vector aligned with the radiative flux.

We now need to specify the Eddington factor in order to close the system. For that purpose we assume that the specific intensity of our radiative transfer model is given by

$$B(\nu, f, T^*) = \frac{2h\nu^3}{c^2}\left[\exp\left(\frac{h\nu}{kT^*}\left(1 - \frac{2-\sqrt{4-3\|\boldsymbol{f}\|^2}}{\|\boldsymbol{f}\|^2}\boldsymbol{f}.\boldsymbol{\Omega}\right)\right) - 1\right]^{-1} \tag{6}$$

where

$$T^* = \frac{2}{\|\boldsymbol{f}\|}\left(-1 + \sqrt{4-3\|\boldsymbol{f}\|^2}\right)^{\frac{1}{4}}\sqrt{\|\boldsymbol{f}\|^2 - 2 + \sqrt{4-3\|\boldsymbol{f}\|^2}}\left(\frac{E_\mathrm{r}}{a_\mathrm{r}}\right)^{\frac{1}{4}}$$

and $\boldsymbol{f} = \frac{\boldsymbol{F}_\mathrm{r}}{cE_\mathrm{r}}$ is the reduced flux. Note that by definition of E_r and $\boldsymbol{F}_\mathrm{r}$, we have $\|\boldsymbol{f}\| \leq 1$, which means that radiative energy is transported at most at the speed of light. This distribution can either be obtained by applying a Lorentz transform to an isotropic one (Levermore 1984) or by minimizing the radiative entropy (Dubroca & Feugeas 1999). As we shall see, this simple assumption for the specific intensity allows us to compute the Eddington factor easily and analytically, but one has to keep in mind that there might be some cases where assuming such a simplified geometry may be a very poor approximation.

In the M_1 model (Dubroca & Feugeas 1999; Ripoll et al. 2001), the previous form of the specific intensity is used to compute the Eddington factor, therefore closing system (4):

$$\chi = \frac{3+4\|\boldsymbol{f}\|^2}{5+2\sqrt{4-3\|\boldsymbol{f}\|^2}}. \tag{7}$$

We can see that this closure relation recovers the two asymptotic regimes of radiative transfer well. In the free-streaming limit (i.e. transparent media), we have $\|\boldsymbol{f}\| = 1, \chi = 1$ and $\mathbb{D} = \boldsymbol{n}\otimes\boldsymbol{n}$. On the other hand, in the diffusion limit, $\|\boldsymbol{f}\| = 0, \chi = 1/3$ and $\mathbb{D} = \frac{1}{3}\mathbb{I}$, which corresponds to an isotropic radiation pressure. Equivalently, we can get these two limits directly with the specific intensity. When $\|\boldsymbol{f}\| = 0$, $T^* = \left(\frac{E_\mathrm{r}}{a_\mathrm{r}}\right)^{\frac{1}{4}}$ and the distribution is a Planck function, whereas when $\|\boldsymbol{f}\| = 1$, it tends to a Dirac in the direction of $\boldsymbol{f}$.

3. Radiation transport in a static fluid

We first start by describing the interaction between a static fluid and radiation. The fluid can only be heated or cooled and its evolution is determined by the classical energy conservation equation with a source term characterizing the energy exchanges between the fluid and the radiation.

To ensure a good conservation of energy, we consider the equation for the total energy (radiation plus matter) instead of only matter energy. The system to be solved is:

$$\begin{cases} \partial_t e + \partial_t E_\mathrm{r} + \nabla\cdot\boldsymbol{F}_\mathrm{r} = 0 \\ \partial_t E_\mathrm{r} + \nabla\cdot\boldsymbol{F}_\mathrm{r} = c(\sigma_\mathrm{P} a_\mathrm{r} T^4 - \sigma_\mathrm{E} E_\mathrm{r}) \\ \partial_t \boldsymbol{F}_\mathrm{r} + c^2\nabla\cdot\mathbb{P}_\mathrm{r} = -(\sigma_\mathrm{F} + \sigma_\mathrm{s})c\boldsymbol{F}_\mathrm{r} \end{cases} \tag{8}$$

where e is the internal matter energy.

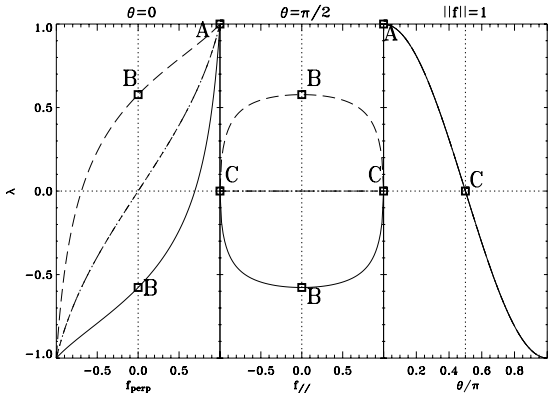

Fig. 1. Eigenvalues of the Jacobian matrix normalized by c.

3.1. The Riemann solver

To numerically solve the system above, we use a second-order *Godunov* type algorithm for the hyperbolic subsystem formed by the last two equations. The first equation is then integrated using the flux obtained by the hyperbolic solver.

It is worth noticing that the wave speeds of this subsystem, which mathematically correspond to the eigenvalues of its Jacobian matrix, depend only on the norm of the reduced flux $\boldsymbol{f}$ and on the angle θ of this flux with the considered interface. These wave speeds describe the speed at which the information is transported in the system, in the same way as the sound speeds in a fluid at rest. Figure 1 illustrates the behavior of the eigenvalues normalized by c for some characteristic values of θ and $\boldsymbol{f}$.

The left plot corresponds to a flux perpendicular to the interface ($\theta = 0$), which is similar to the mono-dimensional problem (cf. Fig. 1 of Audit et al. 2002). In particular, for a unit reduced flux (points A), the four eigenvalues are equal to c so the transport limit is correctly described. The middle plot represents the case where the flux is parallel to the interface. In that particular case, two eigenvalues are always equal to zero and the two others are equal in norms but of opposite sign. We can also notice that, when the reduced flux is unity (points C), the four eigenvalues are null. This is particularly interesting because it corresponds to the physical characteristic speeds of a transverse flux and because it means that there is no transport perpendicular to the radiative flux (cf. shadow test below). In all cases, we find that for $\|\boldsymbol{f}\| = 0$ (points B), the eigenvalues are $\{-c/\sqrt{3}, 0, 0, c/\sqrt{3}\}$, which are the proper propagation speeds in the diffusion limit. These eigenvalues are then used in our Riemann solver, which is an *HLLE (Harten-Lax-van Leer-Einfeldt)* scheme (Einfeldt et al. 1991), see Appendix A for details.

3.2. The system solver

Our scheme is of order two in space. It means that all quantities evaluated at the interfaces are reconstructed by using a linear reconstruction in each cell. To insure numerical stability, the results presented in this paper used a minmod limiter, but another limiter could easily be used instead. HERACLES has been implemented in order to work in either Cartesian, cylindrical, or spherical geometry (cf. Appendix B for the specific divergence discretization in these geometries).

Noticing that the time step given by the Courant condition is much smaller for radiation than for hydrodynamics, and since we are most often interested in studying system over hydrodynamical time scales, we need to develop an implicit algorithm for the

radiation. The time step is then given by the explicit Courant condition for hydrodynamics and by controlling the variation of the variables for the implicit radiative solver. When doing radiation-hydrodynamics, the smallest of these two time steps is taken (see Appendix C for details).

We now have to solve a non-linear set of equations (the non-linearities come from the Eddington factor and the T^4 terms). This is done using a Raphson-Newton method, which can eventually be restricted to a single iteration if solving the linearized system is enough. Either way, we have to invert a $(2+d)N^d \times (2+d)N^d$ matrix, where d is the dimensionality of the problem and N the number of cells along a direction. The typical scale of a simulation makes a direct inversion out of reach, so we need to resort to an iterative inversion method. We have implemented and tested two different methods that are relevant in different physical situations, each one efficient in one of the two limits of the transfer equation.

The Gauss-Seidel method (see Press et al. 1986, for further details) is very efficient in the transport limit. For example, in one dimension if we know a priori the direction in which the information propagates, the algorithm converges theoretically in only one iteration. To take advantage of this feature, we can also use a sweep method that inverts the cells ordering at each iteration. All the tests performed show that this method is very efficient both in time and in memory requirements. One could be tempted to use the improved method called successive over-relaxation (SOR), but it should be taken with care. Indeed, in some cases, too large extrapolation could lead to a non physical iterate that does not respect the condition $\|f\| \leq 1$ and that breaks down the iterations because of the M_1 closure.

On the other hand, the generalized minimal residual (GMRES) method (Saad & Schultz 1986), although more constraining in terms of memory requirement, is well-suited to the diffusion limit in which case the matrix is diagonally dominant. As each method dumps the residual in a different way, we also implemented a coupled version for which we switch between both methods. This version seems to have the best convergence rate (cf. Fig. D.2 and Appendix D for further details).

For both inversion methods, we need a convergence criterion. After trying various possibilities, we found that using the residual of the adimensioned equations gave the best results. In order to adimensionate the equation on the radiative flux, we divide it by the radiative energy times the speed of light and not by the radiative flux, which can be vanishing. In all the tests presented in this paper, the convergence is assumed to be achieved when this residual is less than 10^{-5}.

As our code is parallelized with the MPI library, we also quantified the scaling of these two methods as the number of processors increased. We found that both of them show good scaling; however, the Gauss-Seidel algorithm is nearly perfect, whereas GMRES could have a loss in performance reaching 20% (cf. Appendix D).

4. Radiation hydrodynamics in a moving fluid

We now generalize the previous analysis to a moving fluid. The fluid evolution is determined by the classical conservation equations (mass, momentum, and energy) with source terms characterizing the momentum and energy exchanges between the fluid and the radiation.

In order to write the radiation hydrodynamics equations, one has to choose the frame in which to evaluate the radiative quantities: laboratory frame or comoving frame (i.e. the frame moving with the fluid). The laboratory frame is convenient because the system remains globally conservative, which keeps the hyperbolic part (i.e. the left-hand side) of the system simple (Mihalas & Auer 2001). But in this frame, interactions with matter become complex because of Doppler and aberration effects that have to be incorporated in the source terms. On the other hand, using the radiative quantities expressed in the comoving frame (Lowrie et al. 2001) adds non-conservative terms to the equations. But the source terms remain unaffected by the fluid motions.

In HERACLES, we have chosen to express radiative quantities in the comoving frame. The equations of radiation hydrodynamics can then be written (Mihalas & Mihalas 1984) as

$$\begin{cases} \partial_t \rho & + \nabla \cdot [\rho \boldsymbol{u}] & = 0 \\ \partial_t (\rho \boldsymbol{u}) & + \nabla \cdot [\rho \boldsymbol{u} \otimes \boldsymbol{u} + P\mathbb{I}] & = \frac{\sigma_\mathrm{F}+\sigma_\mathrm{s}}{c} \boldsymbol{F}_\mathrm{r} \\ \partial_t E & + \nabla \cdot [\boldsymbol{u}(E+P)] & = -c(\sigma_\mathrm{P} a_\mathrm{r} T^4 - \sigma_\mathrm{E} E_\mathrm{r}) \\ & & \quad + \frac{\sigma_\mathrm{F}+\sigma_\mathrm{s}}{c} \boldsymbol{F}_\mathrm{r} \cdot \boldsymbol{u} \end{cases} \tag{9}$$

$$\begin{cases} \partial_t E_\mathrm{r} + \nabla \cdot [\boldsymbol{u} E_\mathrm{r}] + \nabla \cdot \boldsymbol{F}_\mathrm{r} + \mathbb{P}_\mathrm{r} : \nabla u \\ \qquad = c(\sigma_\mathrm{P} a_\mathrm{r} T^4 - \sigma_\mathrm{E} E_\mathrm{r}) \\ \partial_t \boldsymbol{F}_\mathrm{r} + \nabla \cdot [\boldsymbol{u} \boldsymbol{F}_\mathrm{r}] + c^2 \nabla \cdot \mathbb{P}_\mathrm{r} + (\boldsymbol{F}_\mathrm{r} . \nabla) u \\ \qquad = -(\sigma_\mathrm{F} + \sigma_\mathrm{s}) c \boldsymbol{F}_\mathrm{r} \end{cases} \tag{10}$$

where ρ is the matter density, $\boldsymbol{u}$ the velocity, E the total matter energy, P and T the pressure, and the temperature of the material. The previous equations are all Eulerian, but the radiative quantities are evaluated in the frame comoving with the fluid.

The resolution of the previous system is split into three steps. The first one updates the hydrodynamical quantities using a classical second-order Godunov type method. In the next step, the radiative quantities are updated implicitly, as described in the previous section. During this step, we use the velocity given by the hydro solver. In the third and final step, the $(\sigma_\mathrm{F} + \sigma_\mathrm{s})F/c$ source term is added to the gas momentum and total energy. Since in most cases this term is rather small, it is not necessary to treat it in the implicit system. This allows the reduction of the number of equations to be solved implicitly and makes the method more efficient:

$$\text{STEP 1} \begin{cases} \partial_t \rho & + \nabla \cdot [\rho \boldsymbol{u}] & = 0 \\ \partial_t (\rho \boldsymbol{u}) & + \nabla \cdot [\rho \boldsymbol{u} \otimes \boldsymbol{u} + P\mathbb{I}] & = 0 \\ \partial_t E & + \nabla \cdot [\boldsymbol{u}(E+P)] & = 0 \end{cases} \tag{11}$$

$$\text{STEP 2} \begin{cases} \partial_t e + \partial_t E_\mathrm{r} + \nabla \cdot [\boldsymbol{u} E_\mathrm{r}] + \nabla \cdot \boldsymbol{F}_\mathrm{r} \\ \qquad + \mathbb{P}_\mathrm{r} : \nabla u = 0 \\ \partial_t E_\mathrm{r} + \nabla \cdot [\boldsymbol{u} E_\mathrm{r}] + \nabla \cdot \boldsymbol{F}_\mathrm{r} \\ \qquad + \mathbb{P}_\mathrm{r} : \nabla u = c(\sigma_\mathrm{P} a_\mathrm{r} T^4 - \sigma_\mathrm{E} E_\mathrm{r}) \\ \partial_t \boldsymbol{F}_\mathrm{r} + \nabla \cdot [\boldsymbol{u} \boldsymbol{F}_\mathrm{r}] + c^2 \nabla \cdot \mathbb{P}_\mathrm{r} \\ \qquad + (\boldsymbol{F}_\mathrm{r} . \nabla) u = -(\sigma_\mathrm{F} + \sigma_\mathrm{s}) c \boldsymbol{F}_\mathrm{r} \end{cases} \tag{12}$$

$$\text{STEP 3} \begin{cases} \partial_t (\rho \boldsymbol{u}) = \frac{\sigma_\mathrm{F}+\sigma_\mathrm{s}}{c} \boldsymbol{F}_\mathrm{r} \\ \partial_t E = \frac{\sigma_\mathrm{F}+\sigma_\mathrm{s}}{c} \boldsymbol{F}_\mathrm{r} \cdot \boldsymbol{u}. \end{cases} \tag{13}$$

5. Verification tests

We performed a series of verification tests in order to better characterize the accuracy of HERACLES and to compare it with other codes. We reproduce here just the three that are particularly relevant to astrophysical conditions. Appendix E compiles others tests: beam test, pipe flow test, diffusion in a moving fluid, and a comparison with simple analytical models of matter-radiation coupling and Marshak wave.

5.1. Shadow test

We performed a 2D shadow test similar to the one presented in Hayes & Norman (2003). This test consists in lighting an oblate spheroid clump in a cylinder $L = 1$ cm, $R = 0.12$ cm. This spheroid is located on the symmetric axis and at the centre of the box width: $(z_c, r_c) = (0.5, 0)$. Its extension is $(z_0, r_0) = (0.1, 0.06)$.

Initially, the medium is at equilibrium with radiation i.e. $T_0 = T_r = 290$ K, and the density is homogeneous ($\rho_0 = 1$ g cm^{-3}) except for the clump with density ρ_1 one thousand times greater. The boundary of this region is smoothed, such as $\rho(z,r) = \rho_0 + \frac{\rho_1-\rho_0}{1+\exp\Delta}$ with $\Delta = 10\left[(\frac{z-z_c}{z_0})^2 + (\frac{r-r_c}{r_0})^2 - 1\right]$. The opacity of the medium is a function of density and temperature $\sigma = \sigma_0(\frac{T}{T_0})^{-3.5}(\frac{\rho}{\rho_0})^2$ with $\sigma_0 = 0.1$ cm^{-1}. Initially, the mean free path is then 10 cm in the cylinder and 10^{-5} cm in the clump. At time $t = 0$, a uniform source is lighted at the left boundary with $T_r = 1740$ K. The mean free path of a photon being much smaller in the clump (by six orders of magnitude), a shadow develops behind it. Until the light has crossed the clump, the shadow should remain stable.

Figure 2 shows the radiative temperature for three runs performed on a 280×80 grid. The first run (upper panel) was performed solving the diffusion equation. It corresponds to the time $t = 0.1$ s, which means 3×10^9 light crossing times. The other two runs used the M_1 model and differs by the method of computing the eigenvalues. In the first case (middle panel), we chose not to compute these eigenvalues and to set them arbitrarily equal to $\pm c$, whereas in the second run (lower panel), the eigenvalues were computed. To compare with the results obtained in Hayes & Norman (2003), we also plotted a radial profile of the radiative temperature at the outer boundary (cf. Fig. 3).

One can see that there is no longer a shadow in the first case. This is due to the fact that the diffusion equation is intrinsically isotropic ($\mathbb{P} = 1/3E\mathbb{I}$). Therefore, the photons can go around the obstacle immediately. In the two other cases, the shadow is better preserved even in the simple case without computing eigenvalues. As could be expected, the first method is more diffusive than the second one. The improvement obtained with the second method is easy to understand when looking at the real eigenvalues (cf. Sect. 3.1). The proper treatment of the propagation speed in the HLLE scheme is effective enough to inhibit large numerical diffusion between the shadowed and enlightened regions.

It is also interesting to compare the propagation speed of the radiation between the diffusion approximation and the M_1 model. For the diffusion, the characteristic length scales as the square root of time: $L \propto \sqrt{2\alpha t}$ where α is the diffusion coefficient. In our example, it means that radiation will cross the box in a few 10^{-9} s, whereas in reality as radiation propagates in a transparent medium, it goes at light speed and the crossing time is 3.33×10^{-11} s. In the two M_1 model simulations, we recover this value.

5.2. Semi-transparent regime

5.2.1. Without scattering

We now present a test of HERACLES in a semi-transparent regime where the validity of the physical model used to treat the transfer has to be assessed. The following test can be seen as a star with solar luminosity illuminating its surrounding disc of gas at a distance approximately equal to 5 AU (which corresponds to the Sun-Jupiter distance).

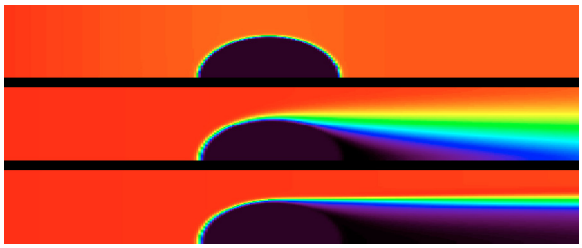

Fig. 2. Radiative temperature in the shadow test using the diffusion equation (*upper panel*), M_1 closure with fixed eigenvalues (*middle panel*), and M_1 closure with calculated eigenvalues (*lower panel*).

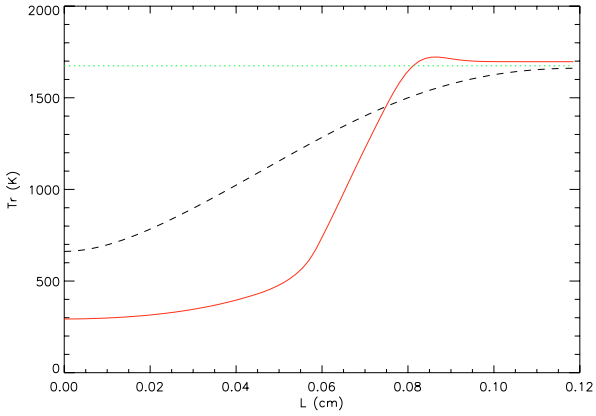

Fig. 3. Radial profiles of the radiative temperature in the shadow test using the diffusion equation (dotted line), M_1 closure with fixed eigenvalues (dashed line), and M_1 closure with calculated eigenvalues (solid line).

The simulation box, whose dimensions are $L_x = 7.48 \times 10^{12}$ cm and $L_y = 3.74 \times 10^{12}$ cm, is at equilibrium, and at $t = 0$ an incoming horizontal radiative flux equal to 5.44×10^4 erg s^{-1} cm^{-2} is set. The box is filled with matter at density 10^{-15} g cm^{-3}, while there is a vacuum on the outside. The width of the box corresponds to seven mean free paths (the absorption coefficient is $\kappa = 10^{-12}$ cm^{-1}) and is sampled over 50 cells. This box is therefore a semi-transparent region, and this run will test the accuracy of the M_1 closure in this particular transient regime. Figure 4 shows the isotherms obtained at equilibrium by HERACLES and by a Monte-Carlo code (Dullemond & Natta 2003).

The two results agree with good precision. The differences could be due to the M_1 model itself or to the slightly different treatment of the boundary conditions. It is important to note that the Monte-Carlo code solves the transfer equation exactly and, therefore, the agreement between these two approaches is a very good test to verify our model, both physically and numerically, in this semi-transparent regime.

5.2.2. With scattering

Scattering is a phenomenon that plays an important role in many astrophysical problems, such as in the interstellar medium where light is scattered by dust grains. The radiative model used in HERACLES allows us to treat scattering at no additional cost and with reasonable accuracy.

By definition, the importance of scattering compared to absorption is quantified by the albedo:

$$\omega = \frac{\sigma_s}{\sigma_F + \sigma_s}.$$

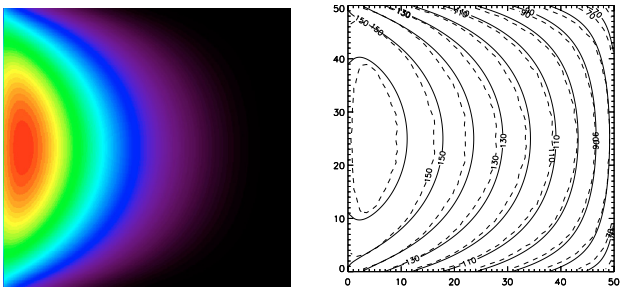

Fig. 4. *Left panel*: HERACLES temperature map. *Right panel*: isotherms for HERACLES (solid lines) and a Monte-Carlo code (dashed lines).

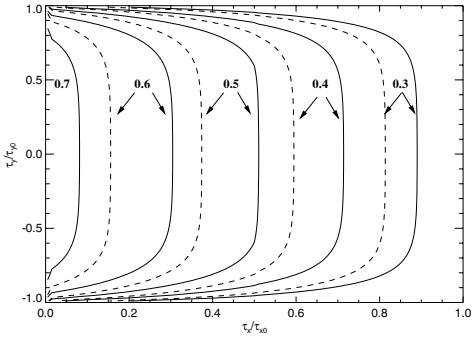

Fig. 5. Normalized radiative energy isocontours for $\omega = 1$ (solid lines) and $\omega = 0.9$ (dashed lines).

When $\omega = 0$, the medium is purely absorptive and, when $\omega = 1$, it is purely scattering. We have already seen (Eq. (4)) that the scattering only appears in the equation on the flux and not in the one on the energy. This is understood because elastic scattering redistributes the photons without changing their frequencies.

We wanted to perform the same test as above but with scattering; but to have results to compare with, we changed the scale of the problem and borrowed initial conditions from the engineering literature (Crosbie & Schrenker 1984). We consider a two-dimensional box whose dimensions are $L_x = \tau_{x0}$ and $L_y = 2\tau_{y_0}$ where $\tau_x = (\sigma_\mathrm{F} + \sigma_\mathrm{s})x$ and $\tau_y = (\sigma_\mathrm{F} + \sigma_\mathrm{s})y$ are the optical coordinates. This box is lit from left by a source at T_s and the steady state is achieved.

We reproduce the results of only one test here, but several others were performed and show good agreement, too. We took $\tau_{x0} = 1$, $\tau_{y_0} = 5$, and each direction is sampled over 100 cells. We chose this particular test because it reproduces a rectangular medium for which the influence of albedo is very important. Figure 5 shows the normalized radiative energy $(T_\mathrm{r}/T_\mathrm{s})^4$ isocontours at five values 0.3, 0.4, 0.5, 0.6, and 0.7, for $\omega = 1$ and $\omega = 0.9$. This figure is very similar to Fig. 12c of Crosbie & Schrenker (1984). As expected, the isocontours penetrate deeper in the domain when there is no absorption. Radiative energy is greater when absorption exists.

The differences in terms of distance covered between our results and those of Crosbie & Schrenker (1984) remain lower than 5%. But for HERACLES, contrary to other methods, the treatment of scattering is nearly free in terms of computational cost. Indeed, in our case, taking scattering into account implies slightly modifying the source term in the radiative flux equation, but it does not change the number of operations needed at each iteration of the implicit solver. On the other hand, when solving the transfer equation, treating scattering implies computing an integral over solid angles of the specific intensity, which is very costly.

5.3. Radiative shocks

Radiative shocks might be encountered in various astrophysical systems: stellar accretion shocks, pulsating stars, interaction of either jets or supernovæ with the interstellar medium, etc. They are also reproduced in laboratory experiments, in a scaled manner, in order to better understand their underlying physics (Bozier et al. 1986; González et al. 2006).

There are two kinds of shocks depending on the initial fluid speed: subcritical and supercritical (Mihalas & Mihalas 1984). When the initial fluid speed is low, the matter temperature before the shock is much lower than the matter temperature behind it and the transition is sharp. The radiative temperature never overshoots the temperature behind the shock. Such shocks are called subcritical. On the other hand, when the initial fluid speed is high enough, the temperature on each side of the shock are equal. The transition is smoother, the radiative precursor is larger, and a matter temperature peak, which extends over roughly one mean free path, appears just behind the shock. This is a supercritical shock. The specific profiles and characteristics of these shocks are the result of the strong coupling between matter and radiation.

We consider a 1D homogeneous medium where the fluid moves uniformly from right to left and the left boundary is a wall. A shock is therefore generated at this boundary and travels the box from left to right. The initial conditions are such that $L_x = 7 \times 10^{10}$ cm (divided in 300 cells) and $\rho = 7.78 \times 10^{-10}$ g cm^{-3}. The gas is perfect with an adiabatic coefficient of 7/5 and temperature at 10 K in equilibrium with radiation. The medium is supposed to have a constant extinction coefficient: $\sigma = 3.1 \times 10^{-10}$ cm^{-1}.

In all the above figures, we plot the temperatures as function of $x_i = x - ut$ to be able to compare our results with those obtained in Ensman (1994) and in Hayes & Norman (2003).

5.3.1. Subcritical shocks

We perform a first test with an initial speed $u = -6$ km s^{-1} so as to have a subcritical shock (cf. Fig. 6). As expected, radiation and matter are not in equilibrium: temperatures differ upstream and downstream. We perform two series of tests: one with the M_1 model and another one with a constant isotropic Eddington tensor $\mathbb{D} = \mathbb{I}/3$ (also known as the P_1 model). We can see that in both cases the shock is located at the same place and the temperatures behind the shock are very similar. However, some differences appear in the precursor that have the greatest effect on the radiative temperature. The radiative precursor appears larger in the M_1 model due to the M_1 ability to deal with large reduced flux and anisotropic photon distribution function. In the precursor, the reduced flux is very large with a value around 0.9. But, in the P_1 model, the reduced flux is limited by $1/\sqrt{3}$. The M_1 model, in which the reduced flux can go from 0 to 1, is therefore more adequate for describing this region.

5.3.2. Supercritical shocks

After setting an initial speed to $u = -20$ km s^{-1}, we obtain a supercritical shock (cf. Fig. 7). In that case, the radiative precursor is indeed larger than in the subcritical case. Radiative and matter temperatures are equal on both sides of the shock, showing that matter and radiation are in equilibrium in a larger zone.

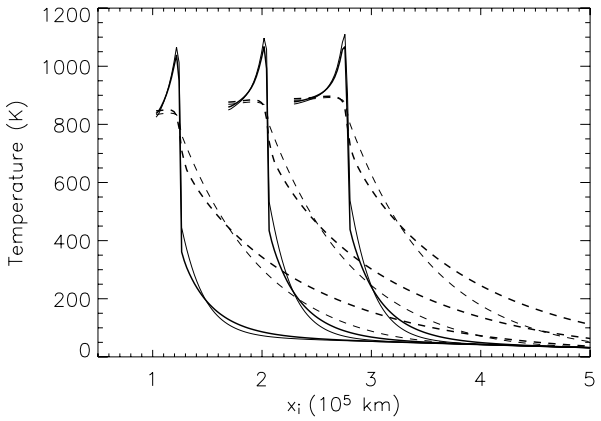

Fig. 6. Subcritical shock: gas (solid line) and radiative (dashed line) temperatures at 1.7e4, 2.8e4, and 3.8e4 s obtained with the M_1 model (thick lines) compared to a constant and isotropic Eddington tensor model (thin lines).

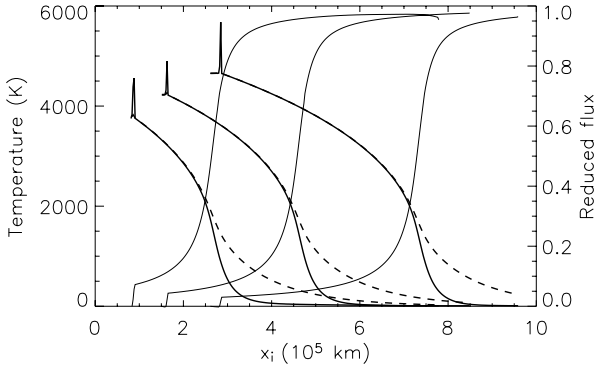

Fig. 7. Supercritical shock: temperatures (thick lines) of gas (solid line) and radiation (dashed line) at 4.0e3, 7.5e3, and 1.3e4 s and the corresponding reduced fluxes (thin lines).

The peak behind the shock in the matter temperature profile is sampled over 4−5 cells, which means about three tenths of the photon mean free path. In the precursor, matter and radiation are in equilibrium over a large zone, implying a small reduced flux. It is only at the end of the radiative precursor that the reduced flux becomes large and that matter and radiation temperature differ significantly.

The ability of HERACLES to treat these radiative shocks properly shows that our resolution method divided in three steps (Eqs. (11)−(13)) does not alter the coupling between matter and radiation.

6. Summary and discussion

We have presented a new, parallelized, three-dimensional radiation hydrodynamics code called HERACLES. The radiative transfer is solved using a moment method and the M_1 closure relation. We have shown that, even though approximate, this model gives an accurate solution even when the radiation field presents large angular anisotropies. The numerical scheme proposed for integrating the M_1 model is implicit and allows us to numerically keep the correct physical properties of M_1.

The tests performed and presented in this paper reveal the accuracy of HERACLES both in the diffusion and transport limit, and despite all the approximations, it compares well to codes that solve the exact transfer equation. In particular, and in opposition to flux limited diffusion, HERACLES can deal with semi-transparent and free-streaming regions. The possibility of easily treating scattering with reasonable accuracy is also an advantage to our method. Finally, it naturally couples to the modern high-resolution numerical schemes used for hydrodynamics, and its reasonable numerical cost allows the treatment of three-dimensional radiation hydrodynamics problems.

The tests presented in this paper show that HERACLES will be very well-suited to studying various astrophysical problems from the study of protoplanetary discs to the formation and fragmentation of dense cores in the interstellar medium. It has already been used to study and interpret multidimensional effects in laboratory astrophysics radiative shocks experiments carried out at the PALS laser (González et al. 2006). And a study of the interaction of molecular jets with the interstellar medium is in preparation (González et al. 2007).

Some further developments of the code are also envisaged. The most useful for astrophysical applications are implementation of a multigroup M_1 model and coupling to an AMR grid to obtain a very high resolution while remaining cost competitive.

Acknowledgements. HERACLES is available at
`http://www-dapnia.cea.fr/Projets/COAST/heracles.htm`
or by sending an e-mail to `edouard.audit@cea.fr`
We would like to thank the CEA computing center, CCRT, where all the computations presented in this paper were done.

References

Audit, E., Charrier, P., Chièze, J. P., & Dubroca, B. 2002, [arXiv:astro-ph/0206281]
Bozier, J. C., Thiell, G., Le Breton, J. P., Azra, S., & Decroisett, M. 1986, Phys. Rev. Lett., 57, 1304
Coelho, P. J. 2002, JQSRT, 73, 231
Crosbie, A. L., & Schrenker, R. G. 1984, JQSRT, 31, 339
Dai, W., & Woodward, P. R. 1998, J. Comput. Phys., 142, 182
Dai, W., & Woodward, P. R. 2000, J. Comput. Phys., 157, 199
Dubroca, B., & Feugeas, J. L. 1999, CRAS, 329, 915
Dullemond, C. P., & Natta, A. 2003, A&A, 408, 161
Einfeldt, B., Munz, C. D., Roe, P. L., & Sjögreen, B. 1991, J. Comput. Phys., 92, 273
Ensman, L. 1994, ApJ, 424, 275
Gehmeyr, M., & Mihalas, D. 1993, A&AS, 25, 1366
Gentile, N. A. 2001, J. Comput. Phys., 172, 543
González, M., Stehlé, C., Audit, E., et al. 2006, Laser Part. Beams, 24, 535
González, M., Audit, E., & Lery, T. 2007, in preparation
Hauschildt, P. H., Baron, E., & Allard, F. 1997, ApJ, 483, 390
Hayes, J. C., & Norman, M. L. 2003, ApJS, 147, 197
Kurucz, R. L. 1996, ASPC, 160
Levermore, C. D. 1984, JQSRT, 31, 149
Lowrie, R. B., Mihalas, D., & Morel, J. E. 2001, JQSRT, 69, 291
Marshak, R. E. 1958, Phys. Fluids, 1, 24
Mihalas, D., & Auer, L. H. 2001, JQSRT, 71, 61
Mihalas, D., & Mihalas, B. D. 1984, Foundation of Radiation Hydrodynamics (Oxford University Press)
Pascucci, I., Wolf, S., Steinacker, J., et al. 2004, A&A, 417, 793
Press, W. H., Teukolsky, S. A., Vetterling, W. T., & Flannery, B. P. 1986, Numerical recipes (Oxford University Press)
Richling, S., Meinköhn, E., Kryzhevoi, N., & Kanschat, G. 2001, A&A, 380, 776
Ripoll, J. F., Dubroca, B., & Duffa, G. 2001, Combust. Theory Modell., 5, 261
Rukolaine, S. A., Vasilyev, M. G., Yuferev, V. S., & Galyukov, A. O. 2002, JQSRT, 73, 205
Saad, Y., & Schultz, M. H. 1986, SIAM J. Sci. Stat. Comput., 7, 856
Stone, J. M., Mihalas, D., & Norman, M. L. 1992, ApJS, 80, 819
Su, B., & Olson, G. L. 1996, JQSRT, 56, 337
Turner, N. J., & Stone, J. M. 2001, ApJS, 135, 95
Turpault, R. 2005, JQSRT, 94, 357
van Noort, M., Hubeny, I., & Lanz, T. 2002, ApJ, 568, 1066

Online Material

Appendix A: The HLLE scheme

We consider the system:

$$\begin{cases} \partial_t E_\mathrm{r} + \nabla \cdot \boldsymbol{F}_\mathrm{r} = c(\sigma_\mathrm{P} a_\mathrm{r} T^4 - \sigma_\mathrm{E} E_\mathrm{r}) \\ \partial_t \boldsymbol{F}_\mathrm{r} + c^2 \nabla \cdot \mathbb{P}_\mathrm{r} = -(\sigma_\mathrm{F} + \sigma_\mathrm{s}) c \boldsymbol{F}_\mathrm{r}. \end{cases} \tag{A.1}$$

Noting down $\mathcal{U}$ the vector of variables and $\mathcal{F}$ the corresponding flux vector, this system can be written as

$$\partial_t \mathcal{U} + \partial_x \mathcal{F}(\mathcal{U}) + \partial_y \mathcal{G}(\mathcal{U}) + \partial_z \mathcal{H}(\mathcal{U}) = \mathcal{S}(\mathcal{U}).$$

First, we have to compute the minimum and maximum eigenvalues (respectively λ_min and λ_max) of the Jacobian matrix $\mathcal{J}(U) = \frac{\partial \mathcal{F}(\mathcal{U})}{\partial \mathcal{U}}$. Then, the intercell fluxes are computed using the HLLE scheme

$$\mathcal{F}_{i+\frac{1}{2}} = \frac{\lambda^+_{i+\frac{1}{2}} \mathcal{F}_i - \lambda^-_{i+\frac{1}{2}} \mathcal{F}_{i+1} + \lambda^+_{i+\frac{1}{2}} \lambda^-_{i+\frac{1}{2}} (\mathcal{U}_{i+1} - \mathcal{U}_i)}{\lambda^+_{i+\frac{1}{2}} - \lambda^-_{i+\frac{1}{2}}} \tag{A.2}$$

where the index $i + \frac{1}{2}$ denotes the interface between cells i and $i+1$, $\lambda^+ = \max(0, \lambda_\mathrm{max})$ and $\lambda^- = \min(0, \lambda_\mathrm{min})$.

The computation of these eigenvalues is rather time-consuming because we need them at each iteration in a time step and at each interface of the mesh. However, since they only depend on two parameters (i.e. $\|\boldsymbol{f}\|$ and θ), they can be tabulated easily. We therefore decided to compute them once for a set of θ and f and to interpolate the value needed. This method performs well because the eigenvalues have a smooth behavior. The maximum difference obtained between the exact eigenvalues and the interpolated ones never exceeds one percent using a 100×100 interpolation grid.

Appendix B: The geometry

In one Cartesian dimension, noting down the time index n and $n+1$, the cell index i, and the interfaces indexes $i \pm 1/2$, the discretized equations we must solve are:

$$\begin{cases} \frac{e_i^{n+1}-e_i^n}{\Delta t}\Delta V_i^n + \frac{E_i^{n+1}-E_i^n}{\Delta t}\Delta V_i^n + F^{n+1}_{i+1/2} S^n_{i+1/2} - F^{n+1}_{i-1/2} S^n_{i-1/2} = 0 \\ \frac{E_i^{n+1}-E_i^n}{\Delta t}\Delta V_i^n + F^{n+1}_{i+1/2} S^n_{i+1/2} - F^{n+1}_{i-1/2} S^n_{i-1/2} = c(\sigma_{\mathrm{P}_i}{}^n T_i^{n+1\,4} - \sigma_{\mathrm{E}_i}{}^n E_i^{n+1}) \Delta V_i^n \\ \frac{F_i^{n+1}-F_i^n}{\Delta t}\Delta V_i^n + c^2 P^{n+1}_{i+1/2} S^n_{i+1/2} - c^2 P^{n+1}_{i-1/2} S^n_{i-1/2} = -(\sigma_{\mathrm{F}_i}{}^n + \sigma_{\mathrm{s}_i}{}^n) c F_i^{n+1} \Delta V_i^n. \end{cases} \tag{B.1}$$

But HERACLES is able to work in either Cartesian, cylindrical, or spherical geometry, and in the two latter cases, the divergence involves terms due to geometrical effects. These terms are written in the Table B.1 where $\boldsymbol{P}$ corresponds to the row vectors of the tensor $\mathbb{P}$, which is the radiative pressure or the total hydrodynamical pressure: $P\mathbb{I} + \rho \boldsymbol{u} \otimes \boldsymbol{u}$.

One should take particular care in the discretization of these terms in order to check three conditions. First, the discrete divergence of a constant must be null. Second, when r tends to infinity, the geometry effects vanish and one should recover the Cartesian divergence. Finally, when the resolution increases (i.e. dr tends to zero), the discrete scheme should not diverge. In order to verify these three conditions in HERACLES, we then discretize the "nabla" terms with the classical formula $\int_V \nabla P \mathrm{d}V = \int_S P \mathrm{d}S = \Sigma P_S S$. For the derivative terms, we use a discretization over the direction considered involving interface values: $\int_V \partial_\mathrm{r} P \mathrm{d}V = \frac{P_{i+1/2} - P_{i-1/2}}{r_{i+1/2} - r_{i-1/2}} V$ and $\int_V \frac{1}{r}\partial_\theta P \mathrm{d}V = \frac{P_{i+1/2} - P_{i-1/2}}{r_i(\theta_{i+1/2} - \theta_{i-1/2})} V$. As for the additional terms, they are cell-centered.

This discretization ensures us that the momentum in the hydrodynamics equations is conserved. One can notice that the additive centered terms drop naturally when the diffusion limit is reached, because in such case the tensor of radiative pressure is isotropic: $P_{rr} = P_{\theta\theta} = P_{\phi\phi}$.

Appendix C: Time step control

The time step in HERACLES is the smallest of the hydrodynamical and the radiative time steps. The hydrodynamical time step is simply given by a Courant condition using a Courant factor of 0.8. For the radiation, we compute two time steps. An explicit one, also given by a Courant condition, and an implicit one controlled by the variation in the variables involved in the implicit step (gas energy, radiative energy, and radiative flux). We set a limit on the allowed variation for these variables during a time step, and the implicit time step is increased (resp. lowered) if the actual variations are lower (resp. higher) than this limit. The final radiative time step is the implicit one if it is at least 10 times greater than the explicit one. This last condition ensures that implicit integration is done only when it is profitable.

Appendix D: Performances

We present here the performances obtained with HERACLES. The code is parallelized with the MPI library in order to run on a large parallel supercomputer. The parallelization scheme used is a classical domain decomposition. This splitting ensures a good equilibrium of charge between all the processors. The communications at the boundary between each domain always take a negligible time in all the tests we have done.

To test the performances, we ran different simulations over 1, 16, 36, 64, and 121 processors such that each processor worked on 150×525 cells. In Fig. D.1, we plot the CPU time per processor and per cell normalized by the Gauss-Seidel CPU time with one processor. We can clearly see that the Gauss-Seidel method has a nearly perfect scaling, whereas the GMRES method has a more complex behavior with a loss of performance that can reach 20%. This is due to the fact that the GMRES algorithm has a more complex communication scheme and is therefore more sensitive to small load unbalances. We can also see that one GMRES iteration nearly corresponds to three Gauss-Seidel iterations in terms of CPU time. Another drawback of the GMRES method is that it is very demanding in terms of memory space. In conclusion, the GMRES method is appropriate if it significantly accelerates the convergence (at least by a factor of 3) and if memory is not a crucial issue.

The convergence rate of the above algorithms can vary significantly from one test to the next. Figure D.2 shows the residual during one time step of a Marshak wave test. We can see that the Gauss-Seidel method in this particular test is far much efficient than the GMRES method. We have performed another Marshak wave test with higher opacities in order to be in a more diffusive regime. In that case, the results are inverted, with the GMRES method better than Gauss-Seidel. We recover the characteristics discussed in Sect. 3.2: Gauss-Seidel is more efficient in the transport limit and GMRES in the diffusion limit. However, we empirically discovered that coupling the two methods gives the best results. We first performed a few iterations with one method and then gave this result as initial guess to the other one. At the switch the residual drops by about one order of magnitude, due to the fact that for each method the first iterations are more efficient than what follows. Pushing this idea further, we tried the

Table B.1. Divergence in the three different geometries handled by HERACLES.

	Cartesian	Cylindrical		Spherical	
$\nabla \cdot \mathbb{P} =$	$\nabla \cdot \boldsymbol{P}_x$	$\partial_r P_{rr} + \nabla_{\theta,z} \cdot \boldsymbol{P}_r$	$+\frac{P_{rr}-P_{\theta\theta}}{r}$	$\partial_r P_{rr} + \nabla_{\theta,\phi} \cdot \boldsymbol{P}_r$	$+\frac{2P_{rr}-P_{\theta\theta}-P_{\phi\phi}}{r}$
	$\nabla \cdot \boldsymbol{P}_y$	$\frac{1}{r}\nabla \cdot (r\boldsymbol{P}_{\boldsymbol{\theta}})$		$\frac{1}{r}\partial_\theta P_{\theta\theta} + \frac{1}{r}\nabla_{r,\phi} \cdot (r\boldsymbol{P}_{\boldsymbol{\theta}})$	$+\cot\theta\frac{P_{\theta\theta}-P_{\phi\phi}}{r}$
	$\nabla \cdot \boldsymbol{P}_z$	$\nabla \cdot \boldsymbol{P}_z$		$\frac{1}{r\sin\theta}\nabla \cdot (r\sin\theta\boldsymbol{P}_{\boldsymbol{\phi}})$	

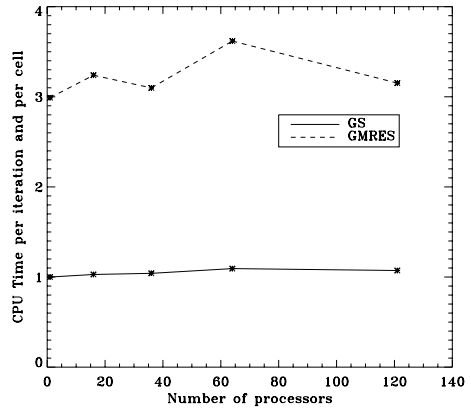

Fig. D.1. Normalized CPU time as a function of the number of processors for simulations with a constant cell number per processor.

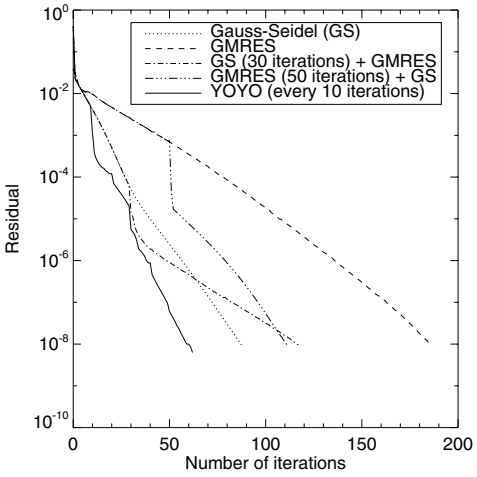

Fig. D.2. Residual in a Marshak wave test for the five following methods: 1. purely Gauss-Seidel (GS) iterations, 2. purely GMRES iterations, 3. 30 iterations of GS before GMRES, 4. 50 iterations of GMRES before GS, and 5. yoyo with a switch between GS and GMRES every 10 iterations.

"yoyo" method, which consists in switching back and forth between the two methods every 10 iterations. In all the tests we have done, this method was the most efficient (if the memory needed by GMRES can be afforded), even though the optimal number of iterations between each switch can vary somewhat.

In all our simulations, the CPU time needed for the radiative transfer was between 3 and 10 times the time taken by the hydrodynamics depending on the variation in the radiative quantities during one hydrodynamical time step and on the convergence criteria used. The memory needed by the radiative transfer is equal to the memory needed by the hydrodynamics if one uses the GS solver but it is higher when using the GMRES algorithm (depending on the size of the Krylov space used to find the solution).

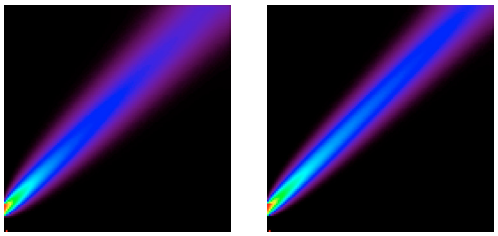

Fig. E.1. Radiative energy for the beam test: eigenvalues set to $\pm c$ (*left*) or calculated (*right*).

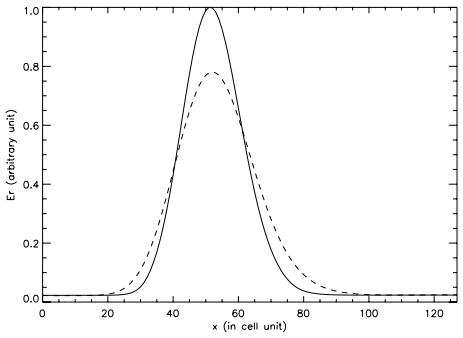

Fig. E.2. Horizontal cut in Fig. E.1 at the middle height. Solid line corresponds to calculated eigenvalues and dashed line to fixed ones.

Appendix E: Extra verification tests

E.1. Beam test

In the shadow test, the numerical diffusion is limited because radiation propagates along mesh axis. In order to quantify this efect, we performed a test where a narrow beam of radiation propagates with a certain angle (cf. Richling et al. 2001).

For this test, we computed a 128×128 mesh that covers the domain $x = [-1, 1]$ and $y = [-1, 1]$. The beam is introduced at $x = -1$ between $y = [-0.875, -0.750]$ with an angle of 45° and with a unit reduced flux. Initially, the temperature is at $T = T_r = 300$ K and the beam is at $T = T_r = 1000$ K. There is no scattering, absorption, or emission: $\sigma = 0$. The beam should therefore cross the medium without dispersion.

If we plot a profile of the radiative energy, the beam is initially a step sampled over 8 cells. In the stationary state, we can see (cf. Fig. E.2) that, for fixed eigenvalues, the FWHM approximately corresponds to 30 cells. When the eigenvalues are computed, this FWHM falls to only 24 cells. The numerical diffusion has been therefore reduced by 20%. This test shows that the eigenvalue computation keeps the numerical diffusion under control even in a direction not along mesh axis.

E.2. Pipe flow test

This test, known as the pipe flow test (Gentile 2001), is not an astrophysical one, but it treats all the physics underlying the radiative transfer. It is very demanding because it involves at the

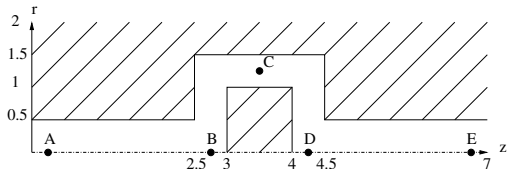

Fig. E.3. Sketch of the geometry for the pipe flow test. The simulation box extends from $r = 0$ to $r = 2$ and from $z = 0$ to $z = 7$. The pipe can be divided in three regions. The first one is a cylinder with a radius of 0.5 which extends from $z = 0$ to $z = 2.5$ and from $z = 4.5$ to $z = 7$. The second is a cylinder with a radius of 1.5 extended from $z = 2.5$ to $z = 3$ and from $z = 4$ to $z = 4.5$. Finally the third one is a cylindrical shell with inner radius $r = 1$ and outer radius $r = 1.5$ which extends from $z = 3$ to $z = 4$. The five characteristic points are A($r = 0$; $z = 0.25$), B(0 ; 2.75), C(1.25 ; 3.5), D(0 ; 4.25), E(0 ; 6.75).

same time regions of free-streaming, of diffusion, shadows, and the results depend strongly on the description of the heating and reemission of the walls.

In this problem, a cylindrical section of dense and opaque material is embedded in less dense and less opaque material (the pipe), which is itself embedded in a cylinder of the dense and opaque material. The geometry is sketched in Fig. E.3.

Both materials have a heat capacity $c_v = 10^{15}$ erg g^{-1} keV^{-1}, but the densities and opacities differ:

$$\begin{cases} \rho = 10 \quad \mathrm{g\,cm^{-3}} \quad \text{and} \quad \sigma = 2000 \quad \mathrm{cm^{-1}} \text{ outside the pipe} \\ \qquad\qquad\qquad\qquad\qquad\quad \text{(dashed region in Fig. E.3)} \\ \rho = 0.01 \quad \mathrm{g\,cm^{-3}} \quad \text{and} \quad \sigma = 0.2 \quad\; \mathrm{cm^{-1}} \quad \text{inside the pipe.} \end{cases}$$

The time unit is such that $c = 300$. The end of the simulation is reached when $t_{\mathrm{end}} = 100$. The simulation box is sampled over 400×1400 cells.

Initially, the medium is at equilibrium $T = T_{\mathrm{r}} = 0.05$ keV everywhere. At time $t = 0$, a uniform source with $T_{\mathrm{s}} = 0.5$ keV is lighted on at the left side of the pipe.

In Fig. E.4, the problem is analyzed with the matter temperature at the five characteristic points A, B, C, D, and E. Points A and B are located in the pipe before the obstacle. Their temperature therefore depends on the code's ability to recover the free-streaming limit. These two plots show good agreement with the results published in Gentile (2001). The next three points depend closely on the physical equations solved. Indeed, in a diffusion model, photons would go round the obstacle very easily since the photon distribution function is isotropic, whereas in fact the photons have to be absorbed by the obstacle, which is heated, and then reemitted from the heated walls. This allows photons initially moving horizontally to go upward and then to go round the obstacle. For these three last points, our results are qualitatively good, although quantitatively some discrepancies exist: point E is heated faster, point C is heated a little bit later, etc. Only few people perform this test, so there are not many results to compare with. Nevertheless, we see that our model, although simple, compares well to exact codes with Monte-Carlo techniques.

E.3. Diffusion in a moving fluid

This simple radiation hydrodynamics test compares diffusion in a moving fluid and in a fluid at rest. We use a Cartesian grid of 100×100 cells. At $t = 0$, we initialize a Gaussian pulse of energy at the center of the simulation box. First, we perform a test without radiation. The energy radiation is advected as a passive scalar in the fluid moving along the diagonal. Secondly, we look at a static diffusion: we turn on both hydrodynamics and

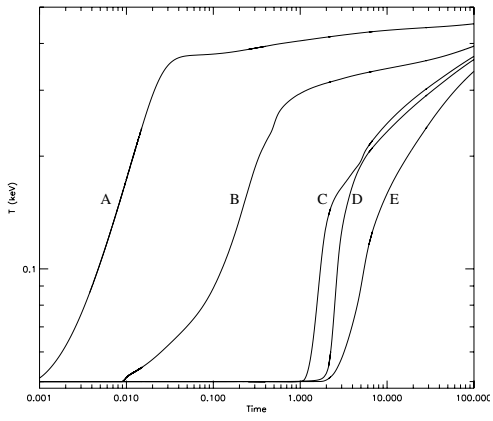

Fig. E.4. Matter temperature at the five characteristic points.

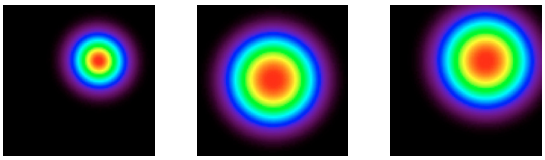

Fig. E.5. Radiative energy for diffusion test: pure advection, static diffusion, diffusion in a moving fluid.

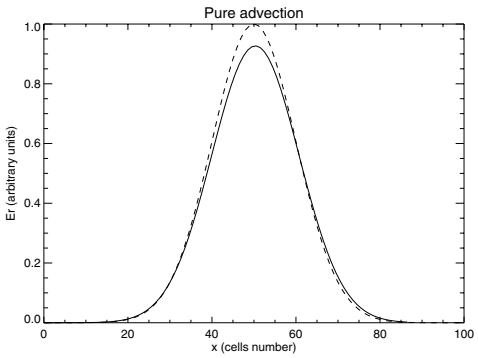

Fig. E.6. Radiative energy for pure advection: initial pulse (dashed line) and pulse after crossing one eighth of the box (solid line). The pulse is recentered by a factor $\boldsymbol{u}\Delta t$.

radiation, but the fluid is at rest $\boldsymbol{u} = \boldsymbol{0}$. Finally, we conjugate the two precedent tests to look at dynamical diffusion: a Gaussian pulse is initialized in a moving fluid. This test will characterize the relative importance of advection and diffusion terms and will verify their coupling.

Figure E.5 shows the radiative energy in these three cases whereas Figs. E.6 and E.7 show slices with the pulse always recentered by a factor $\boldsymbol{u}\Delta t$. In the first case, the Gaussian pulse should be advected without being affected at all. We first verify that the advection speed is correct because the two peaks are centered at the same position. Then we can see that the pulse is slightly diffused (the maximum has decreased by 8% after crossing over 12 cells). This diffusion could easily be lowered by using a more aggressive slope limiter. When we turn on hydrodynamics, all the pulses are again properly centered, which means that advection is still done at the right speed. Moreover, the diffusion of the radiative pulse in the moving and in the static fluids is very similar (the maximum discrepancy is less than 2%). Therefore, our treatment of the comoving terms preserves the good accuracy of the advection scheme and there is no problem in coupling advection with diffusion terms.

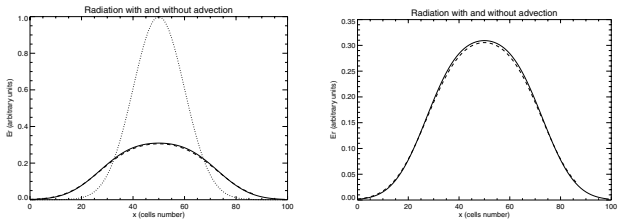

Fig. E.7. Radiative energy for: initial pulse (dotted line) and pulse at the end of the simulation with advection (dashed line) and without (solid line). *Right panel* is a zoom. All the pulses are recentered by a factor $\boldsymbol{u}\Delta t$.

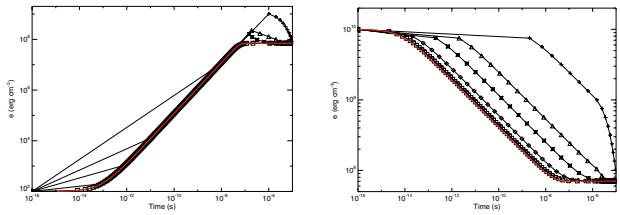

Fig. E.8. Gas energy versus time in the matter-radiation coupling test. The left (resp. right) subfigure corresponds to an initial matter energy of 10^2 (resp. 10^{10}) erg cm^{-3}. The thick solid line corresponds to the analytical solution, and squares (resp. diamonds, stars, triangles, crosses) to HERACLES simulation with a constant time step equal to 0.1 $\tau(e)$ (resp. 1, 10, 100, 10^5). Each point corresponds to a time step of the simulation.

E.4. Matter-radiation coupling

We now present a test of the matter-radiation coupling. If the radiation energy density is much higher than the gas one, the matter-radiation coupling can be solved analytically by assuming a constant radiative energy (Turner & Stone 2001). The matter energy then obeys the following equation where E_r is constant:

$$\partial_t e = -\sigma c(a_\mathrm{r} T^4 - E_\mathrm{r}). \tag{E.1}$$

The previous equation can be integrated by noticing that:

$$\begin{aligned}\int_{x_0}^{x_1} \frac{\mathrm{d}x}{x^4-a^4} = \frac{1}{a^3}\ \Big(&-\frac{1}{2}\Big(\tan^{-1}(\tfrac{x_1}{a}) - \tan^{-1}(\tfrac{x_0}{a})\Big)\\ &+\frac{1}{4}\log(\tfrac{a-x_1}{a-x_0}) - \frac{1}{4}\log(\tfrac{a+x_1}{a+x_0})\Big).\end{aligned} \tag{E.2}$$

We have solved this matter-radiation coupling problem with HERACLES using various time steps. The time step was kept constant in units of $\tau(e) = \frac{e}{\sigma c(a_\mathrm{r} T^4 - E_\mathrm{r})}$. A time step equal to τ corresponds to a variation in e of about 100% at each time step.

We did two tests with a radiative energy $E_\mathrm{r} = 10^{12}$ erg cm^{-3} (i.e. $T_\mathrm{rad} = 3.39 \times 10^6$ K), an opacity $\sigma = 4 \times 10^{-8}$ cm^{-1}, and a heat capacity $c_v = 20.79$ erg cm^{-3} K^{-1}. In the first one, the initial gas energy was 10^2 erg cm^{-3} (i.e. $T_\mathrm{gas} = 4.81$ K $< T_\mathrm{rad}$), and in the second one 10^{10} erg cm^{-3} (i.e. $T_\mathrm{gas} = 4.81 \times 10^8$ K $> T_\mathrm{rad}$). The corresponding results are plotted in Fig. E.8. We can see that if the variation of the energy is well-sampled (i.e. the time step is less than τ), then the analytical solution is properly reproduced. If the time step is large compared to the coupling time, the shape of the energy variation moves away from the analytical solution (as could be expected) but the proper value for the equilibrium is nevertheless found.

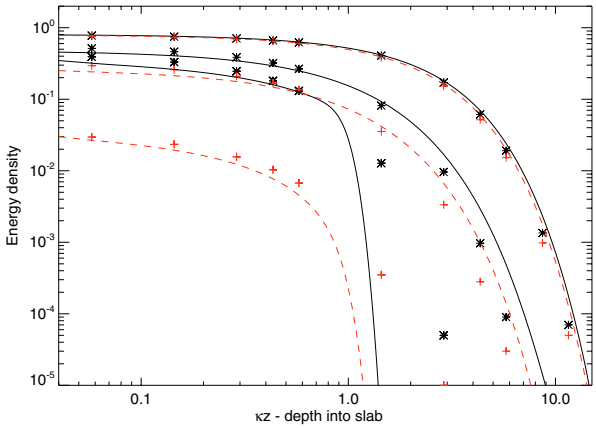

Fig. E.9. Marshak wave test: comparison of Heracles results (radiative energy with a solid line and gas energy with a dashed line) with the Su & Olson (1996) solution (radiative energy with stars and gas energy with crosses) at three different times.

E.5. Marshak wave test

A Marshak wave is the propagation of a radiation heating front in a cold slab (Marshak 1958). An analytical solution of the Marshak wave problem was proposed by Su & Olson (1996) in the context of the diffusion equation and assuming that the gas heat capacity is proportional to T^3 (i.e. $c_v = \alpha T^3$). We compared the solution obtained by HERACLES to their solution for the case $\epsilon \equiv 4a_\mathrm{r}/\alpha = 0.1$.

Figure E.9 represents the radiative and gas energies (normalized by their boundary values) obtained by HERACLES and by Su & Olson (1996) at times given by $\tau \equiv \epsilon c\sigma t = (0.1, 1, 10)$ (cf. their Fig. 3). At early times and at the foot of the Marshak wave, we can see large differences between the two methods. This was to be expected since in this region the radiation is instead in the transport regime and the diffusion approximation is then different from our M_1 model. At later times and inside the wave, the reduce flux is much smaller (i.e. the radiation is almost in the diffusion regime) and, accordingly, the results given by M_1 are in good agreement with the analytical solution.

A&A 578, A12 (2015)
DOI: 10.1051/0004-6361/201525971

Astronomy & Astrophysics

Multigroup radiation hydrodynamics with flux-limited diffusion and adaptive mesh refinement

M. González[1], N. Vaytet[2], B. Commerçon[2], and J. Masson[3,2]

[1] Univ. Paris Diderot, Sorbonne Paris Cité, AIM, UMR 7158, CEA, CNRS, 91191 Gif-sur-Yvette, France
e-mail: matthias.gonzalez@cea.fr
[2] École Normale Supérieure de Lyon, CRAL, UMR CNRS 5574, Université de Lyon, 46 allée d'Italie, 69364 Lyon Cedex 07, France
[3] School of Physics, University of Exeter, Exeter EX4 4QL, UK

Received 26 February 2015 / Accepted 6 April 2015

ABSTRACT

Context. Radiative transfer plays a crucial role in the star formation process. Because of the high computational cost, radiation-hydrodynamics simulations performed up to now have mainly been carried out in the grey approximation. In recent years, multi-frequency radiation-hydrodynamics models have started to be developed in an attempt to better account for the large variations in opacities as a function of frequency.
Aims. We wish to develop an efficient multigroup algorithm for the adaptive mesh refinement code RAMSES which is suited to heavy proto-stellar collapse calculations.
Methods. Because of the prohibitive timestep constraints of an explicit radiative transfer method, we constructed a time-implicit solver based on a stabilized bi-conjugate gradient algorithm, and implemented it in RAMSES under the flux-limited diffusion approximation.
Results. We present a series of tests that demonstrate the high performance of our scheme in dealing with frequency-dependent radiation-hydrodynamic flows. We also present a preliminary simulation of a 3D proto-stellar collapse using 20 frequency groups. Differences between grey and multigroup results are briefly discussed, and the large amount of information this new method brings us is also illustrated.
Conclusions. We have implemented a multigroup flux-limited diffusion algorithm in the RAMSES code. The method performed well against standard radiation-hydrodynamics tests, and was also shown to be ripe for exploitation in the computational star formation context.

Key words. radiation: dynamics – radiative transfer – hydrodynamics – methods: numerical – stars: formation

1. Introduction

Numerical studies of star formation are very demanding, as many physical mechanisms need to be taken into account (hydrodynamics, gravity, magnetic fields, radiative transfer, chemistry, etc.). Models are rapidly increasing in complexity, providing increasingly realistic interpretations of today's highly advanced observations of protostellar systems, such as the recent groundbreaking images taken by the ALMA interferometer[1]. Radiative transfer plays an important role in star formation; it acts as a conduit to remove compressional heating during the initial stages of cloud collapse, enabling an isothermal contraction (Larson 1969; Masunaga et al. 1998), and it also inhibits cloud fragmentation in large-scale simulations (see e.g. Bate 2012). State-of-the-art simulations thus require the solutions to the full radiation magneto-hydrodynamics (RMHD) system of equations, and 3D simulations have only just recently become possible with modern computers (see e.g. Commerçon et al. 2011a; Tomida et al. 2013). In particular, including frequency dependent radiative transfer is essential in order to properly take into account the strong variations of the interstellar gas and dust opacities as a function of frequency (see e.g. Ossenkopf & Henning 1994; Li & Draine 2001; Draine 2003; Semenov et al. 2003; Ferguson et al. 2005). Three-dimensional calculations including full frequency-dependent radiative transfer are still out of reach of current computer architectures.

In order to overcome this difficulty, much effort has been spent in recent years developing mathematically less complicated, yet accurate approximations to the equations of radiative transfer. Such representations include diffusion approximations, the M_1 model, short and long characteristics methods, and Variable Eddington Tensor descriptions. One of the simplest and most widely used is the flux-limited diffusion (FLD) approximation (Levermore & Pomraning 1981) that has been applied to many areas of physics and astrophysics.

These methods tend to drastically reduce computational cost, but still they are often integrated over all frequencies (also known as the grey approximation) as the multifrequency formalism remains too expensive. Only in recent years have multigroup methods (whereby the frequency-dependent quantities are binned into a finite number of groups and averaged over the group extents) appeared in numerical codes (Shestakov & Offner 2008; van der Holst et al. 2011; Vaytet et al. 2011, 2013b; Davis et al. 2012; Zhang et al. 2013, to mention a few) as a first step towards accounting for the frequency dependence of gas and dust quantities in calculations. Multigroup methods are very suited to astrophysics as they allow adaptive widths of groups, thus enabling the use of a small number of groups, concentrating frequency resolution where it is needed (i.e. mostly where opacity gradients are strong). Group boundaries are usually chosen once at the start of the simulations, but more complex schemes have

[1] http://www.almaobservatory.org/en/press-room/press-releases/771-revolutionary-alma-image-reveals-planetary-genesis

also been written with moving adaptive borders (Williams 2005), as absorption and emission coefficients generally vary with the material temperature and density.

Commerçon et al. (2011b) implemented frequency-integrated FLD in the adaptive mesh refinement (AMR) code RAMSES (Teyssier 2002; Fromang et al. 2006), and devised an adaptive time-stepping scheme in a follow-up paper (Commerçon et al. 2014). In this third paper, we extend the method to a multigroup formalism. Even though multigroup effects were found to have only a small impact on 1D simulations of star formation (Vaytet et al. 2012, 2013a), they are expected to be enhanced in 3D where the optical thickness can markedly vary along different lines of sight (see Kuiper et al. 2011). Using a frequency-dependent method is also the only way to correctly model ultraviolet radiation from stars being absorbed by surrounding dust and re-emitted in the infrared. Finally, multigroup formalisms, compared to grey methods, are known to significantly affect the structures of radiative shocks (Vaytet et al. 2013b), alter energy transport in stellar atmospheres (Chiavassa et al. 2011), and are essential to neutrino transport in core collapse supernovae explosions (see e.g. Mezzacappa et al. 1998).

We first present the numerical method we have used, followed by a series of tests against analytical solutions, and we end with an application to the collapse of a gravitationally unstable cloud, comparing grey and multigroup results.

2. Numerical method

The FLD multigroup radiation hydrodynamics equations in the frame comoving with the fluid are

$$\begin{aligned}
\partial_t \rho + \nabla\cdot[\rho\boldsymbol{u}] &= 0\\
\partial_t(\rho\boldsymbol{u}) + \nabla\cdot[\rho\boldsymbol{u}\otimes\boldsymbol{u} + P\mathbb{I}] &= -\sum_{g=1}^{Ng}\lambda_g\nabla E_g\\
\partial_t E_\mathrm{T} + \nabla\cdot[\boldsymbol{u}(E_\mathrm{T}+P)] &= \sum_{g=1}^{Ng}\Bigg[-\mathbb{P}_g:\nabla\boldsymbol{u} - \lambda_g\boldsymbol{u}\cdot\nabla E_g\\
&\quad +\nabla\cdot\left(\frac{c\lambda_g}{\rho\kappa_{\mathrm{R}g}}\nabla E_g\right)\Bigg] \qquad (1)\\
\partial_t E_g + \nabla\cdot[\boldsymbol{u}E_g] &= -\mathbb{P}_g:\nabla\boldsymbol{u} + \nabla\cdot\left(\frac{c\lambda_g}{\rho\kappa_{\mathrm{R}g}}\nabla E_g\right)\\
&\quad +\kappa_{\mathrm{P}g}\rho c\left(\Theta_g(T) - E_g\right)\\
&\quad +\nabla\boldsymbol{u}:\int_{\nu_{g-1/2}}^{\nu_{g+1/2}}\partial_\nu(\nu\mathbb{P}_\nu)\mathrm{d}\nu,
\end{aligned}$$

where c is the speed of light; ρ, $\boldsymbol{u}$, P, and T are the gas density, velocity, pressure, and temperature, respectively; E_T is the total energy $E_\mathrm{T} = \rho\epsilon + 1/2\rho u^2 + \sum_{g=1}^{Ng} E_g$ (ϵ is the internal specific energy); and $\mathbb{I}$ is the identity matrix. We also define

$$X_g = \int_{\nu_{g-1/2}}^{\nu_{g+1/2}} X_\nu \mathrm{d}\nu, \qquad (2)$$

where $X = E, \mathbb{P}$, which represent the radiative energy and pressure inside each group g, which holds frequencies between $\nu_{g-1/2}$ and $\nu_{g+1/2}$; N_g is the total number of groups; and $\Theta_g(T)$ is the energy of the photons having a Planck distribution at temperature T inside a given group. The coefficient λ_g is the flux-limiter, and $\kappa_{\mathrm{P}g}$ and $\kappa_{\mathrm{R}g}$ are the Planck and the Rosseland means of the spectral opacity κ_ν inside a given group.

We employ a commonly used operator splitting scheme whereby the equations of hydrodynamics are first solved explicitly using the second-order Godunov method of RAMSES including the radiative terms involving $\nabla\cdot\boldsymbol{u}$ and ∇E_g, while the evolution of the radiative energy density and its coupling to the gas internal energy is solved implicitly (for more details on the different equations which are solved explicitly and implicitly, see the exhaustive description in Commerçon et al. 2011b).

To discretize the equations solved in the implicit step, we linearize the source term following

$$\Theta_g(T^{n+1}) = \Theta_g(T^n) + \Theta'_g(T^n)(T^{n+1} - T^n)\,, \qquad (3)$$

where the prime denotes the derivative with respect to temperature. This then enables us to write a set of discretized equations, expressed here in 1D for simplicity, for the evolution of the gas temperature (where C_v is the gas heat capacity at constant volume)

$$T_i^{n+1} = \frac{C_{\mathrm{v}i}^n T_i^n - \sum_g \kappa_{\mathrm{P}g,i}^n \rho_i^n c\Delta t\left(\Theta_g(T_i^n) - T_i^n\Theta'_g(T_i^n) - E_{g,i}^{n+1}\right)}{C_{\mathrm{v}i}^n + \sum_g \kappa_{\mathrm{P}g,i}^n \rho_i^n c\Delta t\Theta'_g(T_i^n)} \qquad (4)$$

and the radiative energy

$$\begin{aligned}
&E_{g,i}^{n+1}\left[1+\kappa_{\mathrm{P}g,i}^n\rho_i^n c\Delta t + \frac{c\Delta t}{V_i}\left(\frac{\lambda_g}{\rho^n\kappa_{\mathrm{R}g}^n}\frac{S}{\Delta x}\right)_{i-1/2} + \frac{c\Delta t}{V_i}\left(\frac{\lambda_g}{\rho^n\kappa_{\mathrm{R}g}^n}\frac{S}{\Delta x}\right)_{i+1/2}\right]\\
&-\frac{c\Delta t}{V_i}\left(\frac{\lambda_g}{\rho^n\kappa_{\mathrm{R}g}^n}\frac{S}{\Delta x}\right)_{i-1/2} E_{g,i-1}^{n+1} - \frac{c\Delta t}{V_i}\left(\frac{\lambda_g}{\rho^n\kappa_{\mathrm{R}g}^n}\frac{S}{\Delta x}\right)_{i+1/2} E_{g,i+1}^{n+1}\\
&-\kappa_{\mathrm{P}g,i}^n\rho_i^n c\Delta t\Theta'_g(T_i^n)\sum_\alpha \frac{\kappa_{\mathrm{P}\alpha,i}^n\rho_i^n c\Delta t}{C_{\mathrm{v}i}^n + \sum_\beta \kappa_{\mathrm{P}\beta,i}^n\rho_i^n c\Delta t\Theta'_\beta(T_i^n)} E_{\alpha,i}^{n+1} =\\
&\qquad E_{g,i}^n + \kappa_{\mathrm{P}g,i}^n\rho_i^n c\Delta t\left(\Theta_g(T_i^n) - T_i^n\Theta'_g(T_i^n)\right)\\
&+\kappa_{\mathrm{P}g,i}^n\rho_i^n c\Delta t\Theta'_g(T_i^n)\frac{C_{\mathrm{v}i}^n T_i^n - \sum_\alpha \kappa_{\mathrm{P}\alpha,i}^n\rho_i^n c\Delta t\left(\Theta_\alpha(T_i^n) - T_i^n\Theta'_\alpha(T_i^n)\right)}{C_{\mathrm{v}i}^n + \sum_\alpha \kappa_{\mathrm{P}\alpha,i}^n\rho_i^n c\Delta t\Theta'_\alpha(T_i^n)}.
\end{aligned} \qquad (5)$$

The terms with superscripts $n+1$ refer to the variables evaluated at the end of the timestep Δt, while superscripts n indicate the state at the beginning of the timestep. Subscripts i represent the grid cell, and $i \pm 1/2$ are for cell interfaces. In addition, V, S, and Δx are the cell volume, the interface surface area, and the cell width, respectively. The subscripts α and β denote the frequency groups where the subscript g is already in use.

The implicit step requires the inversion of a large matrix that holds the system of Eqs. (4) and (5), and this is performed using a parallel iterative method[2]. In the case of the grey approach (and in our specific case of Cartesian coordinates), the matrix to invert in the implicit step is symmetric, which allows the use of the conjugate gradient method (for further details, see Commerçon et al. 2011b, 2014). However, in the multigroup case, the interaction between radiative groups adds non-symmetric terms, for which we had to implement a similar but more advanced stabilized bi-conjugate gradient (BiCGSTAB) algorithm (van der Vorst 1992).

Finally, the term that depends on a derivative with respect to frequency (∂_ν) accounts for energy exchanges between neighbouring groups due to Doppler effects. It is computed using the method described in Vaytet et al. (2011), and treated explicitly as part of the final line in Eq. (11) in Commerçon et al. (2011b). We note that we now have one such line per frequency group.

[2] The use of a direct inversion method is not suited to the very large systems of equations that need to be solved in heavy 3D simulations.

3. Method validation

We present the numerical tests performed to assess the accuracy of our method.

3.1. Dirac diffusion

We consider the 1D two-group radiation diffusion equation in a static medium with no coupling to the gas. The equations to solve are then

$$\begin{aligned}\partial_t E_1 - \nabla\left(\tfrac{c}{3\rho\kappa_{\mathrm{R1}}}\nabla E_1\right) &= 0\\ \partial_t E_2 - \nabla\left(\tfrac{c}{3\rho\kappa_{\mathrm{R2}}}\nabla E_2\right) &= 0.\end{aligned} \tag{6}$$

For a constant $\rho\kappa_{\mathrm{R}}$ coefficient and a Dirac amplitude value of E_0 at x_0 as initial condition, the analytical solution E_a in a p-dimensional space is

$$E_{\mathrm{a}}(x,t) = \frac{E_0}{2^p(\pi\chi t)^{p/2}}\mathrm{e}^{-\frac{(x-x_0)^2}{4\chi t}}, \tag{7}$$

where $\chi = c/(3\rho\kappa_{\mathrm{R}})$.

We choose a box of length $L = 1$ cm, where $x_0 = 0.5$ cm. The gas has a uniform density $\rho = 1$ g cm^{-3}. The initial total radiative energy is set to 1 erg cm^{-3} except in the centre (inside the two central cells) where the peak value E_0 is set to 10^5 erg cm^{-3}. The boundaries of the two frequency groups are (in Hz) [10^5, 10^{15}] and [10^{15}, 10^{19}], chosen so that, in the central region, the radiative energy in the first group is about two orders of magnitude lower than in the second one. The Rosseland opacity in the first group is set to $\kappa_{\mathrm{R1}} = 1$ cm^2 g^{-1} and 10 times higher in the second group. The domain is initially divided into 32 cells (coarse grid level of 5) and 4 additional AMR levels are enabled (effective resolution of 512). The refinement criterion is based on the gradient of the total radiative energy. There is no flux-limiter (i.e. $\lambda_g = 1/3$) for both groups, and a fixed timestep of $\Delta t = 2.5\times10^{-15}$ s is used for the coarse level (since we are using the adaptive time-stepping scheme of Commerçon et al. 2014, the timestep is divided by two per AMR level increase).

Figure 1 (top) shows the radiative energy density profiles at time $t = 2\times10^{-13}$ s. The two radiative energies are in good agreement with the analytical curves. The relative error (bottom panel) on the total radiative energy is always less than 10%. The zones where the relative error on group 2 exceeds the 10% mark correspond to regions where this group does not contribute to the total energy, making this error largely unimportant.

3.2. Radiating plane

Graziani (2008) proposed an analytical multigroup test in spherical geometry. We consider a sphere of radius R and temperature T_{s} that is surrounded by a cold medium at temperature $T_0 < T_{\mathrm{s}}$, heat capacity C_{v}, and spectral absorption coefficient $\rho\kappa_\nu = \sigma_\nu$. The test consists in computing the time-dependent spectrum at a given distance $r > R$ from the sphere centre in the absence of any hydrodynamic motion. In the case where the heat capacity tends to infinity, the gas temperature is constant, and the spectrum is the superposition of the black-body spectrum of the cold medium and the spectrum of the radiation emitted by the hot sphere. The analytical solution for the spectral energy is

$$E_\nu = B(\nu,T_0) + \frac{R}{r}\left[B(\nu,T_{\mathrm{s}}) - B(\nu,T_0)\right]F(\nu,r-R,t), \tag{8}$$

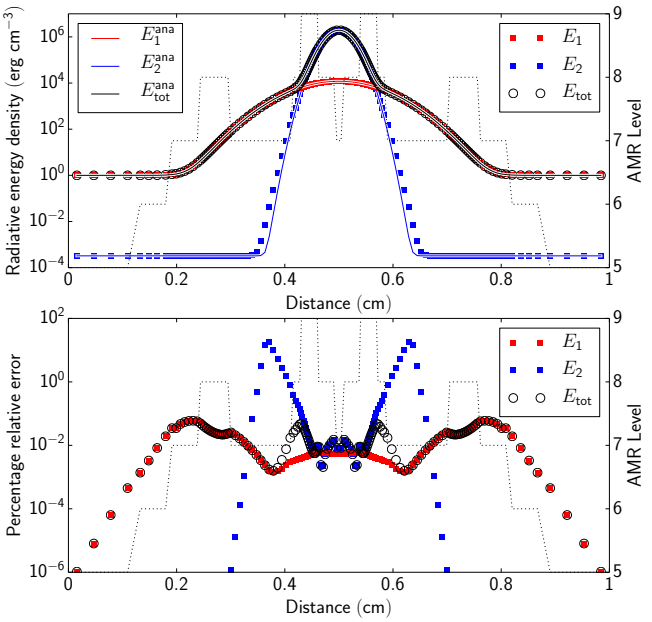

Fig. 1. Diffusion test: numerical (circles and squares) and analytical solutions (solid lines) at time $t = 2\times10^{-13}$ s. *Bottom panel*: relative error. The dotted line corresponds to the AMR levels in the simulation.

where

$$F(\nu,d,t) = \frac{\mathrm{e}^{-\sqrt{3}\sigma_\nu d}}{2}\left[\mathrm{erfc}\left(\frac{1}{2}\sqrt{\frac{3\sigma_\nu}{4ct}}d - \sqrt{ct\sigma_\nu}\right) + \mathrm{erfc}\left(\frac{1}{2}\sqrt{\frac{3\sigma_\nu}{4ct}}d + \sqrt{ct\sigma_\nu}\right)\right]. \tag{9}$$

As our grid is Cartesian, we adapted this test to a slab geometry. Instead of a radiating sphere, we consider a radiating plane. The analytical solution can then be found by setting $r = R = +\infty$ while keeping the distance $r - R$ constant (Gentile 2008). We then simply have

$$E_\nu = B(\nu,T_0) + \left[B(\nu,T_{\mathrm{s}}) - B(\nu,T_0)\right]F(\nu,r-R,t). \tag{10}$$

In our simulation, the temperature of the hot slab was set to $T_{\mathrm{s}} = 1500$ eV and the medium was at $T_0 = 50$ eV. The domain size is 0.1347368 cm with the hot slab located at the left boundary. The domain was divided into 32 identical cells. We considered 60 groups logarithmically evenly spaced in the range [0.5 eV, 306 keV], a fixed timestep of $\Delta t = 10^{-11}$ s was used, and no flux limiter (i.e. $\lambda_g = 1/3$) was applied. The gas absorption coefficient was set to $\sigma_g = 2\times10^{13}\left(\frac{h\nu_g}{1\,\mathrm{eV}}\right)^{-3}$ cm^{-1} with $h\nu_g$ the energy in eV of the middle of each radiative group. Figure 2 shows the spectral radiative energies obtained compared to the analytical ones at a time $t = 10^{-10}$ s, sampled at a distance $x = 0.04$ cm (which implies that $r - R = 0.04$ cm in the analytical solution), which corresponds to the centre of the tenth cell. The numerical results are in excellent agreement with the analytical solution.

3.3. Non-equilibrium radiative transfer with picket fence model

Su & Olson (1999) developed analytical solutions for a 1D problem involving non-equilibrium radiative transfer with two radiative energy groups (see also Zhang et al. 2013). Radiative energy is injected into a small region of a uniform domain, diffuses, and

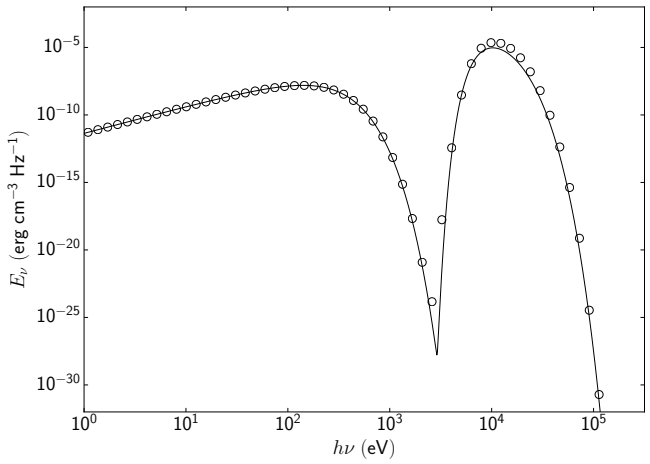

Fig. 2. Radiating plane test: numerical (circles) and analytical solutions at time $t = 10^{-10}$ s.

heats up the gas. The two groups have different opacities, and so the radiative energies propagate at different speeds through the medium. There are several assumptions in their analytical study. The heat capacity at constant volume is assumed to be $C_\mathrm{v} = \mathrm{d}\epsilon/\mathrm{d}T = \alpha T^3$, where α is a parameter. The group integrated Planck distribution is assumed to be

$$B_g = p_g \left(\frac{a_\mathrm{R} c}{4\pi}\right) T^4, \tag{11}$$

where a_R is the radiation constant, and p_g are parameters that verify the condition $\sum_g p_g = 1$. They then define the dimensionless coordinate $x = \bar{\sigma} z$, where z is the coordinate in physical units, and $\bar{\sigma} = \sum_g p_g \sigma_g$. The absorption coefficients σ_g are independent of frequency, and scattering is ignored. The dimensionless time is

$$\tau = \left(\frac{4 a_\mathrm{R} c \bar{\sigma}}{\alpha}\right), \tag{12}$$

and the dimensionless radiative energy density and internal energy are

$$U_g = \frac{E_g}{a_\mathrm{R} T_0^4} \quad \text{and} \quad V = \left(\frac{T}{T_0}\right)^4, \tag{13}$$

respectively, where T_0 is a reference temperature.

The radiation source is applied for a finite period of time ($0 \leq \tau < \tau_0$) inside the region $|x| < x_0$, and gas dynamics are neglected. The equations solved are then

$$\begin{aligned} \partial_t E_\mathrm{T} &= \sum_{g=1}^{Ng} \nabla \cdot \left(\frac{c\lambda_g}{\rho \kappa_{\mathrm{R}g}} \nabla E_g\right) \\ \partial_t E_g - \nabla \cdot \left(\frac{c\lambda_g}{\rho \kappa_{\mathrm{R}g}} \nabla E_g\right) &= \kappa_{\mathrm{P}g} \rho c \left(\Theta_g(T) - E_g + \Gamma_g\right), \end{aligned} \tag{14}$$

where

$$\Gamma_g = \begin{cases} \dfrac{p_g \bar{\sigma} a_\mathrm{R} T_0^4}{\kappa_{\mathrm{P}g} \rho} & \text{if } \tau < \tau_0 \text{ and } |x| < x_0\,, \\ 0 & \text{otherwise.} \end{cases} \tag{15}$$

Following Zhang et al. (2013), we performed case C of Su & Olson (1999) and compared the results with their analytical solution for the radiation diffusion. In case C there are two radiation groups, with $p_1 = p_2 = 1/2$. The absorption coefficients are

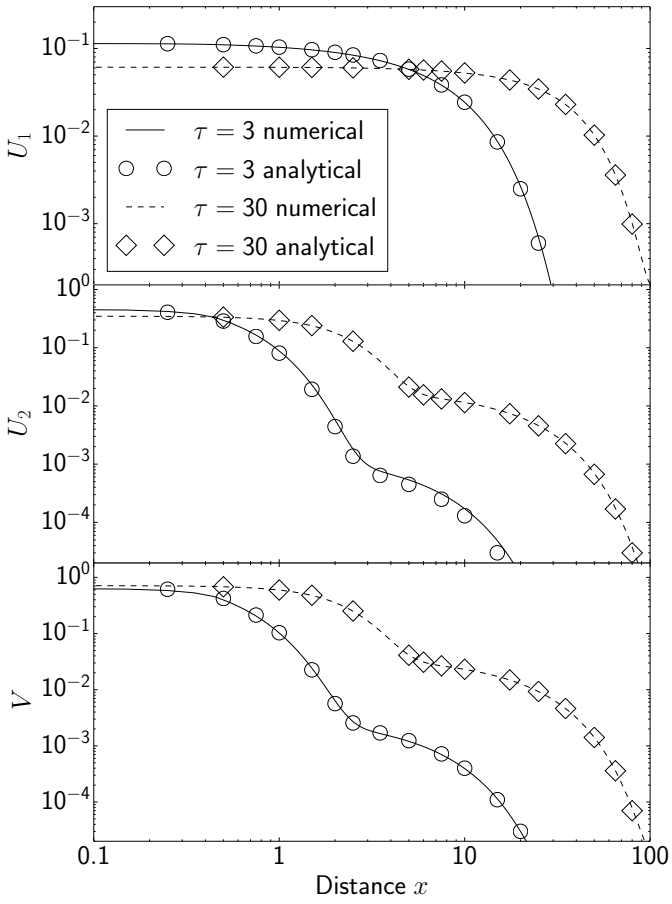

Fig. 3. Non-equilibrium radiative transfer test from Su & Olson (1999). Profiles from the numerical simulation of U_1 (*top*), U_2 (*middle*), and V (*bottom*) are shown for $\tau = 3$ (solid lines) and $\tau = 30$ (dashed lines). The results are compared to the analytical solutions of Su & Olson (1999) for $\tau = 3$ (circles) and $\tau = 30$ (diamonds).

chosen as $\sigma_1 = 2/101$ cm^{-1} and $\sigma_2 = 200/101$ cm^{-1}, and the parameter α used to evaluate the heat capacity is $\alpha = 4a_\mathrm{R}$. The reference temperature is set to $T_0 = 10^6$ K. The radiation source parameters are $x_0 = 1/2$ and $\tau_0 = 10$. To avoid spurious boundary condition effects, we used a computational domain twice the size of Zhang et al. (2013), spanning $-102.4 < x < 102.4$, divided into 2048 identical cells. The left and right boundary conditions were both set to periodic. The initial state of the physical variables were $\rho = 1$ g cm^{-3} and $T = 1$ K, and matter and radiation were in equilibrium. A fixed timestep $\Delta\tau = 0.1$ was used, and no flux limiter (i.e. $\lambda_g = 1/3$) was applied. The results are shown in Fig. 3, where an excellent agreement between the numerical and analytical solutions can be seen.

3.4. Radiative shocks with non-equilibrium diffusion

The fourth test looks at the coupling between the fluid motion and the radiative transfer, solving the complete radiation-hydrodynamics equations (Eq. (1)). Lowrie & Edwards (2008) developed semi-analytic solutions to a 1D non-equilibrium diffusion problem involving radiative shocks of various Mach numbers $\mathcal{M}$. We simulated the $\mathcal{M} = 2$ and $\mathcal{M} = 5$ cases using six frequency groups. For both runs, the domain was split into two uniform regions where the hydrodynamic and radiation variables satisfy the Rankine-Hugoniot jump relations for a radiating fluid in an optically thick medium. The fluid variables inside the ghost

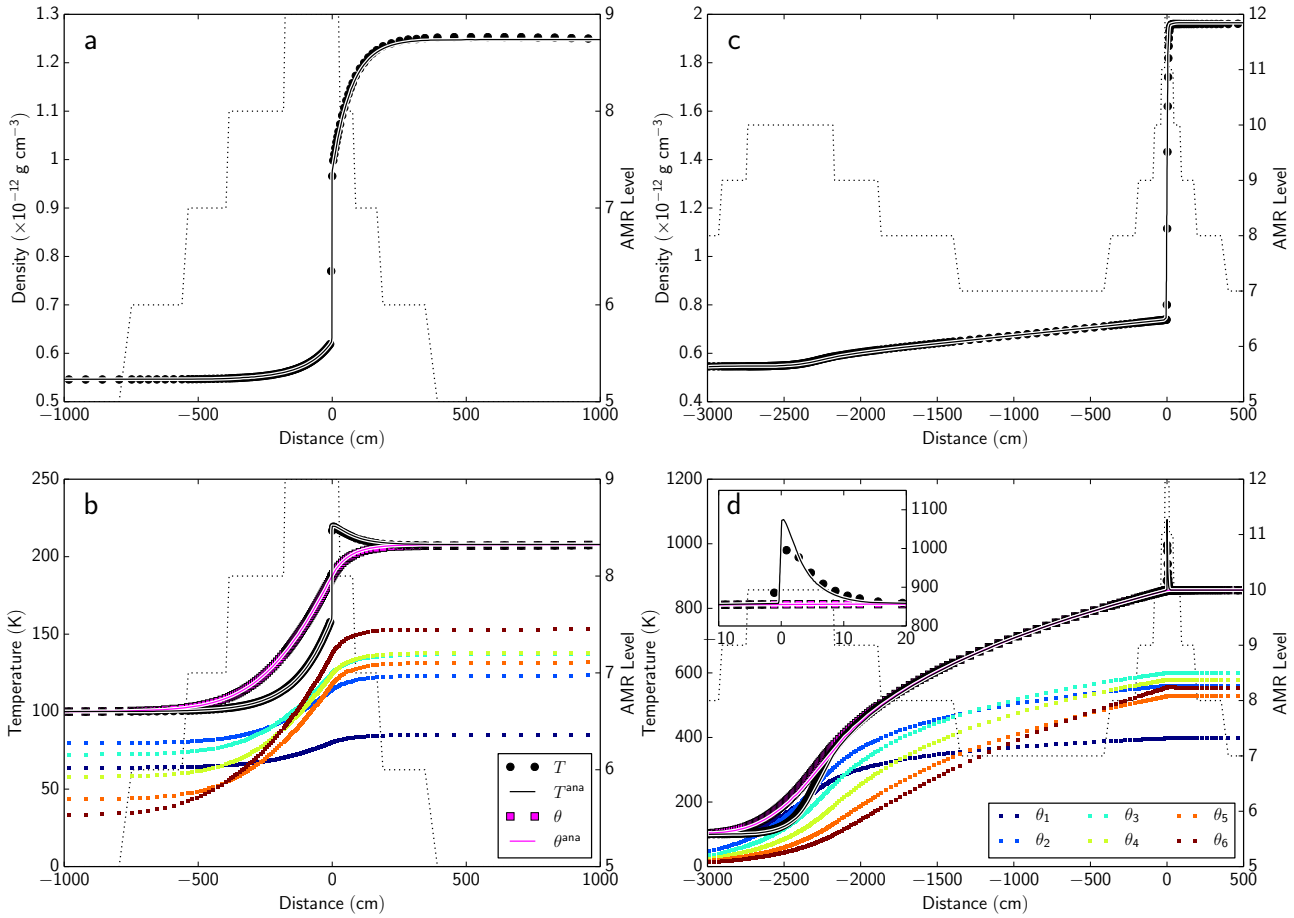

Fig. 4. Radiative shocks with non-equilibrium diffusion. *Left column*: results for the $\mathcal{M} = 2$ case, while the *right column* gives the $\mathcal{M} = 5$ setup. In all panels the numerical results are marked by symbols (circles and squares), the analytical solutions are represented by solid lines, and the mesh AMR level by dotted black lines. Panels **a)** and **c)**: gas density as a function of distance. Panels **b)** and **d)**: gas (black) and total radiative (magenta) temperatures. They also present the radiative temperatures inside the individual groups $\theta_g = (E_g/a_{\rm R})^{1/4}$ with more colours (see legend in panel **d)**).

cells at the left and right boundary conditions were kept as the initial pre- and post-shock state values throughout the simulation (imposed boundary condition). The gas has an ideal equation of state with a mean atomic weight $\mu = 1$ and a specific heat ratio $\gamma = 5/3$, and the Planck and Rosseland opacities are set to $\rho\kappa_{\rm P} = 3.93 \times 10^{-5}$ cm^{-1} and $\rho\kappa_{\rm R} = 0.848902$ cm^{-1}, respectively, in all frequency groups. We used the HLL Riemann solver for the hydrodynamics with a CFL factor of 0.5 and no flux-limiter for the radiation solver (i.e. $\lambda_g = 1/3$).

For the $\mathcal{M} = 2$ case, the initial conditions in the left (pre-shock) region are $\rho_{\rm L} = 5.45887 \times 10^{-13}$ g cm^{-3}, $u_{\rm L} = 2.3547 \times 10^5$ cm s^{-1}, and $T_{\rm L} = 100$ K, and in the right (post-shock) region $\rho_{\rm R} = 1.2479 \times 10^{-12}$ g cm^{-3}, $u_{\rm R} = 1.03 \times 10^5$ cm s^{-1}, and $T_{\rm R} = 207.757$ K. The domain ranges from –1000 cm to 1000 cm. Five frequency groups were evenly (linearly) distributed between 0 and 2×10^{13} Hz, and the sixth group ranged from 2×10^{13} Hz to infinity. The domain was initially divided into 32 cells and four additional AMR levels were enabled (effective resolution of 512). The refinement criterion was based on gas density and total radiative energy gradients. The density and temperature (gas and radiation) profiles are shown in Figs. 4a,b. The numerical solutions show an excellent agreement with the semi-analytical solutions of Lowrie & Edwards (2008). The simulation data were shifted by 13.67 cm to place the density discontinuity at $x = 0$ for comparison with the analytical solutions; this corresponds to the shift the shock suffers as the radiative precursor develops and until the stationary state is reached.

In the $\mathcal{M} = 5$ case, the initial conditions are $\rho_{\rm L} = 5.45887 \times 10^{-13}$ g cm^{-3}, $u_{\rm L} = 5.8868 \times 10^5$ cm s^{-1}, $T_{\rm L} = 100$ K, and $\rho_{\rm R} = 1.96405 \times 10^{-12}$ g cm^{-3}, $u_{\rm R} = 1.63 \times 10^5$ cm s^{-1}, and $T_{\rm R} = 855.72$ K. The domain ranges from –4000 cm to 4000 cm. Five frequency groups were evenly (linearly) distributed between 0 and 10^{14} Hz, and the sixth group ranged from 10^{14} Hz to infinity. The domain was initially divided into 32 cells and seven additional AMR levels were enabled (effective resolution of 4096). The refinement criterion was based on gas density, gas temperature, and total radiative energy gradients. The results in Figs 4c,d show again an excellent agreement with the semi-analytical solutions. The simulation data were this time shifted by 193.5 cm to bring the density discontinuity to $x = 0$.

4. Algorithm performance

We present in this section some tests to assess the scaling performance of our algorithm.

4.1. Strong and weak scaling

The strong and weak scaling runs were performed on the CINES Occigen[3] supercomputer, which uses Intel® E5-2690 (2.60 GHz) processors. We compared the scaling of our

[3] https://www.cines.fr/calcul/materiels-et-logiciels/occigen/

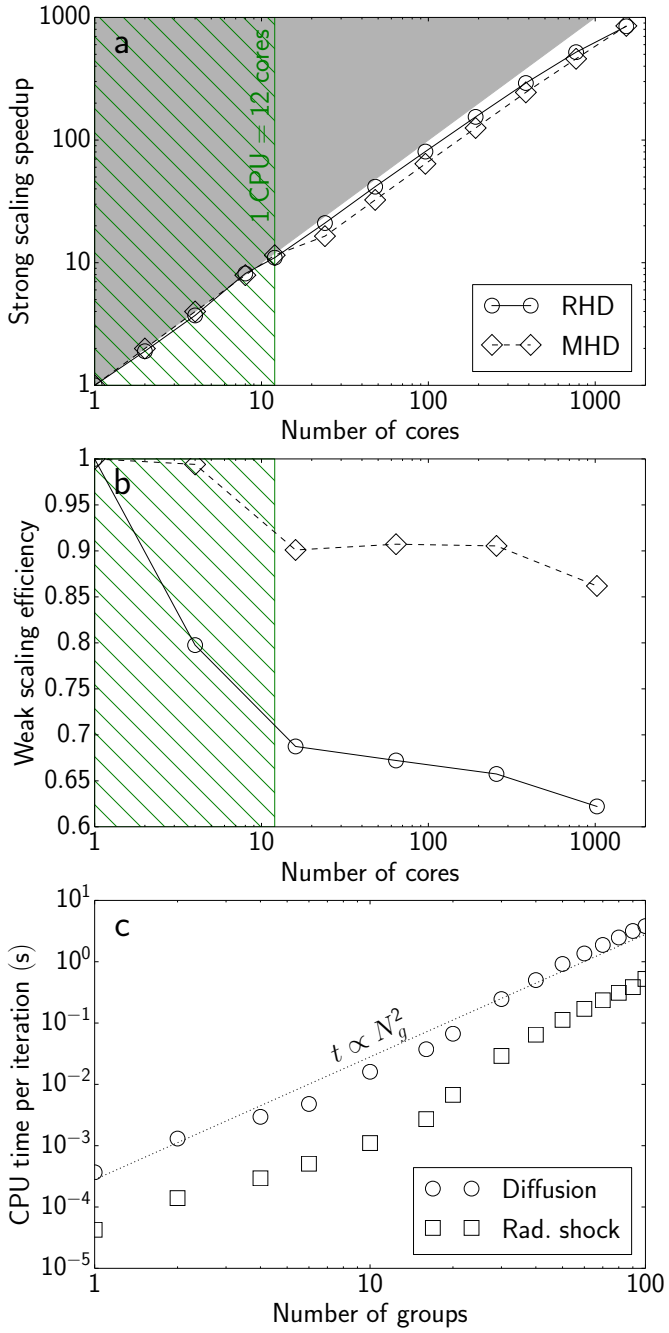

Fig. 5. a) Strong scaling results for the multigroup diffusion test (circles) and the ideal MHD Orszag-Tang vortex calculation (diamonds). The ideal theoretical speedup is at the boundary between the grey and white areas. The Occigen machine has 12-core processors; the 12-core region is marked by the green hatched area. **b)** Weak scaling efficiency for the RHD and MHD runs. **c)** CPU time per BiCGSTAB iteration for a 1D diffusion problem (circles) and a 1D non-stationary radiative shock (squares) as a function of the number of frequency groups N_g used. The curve for a time proportional to N_g^2 is shown as a dotted line.

radiative transfer scheme to the native MHD scheme in RAMSES. The setups used for the RHD and MHD runs were a 2D version of the Dirac diffusion test using four frequency groups and a 2D Orszag-Tang vortex simulation (Orszag & Tang 1979), respectively. In the RHD calculation, the fluid is static and only the radiation solver was called by RAMSES, bypassing the hydrodynamic Godunov solver. Both setups used a 2048^2 mesh.

The strong scaling results are given in Fig. 5a. We can see that as we go beyond the 12-core limit of the Occigen processors, the speedups drop below the ideal curve (grey area) as communications begin to take longer to complete. Our radiative transfer method appears to perform slightly better than the native MHD scheme in RAMSES, as the coupling between hydrodynamics and radiation is ignored (the Godunov solver is not used in the RHD simulations). In the weak scaling RHD runs, when the size of the problem is doubled with the number of CPUs, it takes the implicit BiCGSTAB solver more iterations to converge because there is a stronger propagation of round-off errors originating from the calls to the MPI_ALLREDUCE routine when more CPUs are used. To ensure a fair comparison, we forced all simulations to execute the same number of iterations (500) for every timestep, chosen as the maximum observed number of iterations in the 1024-core run. All simulations also performed the same number of timesteps (100) of a fixed length in time ($\Delta t = 10^{-17}$ s), and each CPU held a grid of 128^2 cells. The weak MHD simulations were run for 300 timesteps, with each CPU processing a grid of 512^2 cells[4]. The results in Fig. 5b show that the weak scaling performance of the RHD solver is below the native MHD solver. The iterative implicit solver suffers from heavy communication operations to compute residuals and scalar quantities which need to be performed at each iteration for each timestep, while the MHD solver only requires one communication operation per timestep. We believe that a weak scaling efficiency of 60% is acceptable for our purposes.

4.2. Group scaling

Our final performance test was to assess the scaling of our multigroup algorithm for a given problem when the number of frequency groups N_g is increased. The results of the simulation time divided by the total number of BiCGSTAB iterations for a 1D multigroup diffusion test performed on a single Intel® Xeon® E5620 (2.40 GHz) CPU core on a local HP-Z800 workstation are shown in Fig. 5c. The algorithm appears to scale with N_g^2, which is expected from the double sum over N_g in the term in the third line of Eq. (5). We carried out a second group scaling study, this time running the subcritical radiative shock test from Sect. 3.4 (although with a lower resolution; only three levels of refinement were used[5]), where the radiative transfer is fully coupled to the hydrodynamics. The results are given in Fig. 5c, and the behaviour is very similar to the diffusion-only solver. The radiative transfer step completely dominates over the hydrodynamic step[6] in terms of computational cost, and it is thus not surprising to see the same scaling for a RHD run as for a calculation which only calls the radiation solver.

5. Application to star formation

In this final section, we apply the multigroup formalism to a simulation of the collapse of a gravitationally unstable dense cloud core, which eventually forms a protostar in its centre. The collapsing material is initially optically thin and all the energy gained from compressional heating is transported away

[4] These resolutions and number of timesteps were chosen so that both RHD and MHD simulations run for approximately the same amount of time.

[5] This explains a smaller time per iteration for the radiative shock simulations than for the diffusion runs.

[6] The radiation solver takes up to 90% of the computation time during one timestep.

by the escaping radiation, which causes the cloud to collapse isothermally. As the optical depth of the cloud rises, the cooling is no longer effective and the system starts heating up, taking the core collapse through its adiabatic phase. A hydrostatic body (also known as the first Larson core; Larson 1969) approximately 10 AU in size is formed and continues to accrete material from the surrounding envelope and accretion disk; this first core will eventually form a young star, after a second phase of collapse triggered by the dissociation of H_2 molecules (see Masunaga & Inutsuka 2000, for instance). In this preliminary astrophysical application, however, we focus on the properties of the first Larson core for the sake of simplicity.

We adopt initial conditions similar to those in Commerçon et al. (2010), who follow Boss & Bodenheimer (1979). A magnetized uniform-density sphere of molecular gas, rotating about the z-axis with solid-body rotation, is placed in a surrounding medium a hundred times less dense. The gas and radiation temperatures are 10 K everywhere. The prestellar core mass has a mass of 1 $M_\odot$, a radius $R_0 = 2500$ AU, and a ratio of rotational over gravitational energy of 0.03. To favor fragmentation, we use an $m = 2$ azimuthal density perturbation with an amplitude of 10%. The magnetic field is initially parallel to the rotation axis. The strength of the magnetic field is expressed in terms of the mass-to-flux to critical mass-to-flux ratio $\mu = (M/\Phi)/(M/\Phi)_c = 5$ (Mouschovias & Spitzer 1976). The field strength is invariant along the z direction, and it is 100 times stronger in a cylinder of radius R_0 (with the dense core in its centre) than in the surrounding medium[7]. We used a gas equation of state modelling a simple mixture of 73% hydrogen and 27% helium (in mass), which takes into account the effects of rotational (for H_2 which is the dominant form of hydrogen for temperatures below 2000 K) and vibrational degrees of freedom. The frequency-dependent dust and gas opacities were taken from Vaytet et al. (2013a), assuming a 1% dust content. We used the ideal MHD solver of `RAMSES`, and the grid refinement criterion was based on the Jeans mass, ensuring the Jeans length was always sampled by a minimum of 12 cells. The coarse grid had a resolution of 32^3, and 11 levels of AMR were enabled, resulting in a maximum resolution of 0.15 AU at the finest level. The Minerbo flux limiter (Minerbo 1978) was used for these simulations.

We performed two simulations; one under the grey approximation and a second using 20 frequency groups. The first and last groups spanned the frequency ranges (in Hz) $[0 \rightarrow 5\times10^{10}]$ and $[1.3\times10^{14} \rightarrow \infty]$, respectively. The remaining 18 groups were evenly (logarithmically) distributed between 5×10^{10} and 1.3×10^{14} Hz. The results are shown in Figs. 6 and 7. The gas temperature as a function of density for all the cells in the computational domain is shown in Fig. 6a. While the two simulations show similar results overall, there are several differences we wish to point out. For relatively low densities in the range $5\times10^{-17} < \rho < 3\times10^{-15}$ g cm^{-3}, the multigroup run is hotter than the grey simulation. This is also visible in the temperature maps of Fig. 7, where the gas is hotter in the 20-group run for $r > 20$ AU, this being most obvious in panel c. It appears that the radiation transport from the central core to the surrounding envelope is more efficient in the multigroup case. More energy has left the core, leaving it colder than in the grey case, while more energy has been deposited in the thus warmer outer envelope.

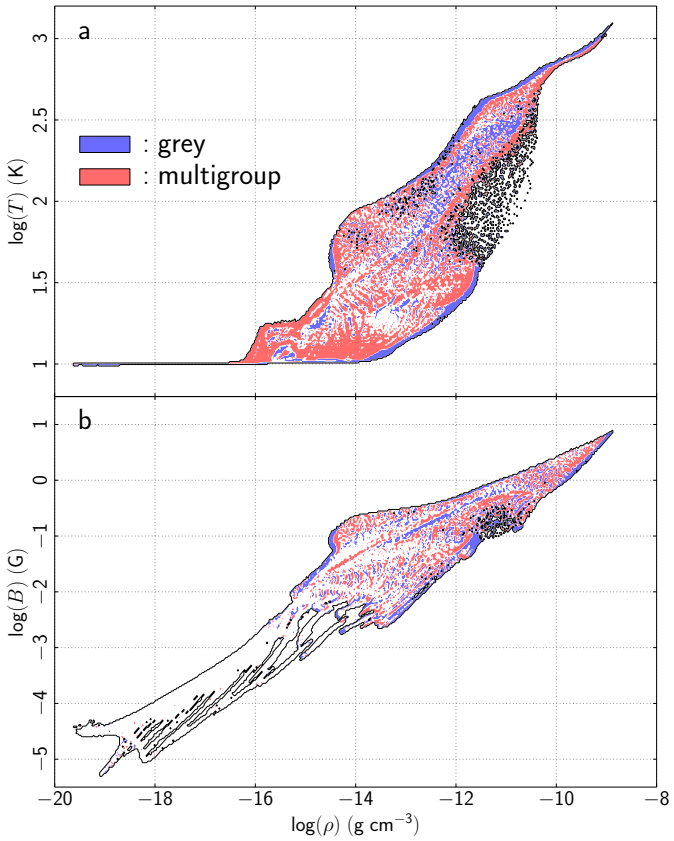

Fig. 6. **a)** Temperature as a function of density in the grey and multigroup simulations at a time $t = 24\,265$ yr. The colour blue represents regions where the grey simulation either dominates (in terms of mass contained within the figure pixels) over the multigroup simulation, or where there is no multigroup data. Likewise, red codes for the regions of the diagram where the multigroup run prevails. The white areas indicate where both simulations yield identical results. The black contour line delineates the region where data are present. **b)** Same as for **a)** but showing the strength of the magnetic field as a function of density.

Higher temperatures are also observed in the bipolar outflow, along the vertical axis, relatively close to the first core. Kuiper et al. (2011) found that using a frequency-dependent scheme in simulations of high-mass stars could enhance radiation pressure in the polar direction compared to the grey simulations of Krumholz et al. (2009), producing much stabler outflows. This could be similar to what we are observing here; confirmation of this would require further study.

Conversely, the strength of the magnetic field does not change significantly when using a multigroup model. For densities below 10^{-15} g cm^{-3}, the two runs are virtually identical (see Fig. 6b). In the ideal MHD limit, the magnetic field is not directly related to the thermal properties of the gas, and it is therefore not surprising that the multigroup formalism has little impact. However, in the future we plan to study star formation using a non-ideal description of MHD (Masson et al. 2012), where magnetic and thermal interactions are twofold. First, magnetic diffusion contributes additional gas heating from ion-neutral frictions and Joule heating. Second, the chemical properties of the gas, which strongly depend on temperature, also affect the magnetic resistivities, which govern the diffusion processes. We will investigate this in detail in a forthcoming study.

[7] This was chosen as an attempt to reproduce the dragging in of field lines that would have happened in the formation of the dense core (see e.g. Gillis et al. 1974), while also retaining in the simplest manner the divergence-free condition for the MHD.

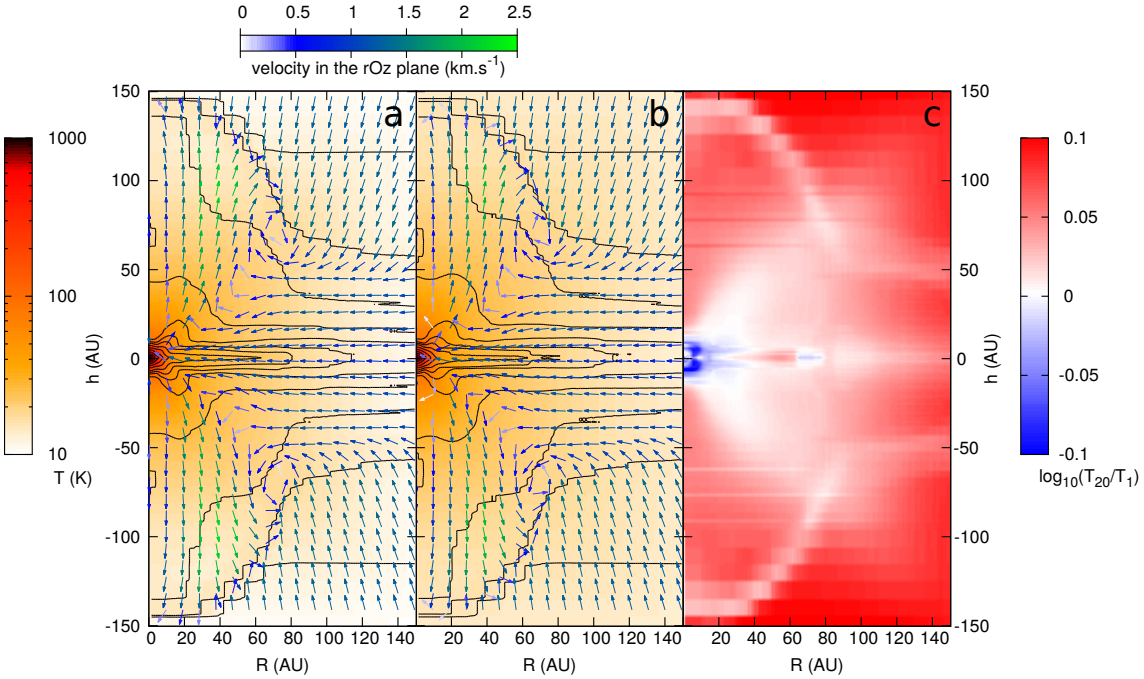

Fig. 7. **a)** Temperature map (colours) at a time $t = 24\,282$ yr in a grey simulation of the collapse of a 1 $M_\odot$ cloud. The data are presented as a function of radius and height over the mid-plane; the data have been averaged around the azimuthal direction. The black lines are logarithmically spaced density contours, in the range $10^{-16} < \rho < 10^{-9}$ g cm^{-3} (two contours per order of magnitude). The arrows represent the velocity vector field in the r-z plane. **b)** Same as for **a)** but using 20 frequency groups. **c)** Map of the logarithm of the ratio of the multigroup temperature over the grey temperature. The colour red indicates where the gas temperature in the multigroup simulation is higher than for the grey run, and vice versa for blue.

The use of multigroup RHD may not yield significantly different results in the early stages of molecular cloud collapse, but it does provide a wealth of physical information in the system. Channel maps such as the ones presented in Fig. 8 or spectral energy distributions (SEDs; Fig. 9) are directly available from the simulation data and do not require any post-processing software. The channel maps show a peak intensity around a wavelength of 100 μm, close to the synthetic observations of Commerçon et al. (2012). Interestingly, the SEDs show departures from a black-body spectrum (most obviously at the low-frequency end) close to the protostar (20 AU; Fig. 9b). We do not wish to carry out a detailed study here on the effects of multifrequency radiative transfer on the structures of protostars, we simply wish to illustrate the power of the method. We leave the detailed work on collapsing objects for a future paper, as this is first and foremost an article focused on methodology.

6. Conclusions and future work

We have implemented a method for multigroup flux-limited diffusion in the RAMSES AMR code for astrophysical fluid dynamics. The method is based on the time-implicit grey FLD solver of Commerçon et al. (2011b), and uses the adaptive time-stepping strategy of Commerçon et al. (2014), where each level is able to evolve with its own timestep using a subcycling procedure. The multigroup method allows the discretization of the frequency domain to any desired resolution, enabling us to take into account the frequency dependence of emission and absorption coefficients. The radiative energy density in the frequency groups are all coupled together through the matter temperature and terms reproducing Doppler shift effects when velocity gradients are present in the fluid. A consequence of this coupling is the apparition of non-symmetric terms in the matrix we have to invert in our implicit time-stepping procedure. We therefore

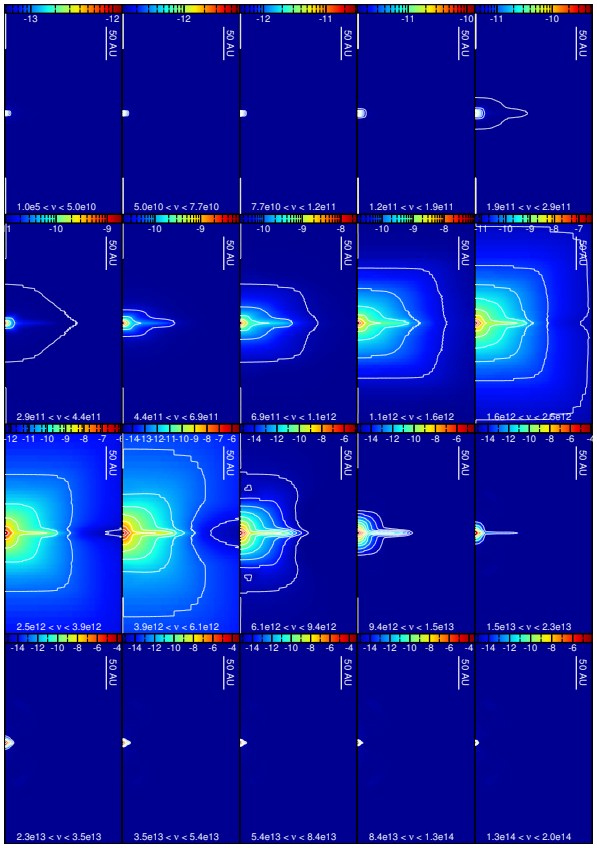

Fig. 8. Radiative energy density map in each frequency group. The white contours have 10 levels logarithmically spaced between the minimum and maximum values of each map. The frequencies of each group are indicated at the bottom of each map. The maps represent the same region as in Fig. 7.

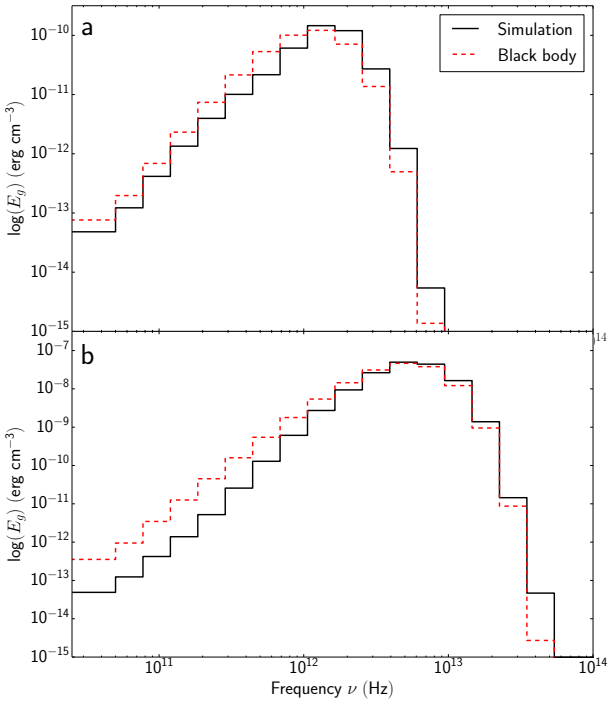

Fig. 9. Spectral energy distributions extracted in a cell located 2000 AU **a)** and 20 AU **b)** from the protostar. The black solid lines represent the energy inside the 20 frequency groups. They are compared to a black-body distribution (dashed red), which would have the same total energy.

had to abandon the original conjugate gradient algorithm of Commerçon et al. (2011b) for a bi-conjugate gradient iterative solver. A more evolved BiCGSTAB solver was preferred for its greater stability compared to a raw bi-conjugate algorithm.

The method was fully tested against standard radiation diffusion, frequency-dependent, and full radiation hydrodynamics tests. It performed extremely well in all of these tests, and its scaling performance was also found to be very satisfactory.

The multigroup formalism was finally applied to a simulation of the gravitational collapse of a dense molecular cloud core in the context of star formation. The method has revealed differences between grey and frequency-dependent simulations, but more importantly uncovered departures from a black-body radiation distribution. We also illustrated the wealth of information the method brings to astrophysical studies, with the ability to directly produce channel maps and SEDs. We will carry out a much more thorough study of the effects of multigroup radiative transfer on the structures of protostars and protoplanetary discs, as well as their observable quantities, as part of a much wider parameter space study in a forthcoming paper.

Acknowledgements. This work was granted access to the CINES HPC resources Jade and Occigen under the allocations x2014-047247 and x2015-047247 made by DARI/GENCI. The research leading to these results has also received funding from the European Research Council under the European Community's Seventh Framework Programme (FP7/2007-2013 Grant Agreement No. 247060). B.C. gratefully acknowledges support from the French ANR Retour Postdoc program (ANR-11-PDOC-0031). Finally, we acknowledge financial support from the "Programme National de Physique Stellaire" (PNPS) of CNRS/INSU, France.

References

Bate, M. R. 2012, MNRAS, 419, 3115
Boss, A. P., & Bodenheimer, P. 1979, ApJ, 234, 289
Chiavassa, A., Freytag, B., Masseron, T., & Plez, B. 2011, A&A, 535, A22
Commerçon, B., Hennebelle, P., Audit, E., Chabrier, G., & Teyssier, R. 2010, A&A, 510, L3
Commerçon, B., Hennebelle, P., & Henning, T. 2011a, ApJ, 742, L9
Commerçon, B., Teyssier, R., Audit, E., Hennebelle, P., & Chabrier, G. 2011b, A&A, 529, A35
Commerçon, B., Launhardt, R., Dullemond, C., & Henning, T. 2012, A&A, 545, A98
Commerçon, B., Debout, V., & Teyssier, R. 2014, A&A, 563, A11
Davis, S. W., Stone, J. M., & Jiang, Y. F. 2012, ApJS, 199, 9
Draine, B. 2003, ARA&A, 41, 241
Ferguson, J. W., Alexander, D. R., Allard, F., et al. 2005, ApJ, 623, 585
Fromang, S., Hennebelle, P., & Teyssier, R. 2006, A&A, 457, 371
Gentile, N. 2008, in Computational Methods in Transport: Verification and Validation, ed. F. Graziani (Berlin, Heidelberg: Springer), Lect. Notes Comp. Sci. Eng., 62, 135
Gillis, J., Mestel, L., & Paris, R. B. 1974, Ap&SS, 27, 167
Graziani, F. 2008, in Computational Methods in Transport: Verification and Validation, ed. F. Graziani (Berlin, Heidelberg: Springer), Lect. Notes Comp. Sci. Eng., 62, 151
Krumholz, M. R., Klein, R. I., McKee, C. F., Offner, S. S. R., & Cunningham, A. J. 2009, Science, 323, 754
Kuiper, R., Klahr, H., Beuther, H., & Henning, T. 2011, ApJ, 732, 20
Larson, R. B. 1969, MNRAS, 145, 271
Levermore, C. D., & Pomraning, G. C. 1981, ApJ, 248, 321
Li, A., & Draine, B. T. 2001, ApJ, 554, 778
Lowrie, R. B., & Edwards, J. D. 2008, Shock Waves, 18, 129
Masson, J., Teyssier, R., Mulet-Marquis, C., Hennebelle, P., & Chabrier, G. 2012, ApJS, 201, 24
Masunaga, H., & Inutsuka, S. 2000, ApJ, 531, 350
Masunaga, H., Miyama, S. M., & Inutsuka, S.-I. 1998, ApJ, 495, 346
Mezzacappa, A., Calder, A. C., Bruenn, S. W., et al. 1998, ApJ, 495, 911
Minerbo, G. N. 1978, J. Quant. Spectr. Rad. Transf., 20, 541
Mouschovias, T. C., & Spitzer, Jr., L. 1976, ApJ, 210, 326
Orszag, S. A., & Tang, C.-M. 1979, J. Fluid Mech., 90, 129
Ossenkopf, V., & Henning, T. 1994, A&A, 291, 943
Semenov, D., Henning, T., Helling, C., Ilgner, M., & Sedlmayr, E. 2003, A&A, 410, 611
Shestakov, A., & Offner, S. 2008, J. Comput. Phys., 227, 2154
Su, B., & Olson, G. 1999, J. Quant. Spectr. Rad. Transf., 62, 279
Teyssier, R. 2002, A&A, 385, 337
Tomida, K., Tomisaka, K., Matsumoto, T., et al. 2013, ApJ, 763, 6
van der Holst, B., Toth, G., Sokolov, I. V., et al. 2011, ApJS, 194, 23
van der Vorst, H. A. 1992, SIAM J. Scientific and Statistical Computing, 13, 631
Vaytet, N., Audit, E., Dubroca, B., & Delahaye, F. 2011, J. Quant. Spectr. Rad. Transf., 112, 1323
Vaytet, N., Audit, E., Chabrier, G., Commerçon, B., & Masson, J. 2012, A&A, 543, A60
Vaytet, N., Chabrier, G., Audit, E., et al. 2013a, A&A, 557, A90
Vaytet, N., González, M., Audit, E., & Chabrier, G. 2013b, J. Quant. Spectr. Rad. Transf., 125, 105
Williams, R. B. 2005, Ph.D. Thesis, Massachusetts Institute of Technology, Dept. of Nuclear Engineering
Zhang, W., Howell, L., Almgren, A., et al. 2013, ApJS, 204, 7

Chapitre 2

Expériences d'astrophysique en laboratoire

L'astrophysique est un domaine de la physique où l'expérimentation n'est que rarement possible. Les conditions physiques observées dans l'univers sont difficilement reproductibles sur Terre. Je décris dans ce chapitre deux cas où des expériences en laboratoire pertinentes pour l'astrophysique sont néanmoins possibles.

2.1 Expériences de chocs radiatifs menées auprès des grands lasers

2.1.1 Contexte

Les chocs hydrodynamiques sont des discontinuités dans les variables classiques (densité, impulsion, énergie) qui ont lieu lorsque le fluide se déplace plus vite que la vitesse du son. Ces discontinuités sont des zones dans lesquelles la viscosité dissipe l'énergie cinétique en énergie thermique, et les relations de saut sont régies par les relations de Rankine-Hugoniot. Contrairement au cas d'un choc purement hydrodynamique, dans un choc radiatif le fluide post-choc peut réémettre une partie de son énergie sous forme de photons qui sont réabsorbés dans le milieu pré-choc. Ainsi, une rétroaction est générée et un précurseur radiatif est créé : il s'agit d'une région en amont du choc qui est préchauffée. Le choc radiatif est donc spatialement étendu, sa longueur étant directement relié au libre parcours moyen de photons dans le milieu pré-choc. Une description détaillée des chocs radiatifs est donnée dans Zel'dovich et Raizer (1967), Mihalas et Weibel Mihalas (1984), Drake (2005). Nous pouvons citer en particulier deux catégories de chocs radiatifs : les chocs sous-critiques, pour lesquels la température du précurseur est inférieure à la température post-choc, et les chocs super-critiques, pour lesquels les deux températures sont égales (cf. Fig 2.1).

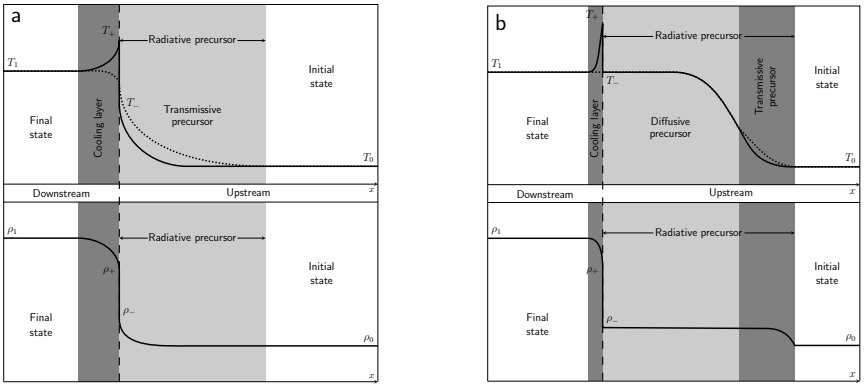

FIGURE 2.1 – Structure d'un choc radiatif sous-critique (a) et super-critique (b). Le fluide se déplace de droite à gauche dans le référentiel du choc. Profils des températures (haut) du gaz (ligne continue) et radiative (pointillés) et de la densité (bas). La position des sauts en température et densité est marquée par la line brisée verticale. Les tailles relatives des différentes zones ne sont qu'indicatives. Extrait de Vaytet *et al.* (2013).

Ces chocs ont lieu aux différents stades de l'évolution stellaire : lors de la formation stellaire, lorsque le gaz accrété tombe sur l'objet stellaire en formation ; dans les atmosphères d'étoiles évoluées, lorsque les chocs sont à l'origine de pulsations (Chadid 2000, Fadeyev et Gillet 1998, Fadeyev et Gillet 2000) et dans les derniers stades d'évolution lors des explosions de supernovæ et l'interaction du reste de supernova avec le milieu interstellaire environnant.

La symétrie sphérique ou mono-dimensionnelle est une approximation souvent faite pour l'étude de ces chocs. Toutefois, si cette approximation peut être justifiée en première approximation dans le cas des chocs d'accrétion ou des étoiles pulsantes, elle est plus sujette à débat pour les colonnes d'accrétion des étoiles T-Tauri classiques, où la matière est supposée suivre les lignes de champ magnétique entre le disque et la surface stellaire.

Les étoiles T-Tauri classiques sont des étoiles jeunes de faible masse entourées par un disque d'accrétion et caractérisées par des mécanismes d'accrétion-éjection. Le gaz s'échappant du disque à la vitesse de plusieurs centaines de km/s tombe sur la photosphère de l'étoile, guidé par le champ magnétique, le long de colonnes d'accrétion. Cette accrétion est déduite d'un excès de flux spectral dans l'UV et le visible ainsi que de signatures dans les raies. Cet excès est utilisé comme traceur du taux d'accrétion qui est un paramètre essentiel pour connaître l'évolution stellaire. Calvet et Gullbring (1998), Lamzin (1998) furent les premiers à suggérer que cet excès provienne de la matière accrétée. Si l'on considère que la matière tombe à la vitesse de chute libre depuis le disque, on obtient des vitesses

de $v = \sqrt{\frac{2GM}{R}} \simeq 440$ km/s pour une étoile de 1 $M_\odot$ et une distance de 2 $R_\odot$. Cela correspond à un nombre de Mach M$\simeq$ 300, donc d'un choc très supersonique. Il est raisonnable de penser que ces derniers sont proches du régime supercritique avec un précurseur radiatif développé.

Des simulations semblent indiquer que la topologie de ces colonnes d'accrétion est complexe et dépend notamment des orientations relatives des axes de rotation et du champ magnétique (Romanova *et al.* 2003). La forme exacte de ces colonnes est encore sujet à débat actuellement. L'absence de résolution angulaire ainsi que la complexité de la structure des chocs radiatifs nécessitent une modélisation fine du système étoile-disque et en particulier de ces chocs d'accrétion radiatifs. Toutefois, les taux d'accrétion déduits des observations reposent sur des modèles de choc 1D (Calvet et Gullbring 1998, Lamzin 2003), dont la justification est discutable. Cela encourage donc l'étude des chocs radiatifs dans une géométrie multidimensionnelle, par le biais d'études théoriques ou d'expériences d'astrophysique en laboratoire.

Dans les quarante dernières années sont apparues des installations de lasers de puissance. Les expériences menées auprès de ces installations peuvent être classées en deux catégories : la mesure des propriétés de la matière dans les conditions astrophysiques (opacités, équations d'état) et la reproduction à des facteurs d'échelle près de situations dynamiques astrophysiques (instabilités hydrodynamiques, jets et hydrodynamique radiative). L'étude des chocs radiatifs se placent dans la seconde catégorie. Le but est de mieux comprendre la physique des chocs radiatifs, et les données fournies par les expériences permettent également de valider les codes numériques, qui sont ensuite utilisés pour analyser les observations.

Des phénomènes astrophysiques purement hydrodynamiques peuvent être étudiés de façon exacte en laboratoire en utilisant des lois d'échelle, afin de garder constants les nombres sans dimension caractéristiques de la situation (Reynolds, Mach...). Cette invariance par changement d'échelle cesse d'être rigoureuse en présence de processus faisant intervenir d'autres échelles qui leur sont propres, comme le transfert radiatif. Toutefois, les expériences reproduisent bien la dynamique et la structure des phénomènes observés.

2.1.2 Expériences de chocs radiatifs

Les installations de laser de puissance sont utilisées pour générer des chocs radiatifs dans des cibles de taille millimétrique. La cible est remplie de gaz noble au poids moléculaire élevé (xénon, argon) afin de maximiser les effets radiatifs. Le laser est focalisé sur la face avant de la cible constituée d'un matériau solide opaque, appelé piston. Celui-ci absorbe l'énergie fournie par l'impulsion laser. La matière le constituant est ablatée et par effet fusée, un choc est généré et se propage dans la cible (cf. Fig. 2.2).

Les premières expériences mettant en évidence la propagation d'un choc radiatif ont été menées dans du xénon à 2 et 6 bars sur le laser du CEA Limeil

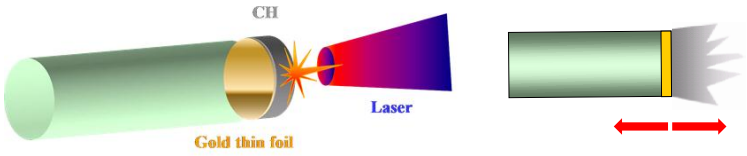

FIGURE 2.2 – Schéma du principe de fonctionnement d'une expérience de choc radiatif (voir le texte pour les détails).

(Bozier *et al.* 1986). Dans celles-ci, le laser de 40 J était focalisé sur un piston d'aluminium, créant un choc à 50 km/s dont l'émissivité du précurseur fut observée sur 10 ns.

Depuis, de nouvelles expériences ont été menées sur diverses installations mondiales (LULI, PALS...) et utilisant de nouveaux diagnostics pour analyser à la fois le précurseur et le front de choc (vitesse, densité, dynamique, forme, etc). Ainsi, sur l'installation laser LULI avec du xénon à 0.2 bar, Fleury *et al.* (2002), Bouquet *et al.* (2004) utilisèrent des interféromètres pour mesurer la vitesse du choc et la densité électronique du précurseur radiatif pour la première fois, sur des temps d'expérience de l'ordre de 6 ns. Les vitesses de chocs atteignaient des valeurs de 60-75 km/s pour des températures de 15 à 20 eV. Les densités électroniques mesurées étaient de l'ordre de 10^{18}-10^{20} cm^{-3}, en accord avec des simulations 1D. Toutefois, les vitesses expérimentales du précurseur étaient plus faibles que celles obtenues numériquement, ce qui fut interprété comme une signature de pertes radiatives latérales.

Aux États-Unis, l'installation OMEGA a permis d'atteindre dans du xénon à 1 bar des chocs entre 110 et 150 km/s (Reighard *et al.* 2006). Pour la première fois, la forme du front de choc a pu être analysée grâce à de la radiographie X. Dans cette expérience, des chocs secondaires issus des parois ont pu être mis en évidence, qui viennent ensuite interagir avec le choc primaire généré par le laser (Doss *et al.* 2009).

Des vitesses encore plus élevées ($\geq$150 km/s) ont été obtenues sur l'installation japonaise GEKKO XII (Dizière *et al.* 2011). Dans ces conditions, la dynamique du choc est affectée par la pression radiative en plus du flux radiatif.

Des expériences utilisent aussi d'autres gaz que le xénon. Par exemple, sur le laser OMEGA, Keiter *et al.* (2002) utilisèrent un aérogel de SiO_2 et Visco *et al.* (2012) furent les premiers à utiliser de l'argon. Les températures électroniques mesurées étaient de 30-60 eV.

2.1.3 Ma contribution

Le but principal de mes recherches dans cette thématique était de caractériser les effets multidimensionnels dans l'évolution des chocs radiatifs.

J'ai pour cela étudier l'influence de plusieurs paramètres sur les vitesses du choc, du précurseur... Afin de pouvoir comparer les résultats numériques aux expériences, toutes les simulations ont été faites avec les conditions expérimentales : du xénon était emprisonné dans une cellule millimétrique dont les parois étaient faites en matériaux divers (ce qui permettait de jouer sur les fuites latérales) et le choc généré par le laser se déplaçait à une vitesse de l'ordre de 65 km/s.

J'ai mené une étude théorique de l'influence de différents paramètres sur la propagation du choc. Les résultats sont présentés dans (González *et al.* 2009) (article joint à la section 2.1.4). J'ai en particulier étudié les effets multidimensionnels dûs à la géométrie de l'écoulement ou aux pertes latérales, soit via le rapport entre la largeur de la cible et le libre parcours moyen de photon, soit via l'albédo des parois latérales. Cette étude a pu mettre en évidence la possible courbure du choc, qui avait pu être observée expérimentalement par l'intermédiaire d'imagerie 2D (Vinci *et al.* 2006). J'ai aussi étudié le temps d'établissement d'un régime stationnaire dans les conditions expérimentales en trouvant une formule simple dépendant seulement de l'albédo des parois.

En plus de mon travail de modélisation, j'ai participé à une campagne d'expérience. Elle a eu lieu en juillet 2007 auprès du laser PALS (Prague, République Tchèque). J'ai participé dans cette campagne à la calibration des cibles et des tirs de laser. J'ai par la suite aidé à l'analyse des résultats obtenus. Le but de cette campagne était d'étudier la dynamique des chocs sur de longues durées (100 ns) et de faire des radiographies X-UV longitudinales résolues en temps et en espace afin de mieux contraindre l'épaisseur et le profil du front de choc ainsi que le milieu post-choc.

Après l'implémentation du schéma M1 multigroupe décrit à la section 1.2.4, j'ai étudié l'influence de la prise en compte de cette dépendance spectrale sur la structure des chocs radiatifs. Les résultats obtenus sont présentés dans Vaytet *et al.* (2013), article joint à la section 2.1.4. Nous avons montré que la prise en compte de plusieurs groupes induit de grandes différences par rapport à des simulations grises (c'est-à-dire ne considérant aucune dépendance spectrale), et ce même pour un faible nombre de groupes. Dans nos conditions expérimentales, il faut par exemple un minimum de 50 groupes pour atteindre une convergence numérique sur la taille du précurseur radiatif.

2.1.4 Publications choisies

González *et al.* 2009 : effet des pertes radiatives latérales

Vaytet *et al.* 2013 : influence du multigroupe sur la structure des chocs radiatifs

A&A 497, 27–34 (2009)
DOI: 10.1051/0004-6361/20079136

Astronomy & Astrophysics

2D numerical study of the radiation influence on shock structure relevant to laboratory astrophysics

M. González[1,2,3], E. Audit[2,3], and C. Stehlé[4]

[1] Instituto de Fusión Nuclear, Universidad Politécnica de Madrid, Madrid, Spain
e-mail: matthias@din.upm.es
[2] Service d'Astrophysique, CEA/DSM/IRFU/SAp, Centre de Saclay, 91191 Gif-sur-Yvette, France
[3] Laboratoire AIM, CNRS, CEA/DSM, Université Paris Diderot, 91191 Gif-sur-Yvette, France
[4] LERMA, Observatoire de Paris, Université Paris VI, CNRS, 5 place J. Janssen, 92195 Meudon, France

Received 23 November 2007 / Accepted 9 January 2009

ABSTRACT

Context. Radiative shocks are found in various astrophysical objects and particularly at different stages of stellar evolution. Studying radiative shocks, their topology, and thermodynamical properties is therefore a starting point to understanding their physical properties. This study has become possible with the development of large laser facilities, which has provided fresh impulse to laboratory astrophysics.
Aims. We present the main characteristics of radiative shocks modeled using cylindrical simulations. We focus our discussion on the importance of multi-dimensional radiative-transfer effects on the shock topology and dynamics.
Methods. We present results obtained with our code HERACLES for conditions corresponding to experiments already performed on laser installations. The multi-dimensional hydrodynamic code HERACLES is specially adapted to laboratory astrophysics experiments and to astrophysical situations where radiation and hydrodynamics are coupled.
Results. The importance of the ratio of the photon mean free path to the transverse extension of the shock is emphasized. We present how it is possible to achieve the stationary limit of these shocks in the laboratory and analyze the angular distribution of the radiative flux that may emerge from the walls of the shock tube.
Conclusions. Implications of these studies for stellar accretion shocks are presented.

Key words. hydrodynamics – radiative transfer – shock waves – plasmas – stars: formation – methods: numerical

1. Introduction

Radiative shocks are shocks in which the structure of the flow is affected by radiation, either because the radiative energy density cannot be neglected or because the energy transport by radiation (i.e., the radiative flux) is significant. For densities relevant to laboratory astrophysics, the radiative flux becomes important at temperature of a few tens of eV. The temperature has to be about one order of magnitude higher before the radiative energy becomes important. In astrophysics and in particular stellar physics, the density can be far lower and radiation therefore becomes important at lower temperatures.

A characteristic of radiative shocks is that at high shock speeds, the shocked matter is strongly heated and radiates energy. Unless the cold upstream gas is completely transparent, it absorbs this radiation creating a hot radiative precursor in front of the shock where the matter is generally ionized. We focus hereafter on shocks that exhibit a developed radiative precursor.

The modeling of these radiative shocks is difficult because of the nonlocal coupling between hydrodynamics and radiation, of the different scales important to radiation and hydrodynamics (Zel'dovich & Raizer 1967; Sincell et al. 1999a,b), and of multi-dimensional effects (Leygnac et al. 2006; González et al. 2006b).

The topology and evolution of radiative shocks depend on several factors, such as the geometry (from 1D, as in shock tubes, to more complex geometries), the energy deposition (impulsive, as for radiative blast waves, or continuously driven by a constant piston velocity), the optical depth of the downstream and upstream regions relative to the shock, and the possible contribution of a magnetic field. A detailed description of radiative shocks is given by Zel'dovich & Raizer (1967), Mihalas & Mihalas (1984), and Drake (2005).

These strong radiative shocks are found at different stages of stellar evolution: from star formation, when the accreting gas falls onto the protostellar forming object; during the accretion – ejection process, which manifests itself in terms of the jets of Young Stellar Objects (YSO) and stellar disks, in the atmospheres of evolved stars, when shocks drive pulsation (Chadid et al. 2000; Fadeyev & Gillet 1998, 2000); and in the last stages of supernovae explosions.

Spherical or 1D symmetry is the usual obvious approximation, which prevails in the lack of further information about the geometry of these astrophysical shocks. However, if this approximation is reasonable as a first step for pulsating stars, accretion shocks, and supernovae explosions, it may become questionable in the case of accretion funnels of classical T-Tauri stars, where the matter is supposed to fall from the stellar disk to the stellar surface by means of channels that follow the magnetic-field lines. Accretion in Classical T-Tauri stars is inferred from veiling in the spectrum and also from signatures in the spectral lines. Simulations indicate that the topology of the accretion funnels is strongly dependent on the relative orientation of the magnetic-field symmetry and rotation axis (Romanova et al. 2003). At the base (on the stellar surface), the column may vary from compact circular to ring geometries, whereas the upper part (connected to

the disk) may exhibit various fold-like, or more compact topologies driven by instabilities. This topic is still the subject of much debate and controversy.

Both the complexity in the structure of the radiative shocks, even for a 1D approximation, and the lack of angular resolution, require accurate simulations coupling radiation transport with hydrodynamics. This motivates the study of radiative shocks in 2D simple cylindrical geometries, to analyze the effect of the finite lateral size of the radiative shock, on its structure and luminosity. One should not use identical simulations to both check with and analyze observations. Experimental validation of these complex hydrodynamic features is thus required.

Obviously, the typical dimensions of astrophysical radiative shocks ensure that they cannot be studied directly in the laboratory. The study of radiative shocks on Earth thus require different gases and physical conditions, which can be recreated by high energy installations such as laser or pulsed electric installations (Remington et al. 2006). Radiative shock experiments have been performed with high power lasers (Bozier et al. 1986, 2000; Keiter et al. 2002; Reighard et al. 2006; Bouquet et al. 2004; González et al. 2006b; Busquet et al. 2006, 2007). Typically, a 200 J laser in about 1 ns can launch a shock at about 60 km s^{-1} in targets of millimeter size (Bouquet et al. 2004) filled with xenon at pressures of some fractions of bars, whereas supercritical shocks at 100 km s^{-1} in SiO_2 aerogel, argon, and xenon have been produced at the OMEGA laser (5 kJ). Strong shocks have also been generated by a compact pulse-power device (Kondo et al. 2006), producing shocks at 45 km s^{-1} in xenon with different gas pressures of up to 10^{-2} bars. We see below that, for a fixed shock velocity accessible to a laser installation, the radiative regime is more easily achieved with a low-density, high-atomic-mass gas, which explains why low-density xenon is often used in these studies.

These experiments enable one to examine the physics of the radiative precursor (dynamics and density) by visible interferometry and provide information about the temperature of the shock front, by visible emissivity. Studies of the dynamics of the precursor of xenon radiative shocks by interferometry (Bouquet et al. 2004), and shadowgraphy (González et al. 2006b), and of its topology by instantaneous X-ray imaging (Vinci et al. 2006) indicate that multi-dimensional effects can affect the shock wave, and, in particular, its precursor. This was attributed to the lateral radiation losses (through the walls of the shock tube), which reduce the amount of radiation heating the precursor and thus affect its structure (Leygnac et al. 2006; González et al. 2006b).

Keilty et al. (2000), Shigemori et al. (2000), Edwards et al. (2001), Calder et al. (2002), and Laming & Grun (2002) focused their studies on the spherical, radiative, blast waves, which are similar to those studied in the previous 1D cases, in terms of the development of radiative precursor, but also exhibit strong differences, such as the importance of radiative cooling and the development of various instabilities. The study of these experimental blast waves is linked to the problem of the evolution and stability of supernova remnants.

After the presentation of the typical structure of 1D radiative shocks, we present a numerical study of laboratory radiative shocks that can be generated by medium-power laser facilities, such as PALS (Prague, Czech Republic), LULI (Palaiseau, France), and similar lasers. The numerical code (HERACLES) used in this work is first briefly presented. We then study the effect of the duration of the shock driven by the piston (Sect. 4). In Sect. 5, we consider the effects of multi-dimensional radiative transfer and their correlation with the width of the shock tube. In Sect. 6, we examine the influence of the radiation boundary-conditions, which are inferred from the albedo of the cell wall, on the topology and propagation of the shock. Finally, we present the perspectives and conditions for obtaining an experimental stationary radiative shock and present the angular dependence of the emerging radiative flux of such a shock.

2. Structure of a 1D radiative shock

In this section, we present the typical features of a radiative shock in terms of 1D geometry. When the flow passes through the shock, it is heated and it re-emits a fraction of its energy by radiation processes. These emitted photons are then absorbed by the cold and opaque unshocked gas. This preheated upstream gas is called the radiative precursor. When the stationary regime is reached, a radiative shock is then composed of both a purely hydrodynamical shock (which consists of a discontinuity in the hydrodynamical quantities) and a radiative precursor, whose length is directly correlated with both the mean free path of photons in the gas and the shock velocity. One usually considers two classes of shocks depending on the temperature reached just ahead of the hydrodynamical discontinuity. If it is lower than the post-shock temperature, the shock is called subcritical, and if it is equal the shock is called supercritical.

By assuming that a strong shock develops in an initially cold gas of density ρ_0 (mass number A) and solving the Rankine-Hugoniot relations, one can show that the temperature reached in the shock equals

$$T = 120.27\ \mathrm{K}\ \frac{A}{\langle Z\rangle + 1}\left(\frac{u_\mathrm{s}}{1\ \mathrm{km\,s^{-1}}}\right)^2 \frac{(\gamma-1)}{(\gamma+1)^2} \times \left[1 + \sqrt{1 + (\gamma^2-1)X} - (\gamma+1)X\right], \quad (1)$$

where $\langle Z\rangle$ is the mean ionization stage in the shocked material, $X = \frac{e_\mathrm{i}}{\frac{1}{2}\mu u_\mathrm{s}^2}$ is the ratio of the ionization energy per atom to the initial kinetic energy per atom, and μ = the mean molecular weight of the non-ionized gas). The photons escaping from the shock front are used to heat the cold gas, incoming onto the front, to a temperature of T_- (which is lower than T). Neglecting the gas compression in the precursor, one has (Zel'dovich & Raizer 1967):

$$\sigma T^4 = \rho_0 u_\mathrm{s} \epsilon(T_-, \rho_0), \quad (2)$$

where $\epsilon = \frac{kT(1+Z)}{\mu(\gamma-1)} + \frac{e_\mathrm{i}}{\mu}$ is the internal specific energy (erg/g) after taking into account the ionization.

When T_- equals T, the shock enters the supercritical regime, which is characterized by an extended precursor. The corresponding critical velocity is obtained formally by resolving the coupled set of Eqs. (1) and (2). This system must be solved numerically because one needs to take account of the temperature dependence of both the internal energy and ionic charge. Using the atomic-physics model described by Michaut et al. (2004) and for xenon of density 10^{-3} g/cm^3, we found a critical velocity around 30 km s^{-1}, achieving a shock temperature of 12 eV and average ionic charge of 8. In the particular case of a perfect gas with $\gamma = 5/3$, and neglecting the ionization-energy term in Eqs. (1) and (2), one obtains the following approximate value of

$$v_\mathrm{s} \geq 450\ \mathrm{km\,s^{-1}} \left(\frac{\langle Z\rangle + 1}{A}\right)^{4/5} \left(\frac{\rho_0}{1\ \mathrm{g/cm^3}}\right)^{1/5} \quad (3)$$

which illustrates that the supercritical regime is more easily obtained at low density and for high-mass gases. Using

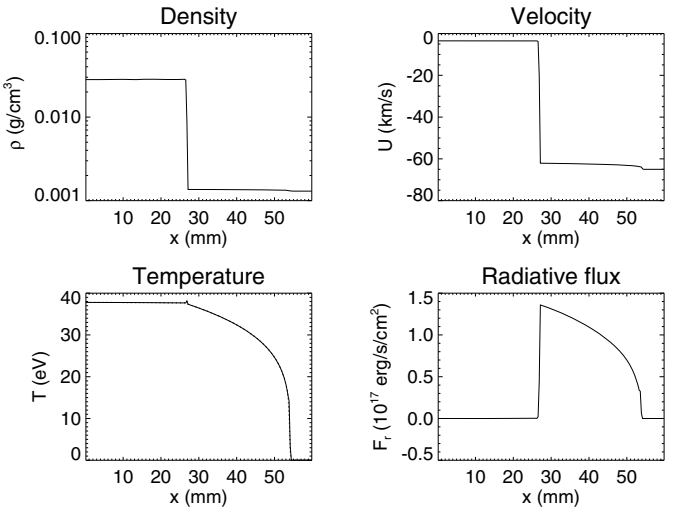

Fig. 1. Typical profiles of a 1D radiative shock: density (*upper left*), velocity (*upper right*), radiative and gas temperature (*lower left*), and radiative flux (*lower right*).

1D hydro-radiative simulations, Ensman (1994) found a supercritical regime at 20 km s^{-1} for hydrogen at 8×10^{-10} g/cm^3 in qualitative agreement with Eq. 3.

The precursor extension, L, can be approximated with a radiative heat-conduction model. One then finds that L is about several photon mean-free-paths close to the supercritical limit (Nemchinov & Shuvalov 1980; Penzo & Tassart 1984).

A typical 1D supercritical shock structure is shown in Fig. 1. These academic profiles were obtained using xenon with a constant ionisation charge of 5, a perfect-gas equation-of-state with $\gamma = 1.1$, and analytic opacities (Bozier et al. 1986). The velocity of the shock is 65 km s^{-1} and the initial density and temperature are 1.3×10^{-3} g/cm^3 and 300 K, respectively. The radiative precursor is clearly evident in the radiative flux and temperature profiles but, at this moderate shock speed, the density and velocity are only slightly affected.

3. The HERACLES code

The simulations presented in this paper were completed using the three-dimensional radiation-hydrodynamics code HERACLES (González et al. 2007). This code solves the Euler equations for hydrodynamics coupled with the moment equations of the transfer equation. The original closure relation used for the radiative model (M_1 model) allows one to be exact both in the diffusive and transport limit regimes. This code output data was verified by analytic models and compared with other codes. It can study a wide variety of astrophysical problems (González et al. 2007). Furthermore, it was used to develop and analyze a laboratory experiment of radiative shocks (González et al. 2006b). This cross-validation between experiment and simulation illustrates the relevance of HERACLES to both laboratory astrophysics and classical astrophysical situations.

The strength of HERACLES is that it can deal with multi-dimensional problems. Until now, radiative shocks have been studied by 1D geometry models, multi-D models with hydrostatic flows, or by adopting the flux-limited diffusion approximation (Bouquet et al. 2004; Drake 2007, and reference therein). On the one hand, the multi-D effects (such as lateral losses) can determine the structure of the flow, and on the other hand, at the foot of the radiative precursor, the reduced flux (ratio of the radiative flux to the product of the radiative energy and the light speed) is nearly one so that we are in the transport limit. In this context, HERACLES is of particular relevance to the study of multi-D radiative shocks.

Although all shocks in reality propagate within 3D media, we performed 2D axisymmetric simulations. As a first step, we considered only the determination of the theoretical influence of different parameters on the shock propagation. Furthermore, we verified that 2D axisymmetric and 3D Cartesian simulations produced identical results (e.g., speeds, positions) if one is careful to ensure that the surface-to-volume ratio is equal in both cases. Our results are therefore relevant to the case of radiative shocks propagating in a rectangular medium, as in most laboratory experiments.

Hereafter, all simulations presented are for shocks propagating in cylindrical cells with the left vertical boundary corresponding to the symmetry axis and the lateral losses located at the right vertical boundary. They are filled with xenon, which is initially at ambient temperature and a pressure of 0.2 bar (i.e., this corresponds to a density of 1.3×10^{-3} g/cm^3). These values are typical of laboratory experiments (Bouquet et al. 2004; González et al. 2006b) where a high molecular weight and a low density are chosen to maximize radiative effects. If not specified, we use a realistic equation of state and opacities. The equation of state of xenon was computed using the OPA-CS code of Stehlé, which uses a screened hydrogenic model and is described in Michaut et al. (2004). The opacities were kindly provided by Busquet, who computed them using the STA code (Bar-Shalom et al. 1989). The shock is driven at a speed of 65 km s^{-1} which is a typical of present-day laser experiments. The boundary of the cells can have a variable albedo, defined as the fraction of the incident radiative flux re-emitted by the wall. We demonstrated in previous work (González et al. 2006b) that this parameter has a strong influence on the precursor propagation. We therefore performed simulations for albedos between 0% (fully transparent or fully absorbing boundaries) and 100% (total reemission).

4. Launching effect

The dynamics of the shock propagation depend strongly on the launching procedure. In laser driven shocks, the conversion of the laser energy to the piston mechanical energy is performed by the shock generated in the piston during the laser ablation (Bouquet et al. 2004; Drake 2005). In this paragraph we compare the dynamics of the shock for two launching scenarios. In the first, the piston moves at a constant velocity. The second corresponds to the case where the piston decelerates with time. Hereafter, we denote these two driving cases as continuous and impulsive respectively.

Figure 2a shows the difference between a shock with a launching phase of the shock that is impulsive and one for which the driving is continuous. In both cases, the lateral albedo is 40%. When the shock driver ("piston") is continuous, the shock propagates at constant velocity equal to the initial velocity of 65 km s^{-1}. In the impulsive case, the driver of 65 km s^{-1} is continuous during 0.3 ns and then decreases with a temporal dependence that reproduces qualitatively the velocities of the experimental shocks (González et al. 2006b). In that case, the shock decelerates as soon as the drive stops because it has little inertia. Regardless of the drive duration, one can observe three different stages in the precursor dynamics. In the first stage, the precursor moves faster than the shock. The photons emitted by the shock propagate in the upstream fluid, which is optically thick, where they are absorbed. This induces a warm, ionized, radiative precursor in the upstream part of the shock. In a second phase,

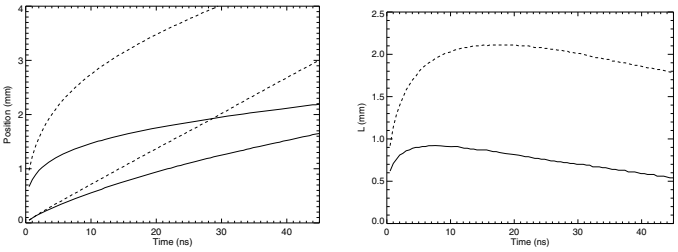

(a) Shock and precursor absolute positions

(b) Distance between shock and precursor

Fig. 2. Influence of the dynamics of the piston launching on the shock dynamics. The shock is driven in xenon at 0.2 bar at room temperature. The shock tube is a cylindrical cell with a 0.7 cm diameter and albedo of 40%. The full line refers to the impulsive lanching whereas the dotted line refers to a shock driven by a piston at constant velocity of 65 km s^{-1} (cf. Sects. 3 and 4).

the precursor decelerates (it can be even slower than the shock front). Finally, it reaches a constant speed equal to that of the shock front. This is the stationary regime.

These three stages are clearly seen in Fig. 2b which shows the distance separating the shock from the precursor leading-edge versus time. Since the precursor goes faster than the shock, this distance increases to a maximum value. Then, as the precursor slows down, this distance decreases until reaching an asymptotic value (stationary limit), when both the shock and precursor leading-edge travel at the same speed.

In a laboratory experiment, the duration of the driving is not a parameter that one can vary simply. It is easier to modify the shock dynamics by changing the radiative lateral losses, which can be achieved by varying the width of the canal or by modifying the albedo of the cells walls. This albedo can be specially adapted by choosing properly the material of the cell or by choosing special coating on these walls.

In the following sections, we examine the influence of these parameters on the dynamics of the shock precursor and in particular on the delay before the stationary regime.

5. Effect of a 2D radiation field

We define R to be the ratio of the transverse width l to the photon mean-free-path λ in the unshocked medium ($\lambda \simeq 1$ mm). In this section, we present the influence of R on the radiative shock structure and evolution. In our bi-dimensional and axisymmetric simulations, the gas is driven at a speed of 35 km s^{-1}, constant both in time and across the cell. Since we impose lateral reflecting boundaries on the hydrodynamics, the shock would remain planar without accounting for the radiative transfer. It would be transversally homogeneous, and temperature and density would vary only with y-position (along the canal axis). However, when accounting for radiative transfer with lateral losses through partially reflective walls, 2D effects can be observed. Density and temperature vary with x-position (perpendicular to the axis) and, in some conditions, curvature of the shock front may even be observed. The influence of the radiation on the shock structure is directly correlated with the possibility of photon escape from the medium, which can be estimated from the dimensionless number $R = l/\lambda$.

The importance of radiative losses on the shock structure, which depends strongly on R, has not been considered in detail by many laboratory experiments nor in the study of radiative shocks encountered in astrophysical objects. For example, the mean free path in xenon at 300 K and 10^{-3} g/cm^3, which is typical of laboratory experiments, is about 0.1 mm whereas the canal width is about 1 mm. For a typical stellar atmosphere ($T = 5000$ K and $\rho = 5 \times 10^{-11}$ g/cm^3), the typical mean free path is 4×10^{11} cm and decreases rapidly when the temperature increases (Seaton et al. 1994) whereas the radius of a classical T Tauri star is about 2×10^{11} cm.

Figure 3 shows bi-dimensional maps at the same time for three different canal widths (i.e., three values of R). The shock position is marked by the jump in density and by the temperature peak. The precursor is located in the lower part of the figure below the shock. Its extension is particularly visible in the maps of temperature and radiative flux.

If R is small (cf. Fig. 3a), the photons don't interact with the gas and they escape freely from the system. As the radiation escapes laterally, the shock loses some part of its energy, it decelerates rapidly, and the precursor remains thin. Since the photons emitted at any point of the downstream medium escape freely, the shock remains planar. In contrast, if R is large (cf. Fig. 3c), the photons cannot escape because they are reabsorbed over a short distance. The shock travels faster than in the first case. In the limit where R tends to infinity, we recover the uni-dimensional case with a planar shock except for a small layer along the walls, similar to a boundary layer. In the intermediate case (cf. Fig. 3b), the shock is curved, since only photons close to the walls escape, and photons emitted on the axis are trapped. The shock then decelerates more close to the walls than on the axis, which tends to bend the shock. Shock curvatures have already been observed experimentally by imaging techniques (Vinci et al. 2006; Reighard et al. 2006), although the dynamical origin of the curvature can be of many different natures.

6. Effect of radiative losses

In the previous section, we showed that the ratio R of the photon mean free path to the canal width was a key parameter for the radiative losses. In this section, we study in more detail the influence of the lateral radiative losses on the shock and precursor dynamics. We therefore consider a canal of fixed width but with walls of variable albedo a, which varies between 0 (no wall reflexion) and 1 (purely reemitting walls).

This wall albedo is a crucial point in the laboratory experiments. Varying the element used for the cells or covering the cell walls with layers of different elements (e.g., gold, aluminium), one can test the radiative-loss effects.

We study the influence of the albedo on the dynamical properties of the shock at short and long times. To illustrate the effect, we have chosen to focus the analysis on the case of impulsive launching. We concentrate our study on the positions of the shock front and of the leading edge of the precursor (defined as the point, on the cell symmetry axis, where the temperature reaches the threshold value of 5 eV). The value of the temperature threshold influences the extension of the precursor only slightly.

Figure 4 shows the shock dynamics obtained with an albedo of 0%, 10%, 20%, 30%, 40%, 50%, 60%, 70%, 80%, 90%, and 100%. One can see that the wall albedo has almost no effect on the shock velocity, at least for the evolution times considered here. However, the precursor is strongly affected by the albedo. As can be seen in Fig. 4b, for small values of the albedo (for important lateral losses), when most of the photons escape, the precursor extension remains small and its deceleration increases. This dependence is non-linear (cf. Sect. 7 below for the

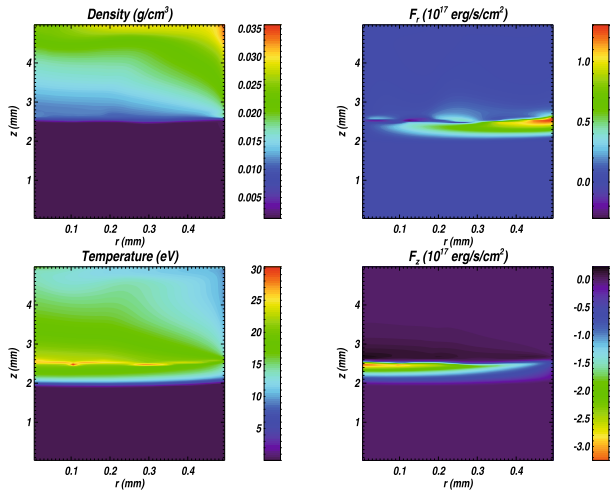

(a) R=0.5

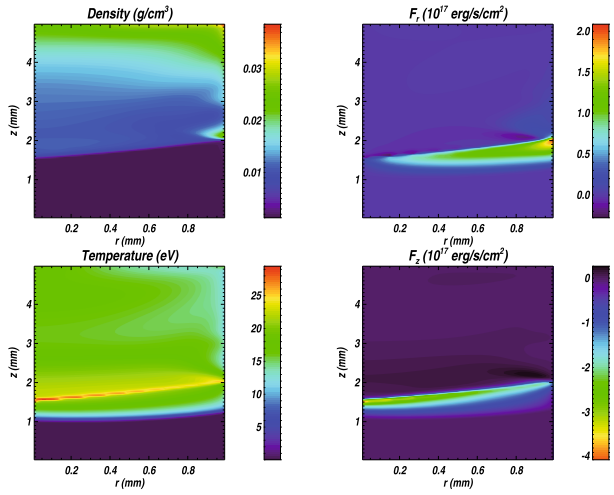

(b) R=1

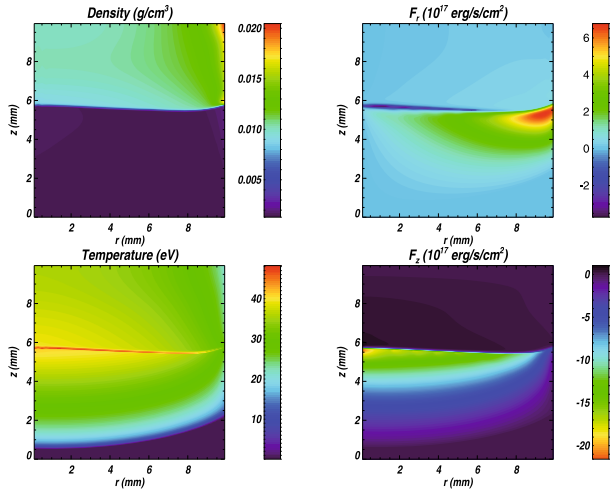

(c) R=10

Fig. 3. At a same instant, snapshots of the maps of density, temperature, radial, and axial radiative flux showing the influence of the canal width compared to the photon mean free path ($R = 0.5$ *top panel*, $R = 1$ *middle panel* and $R = 10$ *bottom panel*). Case of xenon initially at 1.3×10^{-3} g/cm^3 and 300 K, using perfect-gas equation-of-state ($\gamma = 5/3$ and mean molecular weight $\mu = 20$ equivalent to a mean ionization stage of 5), and analytic opacities (Bozier et al. 1986). The shock propagates from top to bottom.

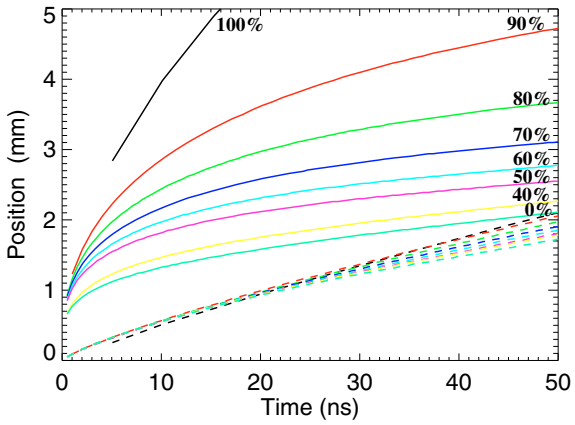

(a)

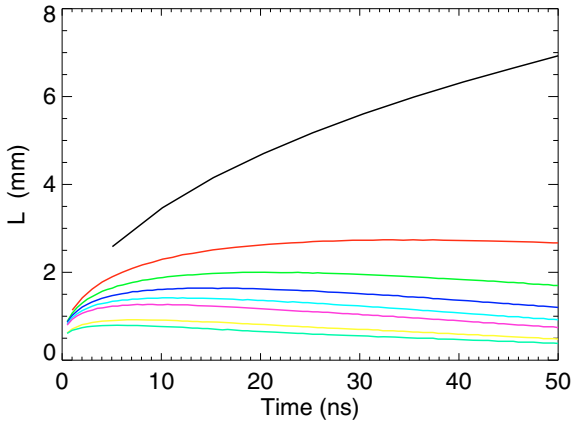

(b)

Fig. 4. **a)** Influence of the walls albedo upon the shock (dashed line) and precursor (solid line) positions. **b)** Influence of the albedo upon the distance between the precursor and the shock. Comparison for an albedo of 0%, 40%, 50%, 60%, 70%, 80%, 90%, and 100% (from bottom to top).

dependence of the time needed to reach the stationary limit on the albedo). The extension of the precursor relative to the shock front reduces slowly with time, as a consequence of the weakening of the shock and the slow deceleration of the piston. This evolution at later times differs from the case where the piston moves at a constant velocity, as can be seen from Fig. 2, which converges at long times towards a stationary limit, where precursor and shock front move at the same velocity. At early times, the precursor front moves far more rapidly than the shock front, and we expect that this regime is close to the case of a Marshak wave (a radiation-driven thermal wave without coupling to hydrodynamics). For t below 5 ns, and $a = 1$, one thus recovers the well-known 1D-Marshak-wave time-dependence of $\sqrt{t}$. For smaller values of the albedo, the structure of the 2D-bent Marshak waves is more complex, even supposing a constant opacity, as one can see from Hurricane & Hammer (2006), who studied the bending and slowing of the front by radiative losses. However, even if similarities exist between the dynamics and topologies of a Marshak wave and those of a radiative precursor at early times, the two processes differ physically, especially at late times where the stationary limit is reached in one process and not in the other.

7. Toward stationary shock

In the case of a shock with continuous driving, the typical evolution of the radiative shocks exhibits, as in the previous case, a first phase of development of the precursor, where the ionization-front velocity exceeds the shock velocity. After this phase, the ionization-front velocity decelerates until it becomes equal to the front velocity. At this time, the stationary limit is reached. The corresponding time at which this stationary radiative shock is formed, $t_{\rm stat}$, is of the order of the ratio of the precursor extension to the shock velocity.

The stationary shock limit is usually assumed for astrophysical flows, because $t_{\rm stat}$ is less than the typical hydrodynamical time, $t_{\rm hyd}$. For instance, in the case of pulsating stars, $t_{\rm hyd}$, which is roughly equal to the ratio of the atmosphere width to the shock velocity, varies between 1500 s for RR Lyrae and 10^6 s for cooler giants such as RV Tauri, whereas $t_{\rm stat}$ is of the order of 50 s for a shock velocity around 10 km s^{-1} (Fokin et al. 2004). In accretion shocks along magnetospheric columns, this time is approximately equal to the ratio of the column length to the shock velocity, or 10^4–10^5 s for classical T Tauri stars (of about 3 solar radius and 300 km s^{-1}). Thus, in the absence of any shorter timescale of hydrodynamical motion (e.g., instabilities), these astrophysical shock waves can be supposed to be stationary from the radiative point of view.

Associated with the 1D approximation, this stationary limit also offers the advantage of simplicity in the observational diagnostics with the help of published stationary-shock structure tabulations (Fadeyev & Gillet 2000).

In the experimental cases, the piston velocity decreases slowly with time. However, as in the academic case of continuously sustained shock, the precursor extension relative to the shock front increases at early times until reaching a maximum value. We have chosen to define the time interval to form a stationary shock, $t_{\rm stat}$, as the time of maximum extension of the precursor because it unambiguously delimits the short accelerating and long decelerating phases of the precursor dynamics.

Using this definition, and in the launching case, which is close to that of previous experiments (González et al. 2006b), we find $t_{\rm stat}$ = 5.6 ns, 6.1 ns, 7.1 ns, 7.6 ns, 8.6 ns, 10.6 ns, 13.1 ns, 18.7 ns, 32.3 ns, and 409 ns for wall albedos of 10, 20, 30, 40, 50, 60, 70, 80, 90, and 100 percent, respectively (cf. Fig. 5). Thus, high lateral radiation losses (small albedo) not only decelerate the radiative precursor, but also strongly decrease the time to reach the stationary limit. From these numerical simulations, we derive an analytical fit

$$t_{\rm stat} = \frac{t_0 t_1}{(t_1 - t_0)(1-a)^{\beta} + t_0} \qquad (4)$$

where a is the wall albedo, t_0 and t_1 are the stationary times for $a = 0$ and $a = 1$, respectively, and β is a constant. Their values are $t_0 = 5.6$ ns, $t_1 = 409$ ns, and $\beta = 0.84$.

In all of these simulations, the shock position is insensitive to the albedo of the tube walls. However, even if the shock speed is constant, the density and temperature of the post-shock matter are sensitive to the radiative losses. Higher losses (smaller albedo) result in a higher density and a lower temperature. As a consequence, the precursor extension tends to be lower in the case of higher losses because the emissivity of the shock front is proportional to T^4 and also because a large fraction of the photons escapes without contributing to the precursor extension.

Until now, we have emphasized the strong dependence of the stationary-shock structure on its radiative parameters (e.g., ratio R of the transverse width to the photon mean free path,

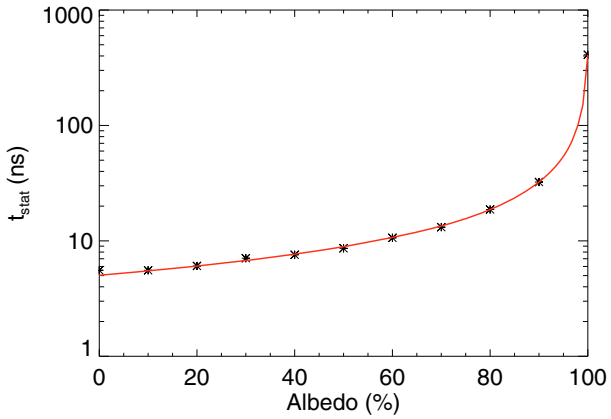

Fig. 5. Influence of the albedo upon the time interval to form a stationary radiative shock, $t_{\rm stat}$ (points: numerical simulations results, line: fit).

and the percentage of radiative losses at the walls of the shock tube), or equivalently to departures from the 1D approximation. Another interesting quantity is the radiation flux, since it is used, for instance, as a tracer of accretion rate. In Fig. 6, we plot, for different tube-wall albedos, the variations in the luminosity as a function of the angle of observation θ ($\theta = 0$ corresponds to a forward flux, $\theta = \pi/2$ to a perpendicular flux, and $\theta = \pi$ to a backward flux). The plotted profiles correspond to the luminosity integrated from the beginning of the radiative precursor to the shock front at time $t = 50$ ns. The integral is evaluated by calculating the photon angular distribution function, which is known from the M_1 model, at each point along the cell wall. We plot a normalized luminosity because we are interested only in the angular distribution and not in the absolute value, which is more difficult to compare. One can see that with increasing lateral losses the angle corresponding to the maximum of the luminosity increases and the distribution sharpens around this angle. This is due to the fact that when the losses are high, the radiative reduced flux is higher, and the luminosity tends to become almost mono-directional (in the limiting case of a unit-reduced flux) rather than an isotropic Planck function (in the limiting case of diffusion). The luminosity is much more directional and the dispersion around the preferred direction is lower. Figure 7 shows that this angle is approximately a linear function of the lateral albedo of the tube walls. All these points illustrate the strong anisotropy of the flux in the radiative shock. Although illustrated for a given time, the conclusions about the influence of the albedo on the peak of the angular distribution and on the dispersion about this value are of a quite general character during the shock propagation.

8. Conclusion

We have illustrated how radiation influences the radiative-shock topology and structure. These effects can be observed with experimental results and used to interpret observational data.

We have in particular shown that lateral radiative losses induce a curvature in the shock front and a strong shortening of the radiative precursor. For laboratory experiments, it means that the tube geometry and the opacities play a key role in the shock propagation and topology. In astrophysical cases, this suggests that the link between accretion rate and photometric observation is strongly dependent on the gas conditions and the possible presence of dust.

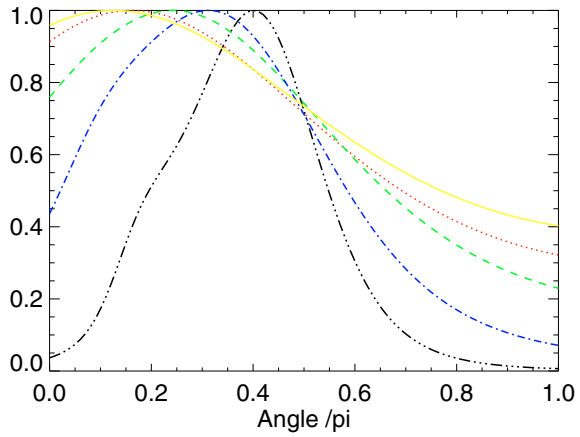

Fig. 6. Normalized luminosities for different values of albedo (80% in yellow solid line, 70% in red dotted line, 50% in green dashed line, 20% in blue dashed-dotted line and 0% in black dashed-double-dotted line).

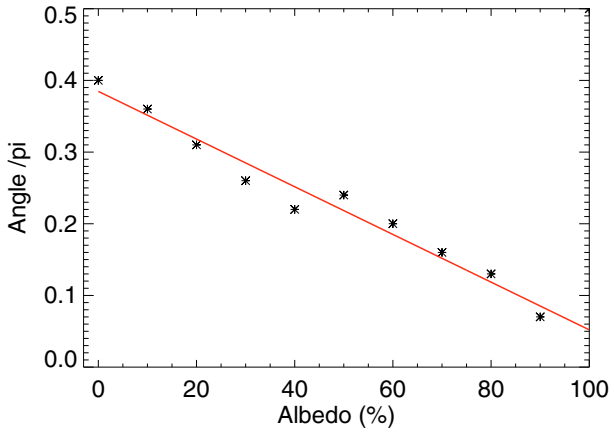

Fig. 7. Angle corresponding to the maximum of the luminosity as a function of the albedo (points: numerical simulation results, line: fit).

Lateral radiative losses through the walls of the tube lead to a weakening of the shock, and a reduction in the precursor extension and temperature. They also strongly reduce the time needed to reach the stationary limit.

The radiative flux that emerges from the tube boundaries evolves from an isotropic situation in the case of low radiation losses to a more anisotropic distribution in the case of strong radiative losses. This effect may have a strong impact on photometric observations of anisotropic accretion flows, such as in the case of T Tauri star accretion through funnels.

High-energy, high-power installations, such as lasers, allow generation of strong radiative shocks with extended precursors. Most studies have focused on the global characterization of the radiative precursor. Only a few have attempted to study the shock front, which requires X-ray diagnostics of high temporal and spatial resolution and is thus very challenging. An important result of our study is the reduction with radiative losses in the time needed to reach the stationary limit. Although some experiments have been close to reaching this limit (González et al. 2006b), this has not been studied until now experimentally.

Shock velocities of 60−80 km s^{-1} are accessible with kJ class lasers. Using more powerful laser-energy installations such as the NIF (Haynam et al. 2007) at Livermore (USA) or the LMJ (Bettinger & Decroisette 1999; Besnard 2008; Ebrardt & Chaput 2008) at Bordeaux (France) will allow us to explore the effects of the radiation pressure on the structure of the shock wave. Using xenon at densities of the order of 5×10^{-4} g/cm^3, such effects start to be visible for shock velocities of the order of 200 km s^{-1} (Michaut et al. 2004).

Another interesting topic that could be addressed is the eventual development of radiative instabilities. These "thermal" instabilities have been studied theoretically and numerically for optically thin radiative shocks, in the context of, for example, accretion onto white dwarfs, and colliding radiative flows (Falle 1975; Chevalier & Imamura 1982; Bertschinger 1986; Ryu & Vishniac 1987; Walder & Folini 1996; Laming & Grun 2002; Mignone 2005). Such an instability was observed experimentally in 3D blast-wave development over a few hundreds of nanoseconds (Grun et al. 1991), although other experiments failed to reproduce it on a shorter timescale (Edwards et al. 2001). The development of these instabilities in an optically-thicker radiative shock (with a radiative precursor) has, to our knowledge, not been studied theoretically. The multidimensional effects, by deforming the front and allowing a transition towards an optically thin case, could be favorable to the development of such instabilities, and this will be the subject of future studies.

These laboratory studies allow us to test the adequacy of modern codes in dealing with astrophysical, hypersonic radiative flows. The HERACLES 3D radiation hydrodynamics code is well adapted to the study of these anisotropic radiative flows. It allows us to test together the cases of both optically thick and optically thin regimes. It has been already used in modeling the propagation of astrophysical radiative jets in the ISM (González et al. 2006a; González 2006). Future improvements will include the inclusions of multigroup radiative-transport (which may influence the fine structure of the shock precursor), the decoupling of ionic and electronic temperatures (which affect the shock front), and non-LTE effects, which play a role in the optically thin regions of the shock structure.

Acknowledgements. The authors are indebted to M. Busquet and to the anonymous referee for valuable comments and suggestions leading to an improvement of this manuscript. This work was carried out under the EU funded RTN JETSET (contract MRTN-CT-2004 005592). The authors acknowledge the financial support of CNRS program PNPS and ANR grant SiNERGHy (ANR-06-CIS6-009-01) and would like to thanks the CEA computing center (CCRT) where all the simulations were done. M.G. acknowledges the financial support provided by the European Commission TUIXS project and the French Ministry of Foreign Affairs through the Lavoisier grant.

References

Bar-Shalom, A., Oreg, J., Goldstein, W. H., Shvarts, D., & Zigler, A. 1989, Phys. Rev. A, 40, 3183
Bertschinger, E. 1986, ApJ, 304, 154
Besnard, D. 2008, J. Phys. Conf. Ser., 112, 012004
Bettinger, A., & Decroisette, M. 1999, Fusion Engineering and Design, 46, 457
Bouquet, S., Stehlé, C., Koenig, M., et al. 2004, Phys. Rev. Lett., 92, 225001
Bozier, J. C., Thiell, G., Le Breton, J. P., Azra, S., & Decroisett, M. 1986, Phys. Rev. Lett., 57, 1304
Bozier, J. C., Le Breton, J. P., Jalinaud, T., & Valadon, J. 2000, ApJS, 127, 253
Busquet, M., Audit, E., Stehlé, C., et al. 2006, Bull. Am. Phys. Soc., 51, 123
Busquet, M., Audit, E., González, M., et al. 2007, High Energy Density Physics, 3, 8
Calder, A. C., Fryxell, B., Plewa, T., et al. 2002, ApJS, 143, 201
Chadid, M., Gillet, D., & Fokin, A. B. 2000, A&A, 363, 568
Chevalier, R. A., & Imamura, J. N. 1982, ApJ, 261, 543
Drake, R. P. 2005, Ap&SS, 298, 49
Drake, R. P. 2007, Phys. Plasmas, 14, 1
Ebrardt, J., & Chaput, J. M. 2008, J. Phys. Conf. Ser., 112, 032005

Edwards, M. J., MacKinnon, A. J., Zweiback, J., et al. 2001, Phys. Rev. Lett., 87, 085004
Ensman, L. 1994, ApJ, 424, 275
Fadeyev, Y. A., & Gillet, D. 1998, A&A, 333, 687
Fadeyev, Y. A., & Gillet, D. 2000, A&A, 354, 349
Falle, S. A. E. G. 1975, A&A, 43, 323
Fokin, A. B., Massacrier, G., & Gillet, D. 2004, A&A, 420, 1047
González, M. 2006, Ph.D. Thesis, University of Paris-Sud XI
González, M., Audit, E., & Lery, T. 2006a, in Semaine de l'Astrophysique Francaise, ed. D. Barret, F. Casoli, G. Lagache, A. Lecavelier, & L. Pagani, SF2A-2006, 235
González, M., Stehlé, C., Audit, E., et al. 2006b, Laser and Particle Beams, 24, 535
González, M., Audit, E., & Huynh, P. 2007, A&A, 464, 429
Grun, J., Stamper, J., Manka, C., Resnick, J., & Burris, R. 1991, Phys. Rev. Lett., 66, 2738
Haynam, C. A., Wegner, P. J., Auerbach, J. M., et al. 2007, Appl. Opt., 46, 3276
Hurricane, O. A., & Hammer, J. H. 2006, Phys. Plasmas, 13, 3303
Keilty, K. A., Liang, E. P., Ditmire, T., et al. 2000, ApJ, 538, 645
Keiter, P. A., Drake, R. P., Perry, T. S., et al. 2002, Phys. Rev. Lett., 89, 165003
Kondo, K., Nakajima, M., Kawamura, T., & Horioka, K. 2006, J. Phys. IV, 133, 1051
Laming, J. M., & Grun, J. 2002, Phys. Rev. Lett., 89, 125002
Leygnac, S., Boireau, L., Michaut, C., et al. 2006, Phys. Plasmas, 13, 3301
Michaut, C., Stehlé, C., Leygnac, S., Lanz, T., & Boireau, L. 2004, Europ. Phys. J. D, 28, 381
Mignone, A. 2005, ApJ, 626, 373
Mihalas, D., & Mihalas, B. W. 1984, Foundations of radiation hydrodynamics (New York, Oxford: University Press)
Nemchinov, I. V., & Shuvalov, V. V. 1980, Sov. Phys. Doklady, 25, 621
Penzo, A., & Tassart, J. 1984, J. Mech. Theor. Appl., 3, 381
Reighard, A. B., Drake, R. P., Dannenberg, K. K., et al. 2006, Phys. Plasmas, 13, 2901
Remington, B. A., Drake, R. P., & Ryutov, D. D. 2006, Rev. Mod. Phys., 78, 755
Romanova, M. M., Ustyugova, G. V., Koldoba, A. V., Wick, J. V., & Lovelace, R. V. E. 2003, ApJ, 595, 1009
Ryu, D., & Vishniac, E. T. 1987, ApJ, 313, 820
Seaton, M. J., Yan, Y., Mihalas, D., & Pradhan, A. K. 1994, MNRAS, 266, 805
Shigemori, K., Ditmire, T., Remington, B. A., et al. 2000, ApJ, 533, L159
Sincell, M. W., Gehmeyr, M., & Mihalas, D. 1999a, Shock Waves, 9, 391
Sincell, M. W., Gehmeyr, M., & Mihalas, D. 1999b, Shock Waves, 9, 403
Vinci, T., Koenig, M., Benuzzi-Mounaix, A., et al. 2006, J. Phys. IV, 133, 1039
Walder, R., & Folini, D. 1996, A&A, 315, 265
Zel'dovich, Y. B., & Raizer, Y. P. 1967, Physics of shock waves and high-temperature hydrodynamic phenomena, ed. W. D. Hayes, & R. F. Probstein (New York: Academic Press)

Journal of Quantitative Spectroscopy & Radiative Transfer 125 (2013) 105–122

Contents lists available at SciVerse ScienceDirect

Journal of Quantitative Spectroscopy & Radiative Transfer

journal homepage: www.elsevier.com/locate/jqsrt

The influence of frequency-dependent radiative transfer on the structures of radiative shocks

N. Vaytet [a,*], M. González [b], E. Audit [c,d], G. Chabrier [a,e]

[a] École Normale Supérieure de Lyon, CRAL, UMR CNRS 5574, Université de Lyon, 46 Allée d'Italie, 69364 Lyon Cedex 07, France
[b] Université Paris Diderot, Sorbonne Paris Cité, AIM, UMR 7158, CEA, CNRS, F-91191 Gif-sur-Yvette, France
[c] Maison de la Simulation, USR 3441, CEA - CNRS - INRIA - Université Paris-Sud - Université de Versailles, F-91191 Gif-sur-Yvette, France
[d] CEA/DSM/IRFU, Service d'Astrophysique, Laboratoire AIM, CNRS, Université Paris Diderot, F-91191 Gif-sur-Yvette, France
[e] School of Physics, University of Exeter, Exeter EX4 4QL, UK

ARTICLE INFO

Article history:
Received 5 November 2012
Received in revised form
18 February 2013
Accepted 6 March 2013
Available online 16 March 2013

Keywords:
Radiative transfer
Moment model
Multigroup
Laboratory astrophysics
Numerical methods
Shock waves

ABSTRACT

Radiative shocks are shocks in a gas where the radiative energy and flux coming from the very hot post-shock material are non-negligible in the shock's total energy budget, and are often large enough to heat the material ahead of the shock. Many simulations of radiative shocks, both in the contexts of astrophysics and laboratory experiments, use a grey treatment of radiative transfer coupled to the hydrodynamics. However, the opacities of the gas show large variations as a function of frequency and this needs to be taken into account if one wishes to reproduce the relevant physics. We have performed radiation hydrodynamics simulations of radiative shocks in Ar using multigroup (frequency dependent) radiative transfer with the HERACLES code. The opacities were taken from the ODALISC database. We show the influence of the number of frequency groups used on the dynamics and morphologies of subcritical and supercritical radiative shocks in Ar gas, and in particular on the extent of the radiative precursor. We find that simulations with even a low number of groups show significant differences compared to single-group (grey) simulations, and that in order to correctly model such shocks, a minimum number of groups is required. Results appear to eventually converge as the number of groups increases above 50. We were also able to resolve in our simulations of supercritical shocks the adaptation zones which connect the cooling layer to the final post-shock state and the precursor. Inside these adaptation zones, we find that the radiative flux just ahead of the shock in one or several high-opacity groups can heat the gas to a temperature higher than the post-shock temperature. Through the use of Hugoniot curves, we have checked the consistency of our radiation hydrodynamics scheme by showing that conservation of mass, momentum and energy (including radiative flux) holds throughout the computational domain for all our simulations. We conclude that a minimum number of frequency groups are required to correctly simulate radiating flows in gases whose opacities present large variations as a function of frequency.

1. Introduction

Radiative shocks are shocks in a gas where the radiative energy and flux coming from the very hot post-shock material are non-negligible in the shock's total energy budget [49,32]. A radiative precursor is formed ahead of the shock when the forward flux of ionizing photons exceeds the flux of atoms approaching the shock front. These conditions are met when the shock velocity exceeds the threshold required to produce the necessary photon flux [22]. Two regimes of radiative shocks are often described in the literature. The first is called the subcritical

* Corresponding author. Tel.: +33 472728703.
E-mail address: neil.vaytet@ens-lyon.fr (N. Vaytet).

0022-4073/$ - see front matter © 2013 Elsevier Ltd. All rights reserved.
http://dx.doi.org/10.1016/j.jqsrt.2013.03.003

regime, where the shock has only a transmissive precursor and the temperature just ahead of the discontinuity is not equal to the final downstream state temperature. The second is known as the supercritical regime which arises as the strength of the shock increases; a diffusive region in the precursor appears and the pre-shock temperature reaches the final state temperature (see [8] for more details).

The classical structure of a subcritical radiative shock is depicted in Fig. 1a. The pre-shock gas is heated by the radiative precursor to a temperature T_- and the shock compression heats it further to a temperature T_+ which is higher than the final post-shock equilibrium state T_1. The gas then cools down inside the cooling layer to reach the equilibrium state T_1 by radiating the excess energy away. The radiation is decoupled from the gas inside the cooling layer and the transmissive precursor. The pressure gradient in the precursor, through the conservation of mass and momentum, causes the velocity to decrease and the density to increase to a value ρ_- ahead of the discontinuity. The sharp density jump of the shock from ρ_- to ρ_+ then takes place on the gas viscous scale. The density increases further from ρ_+ to ρ_1 inside the cooling layer as the gas contracts (see also [49,8]).

In the case of an optically thick supercritical radiative shock (shown in Fig. 1b), we have $T_-\approx T_1$. The radiative temperature is equal to the gas temperature for the most part, except that it remains constant across the cooling layer and is higher than the gas temperature inside the transmissive precursor [32]. As stated above, the pressure gradient at the head of the precursor causes the density to increase. Since the gas temperature is close to being constant in the diffusive part of the precursor, there is no more pressure gradient and the density reaches a plateau value ρ_- ahead of the discontinuity.

The study of radiative shocks begun in the late 1940s with theoretical studies on the Rankine–Hugoniot jump conditions including a non-negligible radiation pressure for very energetic shocks (see [1] for a short review). The studies were very rapidly pursued and extended in the field of astrophysics since no processes on Earth could achieve high enough energies to produce such shocks. Radiative shocks are indeed found in novae [47,36,2], supernovae [7,16,34], stellar atmospheres [13,17], accretion processes in star formation [45,6], symbiotic stars [14,21] and jets [38,41]. This omnipresence makes them a key physical process at the heart of high energy astrophysics, and it is thus essential to fully understand the details of such a mechanism.

In recent years, with the modern advances in technology, radiative shocks have been produced in a number of laboratory laser facilities (see [3,12,15,39,5,30] for example), where very high-energy lasers are used to drive radiative shocks inside gas chambers. This allows new diagnostics of the properties of radiative shocks with a much more detailed view than would ever be possible in astrophysics. Radiative shock experiments allow for the validation of numerical simulations which are overwhelmingly used in high-energy physics and astrophysics to make predictions on high-energy flows.

Semi-analytic studies of the structure of radiative shocks have been carried out by Lowrie and Rauenzahn

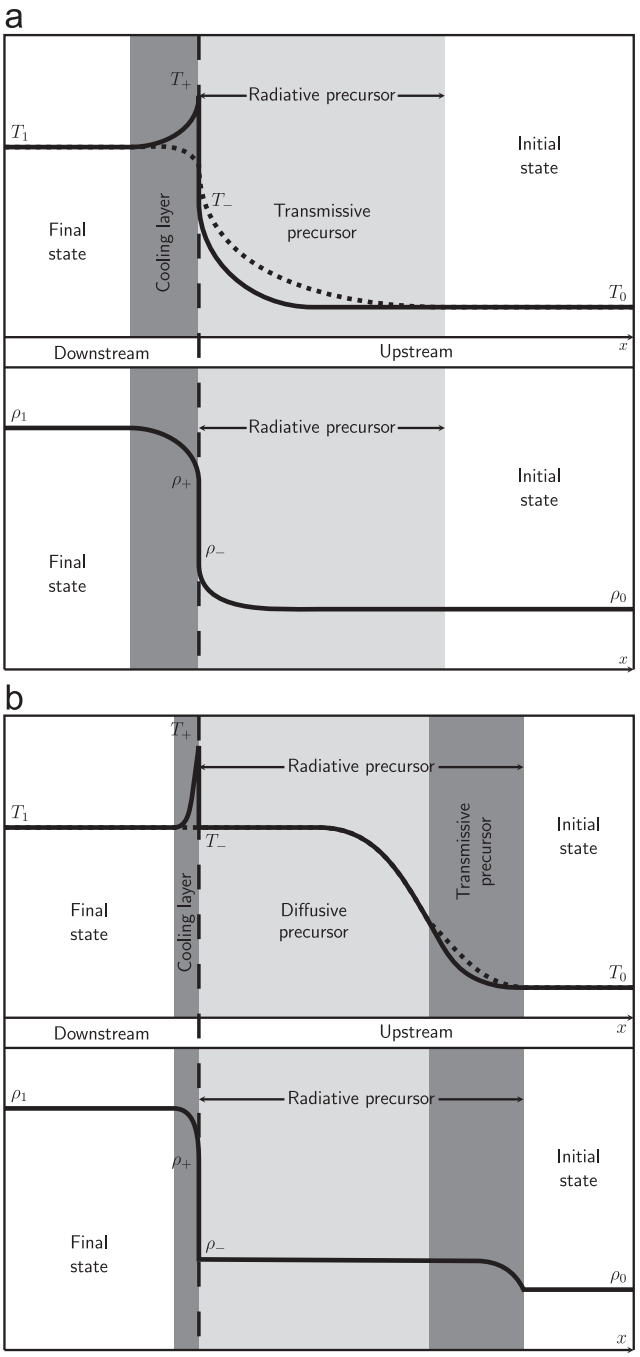

Fig. 1. Classical structure of a subcritical (a) and supercritical (b) radiative shock. The direction of the gas flow is from right to left in the frame where the shock is at rest. The panels show the gas (solid) and radiative (dotted) temperature (top) and the gas density (bottom) as a function of distance in each case. The position of the temperature and density jumps is marked by the vertical dashed line. The relative sizes of the layers are for illustration purposes only.

[27], Lowrie and Edwards [28], and several comparisons between experiments and simulations have also been undertaken by Bouquet et al. [4], Leibrandt et al. [25], Reighard et al. [40], González et al. [20], for example. One key piece of data that is required by the numerical simulations in order to accurately model the flow is the opacities of the gas in which the shock is launched. Gas opacities show large variations as a function of temperature and density as well as frequency, and including

detailed opacities in simulations have crucial effects on the structures of radiative shocks. Vaytet et al. [48] performed simulations of a radiative shock in Xe using a realistic opacity set and showed the importance of taking into account the frequency dependence of the opacities, rather than simply integrating over all frequencies, as is commonly done in simulations of radiative shocks and other more general radiation hydrodynamics (RHD) calculations.

This paper aims to build on the idea that a frequency dependent treatment of radiative transfer is crucial in simulations of radiative shocks. In particular, we experiment further with the multigroup method of Vaytet et al. [48] by studying the effect of the number of frequency groups on the structures of the radiative shocks (mainly the variations in size of the precursor). We performed simulations of stationary radiative shocks (both sub- and supercritical) using 1–100 frequency groups, and the differences between the results are discussed. The opacities are a crucial part of the radiative transfer model; they govern the amount of energy that will be absorbed and emitted by the gas and can hence determine the structure of the flow. Laboratory experiments use high atomic number gases to launch radiative shocks to take advantage of the strong gas heating due to the lower heat capacity. Common choices are argon (Ar) and xenon inert gases, and in this work we have chosen to use Ar (see Section 2.5 for more details).

2. The multigroup RHD simulations of radiative shocks

2.1. Radiative transfer

We use the M_1 moment model [26,11] to approximate the equation of radiative transfer. The M_1 method uses the first two moment equations governing the evolution of the radiative energy and flux

$$\begin{aligned}&\partial_t E+\nabla\cdot\mathbf{F}=\sigma(4\pi B-cE)\\&\partial_t\mathbf{F}+c^2\nabla\cdot\mathbb{P}=-\sigma c\mathbf{F}\end{aligned}\tag{1}$$

where c is the speed of light, σ the absorption/emission coefficient and B the black body specific intensity. E,$\mathbf{F}$, and $\mathbb{P}$ are the zeroth, first and second moments of the radiation specific intensity, namely the radiative energy density, the radiative energy flux, and the radiative pressure, respectively. In order to close system (1), the radiative pressure is expressed as a function of the radiative energy and flux following $\mathbb{P}=\mathbb{D}E$ where $\mathbb{D}$ is known as the Eddington tensor. The expression for $\mathbb{D}$ is obtained by minimizing the radiative entropy which yields

$$\mathbb{D}=\frac{1-\chi}{2}\mathrm{II}+\frac{3\chi-1}{2}\frac{\mathbf{F}\otimes\mathbf{F}}{\|\mathbf{F}\|^2}\tag{2}$$

where

$$\chi=\frac{3+4f^2}{5+2\sqrt{4-3f^2}}\tag{3}$$

and $f=\|\mathbf{F}\|/cE$ is known as the reduced flux. Note that by definition of E and $\mathbf{F}$, we have $f\leq 1$, which implies that the radiative energy is transported at most at the speed of light. In one dimension we simply have $P=\chi E$. This closure relation recovers the two asymptotic regimes of radiative transfer. In the free-streaming limit (i.e. transparent media), we have $f=1$ and $\chi=1$. On the other hand, in the diffusion limit, $f=0$ and $\chi=1/3$, which corresponds to an isotropic radiation pressure.

2.2. The equations of multigroup radiation hydrodynamics

We use the multigroup version of the M_1 model coupled to the gas hydrodynamics described in Vaytet et al. [48] to account for frequency dependence of the absorption and emission coefficients (see [43,46,50] for other examples of Godunov multigroup methods). In the multigroup model, the equations of radiative transfer are integrated into a finite number of frequency bins (or groups) and the opacities are averaged over the same frequency ranges. The closure relation (3) is applied within each frequency group. The more the frequency groups, the more accurate the methods becomes, but the higher the computational cost. The system of multigroup RHD equations in the comoving frame is

$$\partial_t\rho+\nabla\cdot(\rho\mathbf{u})=0\tag{4}$$

$$\partial_t(\rho\mathbf{u})+\nabla\cdot(\rho\mathbf{u}\otimes\mathbf{u}+p\mathbb{I})=\sum_{g=1}^{Ng}(\sigma_{Fg}/c)\mathbf{F}_g\tag{5}$$

$$\partial_t e+\nabla\cdot(\mathbf{u}(e+p))=\sum_{g=1}^{Ng}[c(\sigma_{Eg}E_g-\sigma_{Pg}\Theta_g(T))+(\sigma_{Fg}/c)\mathbf{u}\cdot\mathbf{F}_g]\tag{6}$$

$$\partial_t E_g+\nabla\cdot\mathbf{F}_g+\nabla\cdot(\mathbf{u}E_g)+\mathbb{P}_g:\nabla\mathbf{u}-\nabla\mathbf{u}:\int_{\nu_{g-1/2}}^{\nu_{g+1/2}}\partial_\nu(\nu\mathbb{P}_\nu)\,d\nu=c(\sigma_{Pg}\Theta_g(T)-\sigma_{Eg}E_g)\tag{7}$$

$$\partial_t\mathbf{F}_g+c^2\nabla\cdot\mathbb{P}_g+\nabla\cdot(\mathbf{u}\otimes\mathbf{F}_g)+\mathbf{F}_g\cdot\nabla\mathbf{u}-\nabla\mathbf{u}:\int_{\nu_{g-1/2}}^{\nu_{g+1/2}}\partial_\nu(\nu\mathbb{Q}_\nu)\,d\nu=-\sigma_{Fg}c\mathbf{F}_g\tag{8}$$

where c is the speed of light, and ρ, $\mathbf{u}$, p and e are the gas density, velocity, pressure and total energy, respectively. $\mathbb{Q}_\nu$ is the third moment of the radiation specific intensity; the radiative heat flux. Subscripts ν denote monochromatic quantities, and we also define

$$X_g=\int_{\nu_{g-1/2}}^{\nu_{g+1/2}}X_\nu\,d\nu\tag{9}$$

which represents for $X=E$, $\mathbf{F}$, $\mathbb{P}$ the radiative energy, flux and pressure inside each group g which holds frequencies between $\nu_{g-1/2}$ and $\nu_{g+1/2}$. N_g is the total number of groups and $\Theta_g(T)$ is the energy of the photons having a Planck distribution at temperature T inside a given group. The quantities σ_{Pg}, σ_{Eg} and σ_{Fg} are the means of the absorption/emission coefficient σ_ν inside a given group weighted by the Planck function, the radiative energy and the radiative flux, respectively. The radiative quantities are expressed in the frame comoving with the fluid, which allows simple expressions to be used for the source terms on the right hand side of Eqs. (5)–(8). The terms involving the frequency derivatives of the radiative pressure and heat flux $\partial_\nu(\nu\mathbb{P}_\nu)$ and $\partial_\nu(\nu\mathbb{Q}_\nu)$ are solved using a finite

volume method in the frequency dimension (see [48] for details).

2.3. Numerical method

We have implemented the multigroup radiative transfer module of Vaytet et al. [48] in the three-dimensional radiation hydrodynamics second order Godunov code HERACLES[1] [19]. It uses an explicit solver for the hydrodynamics and an implicit solver for the radiative transfer. The Ar gas equation of state is a simple modified ideal gas equation of state; the ionization energy is neglected but the ionization state is used to compute the mean molecular weight which in turn affects the gas temperature. The disregard of the ionization energy may greatly overestimate the temperature (ionization can represent half of the internal energy for mid- to highly ionized flows; [8]), but since we focus solely on the differences between mono- and multi-frequency radiative transfer methods and no comparison between simulations and experiments is made throughout, this oversight does not matter for the purposes of the present paper.

In the RHD equations, it is not trivial to compute the radiative energy and flux-weighted mean opacities σ_{Eg} and σ_{Fg}. Common practise is to set $\sigma_{Eg}=\sigma_{Pg}$ and $\sigma_{Fg}=\sigma_{Rg}$ where σ_R is the Rosseland mean opacity. In this work, we have used an average opacity $\sigma_{Eg}=\sigma_{Fg}=\sigma_{Ag}$ which varies between the values of σ_{Pg} and σ_{Rg} depending on the reduced flux f (see Appendix A for more details). However, we wish to point out that the inaccuracies which arise from these different approximations are reduced as the number of frequency groups used increases, since in the limit of infinite frequency resolution, all of these quantities simply reduce to σ_ν. Any approximation is thus less crude in a multigroup model than in a grey model. The simulations were run on a varying number of CPUs ranging from 12 for the low numbers of frequency groups to 200 for the heavier calculations.

2.4. Initial and boundary conditions

The simulations of stationary radiative shocks were performed in a one-dimensional regular Cartesian grid comprising 1000 cells (see Appendix B for a discussion on resolution). The grid sizes were $L=1$ cm and $L=6$ cm for the simulations of subcritical and supercritical radiative shocks, respectively. The discontinuity was initially located at $x_s=L/4$ and the gas to the right of the discontinuity was given a density of $\rho_0=10^{-3}$ g cm^{-3} and a temperature of $k_BT=1$ eV. The radiative temperature was in equilibrium with the gas and the radiative flux was zero. The upstream velocity was set to $u_0=-30$ km s^{-1} in the subcritical case and $u_0=-100$ km s^{-1} for the supercritical shock. Once the upstream state was chosen, the downstream state was calculated using the Rankine–Hugoniot jump conditions for a radiating fluid [32], which describe the conservation of mass, momentum and energy across the discontinuity. We find (using the appropriate states of ionization) the downstream quantities for the subcritical shock to be $\rho_1=3.65\times10^{-3}$ g cm^{-3}, $u_1=-8.21$ km s^{-1} and $k_BT_1=6.92$ eV. In the case of the supercritical shock, we obtain $\rho_1=3.97\times10^{-3}$ g cm^{-3}, $u_1=-25.18$ km s^{-1} and $k_BT_1=32.85$ eV. The upstream and downstream values are also imposed inside ghost cells at the right and left boundaries of the computational domain, respectively. In computing the upstream and downstream states, we have assumed that we are sufficiently far from the shock so that the radiative temperature is in equilibrium with the gas temperature and that the radiative flux is zero, which is the case in our simulations.

2.5. The argon opacities and the decomposition of the frequency domain

The opacities for the Ar gas were taken from the ODALISC[2] database, which provides spectral opacities as well as mean opacities (Rosseland and Planck) of many elements for a wide range of physical conditions. We used the Ar opacities in the frequency range $h\nu=1$–16,000 eV, computed with the POTREC code [33] which is based on the average atom model, including l-splitting and $\Delta n=0$ transitions. The spectral opacities for two different densities and temperature are shown in Fig. 2; the pre-shock state is represented by the black line ($\rho_0=10^{-3}$ g cm^{-3}; $k_BT_0=1$ eV) while the magenta line is for the supercritical post-shock state ($\rho_1\sim4\times10^{-3}$ g cm^{-3}; $k_BT_1\sim$ 33 eV). One can see that the opacities show important orders-of-magnitude variations as a function of frequency as well as gas density and temperature, and this can have a large impact on the results. A frequency-averaged model is in this case not an accurate approximation since it cannot model situations where a gas would be optically thick in one part of the spectrum and optically thin in another.

In this work, we performed simulations with 1, 5, 10, 20, 50 and 100 frequency groups. Choosing the appropriate decomposition of the frequency domain among the groups is not very straightforward. Ideally, as soon as a large variation in κ_ν as a function of frequency is present, one would require a new frequency group. When only a small number of groups is used, different boundary choices can have different impacts on the simulation results. Group boundary placing naturally becomes less and less important as the number of frequency groups increases. For the benefit of a fair comparison between simulation results, the decomposition of the frequency domain among the groups was simply done logarithmically, as shown in Fig. 2.

3. Results

We performed simulations of subcritical and supercritical radiative shocks, using 1–100 frequency groups in both cases. The properties of the different runs are listed in Table 1. The initial discontinuity, set up with the Rankine–Hugoniot conditions described in Section 2.4, was left to evolve until all the structure in the radiative shock was

[1] http://irfu.cea.fr/Projets/Site_heracles/

[2] http://irfu.cea.fr/Projets/Odalisc/

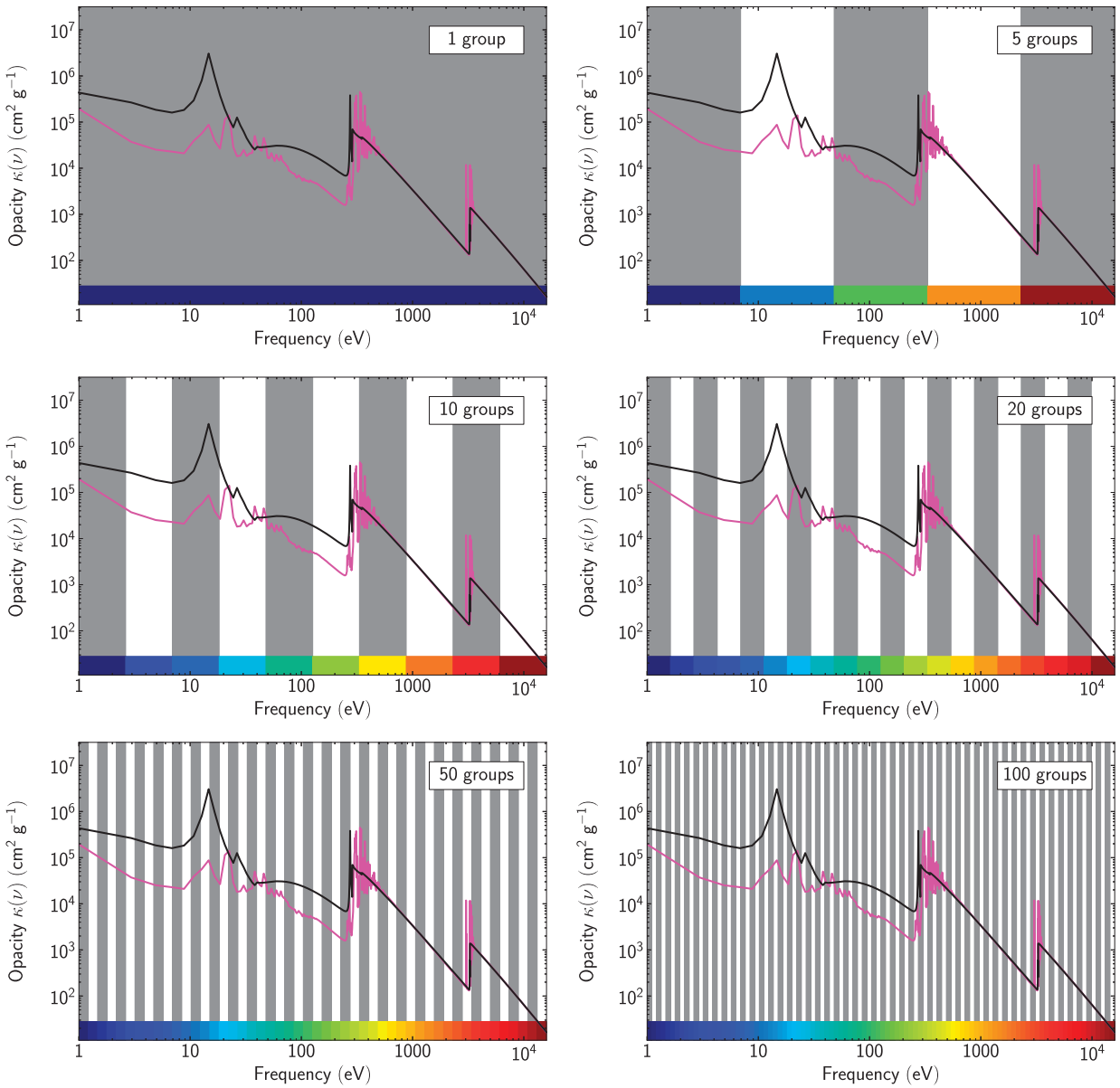

Fig. 2. The Ar opacities with the decomposition of the frequency domain for 1–100 groups. The black line represents the opacities of the gas in the pre-shock (ρ,T) state while the magenta line is for the post-shock state of the supercritical case. The colour-bar at the bottom of each frame codes for the group number; this is used in Figs. 3, 5 and 7. (For interpretation of the references to colour in this figure caption, the reader is referred to the web version of this article.)

fully developed and the stationary regime was reached. All the results shown below (apart from figures showing a time evolution) are in the stationary regime.

3.1. The subcritical case

The results for the simulations of a subcritical radiative shock using 1–100 frequency groups are shown in Fig. 3. Each row is for a different number of groups. The columns from left to right display (as a function of distance) the gas density, the gas (black) and radiative (colours) temperatures, the radiative flux and the gas opacity. In the two middle columns, the magenta curves represent the sums over all groups.

We first take a look at the mono-group simulation; run `SUB001` (top row). The profiles exhibit the classic structure of a subcritical radiative shock; a transmissive radiative precursor extends ahead of the shock heating the upstream gas and altering its density and velocity (not shown), the radiative flux (c) is maximum at the density jump (position of the hydrodynamic discontinuity) and we also note the presence of a cooling region (or Zel'dovich spike) in the temperature plot (b) at the position of the density jump, where the gas temperature exceeds the post-shock temperature. The precursor measures approximately 0.02 cm and the gas opacity (which is averaged over the entire frequency range) lies between 5×10^4 and 3×10^5 cm^2 g^{-1} throughout (note that the size of the precursor is measured between the shock position and the first point from the right hand side where the gas temperature exceeds 1.1 eV).

Table 1
Simulation results.

Run name	Number of groups	Shock velocity (km s^{-1})	Mach number	Shock position (cm)	Precursor size (cm)
SUB001	1	30	5.62	0.250	0.016
SUB005	5			0.250	0.025
SUB010	10			0.250	0.024
SUB020	20			0.250	0.052
SUB050	50			0.250	0.070
SUB100	100			0.250	0.073
SUP001	1	100	18.75	1.269	2.277
SUP005	5			1.245	2.475
SUP010	10			1.239	2.582
SUP020	20			1.233	2.650
SUP050	50			1.227	2.790
SUP100	100			1.227	2.811

Note: The position of the shock is defined as the position where the derivative of the velocity is the maximum. The size of the precursor is measured between the shock position and the first point (from the right hand side) where the gas temperature exceeds 1.1 eV.

The first multigroup simulation was performed using 5 frequency groups (SUB005), the results of which are shown in the second row. The first major difference that emerges when compared to the grey simulation is that the extent of the radiative precursor has increased; even though the gas temperature profile has not changed significantly, the radiative temperature curve extends much further ahead of the discontinuity. This can be explained by the range of opacities observed in the different groups (see Fig. 3h), and in particular the opacity of group 3 (light green), whose radiative energy dominates inside the precursor, which is almost an order of magnitude lower than the grey average. The grey opacity is biased towards a higher value which greatly affects the results, especially the radiative flux which now shows a long tail extending towards the right end of the simulation box.

The results of the subsequent runs, using 10, 20, 50 and 100 groups, are shown in the lower rows. While runs SUB005 and SUB010 are very similar to each other, the gas temperature profile has noticeably changed further in runs SUB020 to SUB100, this being most visible between 0.25 and 0.3 cm where the gas temperature is significantly altered by the radiation. The gas temperatures are overlayed inside the same window in Fig. 4a for a clearer view. The position of the density jump (or hydrodynamic shock) and the size of the precursor for all the simulations are listed in Table 1. The precursor sizes keep increasing with the number of frequency groups used. A greater resolution in the frequency domain allows an accurate treatment of the sharp slopes in the opacity curve (cf. Fig. 2), which affects the amount of absorption ahead of the shock and defines the extent of the precursor. The extent of the precursor is plotted as a function of time in Fig. 4b. The influence of the number of groups described above is very clear on this plot.

3.2. The supercritical case

The results for the simulations of a supercritical radiative shock using 1–100 frequency groups are shown in Fig. 5. The different rows and columns are identical to Fig. 3. The profiles are this time characteristic of a supercritical radiative shock; a diffusive radiative precursor strongly heats the gas ahead of the shock, notably altering the gas density, the post-shock gas and radiative temperatures are identical to the pre-shock ones and the Zel'dovich spike is clearly visible. As in the subcritical case, the size of the precursor increases with the number of frequency groups, growing by more than 20% between 1 and 100 groups, as explicited in Table 1 and illustrated in Fig. 4c and d. The fact that there is very little difference between the 50 and 100-group simulations indicate that we have almost reached convergence of our results. The number of frequency groups used impacts the results less than in the subcritical case, since most of the radiative precursor is in the diffusive regime where the grey approximation is deemed to be accurate.

These findings have important consequences on predictions made by numerical simulations on the structure of radiative shocks. Indeed, due to the very different precursor sizes, studies of radiative shocks which make use of comparisons between observations and numerical calculations will most probably be inaccurate if a grey radiative transfer model is used. One can compare the right column of Fig. 4 to the shock-precursor position diagrams found in the literature (see Fig. 2 in [30] and Figs. 5 and 6 in [18] for example).

3.3. Electron densities

In order to illustrate the differences between the grey and multigroup simulations further, we now consider the effects of our results on the observables commonly obtained in radiative shock experiments. We compare in Fig. 6 the evolution of the electron density N_e as a function of time and distance in the grey and the 100-group simulations for the subcritical (left column) and the supercritical shocks (right column). The middle panels (b), (c), (g) and (h) show the N_e distribution in the simulation frame. The dark red region is the post-shock final state with a dense and highly ionized medium, while the dark blue region is the pre-shock initial state. Between the two, the shock precursor is clearly visible in yellow. The sharp transition between the precursor

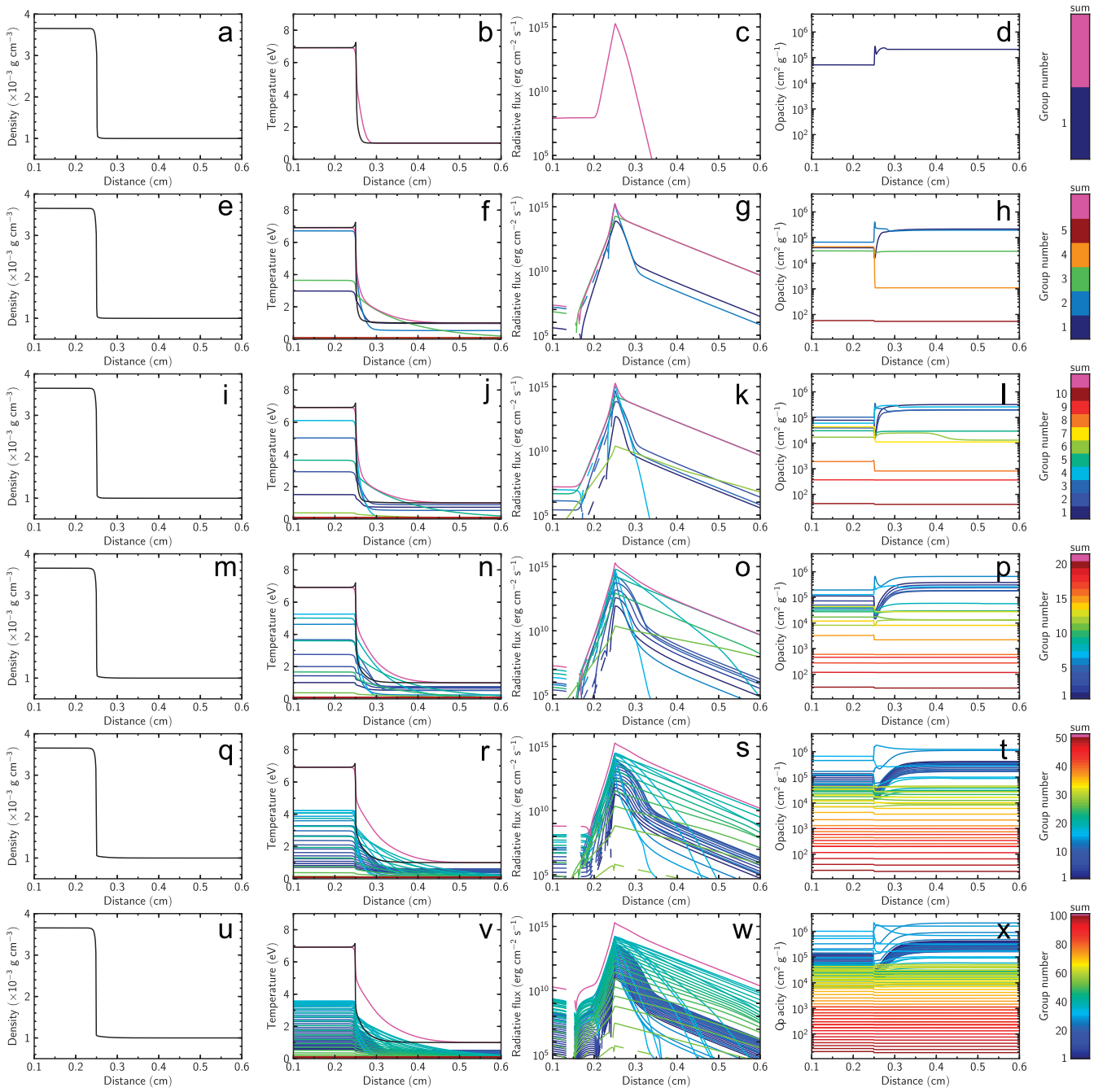

Fig. 3. Stationary subcritical radiative shocks using (from top to bottom) 1–100 frequency groups. From left to right: gas density, gas (black) and radiative (colours) temperatures, radiative flux and gas opacity. At the end of each row is a colour bar coding for the different frequency groups. In the two central columns, the magenta curves represent the sum over all groups for the radiative temperature and flux. Dashed lines represent negative values of the radiative flux (i.e. flowing from right to left). (For interpretation of the references to colour in this figure caption, the reader is referred to the web version of this article.)

(yellow) and the post-shock state (red) represents the position of the density jump as a function of time. The simulation frame panels are very useful in highlighting the differences between the grey and multigroup simulations; the radiative precursor is unmistakably larger in the multigroup case. The top panels (a) and (f) show a slice extracted from the simulation frame data, for an alternative view. We note that for the supercritical shock, the rightmost tip of the precursor is much sharper in the grey than in the multigroup case. The supercritical simulation frame figures also reveal the slight displacement of the density jump towards the left, as the whole structure of the radiative shock develops over time.

The bottom panels (d), (e), (i) and (j) show the N_e distribution in the laboratory frame, and are reminiscent of Fig. 3 in Michaut et al. [30]. These simulated laboratory-frame diagnostics show that the differences between the grey and multigroup simulations would be large enough to be detected in experimental observations.

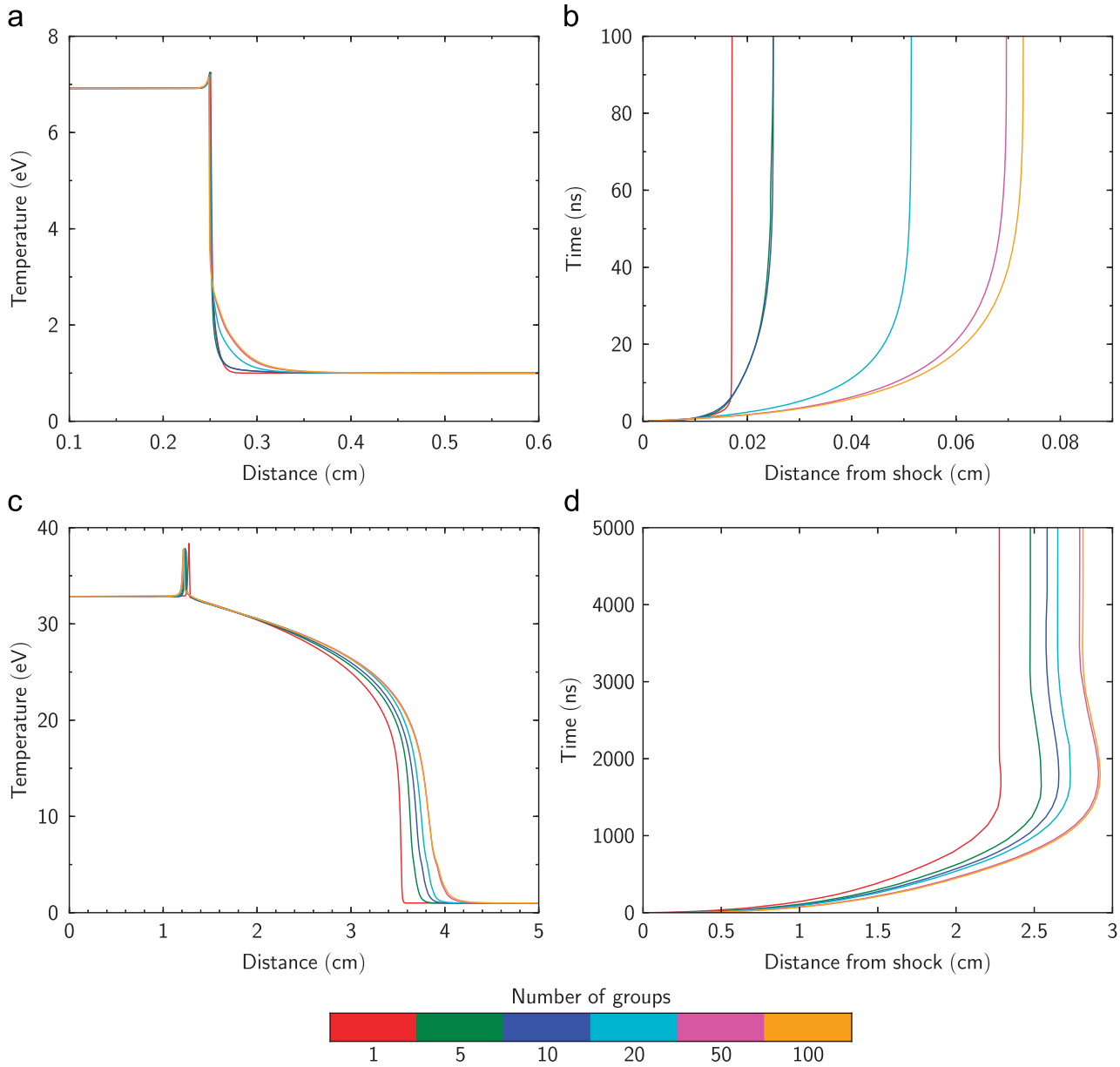

Fig. 4. Left column: gas temperature as a function of distance using 1–100 frequency groups (see colour legend at the top) in the case of subcritical (b) and supercritical (d) radiative shocks. Right column: distance between the head of the radiative precursor and the shock density jump in the case of subcritical (a) and supercritical (c) radiative shocks. (For interpretation of the references to colour in this figure caption, the reader is referred to the web version of this article.)

3.4. Detection of adaptation zones around the Zel'dovich temperature spike

We now turn to describe what is happening in the vicinity of the hydrodynamic discontinuity. Fig. 7 shows a close-up around the Zel'dovich spike for runs (from left to right) `SUP001`, `SUP005` and `SUP100`. The temperature profile of run `SUP001` shows that the classic cooling layer structure, with a sharp edge on the right and a smooth cooling (or relaxation) region on the left (as depicted in Fig. 1b), is almost resolved (see Appendix B for a discussion on resolution).

However, the temperature profile of run `SUP005` shows a rather different structure, especially on the right hand side. There is a smooth region of 'over-temperature' to the right of the spike, spanning from $x=1.26$ to 1.34 cm (indicated by arrow `A1`), where the gas temperature T_- is above the radiation temperature and higher than the final equilibrium temperature T_1. It progressively returns to the same value as the radiation temperature as we move away from the spike towards the right. In a supercritical radiative shock, the pre-shock gas temperature cannot in principle exceed the post-shock temperature [49]. The solutions are converged in both cases and the radiative precursors do not extend out to the right edge of the box. This effect must have another origin.

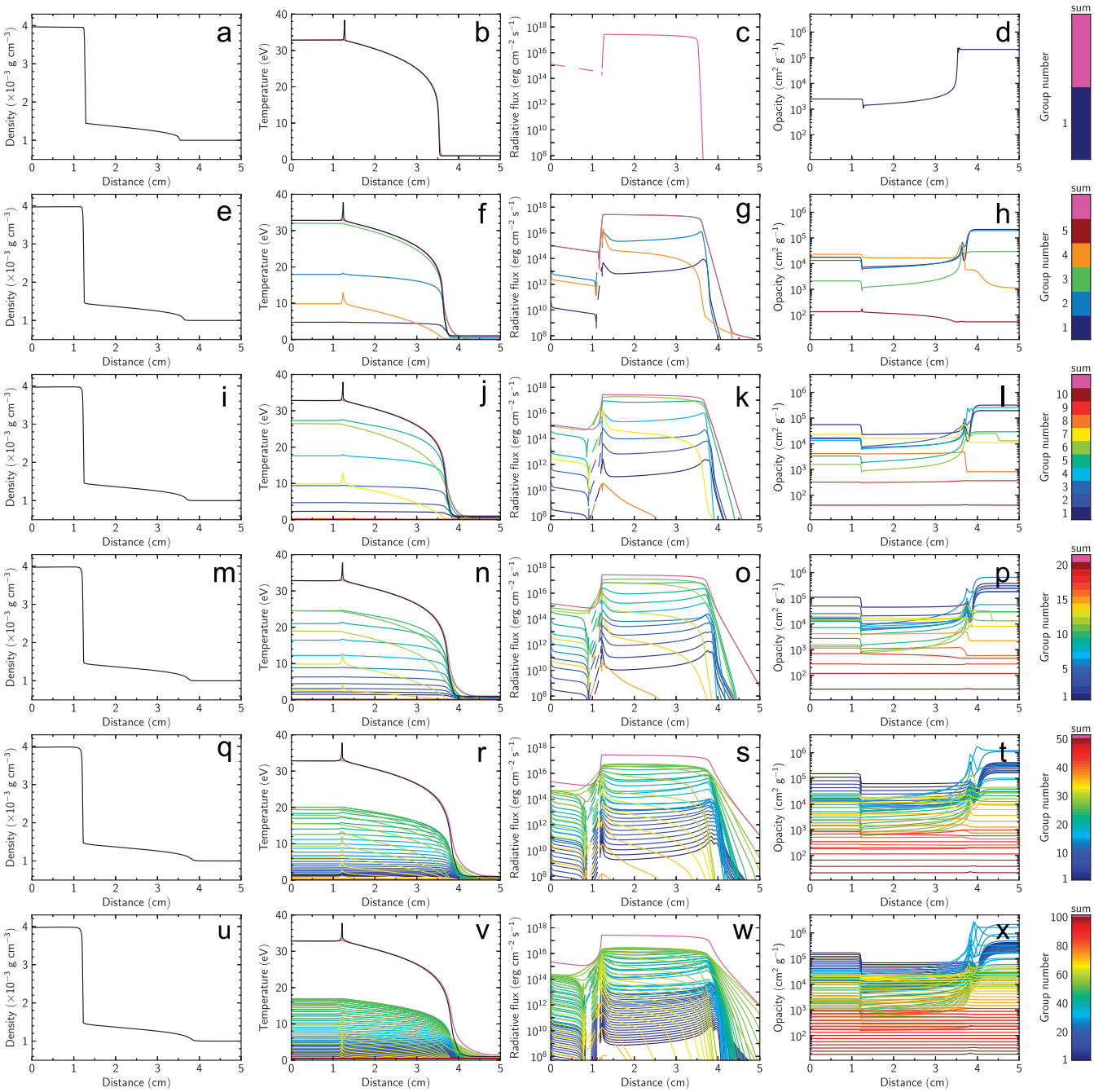

Fig. 5. Same as Fig. 3 for the supercritical shock case.

Looking at the radiative fluxes (panels g and h), we can see that in run SUP001, the flux shows a plateau right after the discontinuity. In SUP005, the same is observed for the dominant group 3 (light green) but group 4 (orange) does not show a plateau to the right of the shock, instead it decreases smoothly as we move away from the shock (see arrow A2). This indicates that the radiation in group 4 is being absorbed by the material to the right of the shock. Indeed, the group 4 opacity of the pre-shock material (panel n) is about an order of magnitude higher than the grey average in SUP001 (panel m) where the radiation can escape 'freely'.

It appears that the high opacity in group 4 causes the pre-shock material to absorb the radiation in that group only, and this consequently heats up the gas a little more. It is like having a small precursor inside a precursor. This can be understood in terms of the following. A small amount of incident radiation energy absorbed by gas per unit angle, time, area and frequency is equal to the specific intensity loss, i.e.

$$dE_\nu^{\mathrm{abs}} = -dI_\nu \cos\theta \, dA \, d\omega \, dt \, d\nu \tag{10}$$

which for a constant opacity along direction s becomes

$$dE_\nu^{\mathrm{abs}} = \kappa_\nu I_\nu \cos\theta \, dA \, d\omega \, dt \, d\nu \, ds. \tag{11}$$

In one dimension, integrating over frequency and solid angle, this reduces to

$$E^{\mathrm{abs}} = \int_0^\infty \kappa_\nu \int_{-1}^{+1} \mu I_\nu \, d\mu \, d\nu \, dA \, dt \, ds = \int_0^\infty \kappa_\nu F_\nu \, d\nu \, dA \, dt \, ds \tag{12}$$

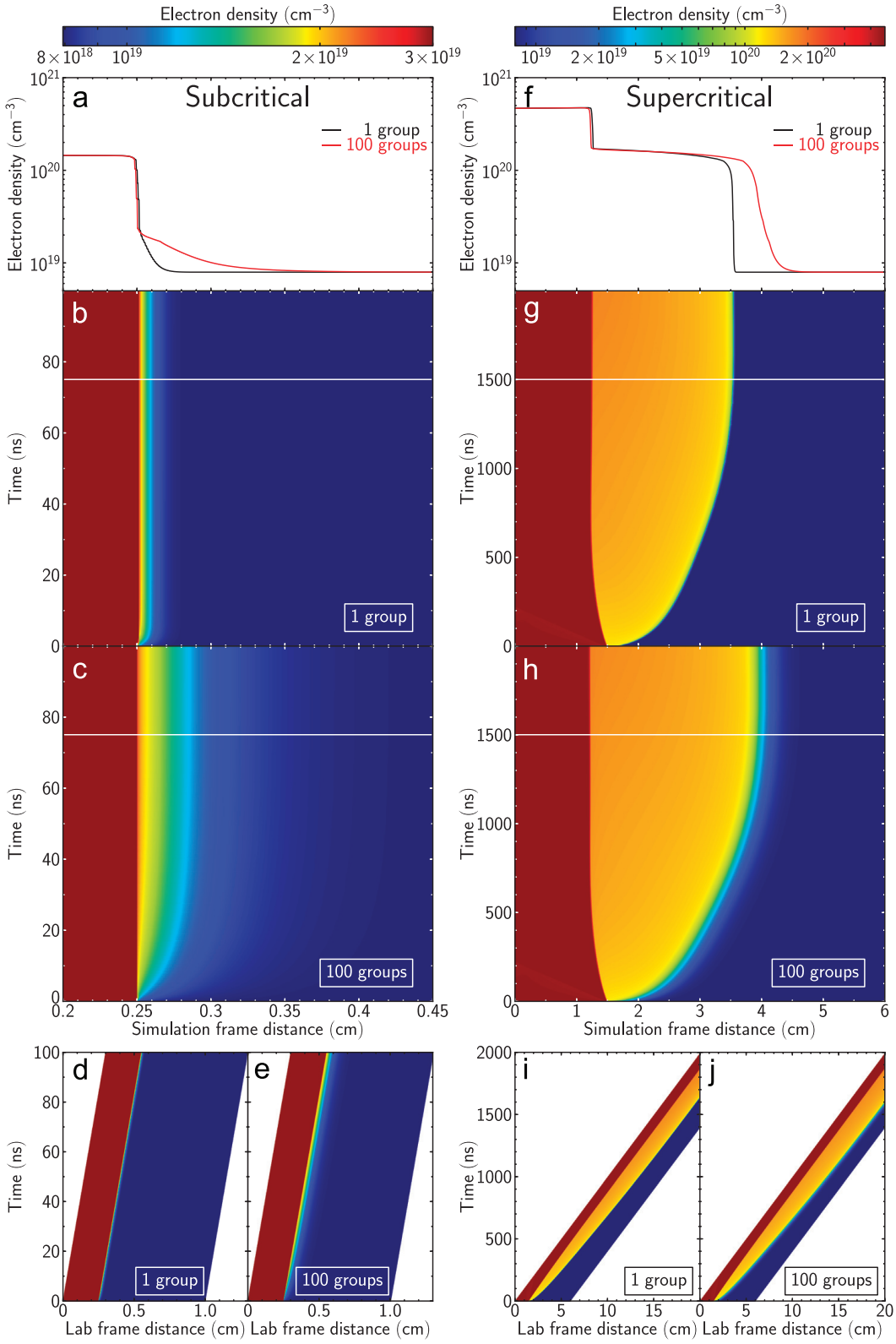

Fig. 6. Time evolution of the electron density (N_e) as a function of distance for the subcritical case (left column) and the supercritical case (right column) using 1 and 100 frequency groups. Panels (a) and (f) show a slice through the 1 (black) and 100 (red) groups simulation rest frame data. Panels (b) and (g) show the distribution of N_e in the simulation frame for 1 group while panels (c) and (h) are for the 100-group case. The bottom row displays the N_e in the laboratory frame. The horizontal white line in panels (b), (c), (g) and (h) show the position at which the slices were extracted. The bottom panels (d), (e), (i) and (j) show the N_e distribution in the laboratory frame. (For interpretation of the references to colour in this figure caption, the reader is referred to the web version of this article.)

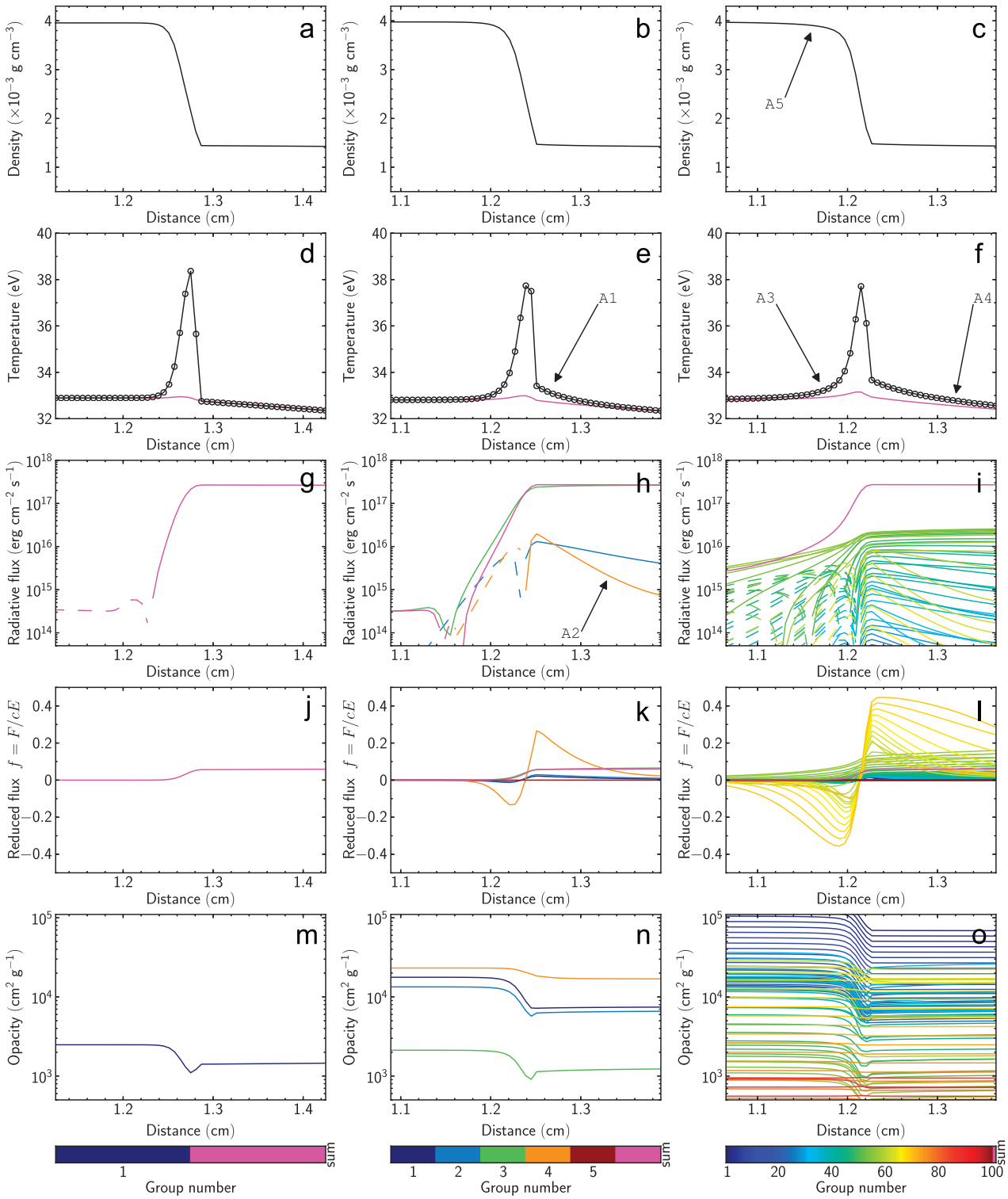

Fig. 7. A close-up view on the region around the Zel'dovich temperature spike for runs `SUP001` (left), `SUP005` (center) and `SUP100` (right). From top to bottom: gas density, gas (black) and radiative (magenta) temperature, radiative flux, reduced flux and gas opacity. In the temperature panels, the circles indicate the grid cells. As in the previous figures, the magenta curves represent the radiative quantities summed over all groups and the dashed lines symbolize negative values of the radiative flux. (For interpretation of the references to colour in this figure caption, the reader is referred to the web version of this article.)

where μ is the direction cosine. So the energy absorbed is proportional to $\int_0^\infty \kappa_\nu F_\nu d\nu$. We now suppose that we have two frequency groups, and to mimic the situation in run `SUP005`, we define the group quantities in the following way. The two groups have the same width in the frequency dimension $\Delta\nu$, and we further assume the radiative flux and gas opacity to be constant within each group, i.e. $\int_0^\infty \kappa_\nu F_\nu \, d\nu = \sum_g \kappa_g F_g \Delta\nu$. The first group can be compared to group 3 in `SUP005`; it dominates the radiative energy and flux, but has small reduced flux and opacity. On the other hand, the second group has a small energy and flux, but a large opacity and reduced flux (similar to group 4 in

SUP005). We choose

Group 1 :	Group 2 :
$E_1 = E_0$	$E_2 = E_0/100$
$\kappa_1 = 0.1$	$\kappa_2 = 1.0$
$f_1 = 0.05$	$f_2 = 0.5$
$F_1 = 0.05cE_0$	$F_2 = 0.005cE_0$

The integral over the frequency range in Eq. (12) now becomes a sum over the two groups and we have

$$E^{\mathrm{abs}} \propto [\kappa_1 F_1 + \kappa_2 F_2]\Delta\nu \propto [5\times10^{-3}cE_0 + 5\times10^{-3}cE_0]\Delta\nu \quad (13)$$

which is twice as much as what is found by considering only the dominant group 1. This shows that a group with very little radiative energy and radiative flux can contribute significantly to the total energy absorbed if it has a large reduced flux and opacity. The fact that $E_1/E_2 = 100$ means that including group 2 does not change the total radiative temperature, but does change the amount of energy absorbed by the gas, and the gas and radiative temperatures can hence be decoupled.

The morphology of the Zel'dovich spike changes again for run SUP100 (Fig. 7f). The decoupled regions both to the left and the right of the hydrodynamic discontinuity are wider than for SUP005 (see arrows A3 and A4). The radiative flux diagram (i) this time shows more components with a noticeable downward trend and large reduced fluxes. The range of opacities in the numerous groups mean that the radiation in different groups are absorbed at different rates, which yields a wider relaxation region to the right of the shock. The same effect is also observed to the left of the spike where the gas and radiation temperatures are also decoupled (with negative fluxes travelling from right to left).

The structure observed here is what is described as an adaptation zone by Drake [9,10]; a region across which the influence of radiation from the cooling layer on the shock structure fades away and where the temperature and other gas quantities make their final small adjustments in order to reach their final steady-state values. Fig. 1 in Drake [9] actually depicts exactly the situation we observe here. There are two adaptation zones on each side of the cooling layer (i.e. the Zel'dovich spike) where the gas temperature is higher than the final state T_1 downstream of the density discontinuity and higher than the precursor temperature T_- upstream. This is precisely what our simulation results show for 10 frequency groups and above. Drake [9] actually depicts the pre-shock temperature just before the discontinuity as below or equal to the final state T_1, but he does mention that "ongoing numerical work by John Castor suggests that the temperature inside the adaptation zone, at the actual density jump, may be pulled up above $[T_1]$".

The extent of the region inside which the radiative flux from the cooling layer still has an effect on the surrounding gas will inevitably depend on the opacity of the gas, which explains the different observed sizes for the adaptation zones as we vary the number of groups. The density is also pictured in Drake's papers as being slightly lower than the final state ρ_1 inside the downstream adaptation zone

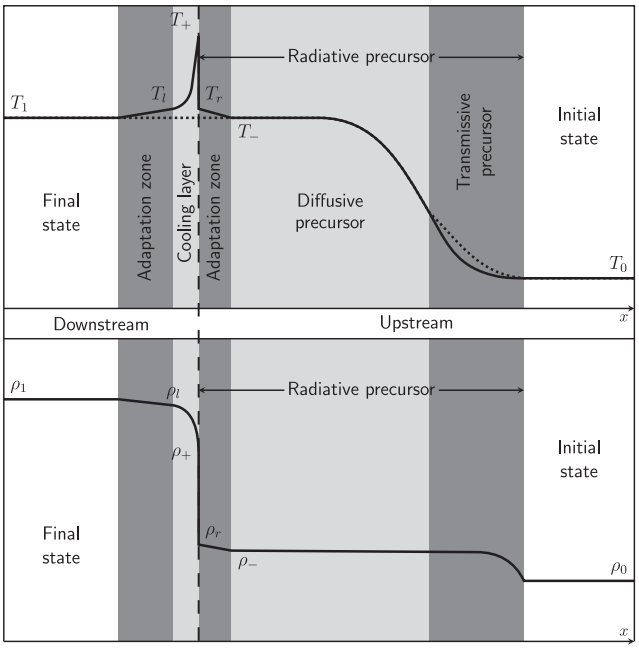

Fig. 8. Structure of a supercritical radiative shock (adapted from [9]). The direction of the gas flow is from right to left in the frame where the shock is at rest. Top panel: gas (solid) and radiative (dotted) temperature as a function of distance. Bottom panel: gas density as a function of distance. The position of the temperature and density jumps is marked by the vertical dashed line. The relative sizes of the layers are for illustration purposes only.

and higher than the leftmost precursor value ρ_- in the upstream zone. This is also the case in our results, as shown by arrow A5 in Fig. 7c.

Drake [10] provides an analytical estimate of the width of the spike for a given shock strength, and when applied to our simulation setup, it predicts that the spike should be narrower by a factor ~30. McClarren and Drake [29] also mention that the M_1 model, even though it describes the total energy flows correctly, might not perform satisfactorily in the vicinity of the cooling layer, but this has yet to be investigated. It would appear from the analytical estimates that we might not be resolving the real 'physical' Zel'dovich spike, but the discussion in Appendix B shows that we are sufficiently resolving the spike (for the purpose of this study) resulting from our numerical model. We also demonstrate that our observation of adaptation zones being absent from grey simulations while being clearly detected in multigroup simulations is not resolution dependent. While we have to acknowledge that we might not be resolving the true width of the spike, as we do not attempt to make any comparisons with experiments, we believe that our results are still legitimate.

Finally, the presence of these adaptation zones in our simulations forces us to revise our depiction of a radiative shock structure and adopt a more up-to-date description (see Fig. 8). The pre-shock gas is heated by the radiative precursor to a temperature $T_- \approx T_1$, and increases slightly to a temperature T_r as we cross the right adaptation zone through radiative heating. The shock compression at the density jump (discontinuity) heats it further to a temperature T_+ which is higher than the final post-shock equilibrium state T_1. The gas then cools down inside the cooling

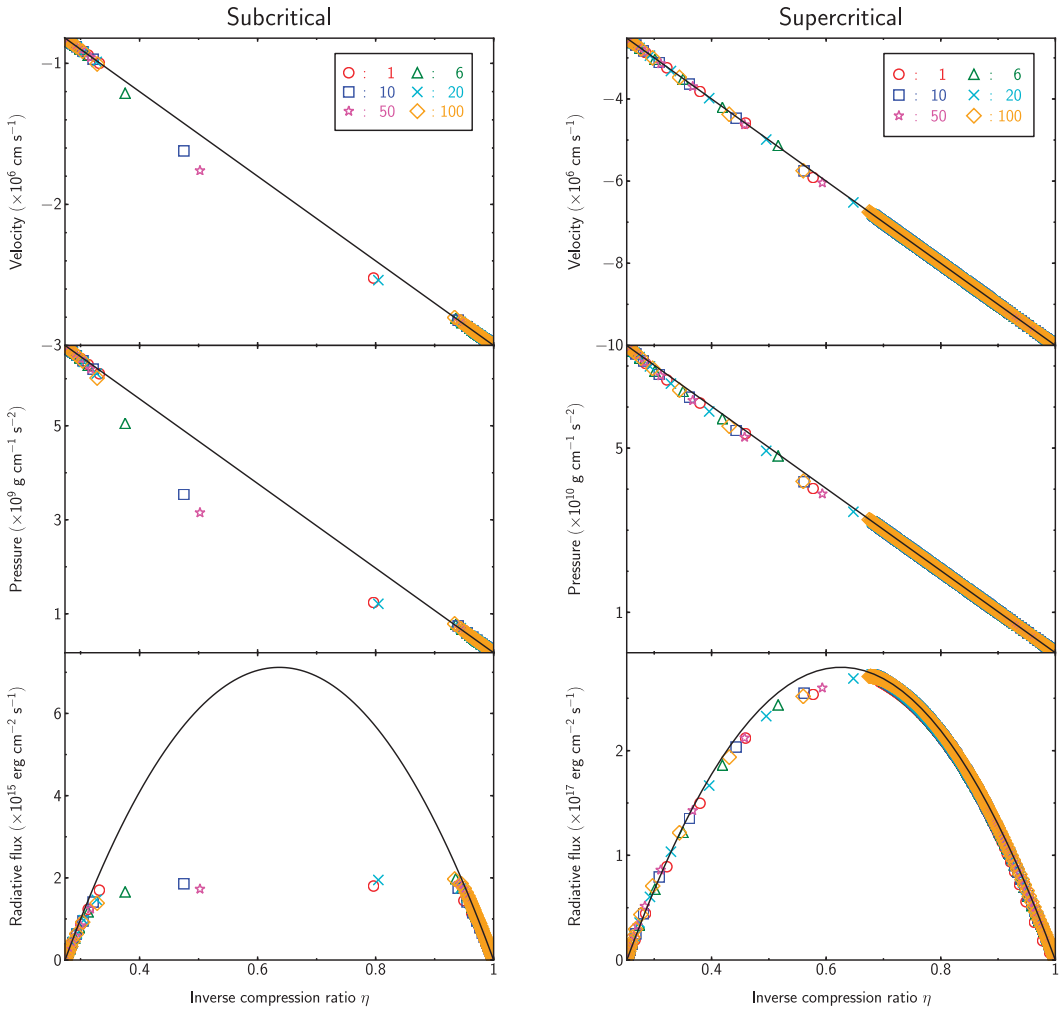

Fig. 9. Hugoniot curves for the radiative shock simulations using 1–100 frequency groups (see legend in the top right corner for the meaning of the symbols): gas velocity (top), pressure (middle) and radiative flux (bottom) as a function of inverse compression ratio in the case of the subcritical shock (left column) and the supercritical shock (right column). The analytical solutions are overlayed for comparison (black solid line). The simulation points not lying on the analytical solutions are all within the shock transition.

layer to reach the intermediate post-shock state T_l by radiating the excess energy away. The final small adjustments are made across the left adaptation zone to reach the final post-shock state T_1 (see also [10]). The radiative temperature (dotted line) is equal to the gas temperature for the most part, except that it remains constant across the cooling layer and the adaptation zones (decoupled from the gas), and is higher than the gas temperature inside the transmissive precursor. The pressure gradient at the head of the precursor, through the conservation of mass (4) and momentum (5), causes the velocity to decrease and the density to increase to a value ρ_- ahead of the discontinuity. Since the gas temperature is close to being constant in the diffusive part of the precursor, there is no more pressure gradient and the density reaches a plateau value ρ_- ahead of the discontinuity. A small compression from ρ_- to ρ_r occurs as we cross the right adaptation zone, then followed by the sharp density jump of the shock from ρ_- to ρ_+ which takes place on the gas viscous scale. The density then rises rapidly to ρ_l inside the cooling layer through strong contraction of the radiating gas. Lastly, the density slowly reaches the final state ρ_1 across the left adaptation zone.

3.5. Hugoniot curves

In this section we look at the Hugoniot curves for gas velocity, pressure and radiative flux in our simulations. The Hugoniot curves are analytical predictions for the state of gas quantities as a function of the inverse compression ratio $\eta = \rho_0/\rho$ for which conservation of mass, momentum and energy hold (see [49,32] for example). Fig. 9 shows (from top to bottom) the gas velocity, pressure and radiative flux as a function of inverse compression ratio for every grid point in our subcritical (left) and supercritical (right) simulations, as well as the analytical solutions (solid black line) which are

$$u(\eta) = -u_0\eta \tag{14}$$

$$p(\eta) = \rho_0 u_0^2(1-\eta)+p_0 \tag{15}$$

$$F(\eta) = \frac{\rho_0 u_0^3}{2}\left(\frac{2\gamma}{\gamma-1}\eta - \frac{\gamma+1}{\gamma-1}\eta^2 - 1\right) - \frac{\gamma p_0 u_0}{\gamma-1}(1-\eta)+F_0 \tag{16}$$

where γ is the ratio of specific heats and the radiative flux F is expressed in the laboratory frame (note that we have

converted our radiative quantities to the laboratory frame using Eqs. (91.16) and (91.17) in [32]).

This illustrates well how our numerical scheme preserves the important physics of conservation of mass, momentum and energy. Any simulation of shocks which has points lying away from these analytical curves does not conserve these fundamental quantities. The points which do not lie on the analytical curves in Fig. 9 are all in the shock transition region which is inevitably spread over a minimum number of cells for a Godunov method and do not strictly match the analytical solution (see [44,10] for example). This is mostly visible in the subcritical case where the radiative flux follows a constant value transition while the gas velocity and pressure follow an approximate Hugoniot curve through the transition to connect the upstream and downstream states. Note that only a single cell for each simulation does not lie on the analytical prediction, illustrating the fact that the transition is spread over only one or two grid cells. We take the opportunity here to point out that the comoving frame formalism, which has been criticized in several works for not rigorously conserving the total energy (see [31,23] for example), appears here to perform very well in conserving the fundamental quantities.

4. Conclusions

We have performed simulations of stationary radiative shocks in Ar gas using a multigroup radiation hydrodynamics scheme. Gas opacities depending on temperature, density and frequency were used in the equations of radiation hydrodynamics to achieve convincing results. The simulations reproduced all the detailed structure of a radiative shock, including the radiative precursor, the cooling layer and even the adaptation zones connecting the cooling layer to the final downstream state and the precursor. Our results show that grey simulations produce very different results compared to multigroup ones, and that frequency-independent calculations are not deemed an accurate description of the problem. Indeed, multigroup simulations showed increases by a factor of four in precursor size in the subcritical case, and an increase of 20% in the supercritical case. The simulations with 5–100 groups also show increasing precursor sizes, with a suspected convergence of results for 50 groups and above. Multigroup effects were also seen to be important in the vicinity of the cooling layer, where adaptation zones absent from grey simulations were clearly detected.

We have to acknowledge that several caveats need to be taken into account when considering the results reported in this work. Firstly, the exact sizes of the radiative precursors are not entirely correct since higher resolution simulations reported in Appendix B yield slightly different results (typical differences are of the order of 5–10%), only the relative increase in precursor sizes between the different simulations are of notorious relevance. Secondly, even though our results are numerically quantitatively converged in the proximity of the Zel'dovich spike, it is not clear whether the M_1 model performs accurately enough on such small scales. We remind the reader that this work is not an attempt at directly comparing numerical simulations to experiments, merely a study of the effects of frequency dependence on the results of radiation hydrodynamic calculations.

Nevertheless, the findings presented still have important consequences on predictions made by numerical simulations on the structure of radiative shocks. Indeed, studies of astrophysical (accretion processes, supernova remnants, jets, etc.) or laboratory radiative shocks will most probably be inaccurate if a grey radiative transfer model is used. The impact can not only be large when looking at the radiative precursor sizes, but also on the total energy budget, determining the amount of energy converted into radiation and absorbed by pre-shock material.

It is difficult to compare the results of this work with experimental data directly since our idealized setup of stationary radiative shocks is very far from the situation in laboratories where laser-driven radiative shocks travel through gas chambers and it is often unclear if they ever reach a stationary state. Realistic calculations using a piston-like shock-driving boundary, as well as a more sophisticated equation of state, will be more appropriate for conducting detailed modelling of laboratory experiments.

Acknowledgements

The research leading to these results has received funding from the European Research Council under the European Community's Seventh Framework Programme (FP7/2007-2013 Grant Agreement no. 247060). The authors also gratefully acknowledge support from Grant ANR-06-CIS6-009-01 for the programme SiNeRGHy. The authors would also like to thank M. Busquet for fruitful discussions which have yielded vast improvements of this paper and J.P. Gauthier for the Ar opacity tables. Finally, the authors would like to thank the reviewers for very useful comments which have helped greatly in improving the robustness and credibility of the paper.

Appendix A. Using the correct opacity average

In the RHD equations (5)–(8), it is challenging to compute the radiative energy and flux-weighted mean opacities κ_E and κ_F (note that $\sigma=\kappa\rho$), since the quantities E_ν and F_ν are not necessarily known at *all* wavelengths. The choice of approximation for these quantities, which are crucial to the RHD calculations, is not trivial (see [37, p. 88+] for a discussion). Common practise is to set $\kappa_E=\kappa_P$ and $\kappa_F=\kappa_R$ where κ_P and κ_R are the Planck and Rosseland mean opacities, respectively (see [24,35] for example). However, for the M_1 model, numerical stability is immensely improved if an identical value for κ_E and κ_F is used, which prompts us to use an average value $\kappa_{\rm av}=\kappa_E=\kappa_F$.

The Planck and Rosseland means are applicable to different regimes. In the diffusion limit, the opacity should be equal to the Rosseland mean, while the Planck mean is appropriate in the free-streaming limit. We need to make sure that we recover this behaviour with our average opacity. Sampson [42] proposed an average which varies between κ_P and κ_R depending on the optical depth. Here, we use the reduced radiative flux $f=\|\mathbf{F}\|/cE$ as a measure

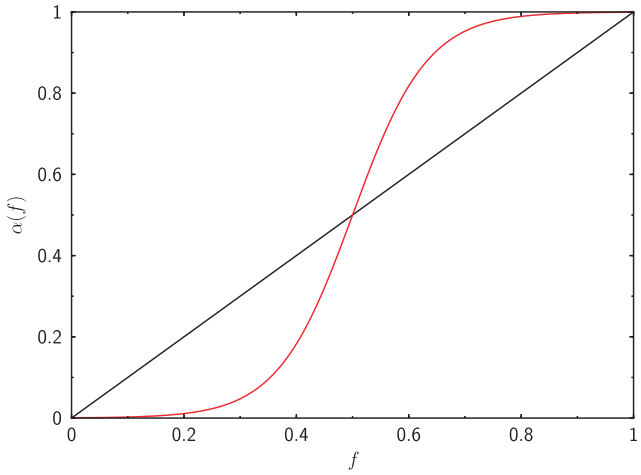

Fig. A1. α parameter as a function of reduced flux f: the black solid line is the simple $\alpha=f$ while the red line is given by Eq. (A.2). (For interpretation of the references to colour in this figure caption, the reader is referred to the web version of this article.)

of the diffusivity (optically thick) or transmissivity (optically thin) of the flow. We define a parameter $\alpha(f)$ which varies between zero and one according to f which then allows us to write the average opacity

$$\kappa_{\rm av} = (1-\alpha)\kappa_R + \alpha\kappa_P. \tag{A.1}$$

In order to recover the diffusion and free-streaming limits, α needs to have the following properties: $\alpha\to 0$ when $f\to 0$ and $\alpha\to 1$ when $f\to 1$. The simplest formula with these properties is just the linear function $\alpha=f$. However, we argue that the α parameter is meant to represent the transition from a regime dominated by diffusion to a radiation-dominated regime. In this sense, one expects the transition from one to the other to be rather rapid, as opposed to a smooth linear averaging between the κ_P and κ_R values. We thus propose a different formula for α which will better reproduce this behaviour. After some experimenting, we finally chose

$$\alpha_s = \frac{1}{e^{-15(f-1/2)}+1} \tag{A.2}$$

which is plotted in Fig. A1 (red) alongside the simpler $\alpha=f$ (black). We would like to point out here that we have no physical explanation for Eq. (A.2), it is simply an *ad-hoc* choice of a function with the correct properties. However, we can justify our choice by testing the method in a simple case.

We performed eight simulations with a single frequency group; four calculations of a subcritical radiative shock and four of a supercritical shock. In each case, the first was carried out using $\alpha=f$, the second using $\alpha=\alpha_s$, the third using $\alpha=0$ (which corresponds to $\kappa_{\rm av}=\kappa_R$) and the fourth using $\alpha=1$ ($\kappa_{\rm av}=\kappa_P$). We show the results in Fig. A2. In the case of the subcritical radiative shock (left column), we see that the average opacities (black and red) are equal to the Rosseland mean far away from the discontinuity (on both sides). They then become close to the Planck average in the intermediate region (between 0.25 and 0.28 cm) where the reduced flux is large. The temperature plot shows that the results for both the averaging schemes are very close to the blue curve (Planck mean) which is the desired result in this optically thin regime. For the supercritical shock (right column), the average opacity should produce results which resemble the green curves, which are appropriate in this diffusive regime (only a small region of the grid has a large f). This time, the simple $\alpha=f$ approximation shows its limitations with a precursor size about two-thirds of the size of the one observed in the $\kappa_{\rm av}=\kappa_R$ case. On the other hand, the $\alpha=\alpha_s$ model performs much better, producing results very similar to the $\kappa_{\rm av}=\kappa_R$ simulation. We thus conclude that the expression given in Eq. (A.2) is an effective model to simulate problems in both diffusive and free-streaming limits.

In a final note, we wish to reiterate that the inaccuracies which arise from the approximation of setting $\kappa_E=\kappa_F=\kappa_{\rm av}$ are reduced as the number of frequency groups used increases, since in the limit of infinite frequency resolution, all of these quantities simply reduce to κ_ν. This approximation is thus less crude in a multigroup model than in a grey model.

Appendix B. A comment on spatial resolution

In Fig. 7 it would appear that with our spatial resolution of 1000 grid cells, we do not fully resolve the very narrow Zel'dovich spike. For completeness, we report in this section a short spatial resolution study to confirm that our results concerning the influence of the number of frequency groups on the size of the radiative precursors and adaptation zones on each side of the spike are robust. Fig. B1 compares the effects of grid resolution and number of frequency groups on the shock structures. The top row shows the temperature profiles in the vicinity of the cooling layer for 1 frequency group using 500, 1000, 5000 and 10,000 cells in the subcritical (a) and supercritical (b) cases (see colour key at the top of the figure). In the subcritical case, the different resolutions appear to yield similar results. For the supercritical runs, the spike appears well resolved in the high resolution simulations. It looks thinner than in the lower resolution calculations and displays a (smooth) maximum to the left of the discontinuity, a structure that much resembles the results of Lowrie and Edwards [28]. At a Mach number of ~19, the spike structure fits well between their depictions of shocks at $\mathcal{M}=3$ (Fig. 9) and $\mathcal{M}=27$ (Fig. B1). A strong convergence of results is observed between 5000 and 10,000 cells.

The middle row shows again the temperature profiles of the cooling layer for different resolutions but this time using 5 frequency groups. Panel (c) reveals that 500 cells is most probably too few to resolve the cooling layer. Both panels also show convergence between 5000 and 10,000 cells. More importantly, panels (b) and (d) demonstrate that our overall conclusions on the presence of adaptation zones in the multigroup simulations remain. Even though the relaxation region to the right of the spike is more pronounced in the 5000-cell simulation (grey), the results from the 1000-cell simulations (cyan) agree qualitatively; an adaptation zone is absent from the grey simulations but is detected in the multigroup simulations.

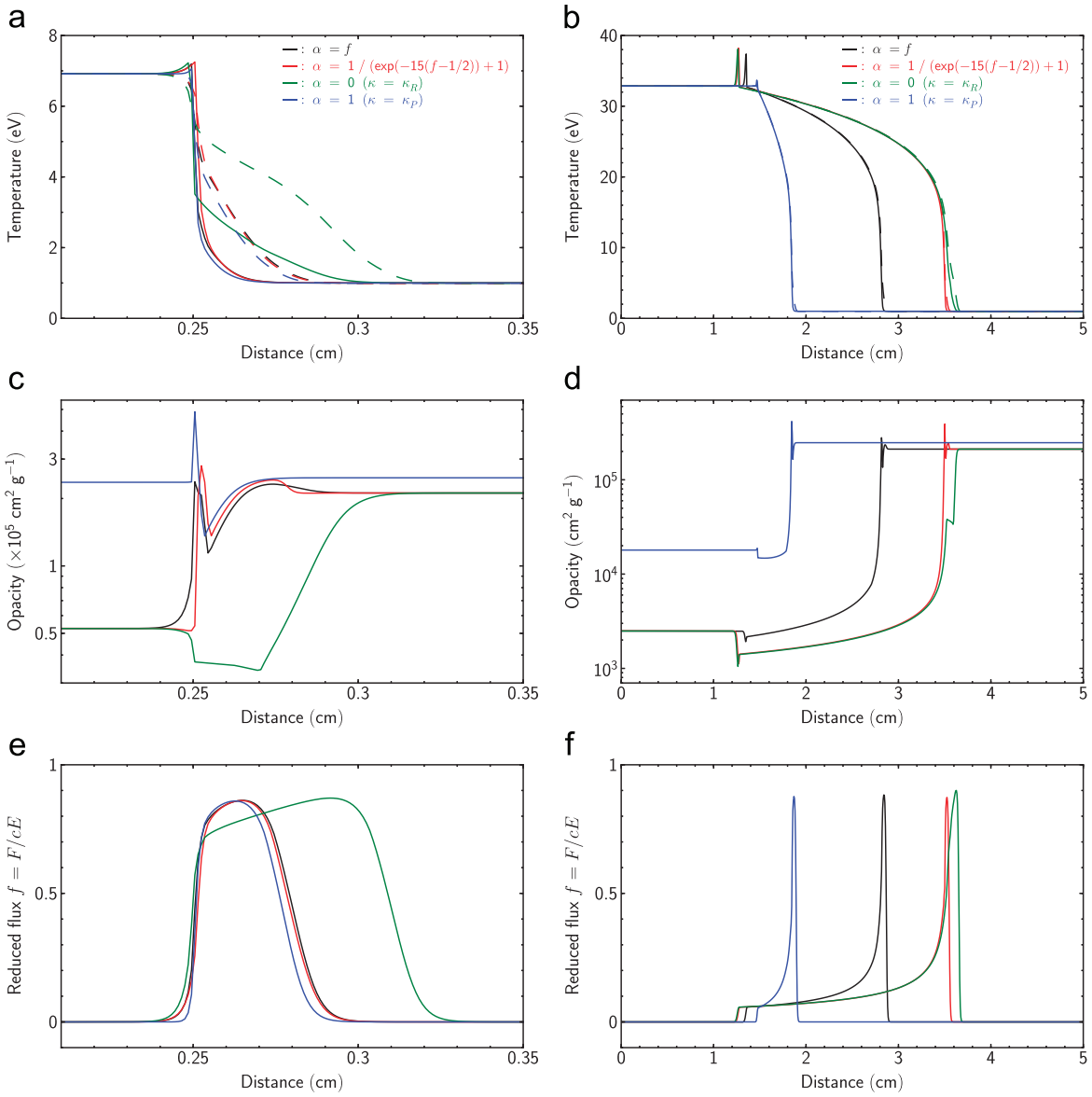

Fig. A2. Comparison of the different opacity averaging functions. The left and right columns show the results for the subcritical and supercritical radiative shocks, respectively. The top row displays the gas (solid) and radiative (dashed) temperatures, the middle row is the gas opacity and the bottom row shows the reduced flux. The colour-coding is as follows: black is for $\alpha = f$, red is for α given by Eq. (A.2), green is for $\kappa_{\rm av} = \kappa_R$ and blue is for $\kappa_{\rm av} = \kappa_P$. (For interpretation of the references to colour in this figure caption, the reader is referred to the web version of this article.)

Analytical estimates of the width of the spike from Drake [10] suggest that the real physical spike for the same values of shock velocity and initial state density might in fact be much narrower (by a factor of ~30). Nevertheless, the fact remains that we have converged spatially on the structure of the cooling layer given by our M_1 model, which is what matters for the present study. In addition, analytical estimates also make use of approximations and the *true* width of the spike is probably not known accurately.

The bottom row displays the size of the radiative precursors as a function of time for the different simulations. To better distinguish the separate runs, we have plotted the simulations using 1 group with dashed lines and the simulations using 5 groups with solid lines (the colours remain the same as in the other panels). These plots reveal that the spatial resolution also affects the total size of the precursor (here again the results have converged for 5000 cells and above). However, as we do not make any direct comparisons with experiments or observations throughout this work but are only interested in the relative differences in precursor sizes, we argue that our conclusions regarding the increase in precursor size as a function of number of frequency groups remain qualitatively correct. Moreover, panels (e) and (f) show quite clearly that the difference in precursor size due to a change in number of groups is larger than the difference observed from a change in number of cells. In addition, Fig. B1 only shows the results using 1 and 5 groups, and the size of the precursor is seen to continue increasing all the way up to 100 groups (see Fig. 4). In the case of the subcritical shock, differences between runs with 1000 and 10,000 cells are ~20% and ~8% for the 1- and 5-group simulations, respectively,

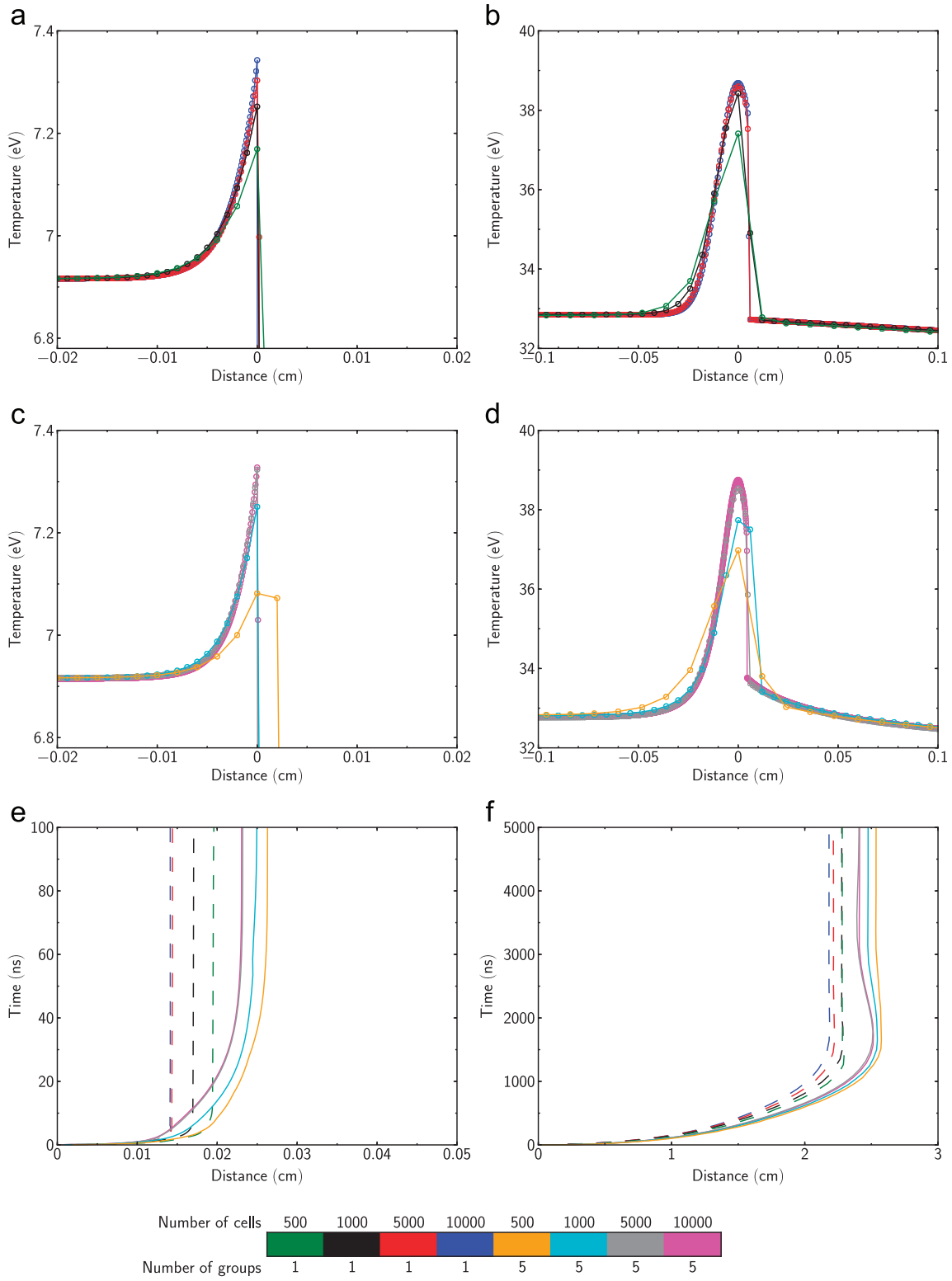

Fig. B1. Comparison between the effects of grid resolution and the number of frequency groups. Top row: temperature profiles in the vicinity of the cooling layer for 1 frequency group using different spatial resolutions in the subcritical (a) and supercritical (b) cases (see colour key at the top of the figure). Middle row: same as the top row but using 5 frequency groups. Bottom row: size of precursor as a function of time for the 1-group (dashed) and 5-group (solid) simulations in the subcritical (e) and supercritical (f) cases. (For interpretation of the references to colour in this figure caption, the reader is referred to the web version of this article.)

while differences between the 1- and 100-group (1000 cells) simulations are higher than 400% (see Table 1). As for the supercritical, resolution alters the precursor sizes by only 2–4% while frequency groups have an effect of the order of 20%. Finally, the relative differences in precursor size between 1- and 5-group simulations for a given resolution remajepo|6541in approximately constant. It was not possible for us to run a 100-group simulation

using 5000 cells on a realistic timescale, but we believe that the results of the 1000-cell simulations are qualitatively robust.

References

[1] Blinnikov SI, Tolstov AG. Astron Lett 2011;37:194.
[2] Bode MF, Evans A. Classical novae. In: Bode MF, Evans A, editors. Cambridge Astrophysics Series, No. 43. 2nd ed. Cambridge: Cambridge University Press; 2008.
[3] Bozier JC, Thiell G, Le-Breton JP, Azra S, Decroisette M, Schirmann D. Phys Rev Lett 1986;57:1304.
[4] Bouquet S, Stéhlé C, Koenig, et al. Phys Rev Lett 2004;92:225001.
[5] Busquet M, Audit E, González M, Stehle C, Thais F, Acef O, et al. High Energy Density Phys 2007;3.
[6] Commerçon B, Audit E, Chabrier G, Chièze J-P. Astron Astrophys 2011;530:A13.
[7] Draine BT, McKee CF. Annu Rev Astron Astrophys 1993;31:373.
[8] Drake RP. High energy density physics: foundations, inertial fusion, and experimental astrophysics.Berlin: Springer; 2006 [Chapter 7.4].
[9] Drake RP. IEEE Trans Plasma Sci 2007;35:171.
[10] Drake RP. Phys. Plasmas 2007;14:043301.
[11] Dubroca B, Feugeas J-L. C R Acad Sci Paris 1999;329:915.
[12] Edwards MJ, MacKinnon AJ, Zweiback J, Shigemori K, Ryutov DD, Rubenchik AM, et al. Phys Rev Lett 2001;87 085004-1.
[13] Fadeyev YA, Gillet D. Astron Astrophys 2000;354:349.
[14] Falize E, Michaut C, Cavet C, Bouquet S, Koenig M, Loupias B, et al. Astrophys Space Sci 2009;322:71.
[15] Fleury X, Bouquet S, Stehlé C, Koenig M, Batani D, Benuzzi-Mounaix A, et al. Laser Part Beams 2002;20:263.
[16] Ghavamian P, Raymond J, Hartigan P, Blair WP. Astrophys J 2000;535:266.
[17] Gillet D. EAS Publ Ser 2006;21:297.
[18] González M, Stehlé C, Audit E, Busquet M, Rus B, Thais F, et al. Laser Part. Beams 2006;24:535.
[19] González M, Audit E, Huynh P. Astron Astrophys 2007;464:429.
[20] González M, Audit E, Stehlé C. Astron Astrophys 2009;497:27.
[21] Imamura JN. Astrophys J 1985;296:128.
[22] Keiter PA, Drake RP, Perry TS, Robey HF, Remington BA, Iglesias CA, et al. Phys Rev Lett 2002;89:165003.
[23] Krumholz M, Klein RI, McKee CF, Bolstad J. Astrophys J 2007;667:626.
[24] Larsen JT, Lane SM. J Quant Spectrosc Radiat Transfer 1994;51:179.
[25] Leibrandt DR, Drake RP, Reighard AB, Glendinning SG. Astrophys J 2005;626:616.
[26] Levermore CD. J Quant Spectrosc Radiat Transfer 1984;31:149.
[27] Lowrie RB, Rauenzahn RM. Shock Waves 2007;16:445.
[28] Lowrie RB, Edwards JD. Shock Waves 2008;18:129.
[29] McClarren RG, Drake RP. J Quant Spectrosc Radiat Transfer 2010;111:2095.
[30] Michaut C, Falize E, Cavet C, Bouquet S, Koenig M, Vinci T, et al. Astrophys Space Sci 2009;322:77.
[31] Mihalas D, Klein RI. J Comput Phys 1982;46:97.
[32] Mihalas D, Mihalas BD. Foundations of radiation hydrodynamics. New York: Oxford University Press; 1984.
[33] Mirone A, Gauthier JC, Gilleron F, Chenais-Popovics C. J Quant Spectrosc Radiat Transfer 1997;58:791.
[34] Nymark TK, Fransson C, Kozma C. Astron Astrophys 2006;449:171.
[35] Offner SSR, Klein RI, McKee CF, Krumholz MR. Astrophys J 2009;703:131.
[36] Orlando S, Drake JJ, Laming JM. Astron Astrophys 2009;493:1049.
[37] Pomraning GC. International series of monographs in natural philosophy.Oxford: Pergamon Press; 1973.
[38] Raga AC, Mellema G, Arthur SJ, Binette L, Ferruit P, Steffen W. Rev Mex Astron Astrofis 1999;35:123.
[39] Reighard AB, Drake RP, Dannenberg KK, et al. Phys Plasmas 2006;13:082901.
[40] Reighard AB, Drake RP, Mucino JE, Knauer JP, Busquet M. Phys Plasmas 2007;14:056504.
[41] B. Reipurth, A.C. Raga, in: NATO ASIC Proceedings of 540: The Origin of Stars and Planetary Systems, 1999, p. 267.
[42] Sampson D. J Quant Spectrosc Radiat Transfer 1965;5:211.
[43] Shestakov AI, Offner SSR. J Chem Phys 2008;227:2154.
[44] Sincell MW, Gehmeyr M, Mihalas D. Shock Waves 1999;9:391.
[45] Stahler SW, Shu FH, Taam RE. Astrophys J 1980;241:637.
[46] van der Holst B, Toth G, Sokolov IV, Powell KG, Holloway JP, Myra ES, et al. Astrophys J Suppl 2011;194:23.
[47] Vaytet NMH, O'Brien TJ, Bode MF. Astrophys J 2007;665:654.
[48] Vaytet NMH, Audit E, Dubroca B, Delahaye F. J Quant Spectrosc Radiat Transfer 2011;112:1323.
[49] Zel'Dovich YB, Raizer YP. Physics of shock waves and high temperature hydrodynamic phenomena.New York: Academic Press; 1967.
[50] Zhang W, Howell L, Almgren A, Burrows A, Dolence J, Bell J. Astrophys J Suppl 2013;204:7.

2.2 Expériences auprès de la fontaine aux supernovæ SWASI

2.2.1 Contexte

Plusieurs faits observationnels tendent à montrer que les explosions de supernovæ sont asymétriques. En particulier, les vitesses observées des pulsars (Hobbs *et al.* 2005) sont beaucoup plus élevées que celles des étoiles massives (Gunn et Ostriker 1970). Cette constatation peut être expliquée par un processus d'explosion asymétrique avec une forte composante $l = 1$, donnant un "kick" supplémentaire à l'étoile à neutrons (Scheck *et al.* 2004). Il est donc important de mieux comprendre les éventuels mécanismes asymétriques d'explosion. Des contraintes directes sur ces mécanismes des premiers instants de l'explosion sont espérées dans le futur avec la détection de neutrinos et d'ondes gravitationnelles en provenance d'une supernova galactique (Kotake 2013).

Un des mécanismes physiques permettant les explosions asymétriques est l'instabilité du choc d'accrétion stationnaire ou SASI (pour "Standing Accretion Shock Instability"). Cette instabilité a été découverte pour la première fois dans des simulations numériques (Blondin *et al.* 2003) avant que son origine physique ne soit élucidée (Foglizzo *et al.* 2007, Scheck *et al.* 2008, Guilet et Foglizzo 2012).

Les étoiles massives (d'au moins 10 $M_\odot$ environ) en fin de vie ont une structure dite "en pelure d'oignon" formée de couches concentriques des produits successifs des fusions nucléaires, éléments de plus en plus lourds (de l'hydrogène au fer) au fur et à mesure que l'on s'approche du centre. Au centre se trouve un cœur de fer d'environ 1500 km qui, lorsque sa masse devient trop grande, s'effondre en moins d'une seconde en une proto-étoile à neutrons d'environ 30 km de rayon. Une onde de choc est alors générée qui devient stationnaire à une distance d'environ 150 km. Ce choc d'accrétion stationnaire est ensuite sujet à une instabilité. Lorsqu'une onde acoustique se propageant vers l'extérieur depuis la proto-étoile à neutrons atteint le choc, elle le déforme et créé des perturbations de vorticité et d'entropie. Ces perturbations sont advectées vers la proto-étoile à neutrons et créent de nouvelles perturbations acoustiques se propageant vers le choc d'accrétion. Si l'amplitude de ces perturbations augmente au cours du cycle, celui-ci déclenche une instabilité. Le choc oscille alors avec des mouvements de grande amplitude et à grande échelle. Dans le régime non-linéaire, un mode spiral peut dominer la dynamique du choc (Blondin et Mezzacappa 2007). Cette instabilité SASI est donc issue d'un cycle advectif-acoustique se développant entre l'onde de choc stationnaire et la région de décélération proche de la proto-étoile à neutrons (cf. Fig 2.3).

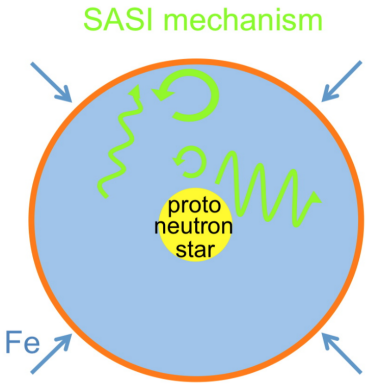

FIGURE 2.3 – Mécanisme de SASI fondé sur le couplage entre des ondes acoustiques (flèches ondulées) et des perturbations advectées (flèches circulaires) entre le choc d'accrétion stationnaire et la surface de la proto-étoile à neutrons. Extrait de Foglizzo *et al.* (2015).

2.2.2 Le dispositif expérimental

En 2012, Thierry Foglizzo a construit un analogue hydrodynamique de l'accrétion de gaz sur la proto-étoile à neutrons dans les supernovæ à effondrement de cœur. Malgré la simplicité de l'expérience par rapport à la complexité des phénomènes mis en jeu lors de l'explosion de la supernova (hydrodynamique, transfert radiatif de neutrinos, physique nucléaire pour l'équation d'état de la proto-étoile à neutrons), cette expérience permet de mettre en évidence les instabilités hydrodynamiques possiblement à l'œuvre dans les supernovæ.

Il s'agit d'une expérience en eau peu profonde, appelée fontaine aux supernovæ (exposée au Palais de la Découverte), dans laquelle les ondes de gravité de surface jouent le rôle des ondes acoustiques du gaz stellaire. Cette expérience permet de mieux appréhender le mécanisme de l'instabilité advective-acoustique SASI. Son analogue dans l'expérience, SWASI (Shallow Water Analogue of a Shock Instability), est une instabilité lié à un cycle entre ondes gravitaires et perturbations de vorticité.

Dans cette expérience, de l'eau est injectée radialement par une fente circulaire au bord externe situé à 33 cm du centre du dispositif (cf. Fig 2.4). Les paramètres expérimentaux ajustables sont le débit et la hauteur de la fente, dont les valeurs typiques sont respectivement de 1 L/s et 0.7 mm. L'eau y est injectée à un nombre de Froude super-critique : la vitesse est plus grande que la vitesse locale des vagues. Il s'agit de l'équivalent d'un écoulement astrophysique supersonique avec un nombre de Mach plus grand que l'unité. La fontaine a un fond de forme hyperbolique permettant de reproduire le potentiel gravitationnel Newtonien. L'eau tombe donc vers le centre de la

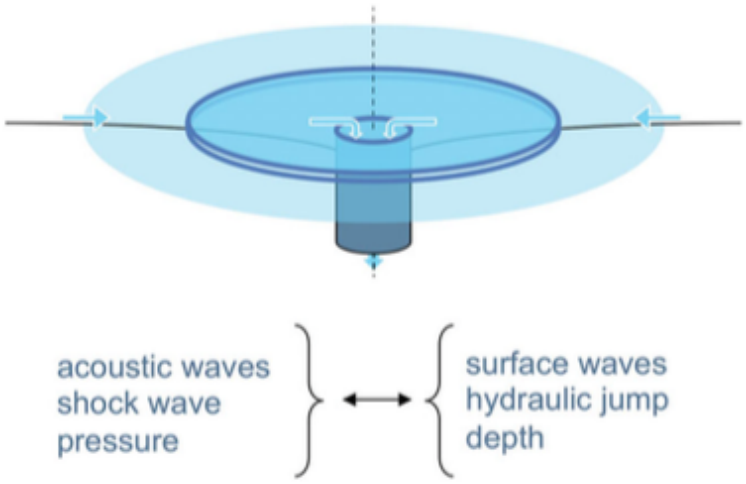

FIGURE 2.4 – Schéma de l'expérience de la fontaine aux supernovæ. L'eau est injectée vers l'intérieur depuis une fente circulaire. L'écoulement est uniforme et stationnaire. Un ressaut hydraulique est produit par la surface verticale d'un cylindre central. L'eau est évacuée en débordant par le bord supérieur de ce cylindre. Extrait de Foglizzo *et al.* (2015).

fontaine et est brutalement décélérée par un cylindre central, puis tombe par simple débordement au-dessus de ce cylindre. Il s'agit de l'analogue de l'accrétion sur la proto-étoile à neutrons et de la décélération à sa surface. Un ressaut hydraulique circulaire stationnaire se développe dans l'expérience, équivalent du choc d'accrétion stationnaire. Ce ressaut est ensuite sujet à SWASI. Notons que les rapports d'échelles de taille et de temps entre l'expérience et le cas astrophysique sont respectivement de 10^6 et 10^{-2} (choc de rayon 150 km vs ressaut de rayon 15 cm et période d'oscillation de 30 ms vs 3 s).

Bien que l'expérience reproduise une dynamique similaire au cas astrophysique (cf. Fig 2.5), il convient de souligner les limitations de l'expérience par rapport à ce dernier, même sur le plan hydrodynamique. En premier lieu, l'expérience est fondamentalement 2D cylindrique alors que l'écoulement astrophysique est 3D sphérique. De plus, il n'y a pas d'équivalent de l'entropie et donc de la poussée d'Archimède dans la fontaine. Inversement, la traînée visqueuse sur le fond de l'expérience n'a pas d'équivalent astrophysique.

2.2.3 La modélisation

Pour modéliser cette expérience, les équations d'Euler 1.1 ne sont pas appropriées. En effet, les termes de viscosité et de friction sur le fond de la fontaine sont importants et ne peuvent donc pas être négligés : l'effet

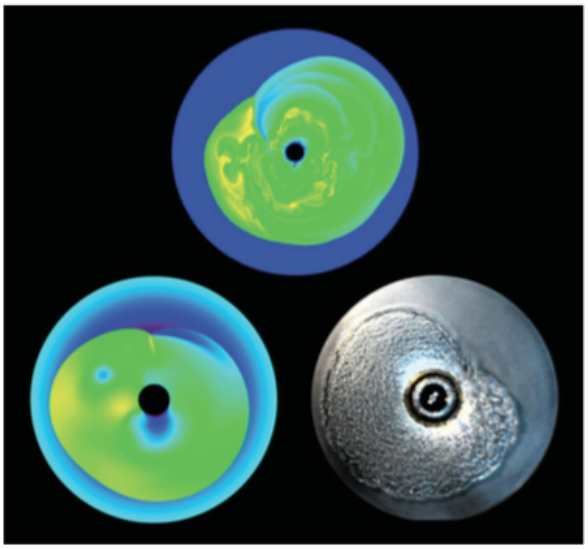

FIGURE 2.5 – La forme du ressaut hydraulique observé dans le régime non-linéaire de SWASI (droite) est similaire à la forme observée dans le modèle en eau peu profonde (gauche) et à celle de SASI dans une simulation de l'accrétion cylindrique d'un gaz avec refroidissement dû aux neutrinos. Extrait de Foglizzo *et al.* (2015).

dominant de la viscosité agit sur les gradients de vitesse dans la direction verticale, plus particulièrement dans la région la moins profonde en amont du ressaut hydraulique. De plus, la faible hauteur d'eau justifie l'approximation des équations de Saint-Venant avec une force de traînée visqueuse. Ces équations sont obtenues à partir des équations de Navier-Stokes en intégrant sur la profondeur d'eau.

On obtient alors les deux équations suivantes (écrites sous forme non conservative) :

$$\left\{ \begin{array}{lll} \partial_t H & +\nabla \cdot [H\mathbf{u}] & = 0 \\ \partial_t \mathbf{u} & +(\nabla \times \mathbf{u}) \times \mathbf{u} + \nabla \cdot \left[\frac{u^2}{2} + c^2 + \phi \right] & = \alpha \nu \frac{\mathbf{u}}{H^2} \end{array} \right. \tag{2.1}$$

avec H la hauteur d'eau, ϕ le potentiel, $\nu \simeq 0.01$ cm^2/s la viscosité cinématique de l'eau, $\alpha \simeq 3$ est un paramètre sans dimension mesuré dans l'expérience et $c = \sqrt{gH}$ est la vitesse des ondes de surface. De manière à imiter le champ de gravitation newtonien autour de l'objet central, le potentiel ϕ a un profil hyperbolique.

Ces équations sont très similaires à celles d'un gaz parfait isentropique d'indice adiabatique $\gamma = 2$ (Foglizzo *et al.* 2015) où la densité est remplacée par la hauteur de la couche d'eau H, la vitesse du son par celle des

vagues et le nombre de Mach par le nombre de Froude. Pour comparaison, le fluide astrophysique dominé par la pression de dégénérescence des électrons relativistes peut être généralement idéalisé comme un gaz parfait avec un coefficient adiabatique $\gamma = 4/3$.

Pour résoudre le système d'équations 2.1, j'ai utilisé le code `Jupiter` (de Val-Borro *et al.* 2006). Il s'agit d'un code développé dans le contexte de l'étude des disques protoplanétaires. Il résout les équations de l'hydrodynamique (avec viscosité) par une méthode de type Godunov sur une grille pouvant être cartésienne, polaire ou sphérique. Il utilise la technique des grilles emboîtées pour améliorer la résolution et est particulièrement adapté pour l'étude des interactions disques-planètes. Frédéric Masset l'a adapté pour obtenir une version résolvant les équations de Saint Venant dans une géométrie cylindrique et pouvant ainsi modéliser la fontaine aux supernovæ.

2.2.4 Résultats et perspectives

Dans la première version du prototype expérimental, la fontaine était fixe et autorisait donc l'injection de l'eau sans moment cinétique initial (analogue d'un effondrement du gaz purement radial dans le cas astrophysique). Dans ce cas, les fréquences des modes d'instabilité de SWASI obtenues dans l'expérience, dans des simulations numériques shallow water et par le calcul analytique perturbatif ont montré un excellent accord (Foglizzo *et al.* 2012).

Depuis, une nouvelle version de l'expérience a été construite, autorisant la rotation de la structure sur elle-même. Cela permet de prendre en compte l'injection d'un gaz avec un moment cinétique initial non nul et de voir son influence sur la rotation finale de l'étoile à neutrons ainsi que sur le sens de rotation des modes spiraux de l'instabilité. En effet, dans le cas d'un écoulement initial purement radial, une fois le mode asymétrique mis en place, l'expérience montre que les parties internes du flot tournent dans le sens opposé au sens de rotation des parties externes (conservant ainsi le moment cinétique global nul). Mais il a été observé que c'est aussi le cas si le flot initial a un moment cinétique faible (Foglizzo *et al.* in prep). Ces résultats expérimentaux sont à mettre en parallèle avec les résultats de Blondin et Mezzacappa (2007), qui montraient qu'une étoile en rotation pouvait donner naissance à une étoile à neutrons tournant en sens inverse par rapport à son progéniteur.

Pour pouvoir simuler cette nouvelle expérience avec rotation initiale, j'ai implémenté dans le code `jupiter` la prise en compte de ce référentiel tournant ainsi que la prise en compte de la viscosité. Nous avons ainsi pu étudier l'influence de cette rotation sur les taux de croissance et les fréquences des modes instables de SWASI. La figure 2.6 gauche montre la comparaison entre les simulations numériques shallow water et le calcul analytique perturbatif. La fréquence et le taux de croissance de l'instabilité sont en parfait accord entre simulation et calcul perturbatif, quel que soit la rotation initiale de la

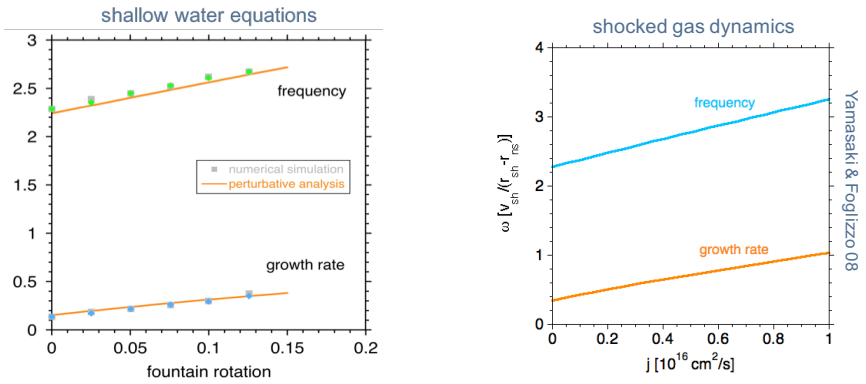

FIGURE 2.6 – Gauche : comparaison de la fréquence et des taux de croissance des modes instables de SWASI obtenus par des simulations numériques shallow water et par le calcul perturbatif. Droite : Fréquence et taux de croissance des modes instables de SASI obtenus par le calcul perturbatif. Extrait de Foglizzo *et al.* (in prep).

fontaine. Yamasaki et Foglizzo (2008) ont montré par un calcul perturbatif que dans la phase linéaire de l'instabilité, le taux de croissance de SASI croissait linéairement avec la rotation (cf. figure 2.6 droite). Les résultats shallow water de SWASI sont en accord avec cette croissance linéaire de SASI obtenue pour un gaz.

Si l'on compare à présent la simulation SWASI à l'expérience (cf. figure 2.7 gauche), les fréquences d'oscillation montrent aussi un très bon accord. Toutefois, les taux de croissance numériques sont systématiquement plus grands que ceux obtenus expérimentalement. La différence entre expérience et simulation est constant quelle que soit la vitesse de rotation de la fontaine, et vaut environ 0.2 s^{-1}. Cet écart est sans doute lié au caractère 2D du modèle de Saint-Venant. Ce modèle fait abstraction par définition de la structure verticale du flot, et ne considère qu'une vitesse moyennée, constante sur toute la hauteur d'eau. Or, le profil exact vertical de la vitesse dépend fortement de la condition de non glissement sur le fond de l'expérience, du régime turbulent ou laminaire de l'écoulement, etc. Ainsi les perturbations de vorticité, constitutives du mécanisme de l'instabilité SWASI, ne sont pas les mêmes en surface qu'en profondeur. En faisant une moyenne sur la hauteur d'eau, la vorticité obtenue est plus faible que la vorticité en surface, par le biais d'un mélange de phase (cf. figure 2.7 droite). Cette plus faible vorticité advectée lors du cycle de SWASI induit une diminution du coefficient de couplage du cycle et donc du taux de croissance de l'instabilité.

Grâce à la possibilité de prendre en compte la vitesse de rotation de l'eau à l'injection, une autre instabilité a aussi pu être mise en évidence expérimentalement. Il s'agit de l'instabilité low-T/|W|, qui comme SASI est caractérisée par des mouvements spiraux aux plus grandes échelles ($m = 1 - 2$),

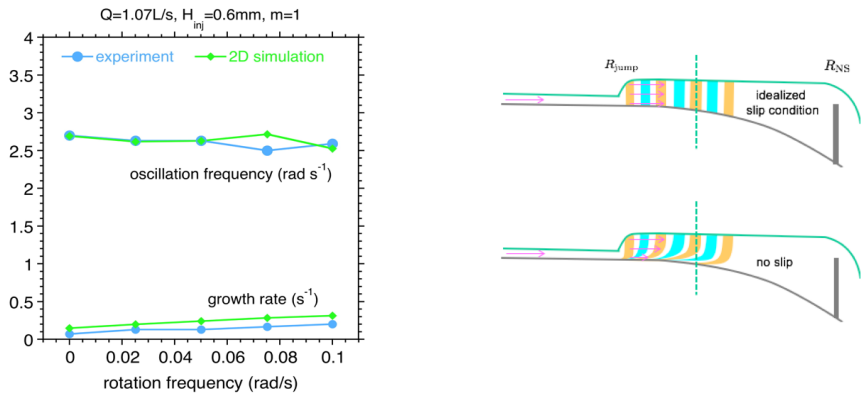

FIGURE 2.7 – Gauche : comparaison de la fréquence et des taux de croissance des modes instables de SWASI obtenus par des simulations numériques shallow water et dans l'expérience. Droite : explication possible pour le désaccord sur les taux de croissance (voir le texte pour les détails). Extrait de Foglizzo *et al.* (in prep).

mais avec l'apparition d'une spirale ouverte contrairement à SASI. Cette instabilité apparaît lorsque le rapport de l'énergie cinétique (T) sur l'énergie gravitationnelle (W) dépasse une valeur critique de l'ordre de quelques pourcents. Elle est liée à la rotation différentielle et se manifeste à la fois dans le contexte des disques (Papaloizou et Pringle 1984) et dans celui des étoiles à neutrons isolées (Shibata *et al.* 2002). Il a été suggéré que le mécanisme physique à l'origine de cette instabilité soit lié à la présence d'une zone de co-rotation dans le flot (Watts *et al.* 2005, Passamonti et Andersson 2015). Le fluide en-deça de ce rayon tournant plus rapidement que le motif spiral, les ondes acoustiques peuvent être amplifiées en échangeant de l'énergie entre les régions internes et externes. Cette instabilité possède une signature caractéristique en ondes gravitationnelles (Kuroda *et al.* 2014) et se superpose à l'instabilité SASI à grande rotation.

Lorsque l'on augmente continûment la fréquence de rotation de la fontaine, on observe expérimentalement et numériquement, le passage d'une spirale fermée de type SWASI à une spirale ouverte. La figure 2.8 montre des photos de l'expérience dans ces deux cas de figure. A grande rotation, les deux instabilités SWASI et low-T/|W| se superposent, si bien qu'il est difficile de savoir lequel des deux mécanismes domine. Un moyen d'être sûr de pouvoir analyser l'instabilité low-T/|W| consiste à se placer dans un domaine de paramètres où SWASI ne se développe pas. C'est le cas en particulier à faible nombre de Froude (Foglizzo *et al.* 2012). Dans ce régime, la seule instabilité pouvant donnant lieu à la spirale ouverte observée est donc low-T/|W|. Toutefois, le ressaut hydraulique a alors une extension radiale, on parle de ressaut ondulé (cf. figure 2.8 droite). La simulation shallow water atteint ici ses limites. En effet, dans ce modèle, le ressaut est une discontinuité n'ayant

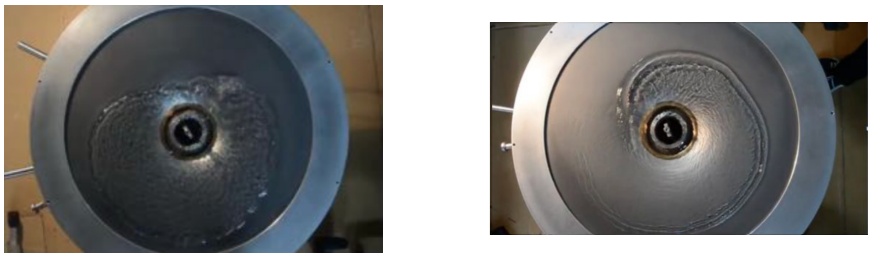

FIGURE 2.8 – Mode spiral de l'instabilité SWASI (gauche) et low-T/|W| (droite) observé expérimentalement. Extrait de Foglizzo *et al.* (in prep).

pas d'extension spatiale. Il conviendra à l'avenir d'étudier spécifiquement ce régime à bas nombre de Froude pour étudier l'instabilité low-T/|W| de manière isolée, et de comparer encore une fois expérience et simulations shallow water, pour vérifier si l'accord entre les deux approches est confirmée même dans ce régime. Une meilleure caractérisation et compréhension de ces deux instabilités, et de leur compétition dans les régimes où elles co-existent, est importante, en particulier dans la perspective d'en détecter la signature par le biais d'ondes gravitationnelles émises.

Une autre perspective sur cette thématique est l'étude d'un nouveau dispositif expérimental. En effet, une nouvelle fontaine est en cours de construction par Thierry Foglizzo et Gilles Durand. Celle-ci a un diamètre de 3.5 m, cinq fois plus grande que l'expérience actuelle. De plus, l'injection d'eau au bord externe est différente, elle ne se fera plus par une fente mais par simple débordement d'un réservoir annulaire. Le nombre de Reynolds de l'expérience étant $\mathrm{Re} = \frac{Hv}{\nu} = \frac{H^{3/2}\mathrm{Fr}\sqrt{g}}{\nu}$, à nombre de Froude fixe, le nombre de Reynolds sera augmenté d'un facteur 10 dans cette nouvelle expérience. Les effets de viscosité seront donc plus négligeables et on se rapprochera du cas astrophysique sans viscosité. Il conviendra de tester l'accord entre les simulations numériques shallow water et l'expérience dans ce nouveau régime de paramètres. Le bon accord obtenu avec le dispositif de 66 cm de diamètre correspondait à une situation où le nombre de Reynolds valait entre 480 et 3200 du bord externe au bord interne. Dans la nouvelle expérience, l'écoulement sera turbulent. La prescription pour la modélisation de la viscosité dans la simulation devra donc en particulier être évaluée pour ce nouveau dispositif.

Chapitre 3

Formation d'étoiles massives

3.1 Contexte

La formation des étoiles massives, de masse $M \gtrsim 8\ M_\odot$, font l'objet d'études approfondies à la fois d'un point de vue théorique et observationnel. Les étoiles massives sont peu nombreuses d'après la fonction de masse initiale des étoiles (Salpeter 1955). Pourtant elles jouent un rôle clé dans le cycle du milieu interstellaire (Zinnecker et Yorke 2007) car ce sont elles qui contribuent majoritairement au budget énergétique à travers leur rétroaction radiative (luminosité, pression de radiation, ionisation) et cinétique (outflows, jets, vents et explosion de supernovæ).

Les contraintes observationnelles pour les étoiles massives sont peu nombreuses car leur observation est difficile. Le temps de vie des étoiles massives est beaucoup plus court que les étoiles de faible masse, rendant leur observation plus rare. De plus, de par leur moindre proportion par rapport aux étoiles de faible masse, il est nécessaire d'observer des régions du ciel plus lointaines, pour lesquelles les instruments ont une moins bonne résolution angulaire.

Le processus de formation d'étoiles de faible masse est bien établi et peut être décrit en étapes successives (Larson 1969, André 2002). Le gaz du milieu interstellaire ($n \simeq 10^6$ cm^{-3}) s'effondre d'abord de façon isotherme (premier collapse) jusqu'à atteindre une densité de $\sim 10^{11}$ cm^{-3}. A cet instant, le gaz devient optiquement épais, l'énergie issue de de l'effondrement ne peut plus être évacuée par le rayonnement. Le premier cœur hydrostatique, appelé cœur de Larson d'environ 10 AU est formé. Ce cœur continue d'accréter l'enveloppe de gaz environnant. La contraction étant à présent adiabatique, la température du gaz augmente, jusqu'à atteindre une température de $\sim$ 2000 K, à laquelle les molécules de H_2 se dissocient. Cette réaction endothermique pompe de l'énergie gravitationnelle, entraînant le second collapse jusqu'à des densités stellaires ($\sim 10^{22}$ cm^{-3}) où le second cœur de Larson, i.e. la proto-étoile, se forme ($\sim$ 0.01 AU).

Le scénario exact de formation des étoiles massives est quant à lui encore sujet à débat. Elle se forment dans des milieux où le champ magnétique, le rayonnement, la turbulence hydrodynamique et l'interaction gaz-poussières sont simultanément à l'œuvre, rendant leur étude complexe (Tan *et al.* 2014). Une différence fondamentale avec les étoiles de faible masse vient du fait que les étoiles massives commencent leur réaction de fusion nucléaire avant d'avoir terminé leur phase d'accrétion. Les processus de rétroaction de la proto-étoile sur le milieu environnant par le biais de la pression de rayonnement ou de la photo-ionisation sont donc primordiaux.

En particulier, deux problématiques majeures sont sujets à discussion : la fragmentation initiale (les régions de formation d'étoiles massives contiennent un grand nombre de masse de Jeans) et la pression de radiation (la luminosité des étoiles massives est suffisamment élevée pour contrebalancer l'effondrement gravitationnel). Pour chacune de ces problématiques, il a été proposé différents modèles qui sont encore débattus aujourd'hui.

En ce qui concerne la fragmentation, deux modèles sont proposés. Le premier, dit de "competitive accretion" (Bonnell *et al.* 2004), considère que les nuages moléculaires se fragmentent en un grand nombre de cœurs de même faible masse, égale à la masse de Jeans. Pour des températures d'environ 10 K et des densités de 10^6 cm^{-3}, cette masse est de $M_{\rm Jeans} \simeq 1\,{\rm M}_\odot \left(\frac{T}{10\,{\rm K}}\right)^{3/2} \left(\frac{\rho}{10^{-19}\,{\rm g/cm^3}}\right)^{-1/2} \simeq 0.3$ M$_\odot$. La masse finale des étoiles est alors déterminée par les interactions dynamiques ultérieures qui ont lieu pendant la phase d'effondrement global du nuage. Dans ce scénario, les étoiles massives se forment au centre du nuage, où le potentiel gravitationnel est le plus fort et accrète le gaz et les étoiles (Smith *et al.* 2009). Les cœurs préstellaires sont donc tous initialement de faible masse, l'accrétion de masse a lieu lors de la phase stellaire et la masse finale des étoiles est plus grande que la masse initiale des cœurs.

A l'inverse, le scénario de "core accretion" (McKee et Tan 2003) considère que les étoiles massives se forment de la même manière que les étoiles de faible masse. Les cœurs issus de la fragmentation n'accrètent pas de masse du milieu environnant. La masse finale des étoiles est donc directement reliée à la masse des cœurs, les étoiles de grande masse se formant dans des cœurs eux-mêmes de grande masse. Dans ce modèle, la fonction de masse initiale est directement reliée à la fonction de masse des cœurs, comme suggéré par des observations (Könyves *et al.* 2010). Toutefois, pour des raisons de coût en temps de calcul, et contrairement au cas des étoiles de faible masse, les simulations numériques sont encore très limitées pour l'étude des étoiles massives. Elles ne couvrent qu'une partie seulement des conditions initiales et ne tiennent pas compte simultanément de tous les processus physiques à l'œuvre. En particulier, la plupart de ces modèles négligent soit le champ magnétique (Krumholz *et al.* 2007, Klassen *et al.* 2016), soit la pression de rayonnement (Peters *et al.* 2010). Peu d'études modélisent de manière cou-

plée l'influence du champ magnétique (et *a fortiori* les effets de MHD non idéale) et du transfert radiatif. Seuls Commerçon *et al.* (2011) et Myers *et al.* (2013) ont étudié le couplage de ces deux mécanismes physiques, et ont pu montré que la fragmentation est dans ce cas réduite.

Une différence fondamentale entre les mécanismes de formation des étoiles de faible et de grande masse provient de la rétroaction due au rayonnement de la proto-étoile. La forte pression radiative issue de l'étoile peut contrebalancer l'effondrement gravitationnel. Elle empêche alors la formation d'étoiles de grande masse, en supposant un fort couplage entre les poussières, sur lesquelles agit la pression radiative, et le gaz. Des estimations analytiques 1D montrent que la masse stellaire maximale que l'on puisse former est de l'ordre de 20 $M_\odot$ (Larson et Starrfield 1971, Hennebelle et Commerçon 2014). Des simulations numériques mono-dimensionnelles ont aussi confirmé ces résultats (Kuiper *et al.* 2010). Pourtant, des étoiles jusqu'à 150 $M_\odot$, voire plus, sont observées (Figer 2005, Crowther *et al.* 2010; 2016). Il a fallu attendre les premières simulations bi-dimensionnelles pour trouver un mécanisme permettant de s'affranchir de cette barrière de pression radiative. Ces simulations ont montré que l'accrétion sur l'étoile massive se faisait de manière anisotrope : le gaz est principalement accrété via le disque (où l'opacité est plus grande), et une éjection de matière d'origine radiative a lieu perpendiculairement à ce disque. C'est le modèle de "disk-accretion" et le "flashlight effect" (Yorke et Sonnhalter 2002, Kuiper *et al.* 2010). Cette anisotropie permet de dépasser la limite des 20 $M_\odot$ puisque ces études obtiennent des étoiles de 30 $M_\odot$ et même 150 $M_\odot$. Les premières simulations 3D furent menées par Krumholz *et al.* (2007) et Krumholz *et al.* (2009). Elles mirent en évidence des instabilités de Rayleigh-Taylor se développant à l'interface de la bulle radiative se propageant perpendiculairement au disque. Ces instabilités permettent à du gaz dense d'atteindre l'objet central et contribue à environ 40 % de la masse totale accrétée. Les différents auteurs utilisant des approximations pour le transfert radiatif distinctes, ces résultats font toujours l'objet de controverses (Kuiper *et al.* 2012, Rosen *et al.* 2016) et il n'est pas clair de savoir quel est le mécanisme dominant. De plus, aucune de ces études n'inclut la présence de champ magnétique.

3.2 Ma contribution

Nous avons réalisé les premières simulations d'effondrement de cœurs massifs en tenant compte des effets de la MHD non-idéale, via les processus de diffusion ambipolaire, du transfert radiatif et de la rétroaction de la proto-étoile.

Les conditions initiales que nous avons prises sont similaires à des travaux antérieurs (Krumholz *et al.* 2009, Kuiper *et al.* 2010). Nous considérons un cœur dense massif isolé de température uniforme $T_0 = 20$ K, de masse $M_0 =$

100 $M_\odot$ et de rayon $r_0 = 0.2$ pc. La densité suit un profil $\rho(r) = \frac{\rho_c}{(1+r/r_c)^2}$ avec un plateau central de rayon $r_c = 0.02$ pc et de densité $\rho_c = 7.78 \times 10^{-18}$ g/cm^3. Le temps de chute libre au centre vaut donc $t_{\rm ff} = \sqrt{\frac{3\pi}{32G\rho_c}} \simeq 2.1 \times 10^5 \text{ years} \left(\frac{\rho_c}{10^{-19}\,\text{g/cm}^3}\right)^{-1/2} \simeq 24$ kyr. Ce cœur tourne en rotation solide autour de l'axe x, de façon suffisamment lente ($\Omega_0 = 3 \times 10^{-15}$ Hz, $\Omega_0 t_{\rm ff} \simeq 2 \times 10^{-3}$) pour éviter une trop grande fragmentation. Le champ magnétique est considéré uniforme et aligné avec l'axe de rotation. Sa valeur est choisie telle que le rapport entre le "mass-to-flux ratio" $(M/\phi)_0 = M_0/(\pi B_0 r_0^2)$ du nuage et le ratio critique $(M/\phi)_{\rm crit} = \frac{0.53}{3\pi}\left(\frac{5}{G}\right)^{1/2}$ (Mouschovias et Spitzer 1976), soit égal à $\mu = \frac{(M/\phi)_0}{(M/\phi)_{\rm crit}} = 2$. Cela correspond à une valeur $B_0 \sim 170$ μG. La résolution numérique maximum atteinte dans nos simulations est de 5 AU, avec une grille AMR dont les niveaux vont de 6 à 15. Le critère de raffinement utilisé est d'un minimum de 10 cellules pour échantillonner la longueur de Jeans. N'ayant pas assez de résolution pour modéliser la proto-étoile directement, il est nécessaire d'utiliser des modèles sous-mailles. Nous utilisons pour cela des particules puits (Bleuler et Teyssier 2014) avec un rayon d'accrétion de 20 AU. La rétroaction de ces particules puits sur le gaz est prise en compte par l'intermédiaire d'une luminosité interne prescrite par des modèles d'évolution proto-stellaires (Hosokawa *et al.* 2010, Kuiper et Yorke 2013).

Pour mettre en évidence les effets de la MHD non-idéale, nous avons utilisé trois modèles : un purement hydrodynamique (HYDRO), un en MHD idéale (iMHD) et un tenant compte de la diffusion ambipolaire (AD). Je détaille ci-après les résultats obtenus.

La figure 3.1 montre les coupes de densité dans le plan du disque. La simulation HYDRO produit un système binaire en interaction. Les deux objets sont à une distance d'environ 250 AU l'un de l'autre et ont une masse d'environ 23 $M_\odot$ et 10 $M_\odot$. Il existe en fait une troisième particule puits dans cette simulation. Elle n'est pas visible sur l'image zoomée car elle a été éjectée du système binaire à très grande distance. Les simulations incluant le champ magnétique ne forment à la fin qu'une étoile isolée. On peut toutefois noter qu'à des temps intermédiaires d'autres particules puits sont créées (cf. Fig 3.1 pour la simulation MHD à 65 kyr). Mais celles-ci ne survivent pas longtemps et finissent par fusionner rapidement avec la particule puits initiale lorsqu'elle s'en approche.

Il convient de remarquer que dans le cas de la simulation iMHD, le plan du disque a subi une rotation de 90^o par rapport à la configuration initiale. La coupe est en effet faite dans le plan (xy) et non (yz) comme pour les deux autres simulations. L'axe de rotation n'est donc plus (x) mais (y). Une analyse de la simulation aux premiers instants permet de comprendre cette rotation. Dans le modèle de MHD idéale, le champ magnétique est gelé dans la matière. Lors de l'effondrement gravitationnel, la densité augmente

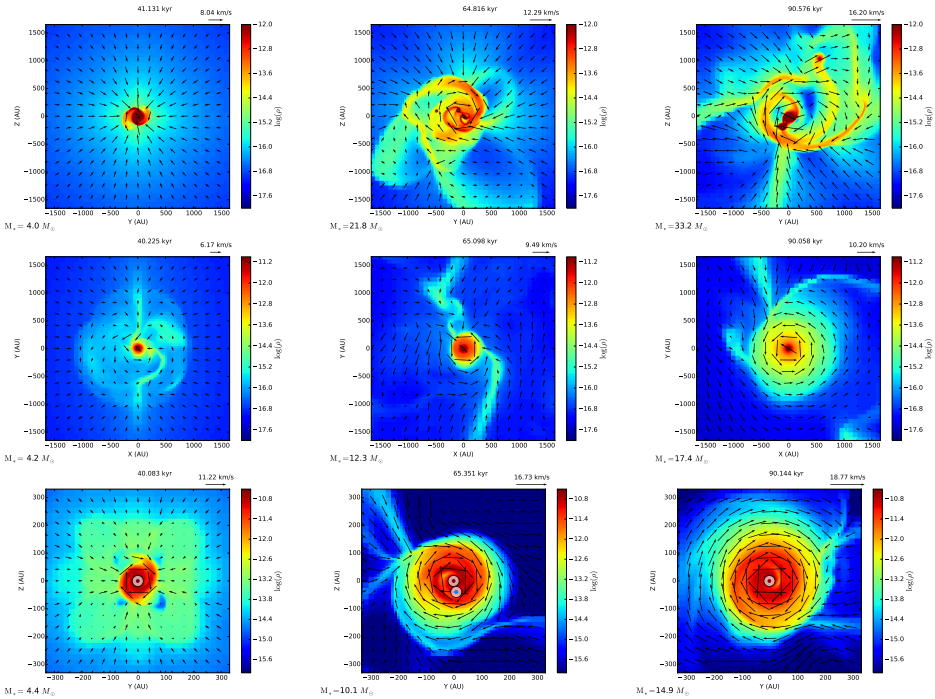

FIGURE 3.1 – Cartes de densité dans le plan du disque pour les modèles hydrodynamique, MHD idéale et MHD non idéale (de haut en bas). Chaque colonne correspond à un temps différent : $t \sim 40$ kyr (gauche), $t \sim 65$ kyr (milieu) et $t \sim 90$ kyr (droite). Les flèches correspondent à la vitesse dans le plan. La masse $M_\star$ correspond à la masse de la particule puits. Extrait de Commerçon *et al.* (in prep).

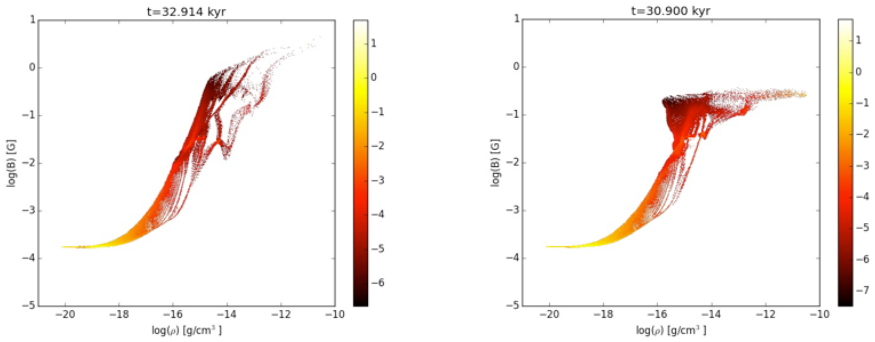

FIGURE 3.2 – Champ magnétique en fonction de la densité pour toutes les cellules des simulations MHD idéale (gauche) et MHD non idéale (droite). La couleur indique la masse contenue dans un pixel (ρ, B) donné. Extrait de Commerçon *et al.* (in prep).

et l'intensité du champ magnétique aussi. Dans un cas mono-dimensionnel, par conservation du flux, on a $B \propto \rho^{2/3}$. Le champ magnétique obtenu près de la proto-étoile est donc très élevé (∼2 G, cf. Fig 3.2 gauche). Cette accumulation donne lieu à une instabilité d'interchange (Krasnopolsky *et al.* 2012, Masson *et al.* 2016) qui est à l'origine d'une complète redistribution du moment cinétique, se traduisant ici par un changement de l'axe de rotation. Si l'on prend en compte la diffusion ambipolaire, le champ magnétique est diffusé et la valeur maximale atteinte près de la proto-étoile est diminué d'un ordre de grandeur (cf. Fig 3.2 droite). Cette plus faible valeur n'est plus à même de générer d'instabilité d'interchange. On observe de plus un plateau à une valeur d'environ 0.3 G, ce qui est cohérent avec des simulations de formation d'étoiles de faible masse (Masson *et al.* 2016).

La figure 3.3 montre les densités et vitesses des disques obtenus. Nous définissons ici le disque comme une structure supportée rotationnelle, ce qui n'est pas le cas de toute la structure à haute densité apparaissant dans la figure 3.4 par exemple (on parle alors de pseudo-disque). Pour qu'une cellule de la simulation appartienne au disque, il faut qu'elle satisfasse plusieurs critères (Joos *et al.* 2012) : une densité élevée ($\rho > 10^{-15}$ g/cm^3), une vitesse azimuthale élevée ($v_\phi > 2v_r$ et $v_\phi > 2v_z$) et un support rotationnel plus grand que le support thermique ($\rho v_\phi^2 > P$). Le disque obtenu dans le cas de la MHD idéale est épais ($h \sim 100$ AU) et grand ($R \sim 500$ AU). A l'inverse, lorsque la diffusion ambipolaire est prise en compte, le disque se rapproche plus d'une structure comme celle obtenue dans le cas hydrodynamique : fine ($h \sim 40$ AU) et plus petite ($R \sim 200$ AU). Si on étudie de plus le rapport entre la pression thermique et la pression magnétique ($\beta = 2P/B^2$) dans le disque, on obtient des valeurs de l'ordre de 0.1 dans le cas de MHD idéale et de 100 avec diffusion ambipolaire. Dans ce cas, la structure est donc

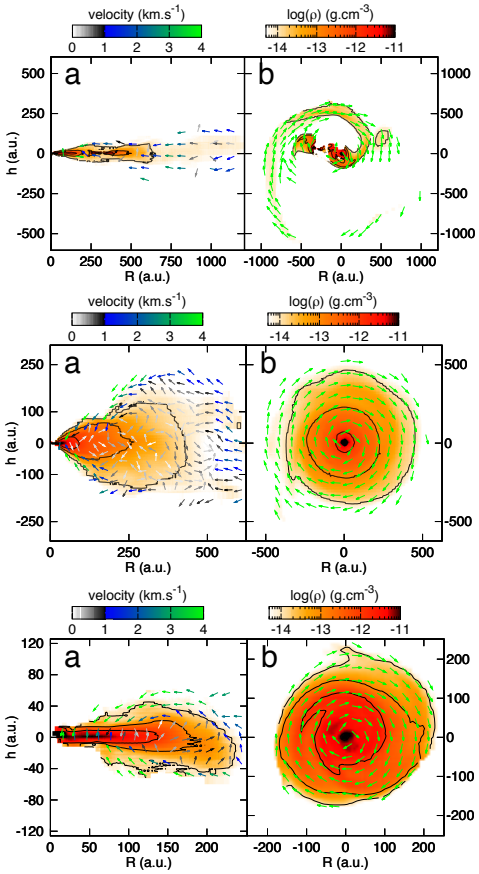

FIGURE 3.3 – Propriétés (densité et vitesses) des disques dans les trois modèles simulés : hydro (haut), MHD idéale (milieu), MHD non idéale (bas). Extrait de Commerçon *et al.* (in prep).

supportée par la pression thermique et non par le champ magnétique.

La figure 3.4 montre les mêmes coupes de densité que la figure 3.1 mais dans le plan perpendiculaire au disque. Elle met en évidence la présence claire d'un outflow dans la simulation avec diffusion ambipolaire, contrairement aux deux autres simulations. Cet outflow atteint une distance de 80 000 AU avec une vitesse maximum de 40 km/s. L'étude du champ magnétique autour de la proto-étoile montre que les lignes de champ sont principalement toroïdales. L'outflow est donc confiné par ce champ magnétique toroïdal. Nous avons aussi comparé les masses de l'outflow à celle du disque et de l'étoile. Pour cela, nous avons considéré qu'une cellule de la simulation appartenait à l'outflow si la vitesse radiale était plus grande que la vitesse de libération à cette position : $v_r > \sqrt{2GM_\star/r}$. En appliquant ce critère, on trouve que l'outflow dans la simulation MHD idéale a une masse négligeable ($M \simeq 10^{-3}\ M_\odot$). En revanche, dans la simulation avec diffusion ambipolaire, cette masse est bien

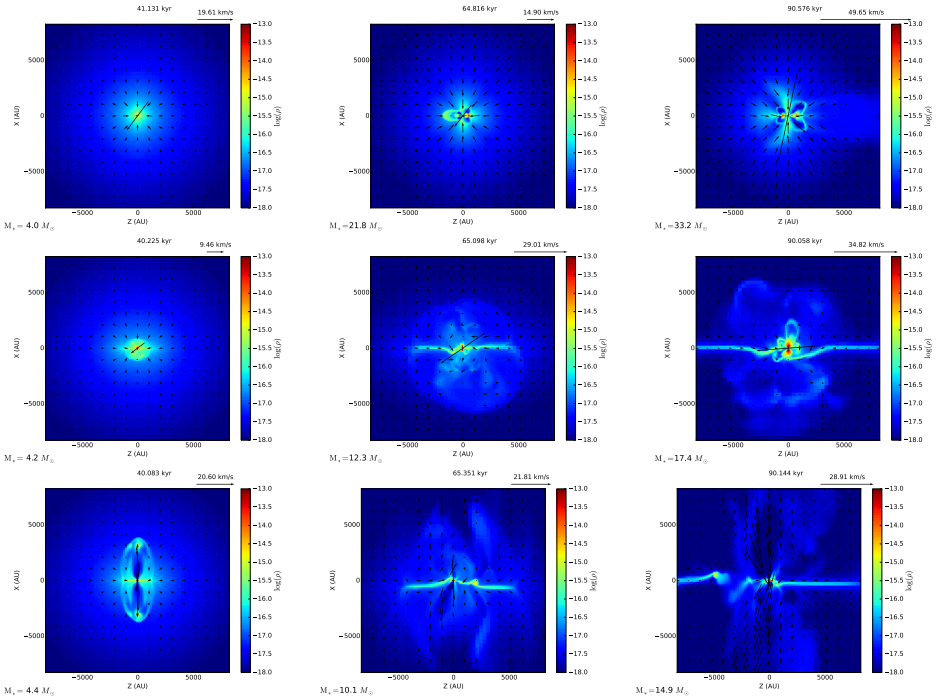

FIGURE 3.4 – Comme Fig. 3.1 mais dans le plan perpendiculaire au disque. Extrait de Commerçon *et al.* (in prep).

plus importante car elle vaut 1.9 $M_\odot$ à $t = 50$ kyr et 13.2 $M_\odot$ à $t = 90$ kyr. Alors que celle du disque vaut 3.4 $M_\odot$ et 7.2 $M_\odot$ aux mêmes instants. Cela signifie que la masse de l'outflow est d'abord plus faible que celle du disque mais augmente plus rapidement pour la dépasser vers 60 kyr.

La figure 3.5 illustre pour les deux simulations avec champ magnétique le rapport entre les forces radiatives, gravitationnelle et magnétique dans la région proche de la proto-étoile. La colonne de gauche montre que dans les deux cas la force radiative domine sur la force gravitationnelle. En revanche, d'après la colonne de droite, alors que dans le cas de MHD idéale, la force radiative domine la force magnétique, c'est l'inverse lorsque l'on tient compte de la diffusion ambipolaire. Dans ce cas, la force radiative contribue donc à la formation de l'outflow mais n'est pas la force dominante. Enfin, nous n'observons pas d'instabilités de Rayleight-Taylor radiatives dans l'outflow..

3.3 Perspectives

Ces premières simulations montrent que la prise en compte de la diffusion ambipolaire est primordiale pour bien modéliser la formation du disque et de l'outflow associé à la proto-étoile massive. Les limitations du modèle de MHD idéale sont encore plus mises en lumière que dans le cas de la formation des

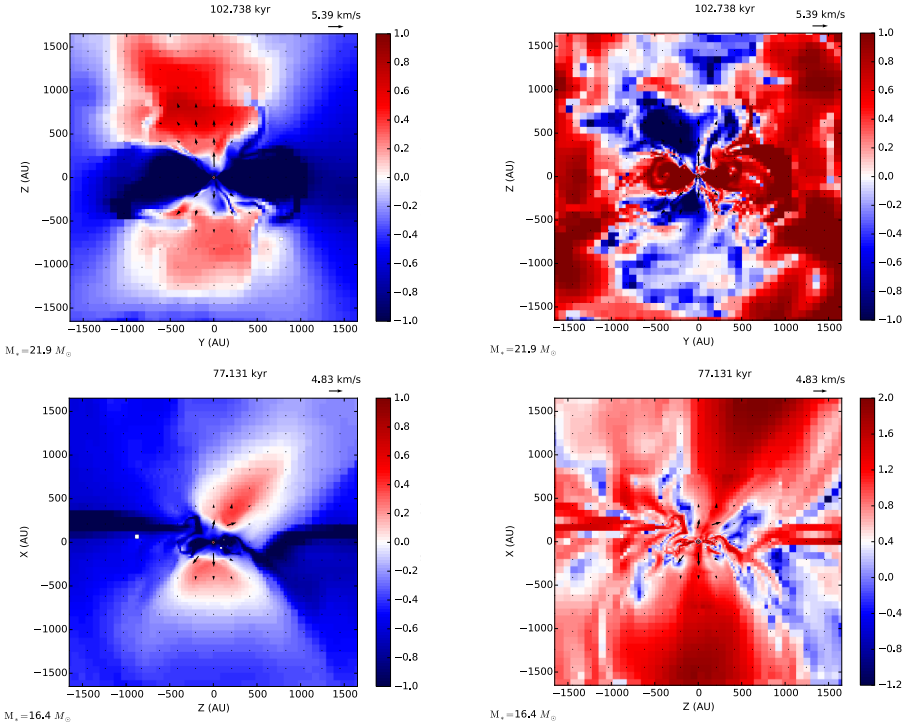

FIGURE 3.5 – Origine de l'outflow. Logarithme du rapport entre la force radiative et la force gravitationnelle (gauche) et entre la force de Lorentz et la force radiative (droite) dans le cas MHD idéale (haut) et avec diffusion ambipolaire (bas). Extrait de Commerçon *et al.* (in prep).

étoiles de faible masse : le champ magnétique s'accumule autour de la proto-étoile en formation donnant naissance à l'instabilité d'interchange (Masson *et al.* 2016).

Il convient toutefois de souligner les limitations inhérentes à nos simulations. En particulier, nous ne tenons pas compte de la turbulence et surtout l'irradiation des proto-étoiles n'est pas traitée de façon distincte. Or, Kuiper et Klessen (2013) a montré l'importance de bien prendre en compte cette irradiation dans le cas de disques circumstellaires irradiés par une étoile. C'est sur ce dernier point que je compte m'investir à l'avenir.

J'ai participé à l'inclusion d'une telle méthode d'irradiation dans le code `PLUTO` afin de réaliser les premières simulations 3D magnéto-hydrodynamiques radiatives d'un disque protoplanétaire stratifié, incluant de manière auto-consistante l'instabilité magnéto-rotationnelle et l'irradiation due à l'étoile centrale (Flock *et al.* 2013b). Le but est d'inclure ce même type de méthode dans le code `RAMSES`.

Pour cela, nous pourrons dans un premier temps utiliser le module FLD multigroupe que j'ai déjà développé (González *et al.* 2015). En effet, les photons stellaires peuvent être traités comme un groupe à part entière, pour lequel le terme d'émission n'est présent que pour la particule puits, ces photons étant absorbés partout ailleurs dans la simulation. Une fois absorbés, ils sont ré-émis dans le deuxième groupe (correspondant physiquement au groupe des photons infrarouges émis par le disque). Dans une seconde étape, il sera intéressant de traiter les photons "stellaires" par l'intermédiaire du module `RAMSES-RT` (Rosdahl et Teyssier 2015). Ce module a été développé pour l'étude de l'ionisation dans un contexte cosmologique. Il est fondé sur le modèle M1 avec un schéma explicite en temps et l'approximation de la vitesse de la lumière réduite (Gnedin et Abel 2001), afin d'éviter des limitations de pas de temps trop restrictives. Le modèle M1 étant bien approprié pour les situations anisotropes ou d'ombres (González *et al.* 2007), ce module est particulièrement adapté pour les photons stellaires émis dans un environnement fortement inhomogène avec la présence d'un disque circumstellaire.

Un autre avantage d'utiliser `RAMSES-RT` sera de pouvoir naturellement tenir compte de la formation de la région HII dans les phases avancées de la proto-étoile massive. En effet, un module de thermo-chimie hors équilibre permet de suivre l'ionisation de l'hydrogène et de l'hélium (Geen *et al.* 2015). Les effets d'ionisation, de rétroaction proto-stellaire et du champ magnétique seront alors traités pour la première fois de façon couplée.

Enfin, il est important que toutes ces études numériques se fassent en lien avec la communauté des observateurs. Nos résultats de simulations seront mis à la disposition de la communauté à travers la base de données actuellement développée à AIM (projet ANAIS financé par la Région Île-de-France). Cette base de données donnera accès aux résultats de simulations brutes mais il sera aussi possible de faire des observations synthétiques en post-traitement. Je compte m'investir dans des collaborations avec des observateurs pour ren-

forcer les synergies entre modélisation et observation, en particulier pour la préparation et l'interprétation des observations des instruments de nouvelle génération (ALMA, NOEMA, JWST).

Conclusion

J'ai détaillé dans ce manuscrit les trois volets de ma recherche : développement numérique, applications en astrophysique de laboratoire et applications en formation d'étoiles.

J'ai activement développé les outils numériques que j'utilise, que ce soit le code `HERACLES` ou `RAMSES`, en me focalisant sur les modules de transfert radiatif. Ces codes sont parallélisés et permettent d'utiliser les moyens de calculs nationaux de façon efficace.

Dans la première partie de ma carrière, j'ai utilisé `HERACLES` pour l'étude des chocs radiatifs. En plus d'études purement théoriques, j'ai également participé à la modélisation d'expériences de chocs radiatifs menées auprès des installations de lasers de puissance.

J'ai eu par la suite l'opportunité d'être associé à la modélisation d'une autre expérience en laboratoire : la fontaine aux supernovæ SWASI. J'utilise pour cela un code d'hydrodynamique de type shallow water.

Enfin, depuis quelques années, je me suis investi dans la recherche sur la formation d'étoiles. J'ai pour cela importé des développements que j'avais fait dans `HERACLES` (transfert multigroupe) dans le code `RAMSES` pour les utiliser dans la thématique de la formation des étoiles massives.

A l'avenir, j'aimerai principalement continuer de mener de front le développement numérique et ma recherche sur la thématique de la formation d'étoiles. En ce qui concerne le premier axe, le passage à l'exascale dans les cinq prochaines années reste un défi majeur. Il convient de développer dès à présent les codes numériques qui pourront être utilisés sur les nouvelles machines. C'est le sens du développement de la plateforme `CanoP`. Quant à la seconde thématique, de grandes améliorations sur le traitement du rayonnement issu de l'étoile massive en formation sont nécessaires et permettront de répondre à certaines des questions encore ouvertes sur les mécanismes exacts de formation de ces étoiles.

Bibliographie

P. André : The Initial Conditions for Protostellar Collapse : Observational Constraints. *In* J. Bouvier et J.-P. Zahn, éditeurs : *EAS Publications Series*, volume 3 de *EAS Publications Series*, pages 1–38, 2002.

P. Anninos, P. C. Fragile et S. D. Murray : Cosmos : A Radiation-Chemo-Hydrodynamics Code for Astrophysical Problems. *ApJS*, 147:177–186, juillet 2003.

D. Aubert, N. Deparis et P. Ocvirk : EMMA : an adaptive mesh refinement cosmological simulation code with radiative transfer. *MNRAS*, 454:1012–1037, novembre 2015.

Dominique Aubert et Romain Teyssier : A radiative transfer scheme for cosmological reionization based on a local Eddington tensor. *Monthly Notices of the Royal Astronomical Society*, 387(1):295–307, jun 2008. ISSN 0035-8711. URL http://doi.wiley.com/10.1111/j.1365-2966.2008.13223.x.

Edouard Audit et Patrick Hennebelle : Thermal condensation in a turbulent atomic hydrogen flow. *Astronomy and Astrophysics*, 433(1):1–13, apr 2005. ISSN 0004-6361. URL http://adsabs.harvard.edu/abs/2005A{&}A...433....1A.

A. Bleuler et R. Teyssier : Towards a more realistic sink particle algorithm for the RAMSES CODE. *MNRAS*, 445:4015–4036, décembre 2014.

J. M. Blondin et A. Mezzacappa : Pulsar spins from an instability in the accretion shock of supernovae. *Nature*, 445:58–60, janvier 2007.

J. M. Blondin, A. Mezzacappa et C. DeMarino : Stability of Standing Accretion Shocks, with an Eye toward Core-Collapse Supernovae. *ApJ*, 584:971–980, février 2003.

I. A. Bonnell, S. G. Vine et M. R. Bate : Massive star formation : nurture, not nature. *MNRAS*, 349:735–741, avril 2004.

S. Bouquet, C. Stéhlé, M. Koenig, J.-P. Chièze, A. Benuzzi-Mounaix, D. Batani, S. Leygnac, X. Fleury, H. Merdji, C. Michaut, F. Thais, N. Grandjouan, T. Hall, E. Henry, V. Malka et J.-P. J. Lafon : Observation of Laser Driven Supercritical Radiative Shock Precursors. *Physical Review Letters*, 92(22):225001, juin 2004.

J. C. Bozier, G. Thiell, J. P. Le Breton, S. Azra et M. Decroisett : Experimental observation of a radiative wave generated in xenon by a laser-driven supercritical shock. *Physical Review Letters*, 57:1304–1307, septembre 1986.

Carsten Burstedde, Lucas C. Wilcox et Omar Ghattas : `p4est` : Scalable algorithms for parallel adaptive mesh refinement on forests of octrees. *SIAM Journal on Scientific Computing*, 33(3):1103–1133, 2011.

N. Calvet et E. Gullbring : The Structure and Emission of the Accretion Shock in T Tauri Stars. *ApJ*, 509:802–818, décembre 1998.

M. Chadid : Irregularities in atmospheric pulsations of RR Lyrae stars. *A&A*, 359:991–997, juillet 2000.

Benoît Commerçon : *Formation d'étoiles : étude de l'effondrement des coeurs prestellaires*. Thèse de doctorat, Ecole Normale Supérieure de Lyon, 2009. URL http://prunel.ccsd.cnrs.fr/tel-00442045/.

Benoît Commerçon, Edouard Audit, Gilles Chabrier et J.-P. Chièze : Physical and radiative properties of the first-core accretion shock. *Astronomy & Astrophysics*, 530:A13, apr 2011. ISSN 0004-6361. URL http://www.aanda.org/articles/aa/full{_}html/2011/06/aa16213-10/aa16213-10.htmlhttp://www.aanda.org/10.1051/0004-6361/201016213.

B. Commerçon, M. González et N. Vaytet : Massive star formation : fragmentation, disk and outflow. in prep.

P. A. Crowther, S. M. Caballero-Nieves, K. A. Bostroem, J. Maíz Apellániz, F. R. N. Schneider, N. R. Walborn, C. R. Angus, I. Brott, A. Bonanos, A. de Koter, S. E. de Mink, C. J. Evans, G. Gräfener, A. Herrero, I. D. Howarth, N. Langer, D. J. Lennon, J. Puls, H. Sana et J. S. Vink : The R136 star cluster dissected with Hubble Space Telescope/STIS. I. Far-ultraviolet spectroscopic census and the origin of He II λ1640 in young star clusters. *MNRAS*, 458:624–659, mai 2016.

P. A. Crowther, O. Schnurr, R. Hirschi, N. Yusof, R. J. Parker, S. P. Goodwin et H. A. Kassim : The R136 star cluster hosts several stars whose individual masses greatly exceed the accepted 150M$_{solar}$ stellar mass limit. *MNRAS*, 408:731–751, octobre 2010.

S. W. Davis, J. M. Stone et Y.-F. Jiang : A Radiation Transfer Solver for Athena Using Short Characteristics. *ApJS*, 199:9, mars 2012.

M. de Val-Borro, R. G. Edgar, P. Artymowicz, P. Ciecielag, P. Cresswell, G. D'Angelo, E. J. Delgado-Donate, G. Dirksen, S. Fromang, A. Gawryszczak, H. Klahr, W. Kley, W. Lyra, F. Masset, G. Mellema, R. P. Nelson, S.-J. Paardekooper, A. Peplinski, A. Pierens, T. Plewa, K. Rice, C. Schäfer et R. Speith : A comparative study of disc-planet interaction. *MNRAS*, 370:529–558, août 2006.

L. Dessart, D. J. Hillier et E. Audit : Explosion of red-supergiant stars : influence of the atmospheric structure on shock breakout and the early-time supernova radiation. *ArXiv e-prints*, avril 2017.

A. Dizière, C. Michaut, M. Koenig, C. D. Gregory, A. Ravasio, Y. Sakawa, Y. Kuramitsu, T. Morita, T. Ide, H. Tanji, H. Takabe, P. Barroso et J.-M. Boudenne : Highly radiative shock experiments driven by GEKKO XII. *Ap&SS*, 336:213–218, novembre 2011.

F. W. Doss, H. F. Robey, R. P. Drake et C. C. Kuranz : Wall shocks in high-energy-density shock tube experiments. *Physics of Plasmas*, 16 (11):112705, novembre 2009.

R. P. Drake : Radiative Shocks in Astrophysics and the Laboratory. *Ap&SS*, 298:49–59, juillet 2005.

B. Dubroca et J. Feugeas : Etude théorique et numérique d'une hiérarchie de modèles aux moments pour le transfert radiatif. *Academie des Sciences Paris Comptes Rendus Serie Sciences Mathematiques*, 329:915–920, novembre 1999.

Y. A. Fadeyev et D. Gillet : The structure of radiative shock waves. II. The multilevel hydrogen atom. *A&A*, 354:349–364, février 2000.

Y.A. Fadeyev et D Gillet : The structure of radiative shock waves I. The method of global iterations. *Astronomy & Astrophysics*, 333:687–701, 1998. URL http://arxiv.org/abs/astro-ph/9802073.

D. F. Figer : An upper limit to the masses of stars. *Nature*, 434:192–194, mars 2005.

X. Fleury, S. Bouquet, C. Stehlé, M. Koenig, D. Batani, A. Benuzzi-Mounaix, J.-P. Chièze, N. Grandjouan, J. Grenier, T. Hall, E. Henry, J.-P. Lafon, S. Leygnac, V. Malka, B. Marchet, H. Merdji, C. Michaut et F. Thais : A laser experiment for studying radiative shocks in astrophysics. *Laser and Particle Beams*, 20:263–268, avril 2002.

M. Flock, S. Fromang, M. González et B. Commerçon : First Radiation Magnetohydrodynamic Global Simulations Of Protoplanetary Disks. *In Protostars and Planets VI Posters*, page 52, juillet 2013a.

M. Flock, S. Fromang, M. González et B. Commerçon : Radiation magnetohydrodynamics in global simulations of protoplanetary discs. *A&A*, 560:A43, décembre 2013b.

T. Foglizzo, P. Galletti, L. Scheck et H.-T. Janka : Instability of a Stalled Accretion Shock : Evidence for the Advective-Acoustic Cycle. *ApJ*, 654:1006–1021, janvier 2007.

T. Foglizzo, M. González et R. Kazeroni : Asymmetric instabilities during the collapse of a rotating stellar core : shallow water experiment and modeling. in prep.

T. Foglizzo, R. Kazeroni, J. Guilet, F. Masset, M. González, B. K. Krueger, J. Novak, M. Oertel, J. Margueron, J. Faure, N. Martin, P. Blottiau, B. Peres et G. Durand : The Explosion Mechanism of Core-Collapse Supernovae : Progress in Supernova Theory and Experiments. *PASA*, 32:9, mars 2015.

Thierry Foglizzo, Frédéric Masset, Jérôme Guilet et Gilles Durand : Shallow Water Analogue of the Standing Accretion Shock Instability : Experimental Demonstration and a Two-Dimensional Model. *Physical Review Letters*, 108(5):051103, jan 2012. ISSN 0031-9007. URL http://arxiv.org/abs/1112.3448http://link.aps.org/doi/10.1103/PhysRevLett.108.051103.

M. Frank, C. D. Hauck et E. Olbrant : Perturbed, Entropy-Based Closure for Radiative Transfer. *ArXiv e-prints*, août 2012.

S. Geen, P. Hennebelle, P. Tremblin et J. Rosdahl : Photoionization feedback in a self-gravitating, magnetized, turbulent cloud. *MNRAS*, 454: 4484–4502, décembre 2015.

Nickolay Y. Gnedin et Tom Abel : Multi-dimensional cosmological radiative transfer with a Variable Eddington Tensor formalism. *New Astronomy*, 6(7):437–455, oct 2001. ISSN 13841076. URL http://arxiv.org/abs/astro-ph/0106278.

M. González, E. Audit et P. Huynh : HERACLES : a three-dimensional radiation hydrodynamics code. *A&A*, 464:429–435, mars 2007.

M. González, E. Audit et C. Stehlé : 2D numerical study of the radiation influence on shock structure relevant to laboratory astrophysics. *A&A*, 497:27–34, avril 2009.

M. González, N. Vaytet, E. Audit et G. Chabrier : The Influence of Frequency-dependent Radiative Transfer on Radiative Shock Precursors. *In* N. V. Pogorelov, E. Audit et G. P. Zank, éditeurs : *8th International Conference of Numerical Modeling of Space Plasma Flows (ASTRONUM 2013)*, volume 488 de *Astronomical Society of the Pacific Conference Series*, page 71, septembre 2014.

M. González, N. Vaytet, B. Commerçon et J. Masson : Multigroup radiation hydrodynamics with flux-limited diffusion and adaptive mesh refinement. *A&A*, 578:A12, juin 2015.

Matthias González, Edouard Audit et Philippe Huynh : HERACLES : a three-dimensional radiation hydrodynamics code. *Astronomy & Astrophysics*, 464:429–435, 2007.

Matthias González, C. García-Fernández et Pedro Velarde : 2D numerical comparison between Sn and M1 radiation transport methods. *Annals of Nuclear Energy*, 36(7):886–895, 2009. URL http://linkinghub.elsevier.com/retrieve/pii/S0306454909001042.

J. Guilet et T. Foglizzo : On the linear growth mechanism driving the standing accretion shock instability. *MNRAS*, 421:546–560, mars 2012.

J. E. Gunn et J. P. Ostriker : On the Nature of Pulsars. III. Analysis of Observations. *ApJ*, 160:979, juin 1970.

T. Heinemann, W. Dobler, Å. Nordlund et A. Brandenburg : Radiative transfer in decomposed domains. *A&A*, 448:731–737, mars 2006.

P. Hennebelle et B. Commerçon : Theories of the Massive Star Formation : A (Short) Review. *In* D. Stamatellos, S. Goodwin et D. Ward-Thompson, éditeurs : *The Labyrinth of Star Formation*, volume 36 de *Astrophysics and Space Science Proceedings*, page 365, 2014.

G. Hobbs, D. R. Lorimer, A. G. Lyne et M. Kramer : A statistical study of 233 pulsar proper motions. *MNRAS*, 360:974–992, juillet 2005.

T. Hosokawa, H. W. Yorke et K. Omukai : Evolution of Massive Protostars Via Disk Accretion. *ApJ*, 721:478–492, septembre 2010.

L. Ibgui, L. de Sá, C. Stehlé, J.-P. Chièze, S. Orlando, I. Hubeny, T. Lanz, T. Matsakos, M. González et R. Bonito : 3D Gray Radiative Properties of a Radiation Hydrodynamic Model of a YSO Accretion Shock. *In* N. V. Pogorelov, E. Audit et G. P. Zank, éditeurs : *8th International Conference of Numerical Modeling of Space Plasma Flows (ASTRONUM 2013)*, volume 488 de *Astronomical Society of the Pacific Conference Series*, page 83, septembre 2014a.

L. Ibgui, M. González, C. Stehlé, I. Hubeny et T. Lanz : 3D modeling of accretion shocks in young stellar objects : Simulation of laboratory experiments. *In* C. Stehlé, C. Joblin et L. d'Hendecourt, éditeurs : *EAS Publications Series*, volume 58 de *EAS Publications Series*, pages 149–154, février 2012a.

L. Ibgui, I. Hubeny, T. Lanz et C. Stehlé : IRIS : a generic three-dimensional radiative transfer code. *A&A*, 549:A126, janvier 2013a.

L. Ibgui, I. Hubeny, T. Lanz, C. Stehlé, M. González et J.-P. Chièze : 3D numerical simulations of laboratory models of accretion shocks in young stellar objects. *In* S. Boissier, P. de Laverny, N. Nardetto, R. Samadi, D. Valls-Gabaud et H. Wozniak, éditeurs : *SF2A-2012 : Proceedings of the Annual meeting of the French Society of Astronomy and Astrophysics*, pages 347–350, décembre 2012b.

L. Ibgui, I. Hubeny, T. Lanz, C. Stehlé, M. González et J. P. Chièze : 3D Spectral Radiative Transfer with IRIS : Application to the Simulation of Laboratory Models of Accretion Shocks in Young Stellar Objects. *In* N. V. Pogorelov, E. Audit et G. P. Zank, éditeurs : *Numerical Modeling of Space Plasma Flows (ASTRONUM2012)*, volume 474 de *Astronomical Society of the Pacific Conference Series*, page 66, avril 2013b.

L. Ibgui, S. Orlando, C. Stehlé, J.-P. Chièze, I. Hubeny, T. Lanz, L. de Sá, T. Matsakos, M. González et R. Bonito : 3D Gray Radiative Properties of Accretion Shocks in Young Stellar Objects. *In European Physical Journal Web of Conferences*, volume 64 de *European Physical Journal Web of Conferences*, page 4005, janvier 2014b.

L. Ibgui, C. Stehlé, M. González, J.-P. Chièze, L. de Sá, T. Lanz et I. Hubeny : Assessment of the gray M_1 model in the case of a laboratory radiative shock simulation. *High Energy Density Physics*, 17:98–105, décembre 2015.

T. Isaac et M. G. Knepley : Support for Non-conformal Meshes in PETSc's DMPlex Interface. *ArXiv e-prints*, août 2015.

M. Joos, P. Hennebelle et A. Ciardi : Protostellar disk formation and transport of angular momentum during magnetized core collapse. *A&A*, 543:A128, juillet 2012.

P. A. Keiter, R. P. Drake, T. S. Perry, H. F. Robey, B. A. Remington, C. A. Iglesias, R. J. Wallace et J. Knauer : Observation of a Hydrodynamically Driven, Radiative-Precursor Shock. *Physical Review Letters*, 89(16):165003, septembre 2002.

D.S. Kershaw : *Flux limiting nature's own way – A new method for numerical solution of the transport equation.* Jul 1976. URL http://www.osti.gov/scitech/servlets/purl/104974.

M. Klassen, R. E. Pudritz, R. Kuiper, T. Peters et R. Banerjee : Simulating the Formation of Massive Protostars. I. Radiative Feedback and Accretion Disks. *ApJ*, 823:28, mai 2016.

S. M. Kolb, M. Stute, W. Kley et A. Mignone : Radiation hydrodynamics integrated in the PLUTO code. *A&A*, 559:A80, novembre 2013.

V. Könyves, P. André, A. Men'shchikov, N. Schneider, D. Arzoumanian, S. Bontemps, M. Attard, F. Motte, P. Didelon, A. Maury, A. Abergel, B. Ali, J.-P. Baluteau, J.-P. Bernard, L. Cambrésy, P. Cox, J. di Francesco, A. M. di Giorgio, M. J. Griffin, P. Hargrave, M. Huang, J. Kirk, J. Z. Li, P. Martin, V. Minier, S. Molinari, G. Olofsson, S. Pezzuto, D. Russeil, H. Roussel, P. Saraceno, M. Sauvage, B. Sibthorpe, L. Spinoglio, L. Testi, D. Ward-Thompson, G. White, C. D. Wilson, A. Woodcraft et A. Zavagno : The Aquila prestellar core population revealed by Herschel. *A&A*, 518:L106, juillet 2010.

K. Kotake : Multiple physical elements to determine the gravitational-wave signatures of core-collapse supernovae. *Comptes Rendus Physique*, 14:318–351, avril 2013.

R. Krasnopolsky, Z.-Y. Li, H. Shang et B. Zhao : Protostellar Accretion Flows Destabilized by Magnetic Flux Redistribution. *ApJ*, 757:77, septembre 2012.

M. R. Krumholz, R. I. Klein, C. F. McKee, S. S. R. Offner et A. J. Cunningham : The Formation of Massive Star Systems by Accretion. *Science*, 323:754, février 2009.

M.R. Krumholz, R.I. Klein, C.F. McKee et John Bolstad : Equations and algorithms for mixed-frame flux-limited diffusion radiation hydrodynamics. *The Astrophysical Journal*, 667:626, 2007. URL http://iopscience.iop.org/0004-637X/667/1/626.

R. Kuiper, H. Klahr, H. Beuther et T. Henning : Circumventing the Radiation Pressure Barrier in the Formation of Massive Stars via Disk Accretion. *ApJ*, 722:1556–1576, octobre 2010.

R. Kuiper, H. Klahr, H. Beuther et T. Henning : On the stability of radiation-pressure-dominated cavities. *A&A*, 537:A122, janvier 2012.

R. Kuiper et H. W. Yorke : On the Simultaneous Evolution of Massive Protostars and Their Host Cores. *ApJ*, 772:61, juillet 2013.

Rolf Kuiper, H Klahr, C Dullemond, W Kley et T Henning : Fast and accurate frequency-dependent radiation transport for hydrodynamics simulations in massive star formation. *Astronomy & Astrophysics*, 511: A81, 2010. URL http://cdsweb.cern.ch/record/1234481.

Rolf Kuiper et R. S. Klessen : The reliability of approximate radiation transport methods for irradiated disk studies. *Astronomy & Astrophysics*, 555:A7, jun 2013. ISSN 0004-6361. URL http://www.aanda.org/articles/aa/full{_}html/2013/07/aa21404-13/aa21404-13.html.

T. Kuroda, T. Takiwaki et K. Kotake : Gravitational wave signatures from low-mode spiral instabilities in rapidly rotating supernova cores. *Phys. Rev. D*, 89(4):044011, février 2014.

S. A. Lamzin : The Structure of the Shock Wave in the Case of an Accretion onto Low Mass Young Stars. *Ap&SS*, 261:137–140, 1998.

S. A. Lamzin : Calculation of profiles of CIV, NV, OVI, and SiIV resonance lines formed in accretion shocks in T Tauri stars : A plane layer. *Astronomy Reports*, 47:498–510, juin 2003.

R. B. Larson : Numerical calculations of the dynamics of collapsing proto-star. *MNRAS*, 145:271, 1969.

R. B. Larson et S. Starrfield : On the formation of massive stars and the upper limit of stellar masses. *A&A*, 13:190–197, juillet 1971.

CD Levermore : RELATING EDDINGTON FACTORS TO FLUX LIMITERS. *Journal of Quantitative Spectroscopy and Radiative Transfer*, 31 (2):149–160, 1984. URL http://linkinghub.elsevier.com/retrieve/pii/0022407384901122.

C.D. Levermore et G.C. Pomraning : A flux-limited diffusion theory. *The Astrophysical Journal*, 248:321–334, 1981. URL http://adsabs.harvard.edu/full/1981ApJ...248..321L.

J. Masson, G. Chabrier, P. Hennebelle, N. Vaytet et B. Commerçon : Ambipolar diffusion in low-mass star formation. I. General comparison with the ideal magnetohydrodynamic case. *A&A*, 587:A32, mars 2016.

T. Matsakos, J.-P. Chièze, C. Stehlé, M. González, L. Ibgui, L. de Sá, T. Lanz, S. Orlando, R. Bonito, C. Argiroffi, F. Reale et G. Peres : YSO accretion shocks : magnetic, chromospheric or stochastic flow effects can suppress fluctuations of X-ray emission. *A&A*, 557:A69, septembre 2013.

T. Matsakos, J.-P. Chièze, C. Stehlé, M. González, L. Ibgui, L. de Sá, T. Lanz, S. Orlando, R. Bonito, C. Argiroffi, F. Reale et G. Peres : 3D numerical modeling of YSO accretion shocks. *In European Physical Journal Web of Conferences*, volume 64 de *European Physical Journal Web of Conferences*, page 4003, janvier 2014a.

T. Matsakos, J.-P. Chièze, C. Stehlé, M. González, L. Ibgui, L. de Sá, T. Lanz, S. Orlando, R. Bonito, C. Argiroffi, F. Reale et G. Peres : 3D YSO accretion shock simulations : a study of the magnetic, chromospheric and stochastic flow effects. *In* P. Petit, M. Jardine et H. C. Spruit, éditeurs : *IAU Symposium*, volume 302 de *IAU Symposium*, pages 66–69, août 2014b.

C. F. McKee et J. C. Tan : The Formation of Massive Stars from Turbulent Cores. *ApJ*, 585:850–871, mars 2003.

D. Mihalas et B. Weibel Mihalas : *Foundations of radiation hydrodynamics*. 1984.

GN Minerbo : MAXIMUM ENTROPY EDDiNGTON FACTORS. *Journal of Quantitative Spectroscopy and Radiative*, 20:541–545, 1978. URL http://linkinghub.elsevier.com/retrieve/pii/0022407378900249.

T. C. Mouschovias et L. Spitzer, Jr. : Note on the collapse of magnetic interstellar clouds. *ApJ*, 210:326, décembre 1976.

L. Murchikova, E. Abdikamalov et T. Urbatsch : Analytic Closures for M1 Neutrino Transport. *ArXiv e-prints*, janvier 2017.

Andrew T. Myers, Christopher F. McKee, Andrew J. Cunningham, Richard I. Klein et Mark R. Krumholz : the Fragmentation of Magnetized, Massive Star-Forming Cores With Radiative Feedback. *The Astrophysical Journal*, 766(2):97, 2013. ISSN 0004-637X. URL http://arxiv.org/abs/1211.3467.

F. Ogando et P. Velarde : Development of a radiation transport fluid dynamic code under AMR scheme. *J. Quant. Spec. Radiat. Transf.*, 71: 541–550, octobre 2001.

J. C. B. Papaloizou et J. E. Pringle : The dynamical stability of differentially rotating discs with constant specific angular momentum. *MNRAS*, 208:721–750, juin 1984.

A. Passamonti et N. Andersson : The intimate relation between the low T/W instability and the corotation point. *MNRAS*, 446:555–565, janvier 2015.

T. Peters, R. S. Klessen, M.-M. Mac Low et R. Banerjee : Limiting Accretion onto Massive Stars by Fragmentation-induced Starvation. *ApJ*, 725:134–145, décembre 2010.

A. B. Reighard, R. P. Drake, K. K. Dannenberg, D. J. Kremer, M. Grosskopf, E. C. Harding, D. R. Leibrandt, S. G. Glendinning, T. S. Perry, B. a. Remington, J. Greenough, J. Knauer, T. Boehly, S. Bouquet, L. Boireau, M. Koenig et T. Vinci : Observation of collapsing radiative shocks in laboratory experiments. *Physics of Plasmas*, 13(8):082901, aug 2006. ISSN 1070664X. URL http://link.aip.org/link/PHPAEN/v13/i8/p082901/s1{&}Agg=doihttp://link.aip.org/link/?PHPAEN/13/082901/1.

E.-J. Rijkhorst, T. Plewa, A. Dubey et G. Mellema : Hybrid characteristics : 3D radiative transfer for parallel adaptive mesh refinement hydrodynamics. *A&A*, 452:907–920, juin 2006.

M.M. Romanova, G.V. Ustyugova, A.V. Koldoba, J.V. Wick et R.V.E. Lovelace : Three-dimensional Simulations of Disk Accretion to an Inclined Dipole. I. Magnetospheric Flows at Different Theta. *The Astrophysical Journal*, 595:1009–1031, 2003. URL http://iopscience.iop.org/0004-637X/595/2/1009/58084.text.html.

J. Rosdahl, J. Blaizot, D. Aubert, T. Stranex et R. Teyssier : RAMSES-RT : radiation hydrodynamics in the cosmological context. *MNRAS*, 436:2188–2231, décembre 2013.

J. Rosdahl et R. Teyssier : A scheme for radiation pressure and photon diffusion with the M1 closure in RAMSES-RT. *MNRAS*, 449:4380–4403, juin 2015.

A. L. Rosen, M. R. Krumholz, C. F. McKee et R. I. Klein : An unstable truth : how massive stars get their mass. *MNRAS*, 463:2553–2573, décembre 2016.

E. E. Salpeter : The Luminosity Function and Stellar Evolution. *ApJ*, 121:161, janvier 1955.

L. Scheck, H.-T. Janka, T. Foglizzo et K. Kifonidis : Multidimensional supernova simulations with approximative neutrino transport. II. Convection and the advective-acoustic cycle in the supernova core. *A&A*, 477:931–952, janvier 2008.

L. Scheck, T. Plewa, H.-T. Janka, K. Kifonidis et E. Müller : Pulsar Recoil by Large-Scale Anisotropies in Supernova Explosions. *Physical Review Letters*, 92(1):011103, janvier 2004.

M. Shibata, S. Karino et Y. Eriguchi : Dynamical instability of differentially rotating stars. *MNRAS*, 334:L27–L31, août 2002.

M. Aaron Skinner et Eve C. Ostriker : A TWO-MOMENT RADIATION HYDRODYNAMICS MODULE IN ATHENA USING A TIME-EXPLICIT GODUNOV METHOD. *The Astrophysical Journal Supplement Series*, 206(2):21, jun 2013. ISSN 0067-0049. URL http://arxiv.org/abs/1306.0010http://stacks.iop.org/0067-0049/206/i=2/a=21?key=crossref.495f8e02d6362a50c1419528bc13d5e0.

R. J. Smith, S. Longmore et I. Bonnell : The simultaneous formation of massive stars and stellar clusters. *MNRAS*, 400:1775–1784, décembre 2009.

J. C. Tan, M. T. Beltrán, P. Caselli, F. Fontani, A. Fuente, M. R. Krumholz, C. F. McKee et A. Stolte : Massive Star Formation. *Protostars and Planets VI*, pages 149–172, 2014.

R. Teyssier : Cosmological hydrodynamics with adaptive mesh refinement. *Astronomy and Astrophysics*, 385(1):337–364, apr 2002. ISSN 0004-6361. URL http://adsabs.harvard.edu/abs/2002A{%}26A...385..337Thttp://www.edpsciences.org/10.1051/0004-6361:20011817.

P. Tremblin, E. Audit, V. Minier et N. Schneider : 3D simulations of pillar formation around HII regions : the importance of shock curvature. *A&A*, 538:A31, février 2012.

NJ Turner et JM Stone : A module for radiation hydrodynamic calculations with zeus-2d using flux-limited diffusion. *The Astrophysical Journal Supplement Series*, 135:95, 2001. URL http://iopscience.iop.org/0067-0049/135/1/95.

R. Turpault : A consistent multigroup model for radiative transfer and its underlying mean opacities. *J. Quant. Spec. Radiat. Transf.*, 94:357–371, septembre 2005.

N. Vaytet, E. Audit, B. Dubroca et M. González : A Numerical Model for Multigroup Radiation Hydrodynamics. *In* N. V. Pogorelov, J. A. Font, E. Audit et G. P. Zank, éditeurs : *Numerical Modeling of Space Plasma Slows (ASTRONUM 2011)*, volume 459 de *Astronomical Society of the Pacific Conference Series*, page 180, juillet 2012.

N. Vaytet, M. González, E. Audit et G. Chabrier : The influence of frequency-dependent radiative transfer on the structures of radiative shocks. *J. Quant. Spec. Radiat. Transf.*, 125:105–122, août 2013.

N.M.H. Vaytet, Edouard Audit, Bruno Dubroca et Franck Delahaye : A numerical model for multigroup radiation hydrodynamics. *Journal of Quantitative Spectroscopy and Radiative Transfer*, 112(8):1323–1335, may 2011. ISSN 00224073. URL http://linkinghub.elsevier.com/retrieve/pii/S0022407311000525.

T. Vinci, M. Koenig, A. Benuzzi-Mounaix, N. Ozaki, A. Ravasio, L. Boireau, C. Michaut, S. Bouquet, S. Atzeni, A. Schiavi et O. Peyrusse : Radiative shocks : New results for laboratory astrophysics. *Journal de Physique IV*, 133:1039–1041, juin 2006.

A. J. Visco, R. P. Drake, S. H. Glenzer, T. Döppner, G. Gregori, D. H. Froula et M. J. Grosskopf : Measurement of Radiative Shock Properties by X-Ray Thomson Scattering. *Physical Review Letters*, 108 (14):145001, avril 2012.

A. L. Watts, N. Andersson et D. I. Jones : The Nature of Low T/|W| Dynamical Instabilities in Differentially Rotating Stars. *ApJ*, 618:L37–L40, janvier 2005.

S. C. Whitehouse, M. R. Bate et J. J. Monaghan : A faster algorithm for smoothed particle hydrodynamics with radiative transfer in the flux-limited diffusion approximation. *MNRAS*, 364:1367–1377, décembre 2005.

T. Yamasaki et T. Foglizzo : Effect of Rotation on the Stability of a Stalled Cylindrical Shock and Its Consequences for Core-Collapse Supernovae. *ApJ*, 679:607–615, mai 2008.

H. W. Yorke et C. Sonnhalter : On the Formation of Massive Stars. *ApJ*, 569:846–862, avril 2002.

Y. B. Zel'dovich et Y. P. Raizer : *Physics of shock waves and high-temperature hydrodynamic phenomena*. 1967.

H. Zinnecker et H. W. Yorke : Toward Understanding Massive Star Formation. *ARA&A*, 45:481–563, septembre 2007.